JSCSEN 91(1)1-97(2026)

ISSN 1820-7421(Online)

Journal of the Serbian Chemical Society

Electronic version

VOLUME 91

No 1

BELGRADE 2026

Available on line at

www.shd.org.rs/JSCS/

The **Journal of the Serbian Chemical Society** (formerly Glasnik Hemijskog društva Beograd), one volume (12 issues) per year, publishes articles from the fields of chemistry. The **Journal** is financially supported by the **Ministry of Education, Science and Technological Development of the Republic of Serbia.**
Articles published in the **Journal** are indexed in **Clarivate Analytics products: Science Citation Index-Expanded™** – accessed *via* **Web of Science®** and **Journal Citation Reports®**.
Impact Factor announced for the year 2024: **0.700; 5-year Impact Factor**: **0.900**.
Articles appearing in the **Journal** are also abstracted by: **Scopus, Chemical Abstracts Plus (CAplus℠), Directory of Open Access Journals, Referativnii Zhurnal (VINITI), RSC Analytical Abstracts, EuroPub, Pro Quest** and **Asian Digital Library.**

Publisher:	**Serbian Chemical Society**, Karnegijeva 4/III, P. O. Box 36, 1120 Belgrade 35, Serbia tel./fax: +381–11–3370–467, E-mails: **Society** – shd@shd.org.rs; **Journal** – jscs@shd.org.rs Home Pages: **Society** – http://www.shd.org.rs/, **Journal** – http://www.shd.org.rs/JSCS/
Internet Service:	Contents, Abstracts and full papers (from Vol. 64, No. 1, 1999) are available in the electronic form at the Web Site of the **Journal** (http://www.shd.org.rs/JSCS/).
Former Editors:	**Nikola A. Pušin** (1930–1947), **Aleksandar M. Leko** (1948–1954), **Panta S. Tutundžić** (1955**–**1961), **Miloš K. Mladenović** (1962–1964), **Đorđe M. Dimitrijević** (1965–1969), **Aleksandar R. Despić** (1969–1975), **Slobodan V. Ribnikar** (1975–1985), **Dragutin M. Dražić** (1986–2006).
Editor-in-Chief:	BRANISLAV Ž. **NIKOLIĆ**, Serbian Chemical Society (E-mail: jscs-ed@shd.org.rs)
Deputy Editor:	DUŠAN **SLADIĆ**, Faculty of Chemistry, University of Belgrade
Sub editors:	
Organic Chemistry	DEJAN **OPSENICA**, Institute of Chemistry, Technology and Metallurgy, University of Belgrade JÁNOS **CSANÁDI**, Faculty of Science, University of Novi Sad
Biochemistry and Biotechnology	OLGICA **NEDIĆ**, INEP – Institute for the Application of Nuclear Energy, University of Belgrade
Inorganic Chemistry	BILJANA **GLIŠIĆ**, Faculty of Science, University of Kragujevac
Theoretical Chemistry	MATIJA **ZLATAR**, Institute of Chemistry, Technology and Metallurgy, University of Belgrade MILOŠ **MILIČIĆ**, Faculty of Chemistry, University of Belgrade
Physical Chemistry	LJILJANA **DAMJANOVIĆ-VASILIĆ**, Faculty of Physical Chemistry, University of Belgrade
Electrochemistry	SNEŽANA **GOJKOVIĆ**, Faculty of Technology and Metallurgy, University of Belgrade
Analytical Chemistry	RADA **BAOŠIĆ**, Faculty of Chemistry, University of Belgrade
Polymers	BRANKO **DUNJIĆ**, Faculty of Technology and Metallurgy, University of Belgrade
Thermodynamics	MIRJANA **KIJEVČANIN**, Faculty of Technology and Metallurgy, University of Belgrade
Chemical Engineering	TATJANA **KALUĐEROVIĆ RADOIČIĆ**, Faculty of Technology and Metallurgy, University of Belgrade
Materials	RADA **PETROVIĆ**, Faculty of Technology and Metallurgy, University of Belgrade
Metallic Materials and Metallurgy	ANA **KOSTOV**, Mining and Metallurgy Institute Bor, University of Belgrade
Environmental and Geochemistry	VESNA **ANTIĆ**, Faculty of Agriculture, University of Belgrade
History of and Education in Chemistry	DRAGICA **TRIVIĆ**, Faculty of Chemistry, University of Belgrade
English Language Editors:	VLATKA **VAJS**, Serbian Chemical Society MIROSLAV **PAVLOVIĆ**, Institute of Chemistry, Technology and Metallurgy, University of Belgrade
Technical Editors:	VLADIMIR **PANIĆ**, Institute of Chemistry, Technology and Metallurgy, University of Belgrade, MARIO **ZLATOVIĆ**, Faculty of Chemistry, University of Belgrade
Journal Manager & Web Master:	MARIO **ZLATOVIĆ**, Faculty of Chemistry, University of Belgrade
Office:	VERA **ĆUŠIĆ**, Serbian Chemical Society

Editorial Board
From abroad: **R. Adžić**, Brookhaven National Laboratory (USA); **A. Casini**, University of Groningen (The Netherlands); **G. Cobb**, Baylor University (USA); **D. Douglas**, University of British Columbia (Canada); **G. Inzelt**, Etvos Lorand University (Hungary); **J. Kenny**, University of Perugia (Italy); **Ya. I. Korenman**, Voronezh Academy of Technology (Russian Federation); **M. D. Lechner**, University of Osnabrueck (Germany); **S. Macura**, Mayo Clinic (USA); **M. Spiteller**, INFU, Technical University Dortmund (Germany); **M. Stratakis**, University of Crete (Grecce); **M. Swart**, University de Girona (Cataluna, Spain); **G. Vunjak-Novaković**, Columbia University (USA); **P. Worsfold**, University of Plymouth (UK); **J. Zagal**, Universidad de Santiago de Chile (Chile).
From Serbia: **B. Abramović**, **V. Antić**, **R. Baošić**, **V. Beškoski**, **J. Csanadi**, **Lj. Damjanović-Vasilić**, **A. Dekanski**, **V. Dondur**, **B. Dunjić**, **M. Đuran, B. Glišić, S. Gojković**, **I. Gutman**, **B. Jovančićević**, **I. Juranić**, **T. Kaluđerović Radiočić**, **L. Katsikas**, **M. Kijevčanin**, **A. Kostov**, **V. Leovac**, **S. Milonjić**, **V.B. Mišković-Stanković**, **O. Nedić**, **B. Nikolić**, **D. Opsenica**, **V. Panić**, **M. Pavlović**, **M. Petkovska**, **R. Petrović**, **I. Popović**, **B. Radak**, **S. Ražić**, **D. Sladić**, **S. Sovilj**, **S. Šerbanović**, **B. Šolaja**, **Ž. Tešić**, **D. Trivić**, **V. Vajs, M. Zlatović**.

Subscription: The annual subscription rate is **150.00 €** including postage (surface mail) and handling. For Society members from abroad rate is **50.00 €**. For the proforma invoice with the instruction for bank payment contact the Society Office (E-mail: shd@shd.org.rs) or see JSCS Web Site: http://www.shd.org.rs/JSCS/, option Subscription.
Godišnja pretplata: Za članove SHD: **2.500,00 RSD**, za penzionere i studente: **1000,00 RSD**, a za ostale: **3.500,00 RSD**:za organizacije i ustanove: **16.000,00 RSD**. Uplate se vrše na tekući račun Društva: **205-13815-62**, poziv na broj **320**, sa naznakom "pretplata za JSCS".

Nota: Radovi čiji su svi autori članovi SHD prioritetno se publikuju.
Odlukom Odbora za hemiju Republičkog fonda za nauku Srbije, br. 66788/1 od 22.11.1990. godine, koja je kasnije potvrđena odlukom Saveta Fonda, časopis je uvršten u kategoriju međunarodnih časopisa (**M-23**). Takođe, aktom Ministarstva za nauku i tehnologiju Republike Srbije, 413-00-247/2000-01 od 15.06.2000. godine, ovaj časopis je proglašen za publikaciju od posebnog interesa za nauku. **Impact Factor** časopisa objavljen za 2024. godinu je **0,700**, a petogodišnji **Impact Factor 0,900**.

Journal of the Serbian Chemical Society
JSCS-info@shd.org.rs • www.shd.org.rs/JSCS

J. Serb. Chem. Soc. Vol. 91, No. 1 (2026)

CONTENTS*

Published by the Serbian Chemical Society
Karnegijeva 4/III, P.O. Box 36, 11120 Belgrade, Serbia
Printed by the Faculty of Technology and Metallurgy
Karnegijeva 4, P.O. Box 35-03, 11120 Belgrade, Serbia

* For colored figures in this issue please see electronic version at the Journal Home Page: http://www.shd.org.rs/JSCS/

Journal of the Serbian Chemical Society
JSCS@tmf.bg.ac.rs • www.shd.org.rs/JSCS
J. Serb. Chem. Soc. *91* (1) 1–10 (2026)
JSCS–5473
Original scientific paper
Published 5 February, 2026

Synthesis and mechanism of formation of hybrid structures comprising 2-oxochromene, thiazole and hydrazilidenechromene fragments

OLGA A. MAZHUKINA[1]*, ALEXANDER YU. KOSTRITSKY[1], VYACHESLAV S. GRINEV[1,2], YEKATERINA M. ARZYAMOVA[1] and ALEVTINA YU. YEGOROVA[1]

[1]*Institute of Chemistry, N.G. Chernyshevsky Saratov National Research State University, 83 Astrakhanskaya St., 410012 Saratov, Russian Federation and* [2]*Institute of Biochemistry and Physiology of Plants and Microorganisms—Subdivision of the Federal State Budgetary Research Institution Saratov Federal Scientific Centre of the Russian Academy of Sciences (IBPPM RAS), 13 Entuziastov Pr., 410049 Saratov, Russian Federation*

(Received 11 July, revised 22 September 2024, accepted 21 December 2025)

Abstract: Molecules with a hybrid structure containing 1,3-, 1,5-dicarbonyl fragments, based on 2*H*-chromen-2-one, hold significant potential as biologically active substances. A direct method has been developed for the preparation of thiosemicarbazones 2-(7-(aryl)-10,10-dimethyl-6-oxo-7,9,10,11-tetrahydro-6*H*,8*H*-chromeno[4,3-*b*]chromen-8-ylidene)hydrazine-1-carbothioamides. Their further modification by reaction with 3-bromoacetyl-2*H*-chromen-2-one was carried out, involving the thioamide group to form hybrid structures comprising 2-oxochromene, thiazole and hydrazineylidenechromene fragments (yield 71–97%). It is shown that hydrazine-1-carbothioamides can be obtained from both the initial 1,5-dicarbonyl compound and the product of its intramolecular *O*-heterocyclization. A one-step method is preferable, because the one-step method is preferred over the more labour-intensive two-step approach (with a similar yield). A plausible reaction mechanism is presented, based on quantum chemical calculations of few possible tautomeric forms of the intermediates and the corresponding products. A comparative analysis of the ^{1}H NMR spectrum of the experimental sample and the spectra of several possible final products calculated by a quantum chemical method has also confirmed the chosen reaction pathway.

Keywords: 2*H*-chromen-2-one; hydrazine-1-carbothioamide; tautomeric system; DFT.

* Corresponding author. E-mail: mazhukinaoa@gmail.com
https://doi.org/10.2298/JSC240711091M

INTRODUCTION

Nowadays, the interest in chromenone-containing systems is increasing due to their wide biological activity. Polyfunctional 4*H*-pyrans, most often used as antispasmodics,[1,2] have anti-HIV,[3] antioxidant[4] and antihistamine activities.[4] These compounds can also be used to treat neurodegenerative diseases, including Alzheimer's disease, schizophrenia and myoclonus. In addition, some 2-amino-4*H*--pyran derivatives can be used as photoactive materials. [5]

There are works[6–8] in the literature that demonstrate the possibility of carrying out a multi-component synthesis involving 3-substituted chromanone or 1,3-indanedione systems with urea derivatives and 3-bromomethylcoumarin. However, modifying the initial system by combining coumarin and a carbocyclic 1,3-diketone expands the synthetic capabilities to combine biologically relevant scaffolds.

In our previous studies, we found that 4-hydroxy-3-((2-hydroxy-4,4-dimethyl--6-oxocyclohex-1-en-1-yl)(aryl)methyl)-2*H*-chromen-2-ones **1a**, **b** and **d** (Fig. 1) exhibited anticoagulant activity, and Compound **1c** significantly reduced the rate of platelet aggregation. It has been also found that compound **1b** has a proplatelet effect, enhancing and accelerating platelet aggregation.[9]

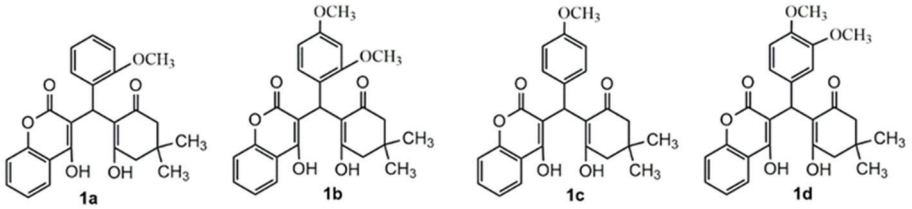

Fig. 1. Structures of biologically active 4-hydroxy-3-((2-hydroxy-4,4-dimethyl-6-oxocyclohex-1-en-1-yl)(aryl)methyl)-2*H*-chromen-2-ones **1a**–**d**.

EXPERIMENTAL

General information

Thin-layer chromatography (TLC), Fourier IR and ^{1}H-NMR spectroscopy were used to monitor the reaction progress, to analyze the main mixtures and isolated individual products, and to identify them. TLC analysis was performed on Silufol UV-254 plates, eluent – ethyl acetate:hexane:chloroform (2:2:1), developer – iodine vapor. FTIR spectra were recorded on a Nicolet 6700 spectrometer (Thermo Scientific, USA) in KBr pellets (wavenumber range 4000––400 cm^{-1}) with a spectral resolution of 4 cm^{-1}. ^{1}H-, ^{13}C-NMR, HSQC and HMBC spectra were recorded on a Varian 400 MHz spectrometer (USA) at 400 MHz for protons (^{1}H) and at 100 MHz for carbons (^{13}C). Chemical shifts are given here in ppm from tetramethylsilane (TMS) as an internal standard in deuterated chloroform ($CDCl_3$). Coupling constants (*J*) are reported in Hz. All spectra were recorded at 25 °C, unless otherwise specified. Melting points were measured at a heating rate of 4 °C/min with no correction. Elemental analysis was performed on a Vario micro cube – C, H, N, S elemental analyzer (Elementar Analysensysteme GmbH, Germany).

Quantum chemical calculations

Quantum chemical calculations were performed using the density functional theory (DFT) with Becke's three-parameter Lee–Yang–Parr (B3LYP) hybrid functional and the 6-311G(d,p) basis set, involving p-orbitals for hydrogen and d-orbitals for heavier atoms, as well as polarization functions (B3LYP/6-311G++ (d,p)).

The complete geometry was optimized for each possible isomer with a strict convergence criterion.

*General procedure for the synthesis of 7-aryl-10,10-dimethyl-7,9,10,11-tetrahydro-6*H*,8*H*--chromeno[4,3*-b*]chromene-6,8-diones **2a**–**e***

A mixture of 4-hydroxy-3-((2-hydroxy-4,4-dimethyl-6-oxocyclohex-1-en-1-yl)(aryl)methyl)-2*H*-chromen-2-ones **1a**–**e** (1.2 mmol) and acetyl acetate (3 mL, 31.8 mmol) was refluxed for 30–90 min. The liquid fraction was evaporated, and the crystals precipitated were filtered out.

*General procedure for the synthesis of 2-(7-aryl-10,10-dimethyl-6-oxo-7,9,10,11-tetrahydro--6*H*,8*H*-chromeno[4,3*-b*]chromen-8-ylidene)hydrazine-1-carbothioamides **3a**–**e***

Method 1. A mixture of 7-aryl-10,10-dimethyl-7,9,10,11-tetrahydro-6*H*,8*H*-chromeno[4,3--*b*]chromene-6,8-dione **2a**–**e** (0.6 mmol) and TSC (0.065 g, 0.7 mmol) in absolute ethanol (15 ml) was refluxed for 3 h. The liquid fraction was evaporated, and the crystals precipitated were filtered out.

Method 2. A mixture of 4-hydroxy-3-((2-hydroxy-4,4-dimethyl-6-oxocyclohex-1-en-1--yl)arylmethyl)-2*H*-chromen-2-one **1a**–**e** (0.6 mmol) and TSC (0.065 g, 0.7 mmol) in absolute ethanol (15 ml) was refluxed for 90 min. The liquid fraction was evaporated, and the precipitated crystals were filtered out.

*General procedure for the synthesis of 7-aryl-10,10-dimethyl-8-(2-(4-(2-oxo-2*H*-chromen-3-yl))-thiazol-2-yl)hydrazilidene)-8,9,10,11-tetrahydro-6*H*,7*H*-chromeno[4,3*-b*]chromene-6-ones **5a**–**e***

A mixture of carbothioamides **3a**–**e** (0.42 mmol) and 3-bromoacetyl-2*H*-chromen-2-one (0.11 g, 0.42 mmol) in absolute ethanol (15 ml) was refluxed for 2 h. The liquid fraction was evaporated, and the precipitated crystals were filtered out.

Analytical and spectral data of the compounds are given in the Supplementary material to this paper.

RESULTS AND DISCUSSION

In this work, we obtained polycyclic condensed compounds by reaction of the initial 4-hydroxy-3-((2-hydroxy-4,4-dimethyl-6-oxocyclohex-1-en-1-yl)(aryl)methyl)-2*H*-chromen-2-ones **1a**–**e** with acetic anhydride (Fig. 2). As a result, *O*--heterocyclization products with sufficiently high yields were obtained, namely: 7--aryl-10,10-dimethyl-7,9,10,11-tetrahydro-6*H*,8*H*-chromeno[4,3-*b*]chromene-6,8--diones **2a**–**e** (Fig. 2), whose structure was confirmed by ^{1}H-, ^{13}C-NMR, HSQC and HMBC spectroscopy data.

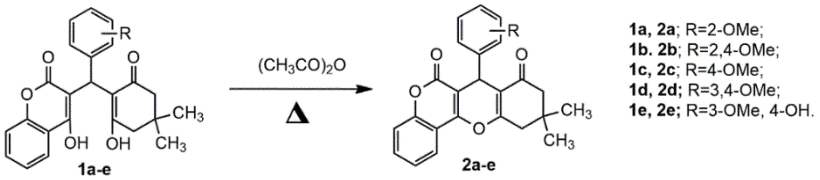

Fig. 2. *O*-Heterocyclization of 4-hydroxy-3-((2-hydroxy-4,4-dimethyl-6-oxocyclohex-1-en-1--yl)(aryl)methyl)-2*H*-chromen-2-ones **1a**–**e**.

In the ^{1}H-NMR spectra of the isolated chromeno[4,3-*b*]chromen-6,8-diones **2a**–**e**, as compared with those of the initial compounds, there are no signals of hydroxyl groups in a weak field, while the methine proton signal has shifted to a higher field (4.87–6.15 ppm). The protons of the methylene groups are characterized by magnetic non-equivalence, so each methylene group is displayed in the spectrum as a doublet of doublets at 2.45–2.69 and 2.13–2.29 ppm. This is explained by fixation of the dimedonyl ring, whose rotation around the single C–C bond gets impossible, which leads to the possibility of implementing an asymmetric spatial structure of the fragment.

The HSQC spectrum shows a difference in the chemical shifts of the methyl groups along both axes, due to the dimedonyl ring fixation.

A difference in the nature of the protons in the methylene groups is clearly visible in the HMBC spectrum. The protons in the methylene group located at the carbonyl group correlate with the carbonyl carbon atom at 2.28/195.67 ppm and the cross peak at 2.63/163.55 ppm reflects interaction between the protons in the methylene group and the C-2 atom of the 4*H*-pyran moiety in the compound.

For the purpose of further functionalization and expansion of synthetic capabilities, the behavior of the initial polyoxo compounds in their nucleophilic transformations with TSC was studied. Our choice of this reagent was not accidental, since numerous studies have shown that thiosemicarbazones exhibit antimicrobial, antitumor properties and can inhibit the central nervous system activity.[10–15] It is believed that this is due to TSC being able to form various complex compounds with proteins and metal ions.[16] Therefore, of current interest is the preparation of polycondensed structures to combine the properties of semicarbazides and chromenochromenediones **2a**–**e** (polyfunctional compounds containing several electron--deficient centers).

This reaction was found to involve the dimedonyl carbonyl group of oxo compounds **2a**–**e** and the hydrazine fragment due to its greater activity compared to thioamide. The reaction produced carbothioamides **3a**–**e** in 44–51 % yields (Fig. 3).

A similar product was also obtained by direct reaction of the initial 2*H*--chromene-2-ones **1a**–**e** with TSC, which made it possible to bypass the isolation of the cyclization product into tetrahydrochromenochromendione **2** and, in general, significantly reduced the reaction time.

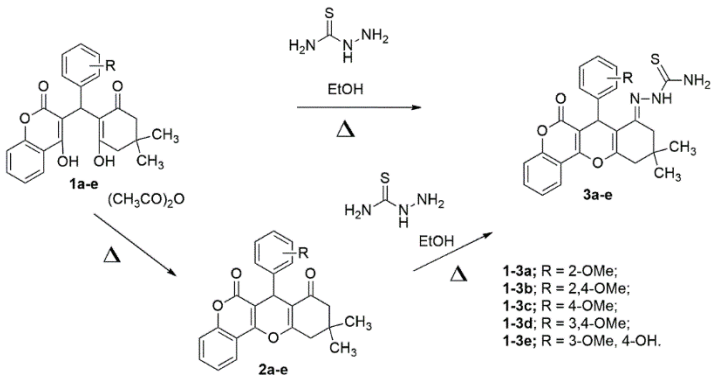

Fig. 3. Synthesis of chromeno[4,3-*b*]chromenhydrazine-1-carbothioamides **3a**–**e**.

Such a course of the process, namely, no products of nucleophilic attack at the competing reaction center in substrate **1**, allows us to conclude on the primary process of *O*-heterocyclization in compounds **2a**–**e**.

In the ^{1}H-NMR spectrum of carbothioamide **3** two protons of the thioamide group are located at 6.21–6.25 and 8.17–8.25 ppm, respectively; the NH proton singlet is located at 8.50–8.54 ppm, which is confirmed by the absence of correlation signals in the HSQC spectrum.

It is worth noting the signals at 8.52/178.6 ppm and 8.51/145.7 ppm in the HMBC spectrum, responsible for the interaction of the thioamide proton in the hydrazine fragment with the imine carbon atom, as well as with the α-carbon atom of the dihydropyran fragment, respectively; correlations of the protons of one of the methylene moieties at 2.24/145.2 ppm are also observed with the *α*-carbon atom and the tertiary proton of the dihydropyran heteroring at 5.48/145.2 ppm, which indicates the formation of thiosemicarbazone **3a**.

In order to obtain a series of novel complex polycyclic structures, carbothioamides **3** were reacted with 3-bromoacetylcoumarin. As a result of the reaction, the thiol group of compounds **3a**–**e** initially interacted with the haloalkyl fragment of the reagent to eliminate hydrogen bromide, which led to the formation of hydrazinecarbimidothiolate **4a**–**e** and its respective tautamers **4'a**–**e** and subsequent cyclization into either thiazoles **5a**–**e**, which can be tautomerized to **5'a**–**e** or **6a**–**e**, or mixture thereof.

In order to evaluate the reactivity of the nucleophilic centers of tautomers **4** and **4'**, the Fukui indices were calculated (Table I).

Quantum chemical calculations were carried out in the Firefly 8.2.0 program within the framework of density functional theory (DFT) using the B3LYP hybrid functional and the 6-31G(d,p) basis set.[17–20]

Full geometry optimization was done for neutral molecules; the energies of radical cations and radical anions were calculated based on the geometry of the

neutral molecule in accordance with Koopmans' theorem. From these values, ionization energies (I) and electron affinities (A) were calculated. For an N-electron system, the Fukui indices (FI) were calculated using the Mulliken populations (q) by the following equations:

$$FI^{+} = q(N+1) - q(N) \quad (1)$$

$$FI^{-} = q(N) - q(N-1) \quad (2)$$

where $q(N)$ is the population of the atom in a neutral molecule (cluster), and $q(N-1)$ and $q(N+1)$ are the population of the atom in the cation and anion of the molecule (cluster), respectively.

TABLE I. Reactivity indices of hydrazinecarbimidothioate **4'a** and carbamohydrazonothioate **4a**

Compound	Reactivity indices (FI^{-}/FI^{+})	
	N (27)	N (29)
4a	0.049118/−0.0028	0.062148/0.002623
4'a	0.026116/0.019385	0.030662/−0.02827

According to the calculated Fukui indices, N (29) is more nucleophilic in both tautomeric forms **4** and **4'a**, which suggests its nucleophilic attack at the free carbonyl group in compounds **5a**–**e** or its tautamer forms **5'a**–**e**. Then, the attack of compound **4'a** with hydrazine N (27) to form adduct **6** would not be beneficial (Fig. 4).

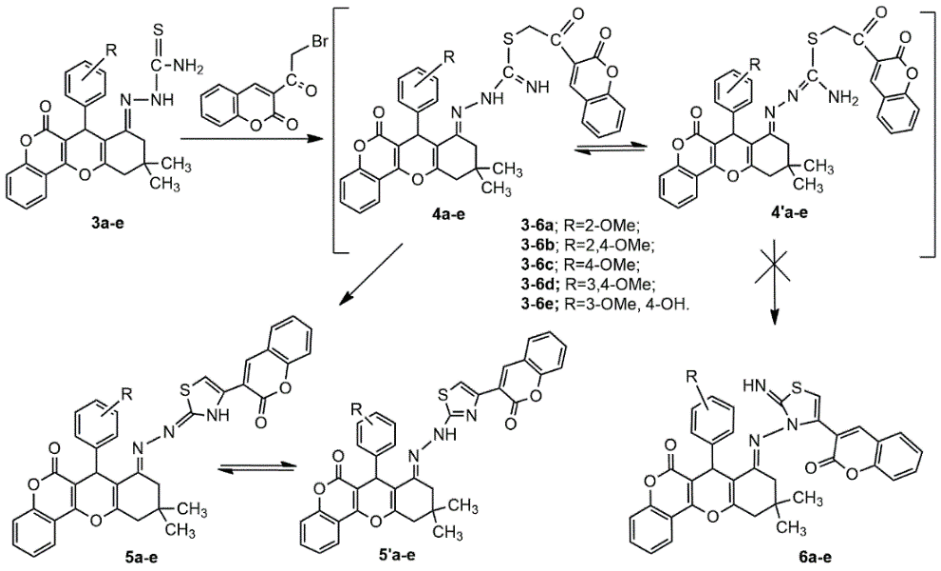

Fig. 4. Synthesis of thiazolehydrazonotetrahydrochromeno[4,3-*b*]chromen-6(7*H*)-ones **5a**–**e**.

To prove the above, the energy profile of the *N*-heterocyclization reaction was computed. Hydrazinecarbimidothiolate **4** can be considered as a common intermediate in the process of formation of all three possible products. The energy barrier for the reaction, calculated using DFT/B3LYP/6-31G(d) in vacuum, was thus estimated to be 11.70 kcal*/mol. Regardless of the choice of the reaction center, a new thiazole ring is formed as a result of intramolecular nucleophilic attack of the carbonyl carbon atom by the nitrogen atom. Considering the geometry optimization of the molecules of all three hypothetical products using 7-(2-methoxy)-phenyl derivatives as an example, it should be noted that chromenylthiazole-2(3*H*)--ylidene)hydrazono)tetrahydrochromeno[4,3-*b*]chromen-6(7*H*)-one (**5**) has turned out to be stabilized due to the formation of a hydrogen bond (1.983 Å) between the hydrogen atom of the NH group of the thiazole ring and the oxygen of the lactone carbonyl group, which ensures the coplanarity of the chromene and thiazole rings and the entire structure as a whole and reduces the overall energy of the molecule (Fig. 5).

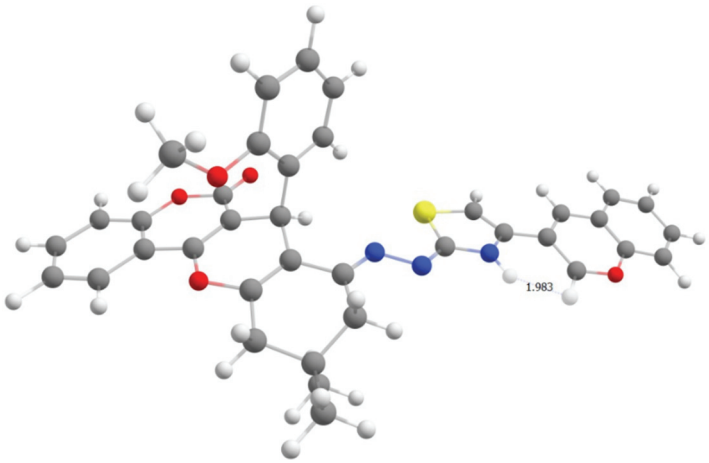

Fig. 5. Optimized geometry of 10,10-dimethyl-8-((4-(2-oxo-2*H*-chromen-3-yl)thiazol-2(3*H*)--ylidene)hydrazono)-7-(2-methoxyphenyl)-8,9,10,11-tetrahydrochromeno[4,3-*b*]chromen--6(7*H*)-one (**5a**).

As for the third option of *N*-heterocyclization due to nucleophilic attack by the hydrazine nitrogen in chromenylthiazol-3(2*H*)-ylimino-tetrahydrochromeno[4,3--*b*]chromen-6(7*H*)-one (**6a**), having considered the optimized geometry of the adduct, where in addition to the lack of coplanarity of the cycles, their proximity is observed, which determines an unfavorable spatial structure reaction. Moreover, having computed its formation energy, we can definitely state the impossibility of

* 1 kcal = 4184 J

its formation in the course of this reaction, since it significantly exceeds even the energy of the selected intermediate.

The energy diagram of the proposed simplified *N*-heterocyclization scheme was computed using the example of 2-methoxy derivative (**a**) within the framework of DFT/B3LYP/6-31G(d) in vacuum with complete optimization of the geometry of all proposed structures (Fig. 6). According to these calculations, a probable pathway of the process can be deduced as the transition of tautomer **4** to the energetically more favorable carbamohydrazonothiolate **4'**, followed by cyclization to thiazolehydrazonotetrahydrochromenochromenone (**5**).

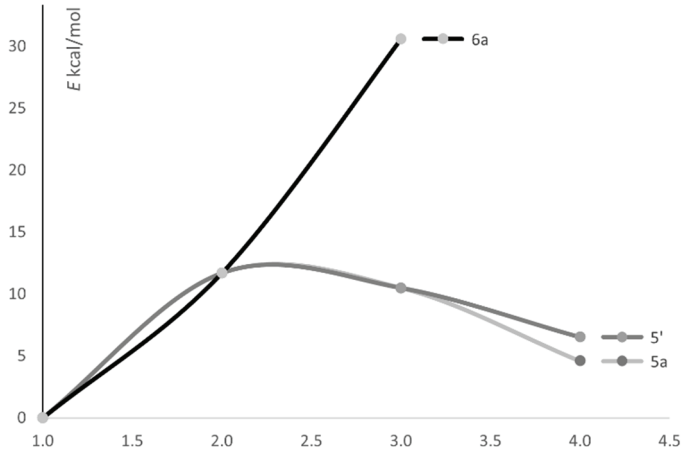

Fig. 6. Energy diagram of the reaction of hydrazinecarbothioamide (**3a**) with 3-bromoacetylcoumarin.

There is only one set of signals in the ^{1}H-NMR spectra of the products **5a**–**e**. This suggests that only one of the tautomeric forms is stabilized (at least in deuteronchloroform). Compared with the spectrum of the precursor, there are no signals from the thioamide group protons. A signal is observed of the vinyl proton in the thiazole heteroring at 7.87–7.93 ppm. The vinyl proton of the chromenone ring is located at 8.48–8.56 ppm, the broadened signal of the NH group is at 10.61–10.93 ppm. But since the resulting set of signals, in general, could correspond to any of the tautomeric forms of the final thiazole **5** or **5'**, to clarify the structure of the final product, we calculated the chemical shifts of protons in the putative tautomers both in vacuum and in the solvent, which was most close to deuterochloroform (which the spectra were experimentally recorded in) according to its characteristics. The calculated chemical shifts of the vinyl, methine protons and amino group protons correlate well with the experimental data. A distinctive feature of this type of compounds is the shift of the key signal of the amine proton to a weak field, which is probably explained by the formation of an intramolecular hydrogen bond with its participation, which is consistent with the structure of compounds **5a**–**e**.

In the 2D correlation HSQC spectrum of chromenylthiazol-2(3*H*)-ylidene)-hydrazono)-tetrahydrochromeno[4,3-*b*]chromen-6(7*H*)-one (**5a**), the previously absent signals are noted at 7.91/110.55 ppm, belonging to the vinyl proton of the newly formed thiazole heteroring, as well as a signal from the vinyl proton of the chromenone fragment at 8.50/139.0 ppm.

In the HMBC spectrum, the key correlation signal means contact of the vinyl proton of the thiazole heterofragment H62 with the carbonyl carbon of the lactone fragment of chromenone C38 at 7.82/167.89 ppm. As the HMBC spectrum lacks any correlation between the protons of the hydrazine group and the carbon atom of the methylene unit of the dimedone ring, characteristic of structure **5'**, this finally confirms the formation of tautomer **5**.

CONCLUSION

Thus, as a result of a series of chemical transformations, it is possible to derivatize the molecules of oxocyclohexenyl(aryl)methyl-2*H*-chromen-2-ones **1a**–**e** by introducing pharmacophoric fragments (thiazole and chromen-2-one) therein. Using calculated and experimental data, a probable pathway of the transformations, the structure of the intermediates and final reaction products are shown.

SUPPLEMENTARY MATERIAL

Additional data and information are available electronically at the pages of journal website: https://www.shd-pub.org.rs/index.php/JSCS/article/view/12976, or from the corresponding author on request.

ИЗВОД

СИНТЕЗА И МЕХАНИЗАМ ФОРМИРАЊА ХИБРИДНИХ СТРУКТУРА КОЈИ КАО СТРУКТУРНЕ ДЕЛОВЕ САДРЖЕ 2-ОКСОХРОМЕН, ТИАЗОЛ И ХИДРАЗИЛИДЕНХРОМЕН

OLGA A. MAZHUKINA[1], ALEXANDER YU. KOSTRITSKY[1], VYACHESLAV S. GRINEV[1,2], YEKATERINA M. ARZYAMOVA[1] и ALEVTINA YU. YEGOROVA[1]

[1]Institute of Chemistry, N.G. Chernyshevsky Saratov National Research State University, 83 Astrakhanskaya St., 410012 Saratov, Russian Federation u [2]Institute of Biochemistry and Physiology of Plants and Microorganisms—Subdivision of the Federal State Budgetary Research Institution Saratov Federal Scientific Centre of the Russian Academy of Sciences (IBPPM RAS), 13 Entuziastov Pr., 410049 Saratov, Russian Federation

Хибридни молекули која садржи 1,3- и 1,5-дикарбонилне фрагменте, засновани на 2*H*-хромен-2-ону, имају значајан потенцијал као биолошки активне супстанце. Развијена је директна метода за припрему тиосемикарбазона 2-(7-(арил)-10,10-диметил-6-оксо-7,9,10,11-тетрахидро-6*H*,8*H*-хромено[4,3-*b*]хромен-8-илиден)хидразин-1-карботиоамида. Извршена је њихова даља модификација реакцијом са 3-бромоацетил-2*H*-хромен-2-оном, која укључује тиоамидну групу, ри чему су добијене хибридне структуре које садрже 2-оксохроменске, тиазолне и хидразинилиденхроменске фрагменте (принос 71–97 %). Показано је да се хидразин-1-карботиоамиди могу добити и из почетног 1,5-дикарбонилног једињења и из производа његове интрамолекуларне *O*-хетероциклизације. Једностепени метод је пожељнији, јер је једностепени метод пожељнији у односу на радно интензивнији двостепени приступ (са сличним приносом). Представљен је вероватан

механизам реакције, заснован на квантно-хемијским прорачунима неколико могућих таутомерних облика интермедијера и одговарајућих производа. Упоредна анализа ^{1}H--NMR спектра експерименталног узорка и спектара неколико могућих финалних производа израчунатих квантно-хемијском методом такође је потврдила изабрани реакциони пут.

(Примљено 11. јула, ревидирано 22. септембра 2024, прихваћено 21. децембра 2025)

REFERENCES

1. L. Bonsignore, G. Loy, D. Secci, A. Calignano, *Eur. J. Med. Chem*. **28** (1993) 517 (https://doi.org/10.1016/0223-5234(93)90020-F)
2. C. Seoane, N. Martin, C. Pascual, L. L. Soto, *Heterocycles* **26** (1987) 2811 (https://doi.org/10.3987/R-1987-11-2811)
3. T. Pengsuparp, M. Serit, S. H. Hughes, D. D. Soejarto, J. M. Pezzuto, *J. Nat. Prod*. **59** (1996) 839 (https://doi.org/10.1021/np960399y)
4. B.-S. Yun, I.-K. Lee, I.-J. Ryoo, I.-D. Yoo, *J. Nat. Prod*. **64** (2001) 1238 (https://doi.org/10.1021/np0100946)
5. E.-W. Abd, H. F. Ashraf, *Pharmaceuticals* **5** (2012) 745 (https://doi.org/10.3390/ph5070745)
6. G. Rajitha, V. Ravibabu, G. Ramesh, B. Rajitha, R. Jobina, B. Siddhardha, V. Laxmi, *Res. Chem. Intermed*. **41** (2015) 9703 (https://doi.org/10.1007/s11164-015-1959-8)
7. S. B. Mohamed, Y. Rachedi, M. Hamdi, F. Le Bideau, C. Dejean, F. Dumas, *Eur. J. Org. Chem*. (2016) 2628 (https://doi.org/10.1002/ejoc.201600173)
8. R. Velpula, R. Deshineni, R. Gali, R. Bavantula, *Res. Chem. Intermed*. **42** (2016) 1729 (https://doi.org/10.1007/s11164-015-2114-2)
9. A. Yu. Kostritsky, A. Yu. Yegorova, O. V. Fedotova, *Int. J. Appl. Fund. Res*. **12** (2021) 88 (https://doi.org/10.17513/mjpfi.13336)
10. D. Armesto, W. M. Horspool, N. Martin, A. Ramos, C. Seoane, *J. Org. Chem*. **54** (1989) 3069 (https://doi.org/10.1021/jo00274a021)
11. P. Chellan, S. Nasser, L. Vivas, K. Chibale, G. S. Smith, *J. Organomet. Chem*. **695** (2010) 2225 (https://doi.org/10.1016/j.jorganchem.2010.06.010)
12. C. C. García, B. N. Brousse, M. J. Carlucci, A. G. Moglioni, M. M. Alho, G. Y. Moltrasio, N. B. D'Accorso, E. B. Damonte, *Antivir. Chem. Chemother*. **14** (2003) 61 (https://doi.org/10.1177/095632020301400205)
13. R. J. Glisoni, D. A. Chiappetta, L. M. Finkielsztein, A. G. Moglioni, A. Sosnik, *New J. Chem*. **34** (2010) 2047 (https://doi.org/10.1039/C0NJ00061B)
14. A. S. Shawali, *J. Adv. Res*. **5** (2014) 1 (https://doi.org/10.1016/j.jare.2013.01.004)
15. P. Zhan, X. Liu, Y. Cao, Y. Wang, C. Pannecouque, E. De Clercq, *Bioorg. Med. Chem. Lett*. **18** (2008) 5368 (https://doi.org/10.1016/j.bmcl.2008.09.055)
16. A. M. Vijesh, A. M. Isloor, S. Telkar, S. K. Peethambar, S. Rai, N. Isloor, *Eur. J. Med. Chem*. **46** (2011) 3531 (https://doi.org/10.1016/j.ejmech.2011.05.005)
17. A. D. Becke, *J. Chem. Phys*. **98** (1993) 5648 (https://doi.org/10.1063/1.464913)
18. A. D. Becke, *Phys. Rev., A* **38** (1988) 3098 (https://doi.org/10.1103/PhysRevA.38.3098)
19. C. Lee, W. Yang, R. G. Parr, *Phys. Rev., B* **37** (1988) 785 (https://doi.org/10.1103/PhysRevB.37.785)
20. R. Krishnan, J. S. Binkley, R. Seeger, J. A. Pople, *J. Chem. Phys*. **72** (1980) 650 (https://doi.org/10.1063/1.438955).

Journal of the Serbian Chemical Society
JSCS@tmf.bg.ac.rs • www.shd.org.rs/JSCS
J. Serb. Chem. Soc. *91* (1) S1–S14 (2026) *Supplementary material*

SUPPLEMENTARY MATERIAL TO

Synthesis and mechanism of formation of hybrid structures comprising 2-oxochromene, thiazole and hydrazilidenechromene fragments

OLGA A. MAZHUKINA[1]*, ALEXANDER YU. KOSTRITSKY[1], VYACHESLAV S. GRINEV[1,2], YEKATERINA M. ARZYAMOVA[1] and ALEVTINA YU. YEGOROVA[1]

[1]Institute of Chemistry, N.G. Chernyshevsky Saratov National Research State University, 83 Astrakhanskaya St., 410012 Saratov, Russian Federation, and [2]Institute of Biochemistry and Physiology of Plants and Microorganisms—Subdivision of the Federal State Budgetary Research Institution Saratov Federal Scientific Centre of the Russian Academy of Sciences (IBPPM RAS), 13 Entuziastov Pr., 410049 Saratov, Russian Federation

J. Serb. Chem. Soc. *91* (1) (2026) 1–10

*7-(2-Methoxyphenyl)-10,10-dimethyl-7,9,10,11-tetrahydro-6H,8H-chromeno[4,3--b]chromene-6,8-dione (**2a**)*

This compound was obtained as a white solid, yield 0.35 g (74%), mp 193–195°C. IR; 3057, 3001, 2958, 2870, 2837 (C–H), 1725 (O–C=O), 1665 (C=O), 1611, 1568, 1502, 1489 (C=C), 1227 (=C–O–C). ^{1}H NMR (400 MHz, $CDCl_3$, δ/ ppm): 1.03 (s, 3H, CH_3), 1.15 (s, 3H, CH_3), 2.26 (q, J = 16.2 Hz, 2H, CH_2), 2.65–2.58 (m, 2H, CH_2), 3.69 (s, 3H, OCH_3), 5.04 (s,1H, CH), 6.79–6.75 (m, 1H, Ar), 6.91 (dd, 1H, J = 7.5, 1.2 Hz, Ar), 7.15 (td, 1H, J = 7.8, 1.7 Hz, Ar), 7.26 (s, 1H, Ar), 7.37–7.27 (m, 2H, Ar), 7.52 (dd, 1H, J = 5.0, 3.2 Hz, Ar), 7.89–7.86 (m, 1H, Ar). ^{13}C NMR (100 MHz, $CDCl_3$, δ / ppm): 162.45, 160.62, 157.96, 154.46, 152.63, 132.48, 131.77, 129.09, 128.46, 124.02, 122.17, 120.60, 116,80, 113.91, 113.33, 111.15, 105.08, 55.41, 50.76, 40.94, 31.19, 31.18, 29.35, 26.92; calcd for $C_{25}H_{22}O_5$: C, 74.61; H, 5.51, found: C, 75.21; H, 5.28.

*7-(2,4-Dimethoxyphenyl)-10,10-dimethyl-7,9,10,11-tetrahydro-6H,8H-chromeno-[4,3-b]chromene-6,8-dione (**2b**)*

This compound was obtained as a white solid, yield 0.33 g (69%), mp 201–202°C. IR; 3082, 2962, 2935, 2873 (C–H), 1734 (O–C=O), 1688 (C=O), 1630, 1611, 1599, 1584, 1557 (C=C), 1223 (=C–O–C). ^{1}H NMR (400 MHz, $CDCl_3$, δ/ ppm): 1.03 (s, 3H, CH_3), 1.15 (s, 3H, CH_3), 2.25 (q, J = 8 Hz, J = 8 Hz, 2H, CH_2), 2.59 (m, 2H, CH_2), 3.64 (s, 3H, OCH_3), 3.74 (s,3H, OCH_3), 4.95 (s,1H, CH), 6.32

* Corresponding author. E-mail: mazhukinaoa@gmail.com

(d, 1H, J = 2.4 Hz, Ar), 6.46 (dd, 1H, J = 8.3, 2.3 Hz, Ar), 7.32–7.20 (m, 2H, Ar), 7.43 (d, 1H, J = 8.3 Hz, Ar), 7.52 (t, 1H, J = 7.8 Hz, Ar), 7.86 (d, 1H, J = 7.8 Hz, Ar). ^{13}C NMR (100 MHz, $CDCl_3$, δ / ppm): 162.40, 160.73, 160.11, 158.82, 154.35, 152.58, 137.03, 132.95, 131.71, 124.04, 122.17, 121.73, 116.77, 113.95, 113.33, 105.29, 104.40, 98.97, 55.35, 50.78, 40.93, 32.19, 30.67, 29.41, 26.87, 20.33; calcd for $C_{26}H_{24}O_6$: C, 72.21; H, 5.59, found: C, 72.85; H, 5.82.

*7-(4-Methoxyphenyl)-10,10-dimethyl-7,9,10,11-tetrahydro-6H,8H-chromeno[4,3--b]chromene-6,8-dione (**2c**)*

This compound was obtained as a white solid, yield 0.33 g (69%), mp 290–291°C. IR; 3074, 2958, 2906, 2908, 2873 (C–H), 1706 (O–C=O), 1646 (C=O), 1634, 1607, 1511, 1483 (C=C), 1225 (=C–O–C). ^{1}H NMR (400 MHz, $CDCl_3$, δ / ppm): 1.13 (s, 3H, CH_3), 1.23 (s, 3H, CH_3), 2.32 (s, 2H, CH_2), 2.54–2.81 (m, 2H, CH_2), 3.84 (s, 3H, OCH_3), 4.98 (s, 1H, CH), 6.62–6.77 (m, 1H, Ar), 6.75–6.92 (m, 1H, Ar), 7.18 (d, 1H, J = 1.9 Hz, Ar), 7.26 (s, 1H, Ar), 7.35 (t, 2H, J = 8.0 Hz, Ar), 7.57 (t, 1H, J = 7.4 Hz, Ar), 7.85 (d, 1H, J = 7.9 Hz, Ar). ^{13}C NMR (100 MHz, $CDCl_3$, δ / ppm): 168.81, 160.16, 160.56, 154.01, 152.63, 150.73, 141.15, 138.77, 136.89, 132.24, 124.23, 122.34, 119.70, 116.94, 115.01, 114.00, 113.70, 106.63, 55.97, 50.73, 40.89, 33.01, 29.03, 27.70, 20.63; calcd for $C_{25}H_{22}O_5$: C, 74.61; H, 5.51, found: C, 74.15; H, 5.27.

*7-(3,4-Dimethoxyphenyl)-10,10-dimethyl-7,9,10,11-tetrahydro-6H,8H-chromeno-[4,3-b]chromene-6,8-dione (**2d**)*

This compound was obtained as a white solid, yield 0.33 g (69%), mp 223–224°C. IR; 3098, 3008, 2954, 2925, 2866, 2833 (C–H), 1700 (O–C=O), 1648 (C=O), 1615, 1567, 1503, 1470 (C=C), 1208 (=C–O–C). ^{1}H NMR (400 MHz, $CDCl_3$, δ / ppm): 1.13 (s, 3H, CH_3), 1.26 (s, 3H, CH_3), 2.16 (dd, J = 16.2 Hz, J = 8.8 Hz, 2H, CH_2), 2.46 (s, 2H, CH_2), 3.74 (s, 3H, OCH_3), 3.87 (s,3H, OCH_3), 5.08 (s,1H, CH), 6.71 (d, 1H, J = 2.6 Hz, Ar), 6.78 (dd, 1H, J = 8.3, 2.3 Hz, Ar), 7.32–7.25 (m, 2H, Ar), 7.48 (d, 1H, J = 8.3 Hz, Ar), 7.52 (t, 1H, J = 7.8 Hz, Ar), 8.01 (d, 1H, J = 7.8 Hz, Ar). ^{13}C NMR (100 MHz, $CDCl_3$, δ / ppm): 161.48, 161.19, 160.05, 158.52, 155.36, 153.36, 133.06, 132.92, 125.24, 122.84, 120.68, 117.85, 115.82, 113.67, 110.25, 108.82, 106.07, 101.93, 56.58, 53.05, 43.54, 32.92, 31.08, 28.24, 26.43, 24.93; calcd for $C_{26}H_{24}O_6$: C, 72.21; H, 5.59, found: C, 72.48; H, 5.43.

*7-(3-Methoxy-4-hydroxyphenyl)-10,10-dimethyl-7,9,10,11-tetrahydro-6H,8H--chromeno[4,3-b]chromene-6,8-dione (**2e**)*

This compound was obtained as a white solid, yield 0.32 g (69%), mp 246–248°C. IR; 3365 (O–H), 3170, 3049, 2958, 2873, 2835 (C–H), 1688 (O–C=O), 1648 (C=O), 1624, 1513, 1489, 1473, 1434 (C=C), 1244 (=C–O–C). ^{1}H NMR (400 MHz, $CDCl_3$, δ / ppm): 1.10 (s, 3H, CH_3), 1.16 (s, 3H, CH_3), 2.30 (dd, 2H, J = 4.7,

1.9 Hz, CH_2), 2.64–2.70 (m, 2H, CH_2), 3.91 (s, 3H, OCH_3), 4.88 (s, 1H, CH), 5.50 (s, 1H, OH), 6.62 (dt, 1H, J = 8.3, 2.0 Hz, Ar), 6.74 (dd, 1H, J = 8.1, 1.9 Hz, Ar), 7.12 (d, 1H, J = 2.0 Hz, Ar), 7.26 (d, 1H, J = 1.9 Hz, Ar), 7.32–7.34 (m, 2H, Ar), 7.55 (d, 1H, J = 7.9 Hz, Ar), 7.85 (dd, 1H, J = 7.9, 1.9 Hz, Ar). ^{13}C NMR (100 MHz, $CDCl_3$, δ / ppm): 161.81, 160.76, 153.67, 152.55, 146.07, 144.61, 134.79, 132.11, 124.22, 122.37, 120.24, 116.89, 115.25, 114.09, 113.78, 112.51, 106.98, 95.34, 55.97, 50.74, 40.83, 32.85, 32.32, 29.16, 27.52; calcd for $C_{25}H_{22}O_6$: C, 72.76; H, 5.30, found: C, 72.54; H, 5.94.

2-(7-(2-Methoxyphenyl)-10,10-dimethyl-6-oxo-7,9,10,11-tetrahydro-6H,8H--chromeno[4,3-b]chromen-8-ylidene)hydrazine -1-carbothioamide (3a)

This compound was obtained as a yellow solid, yield 0.13 g (45%) (*method 1*) or 0.21 g (72%) (*method 2*) , mp 274–276°C. IR; 3458, 3346 (N–H, NH_2), 3147 (N–H), 2957, 2921, 2837 (C–H), 1736 (O–C=O), 1675 (C=N), 1629, 1609, 1559, 1495 (C=C), 1096 (C=S). ^{1}H NMR (400 MHz, $CDCl_3$, δ/ ppm): 1.04 (s, 3H, CH_3), 1.18 (s, 3H, CH_3), 2.08–2.27 (m, 2H, CH_2), 2.54 (s, 2H, CH_2), 3.97 (s, 3H, OCH_3), 5.49 (s, 1H, CH), 6.23 (s, 1H, NH_2), 8.25 (s, 1H, NH), 8.50 (s, 1H, NH_2), 6.23 (s, 1H, Ar), 6.88 (dd, 2H, J = 15.7, 7.8 Hz, Ar), 7.02–7.15 (m, 2H, Ar), 7.21 – – 7.27 (m, 2H, Ar), 7.44–7.57 (m, 1H, Ar), 7.85 (dt, 1H, J = 8.0 Hz, Ar). ^{13}C NMR (100 MHz, $CDCl_3$, δ / ppm): 178.71, 161.97, 160.81, 156.72, 154.02, 152.46, 145.18, 139.32, 131.89, 129.37, 128.28, 124.08, 122.36, 121.71, 116.76, 113.95, 113.27, 111.83, 105.96, 57.06, 40.13, 36.77, 31.07, 29.66, 27.76, 27.36; calcd for $C_{26}H_{25}O_4N_3S$: C, 65.67; H, 5.30; S, 6.74; N, 8.84, found: C, 66.31; H, 5.84; S, 6.57; N, 8.13.

2-(7-(2,4-Dimethoxyphenyl)-10,10-dimethyl-6-oxo-7,9,10,11-tetrahydro-6H,8H-chromeno[4,3-b]chromen-8-ylidene)hydrazine -1-carbothioamide (3b)

This compound was obtained as a light yellow solid, yield 0.15 g (51%) (*method 1*) or 0.24 g (83%) (*method 2*), mp 233–235°C. IR; 3502, 3439 (N–H, NH_2), 3155 (N–H), 3068, 2968, 2929, 2831 (C–H), 1721 (O–C=O), 1677 (C=N), 1630, 1611, 1582, 1499 (C=C), 1094 (C=S). ^{1}H NMR (400 MHz, $CDCl_3$, δ/ ppm): 1.03 (s, 3H, CH_3), 1.17 (s, 3H, CH_3), 2.13–2.28 (m, , 2H, CH_2), 2.47–2.69 (m, 2H, CH_2), 3.73 (s, 3H, OCH_3), 3.93 (s, 3H, OCH_3), 5.37 (s, 1H, CH), 6.24 (s, 1H, NH_2), 8.16 (s, 1H, NH), 8.52 (s, 1H, NH_2), 6.30–6.45 (m, 3H, Ar), 6.98 (d, 1H, J = 8.4 Hz, Ar), 7.19–7.30 (m, 2H, Ar), 7.52 (ddd, 2H, J = 8.9, 7.5, 1.7 Hz, Ar), 7.85 (ddd, 1H, J = 7.9, 5.9, 1.6 Hz, Ar). ^{13}C NMR (100 MHz, $CDCl_3$, δ/ ppm): 178.84, 162.39, 160.07, 159.72, 157.64, 153.85, 152.49, 152.43, 146.30, 131.78, 129.94,125.10, 124.04, 122.31, 116.74, 114.01, 110.00, 106.31, 100.12, 56.90, 55.26, 40.90, 40.13, 32.22, 31.06, 29.68, 27.32; calcd for $C_{27}H_{27}O_5N_3S$: C, 64.14; H, 5.38; S, 6.34; N, 8.31, found: C, 63.75; H, 5.85; S, 6.48; N, 8.65.

2-(7-(4-Methoxyphenyl)-10,10-dimethyl-6-oxo-7,9,10,11-tetrahydro-6H,8H-chromeno[4,3-b]chromen-8-ylidene)hydrazine-1-carbothioamide (3c)

This compound was obtained as a light yellow solid, yield 0.16 g (54%) (*method 1*) or 0.20 g (69%) (*method 2*), mp 248–249°C. IR; 3506, 3485 (N–H, NH_2), 3074 (N–H), 3003, 2957, 2904 (C–H), 1719 (O–C=O), 1675 (C=N), 1619, 1607, 1565, 1509 (C=C), 1092 (C=S). ^{1}H NMR (400 MHz, $CDCl_3$, δ/ ppm): 1.05 (s, 3H, CH_3), 1.15 (s, 3H, CH_3), 2.18 (dd, J = 16.4 Hz, J = 32 Hz, 2H, CH_2), 2.51 (s, 2H, CH_2), 3.95 (s, 3H, OCH_3), 5.42 (s, 1H, CH), 6.21 (s, 1H, NH_2), 8.19 (s, 1H, NH), 8.50 (s, 1H, NH_2), 6.92 (s, 1H, Ar), 6.88 (dd, 2H, J = 15.7, 7.8 Hz, Ar), 7.02––7.15 (m, 2H, Ar), 7.21–7.27 (m, 2H, Ar), 7.44–7.57 (m, 1H, Ar), 7.88 (dd, 1H, J = 8.0, 1.6Hz, Ar)6.92–8.03 (m, 8H, Ar). ^{13}C NMR (100 MHz, $CDCl_3$, δ/ ppm): 178.85, 165.61, 164.52, 158.41, 152.52, 152.28, 145.71, 135.95, 132.80, 127.61, 126.91, 124.85, 124.36, 116.93, 116.61, 114.01, 105.80, 104.18, 97.11, 55.26, 46.11, 45.52, 39.79, 35.49, 30.07, 29.43; calcd for $C_{26}H_{25}O_4N_3S$: C, 65.67; H, 5.30; S, 6.74; N, 8.84, found: C, 66.31; H, 5.84; S, 6.57; N, 8.13.

2-(7-(3,4-Dimethoxyphenyl)-10,10-dimethyl-6-oxo-7,9,10,11-tetrahydro-6H,8H--chromeno[4,3-b]chromen-8-ylidene)hydrazine-1-carbothioamide (3d)

This compound was obtained as a light yellow solid, yield 0.14 g (48%) (*method 1*) or 0.21 g (75%) (*method 2*), mp 283–285°C. IR; 3504, 3452 (N–H, NH_2), 3145 (N–H), 3090, 2975, 2931, 2850 (C–H), 1724 (O–C=O), 1675 (C=N), 1638, 1615, 1580, 1503 (C=C), 1093 (C=S). ^{1}H NMR (400 MHz, $CDCl_3$, δ/ ppm): 1.07 (s, 3H, CH_3), 1.21 (s, 3H, CH_3), 2.14 (dd, J = 16.2 Hz, J = 34 Hz, 2H, CH_2), 2.48 (s, 2H, CH_2), 3.74 (s, 3H, OCH_3), 3.87 (s, 3H, OCH_3), 5.42 (s, 1H, CH), 6.24 (s, 1H, NH_2), 8.19 (s, 1H, NH), 8.50 (s, 1H, NH_2), 6.38–6.45 (m, 3H, Ar), 6.68–6.91 (m, 1H, Ar), 7.08–7.20 (m, 2H, Ar), 7.36 (ddd, 2H, J = 8.9, 7.5, 1.7 Hz, Ar), 7.98 (dd, 1H, J = 7.9, 1.6 Hz, Ar). ^{13}C NMR (100 MHz, $CDCl_3$, δ/ ppm): 178.31, 163.39, 160.75, 156.62, 153.65, 146.67, 144.37, 138.30, 136.18, 135.08, 129.28, 126.92, 122.31, 120.81, 120.05, 118.13, 116.35, 113.64, 102.24, 67.32, 58.69, 41.62, 40.36, 36.18, 31.44, 29.16, 27.39; calcd for $C_{27}H_{27}O_5N_3S$: C, 64.14; H, 5.38; S, 6.34; N, 8.31, found: C, 63.43; H, 5.82; S, 6.48; N, 8.15.

2-(7-(3-Methoxy-4-hydroxyphenyl)-10,10-dimethyl-6-oxo-7,9,10,11-tetrahydro--6H,8H-chromeno[4,3-b]chromen-8-ylidene)hydrazine -1-carbothioamide (3e)

This compound was obtained as a yellow solid, yield 0.13 g (44%) (*method 1*) or 0.23 g (81%) (*method 2*), mp 263–264°C. IR; 3487, 3347 (N–H, NH_2), 3148 (N–H), 2963, 2923, 2878 (C–H), 1719 (O–C=O), 1675 (C=N), 1628, 1611, 1563, 1511 (C=C), 1094 (C=S). ^{1}H NMR (400 MHz, $CDCl_3$, δ/ ppm): 1.12 (s, 3H, CH_3), 1.21 (s, 3H, CH_3), 2.10–2,353 (m, 2H, CH_2), 2.59 (s, 2H, CH_2), 3.83 (s, 3H, OCH_3), 4.93 (s, 1H, CH), 5.49 (s, 1H, OH), 6.13 (s, 1H, NH_2), 6.92 (s, 1H, NH), 8.55 (s, 1H, NH_2),6.75–6.84 (m, 2H, Ar), 6.95–7.03 (m, 1H, Ar), 7.29–7.36 (m,

2H, Ar), 7.55 (ddd, 1H, *J* = 8.4, 7.4, 1.6 Hz, Ar), 7.84 (dd, 1H, *J* = 7.8, 1.6 Hz, Ar). ^{13}C NMR (100 MHz, $CDCl_3$, δ / ppm): 175.86, 165.39, 161.70, 158.39, 152.66, 146.58, 140.33, 136.15, 135.38, 131.91, 126.68, 124.23, 122.39, 120.73, 116.84, 114.39, 111.01, 102.49, 100.20, 66.76, 55.96, 40.10, 36.85, 31.26, 29.79, 27.52; calcd for $C_{26}H_{25}O_5N_3S$: C, 63.53; H, 5.13; S, 6.52; N, 8.55, found: C, 63.12; H, 5.85; S, 6.58; N, 8.85.

7-(2-Methoxyphenyl)-10,10-dimethyl-8-(2-(4-(2-oxo-2H-chromen-3-yl)thiazol-2--yl)hydrazilidene)-8,9,10, 11-tetrahydro-6H,7H-chromeno[4,3-b]chromene-6-one (5a)

This compound was obtained as a yellow solid, yield 0.26 g (97%), mp 275–277°C. IR; 3354 (N–H), 3269, 3182, 3068, 2966, 2963, 2914, 2831 (C–H), 1729 (O–C=O), 1675 (C=N), 1624, 1609, 1576, 1513 (C=C). ^{1}H NMR (400 MHz, $CDCl_3$, δ / ppm): 1.05 (s, 3H, CH_3), 1.25 (s, 3H, CH_3), 2.11–2.48 (m, 2H, CH_2), 2.54 (d, 2H, *J* = 16.6 Hz, CH_2), 3.67 (s, 3H, OCH_3), 5.17 (s, 1H, CH), 6.95 (t, 1H, *J* = 8.0 Hz, Ar), 6.77 (d, 1H, *J* = 8.3 Hz, Ar), 7.18 (t, 1H, *J* = 8.0 Hz, Ar), 7.34 (dt, 4H, *J* = 14.6, 8.1 Hz, Ar), 7.63 (ddd, 4H, *J* = 44.2, 19.1, 8.4 Hz, Ar), 7.91 (s, 1H, H-5$_{(tiazol)}$), 8.51 (s, 1H, H-4$_{(chromen)}$), 10.92 (s, 1H, NH). ^{13}C NMR (100 MHz, $CDCl_3$, δ / ppm): 168.40, 160.59, 160.44, 144.77, 139.05, 138.47, 137.51, 135.51, 135.34, 133.68, 131.70, 131.67, 129.03, 128.54, 128.29, 124.02, 122.21, 121.76, 120.70, 120.05, 118.8, 117.81, 117.48, 116.78, 116.40, 110.92, 110.39, 109.91, 103.78, 55.10, 49.15, 40.60, 40.33, 32.63, 29.89, 27.50, 26.92; calcd for $C_{37}H_{29}O_6N_3S$: C, 69.04; H, 4.54; S, 4.98; N, 6.53, found: C, 68.59; H, 4.92; S, 5.16; N, 6.78.

7-(2,4-Dimethoxyphenyl)-10,10-dimethyl-8-(2-(4-(2-oxo-2H-chromen-3-yl)thia-zol-2-yl)hydrazilidene)-8,9,10, 11-tetrahydro-6H,7H-chromeno[4,3-b]chromene--6-one (5b)

This compound was obtained as a yellow solid, yield 0.21 g (79%), mp 244–245°C. IR; 3490 (N–H), 3419, 3358, 3294, 3267, 3176, 3062, 2963, 2931 (C–H), 1727 (O–C=O), 1675 (C=N), 1626, 1607, 1505, 1491 (C=C). ^{1}H NMR (400 MHz, $CDCl_3$, δ / ppm): 1.03 (s, 3H, CH_3), 1.24 (s, 3H, CH_3), 2.14–2.64 (m, 4H, CH_2), 3.62 (s, 3H, OCH_3), 3.75 (s, 3H, OCH_3), 5.11 (s, 1H, CH), 6.32 (d, 1H, *J* = 2.4 Hz, Ar), 6.48 (dt, 1H, *J* = 8.4, 1.8 Hz, Ar), 7.27–7.39 (m, 4H, Ar), 7.43–7.63 (m, 4H, Ar), 7.69 (dd, 1H, *J* = 7.9, 1.6 Hz, Ar), 7.86 (dd, 1H, *J* = 8.0, 1.6 Hz, Ar), 7.92 (s, 1H, H-5$_{(tiazol)}$), 8.50 (s, 1H, H-4$_{(chromen)}$), 10.58 (s, 1H, NH). ^{13}C NMR (100 MHz, $CDCl_3$, δ / ppm): 168.38, 160.13, 158.84, 152.94, 139.62, 139.08, 137.13, 135.40, 135.38, 134.04, 132.44, 131.71, 130.67, 130.14, 129.07, 125.99, 124.97, 124.01, 122.17, 120.99, 118.80, 116.76, 116.39, 114.15, 113.36, 110.31, 109.46, 103.67, 98.81, 56.78, 55.25, 50.02, 40.30, 38.48, 32.02, 31.17, 29.94, 26.79; calcd for $C_{38}H_{31}O_7N_3S$: C, 67.74; H, 4.64; S, 4.76; N, 6.24, found: C, 68.27; H, 4.82; S, 4.58; N, 6.51.

7-(4-Methoxyphenyl)-10,10-dimethyl-8-(2-(4-(2-oxo-2H-chromen-3-yl)thiazol-2--yl)hydrazilidene)-8,9,10, 11-tetrahydro-6H,7H-chromeno[4,3-b]chromene-6-one (5c)

This compound was obtained as a yellow solid, yield 0.24 g (85%), mp 281–283°C. IR; 3499 (N–H), 3425, 3327, 2954, 3076, 3059 (C–H), 1733, 1717 (O–C=O), 1667 (C=N), 1624, 1611, 1588, 1513 (C=C). ^{1}H NMR (400 MHz, $CDCl_3$, δ/ ppm): 1.01 (s, 3H, CH_3), 1.28 (s, 3H, CH_3), 2.37 (d, J = 16.2 Hz, 1H, CH_2), 2.49 (m, 3H, CH_2), 3.72 (s, 3H, OCH_3), 5.23 (s, 1H, CH), 6.95 (t, 1H, J = 8.0 Hz, Ar), 6.77 (d, 1H, J = 8.3 Hz, Ar), 7.18 (t, 1H, J = 8.0 Hz, Ar), 7.34 (dd, 4H, J = 44.8, 20.4, 8.2, Ar), 7.63 (dd, 4H, J = 44.2, 19.1, 8.4 Hz, Ar) 6.83–7.95 (m, 12H, Ar), 7.93 (s, 1H, H-5$_{(tiazol)}$), 8.50 (s, 1H, H-4$_{(chromen)}$), 10.93 (s, 1H, NH). ^{13}C NMR (100 MHz, $CDCl_3$, δ/ ppm): 168.87, 160.85, 160.07, 159.72, 157.63, 153.85, 152.49, 152.43, 145.30, 134.72, 132.96, 131.78, 129.94, 125.53, 125.09, 124.84, 124.01, 122.31, 122.15, 116.70, 114.01, 111.81, 111.46, 110.03, 106.81, 106.01, 104.25, 100.12, 98.94, 56.60, 55.30, 40.90, 40.13, 32.22, 31.06, 29.67, 27.32; calcd for $C_{37}H_{29}O_6N_3S$: C, 69.04; H, 4.54; S, 4.98; N, 6.53, found: C, 69.45; H, 4.85; S, 4.58; N, 6.45.

7-(3,4-Dimethoxyphenyl)-10,10-dimethyl-8-(2-(4-(2-oxo-2H-chromen-3-yl)thiazol-2-yl)hydrazilidene)-8,9,10, 11-tetrahydro-6H,7H-chromeno[4,3-b]chromene--6-one (5d)

This compound was obtained as a yellow solid, yield 0.21 g (75%), mp 244–245°C. IR; 3489 (N–H), 3421, 3360, 3280, 3176, 3058, 2985, 2896 (C–H), 1723 (O–C=O), 1677 (C=N), 1625, 1615, 1599, 1511(C=C). ^{1}H NMR (400 MHz, $CDCl_3$, δ/ ppm): 1.02 (s, 3H, CH_3), 1.23 (s, 3H, CH_3), 2.25–2.61 (m, 4H, CH_2), 3.61 (s, 3H, OCH_3), 3.73 (s, 3H, OCH_3), 5.09 (s, 1H, CH), 6.31 (d, 1H, J = 2.2 Hz, Ar), 6.46–6.53 (m, 1H, Ar), 7.24–7.37 (m, 4H, Ar), 7.50–7.58 (m, 3H, Ar), 7.67 (dd, J = 7.8, 1.9 Hz, 1H), 7.84 (dd, J = 8.0, 2.0 Hz, 1H), 7.90 (s, 1H, H-5$_{(tiazol)}$), 8.49 (s, 1H, H-4$_{(chromen)}$), 10.61 (s, 1H, NH). ^{13}C NMR (100 MHz, $CDCl_3$, δ/ ppm): 168.36, 161.16, 160.12, 154.94, 158.83, 154.60, 153.28, 152.92, 152.52, 139.35, 138.95, 137.83, 134.03, 133.94, 132.39, 131.58, 129.05, 124.94, 123.98, 122.15, 120.99, 118.79, 116.73, 116.35, 114.14, 110.33, 110.00,109.45, 103.63, 98.80, 55.23, 55.06, 52.68, 40.28, 38.47, 32.00, 31.14, 29.94, 26.82; calcd for $C_{38}H_{31}O_7N_3S$: C, 67.74; H, 4.64; S, 4.76; N, 6.24, found: C, 67.25; H, 5.12; S, 5.13; N, 6.10.

7-(3-Methoxy-4-hydroxyphenyl)-10,10-dimethyl-8-(2-(4-(2-oxo-2H-chromen-3--yl)thiazol-2-yl)hydrazilidene)-8,9,10,11-tetrahydro-6H,7H-chromeno[4,3-b]-chromene-6-one (5e)

This compound was obtained as an orange solid, yield 0.20 g (71%), mp 285–286°C. IR; 3506(O–H), 3419 (N–H), 3347, 3167, 2954, 2933, 2873 (C–H), 1704

(O–C=O), 1675 (C=N), 1624, 1609, 1576, 1513 (C=C). ^{1}H NMR (400 MHz, $CDCl_3$, δ / ppm): 1.01 (s, 3H, CH_3), 1.21 (s, 3H, CH_3), 2.33 (d, J = 16.4 Hz, 1H, CH_2), 2.38 (m, 3H, CH_2), 3.62 (s, 3H, OCH_3), 5.23 (s, 1H, CH), 6.03 (s, 1H, OH), 6.35 (d, 1H, J = 2.4 Hz, Ar), 6.51–6.54 (m, 1H, Ar), 7.24–7.40 (m, 4H, Ar), 7.51–7.56 (m, 3H, Ar), 7.68 (dd, J = 7.9, 2.1 Hz, 1H), 7.91 (dd, J = 8.0, 2.0 Hz, 1H), 7.89 (s, 1H, H-5$_{(tiazol)}$), 8.56 (s, 1H, H-4$_{(chromen)}$), 10.74 (s, 1H, NH). ^{13}C NMR (100 MHz, $CDCl_3$, δ / ppm): 168.83, 161.06, 160.37, 159.72, 157.83, 156.85, 155.99, 155.43, 148.32, 135.74, 133.06, 131.75, 130.04, 126.53, 125.39, 124.95, 124.22, 122.30, 121.95, 116.50, 114.67, 112.31, 110.86, 110.03, 108.01, 106.21, 104.55, 102.12, 100.94, 57.30, 55.35, 41.93, 40.03, 32.42, 31.96, 30.32, 28.67; calcd for $C_{37}H_{29}O_7N_3S$: C, 67.36; H, 4.43; S, 4.86; N, 6.37, found: C, 67.82; H, 4.86; S, 5.14; N, 6.48.

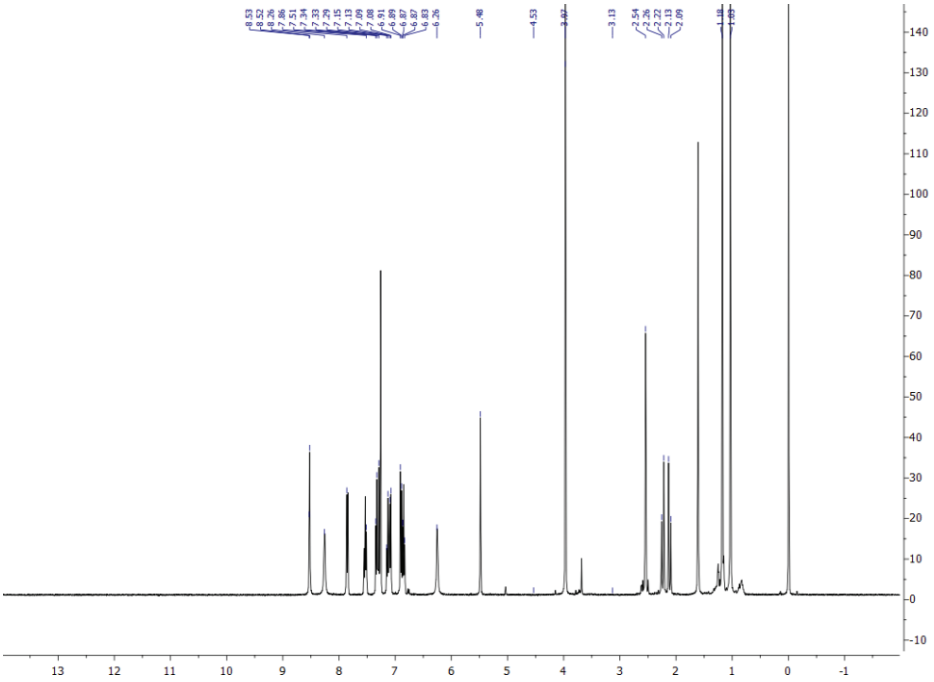

Figure S-1. ^{1}H NMR spectrum of 2-(7-(2-methoxyphenyl)-10,10-dimethyl-6-oxo-7,9,10,11-tetrahydro-6H,8H-chromeno[4,3-b]chromene -8-ylidene)hydrazine-1-carbothioamide **(3a)**, $CDCl_3$

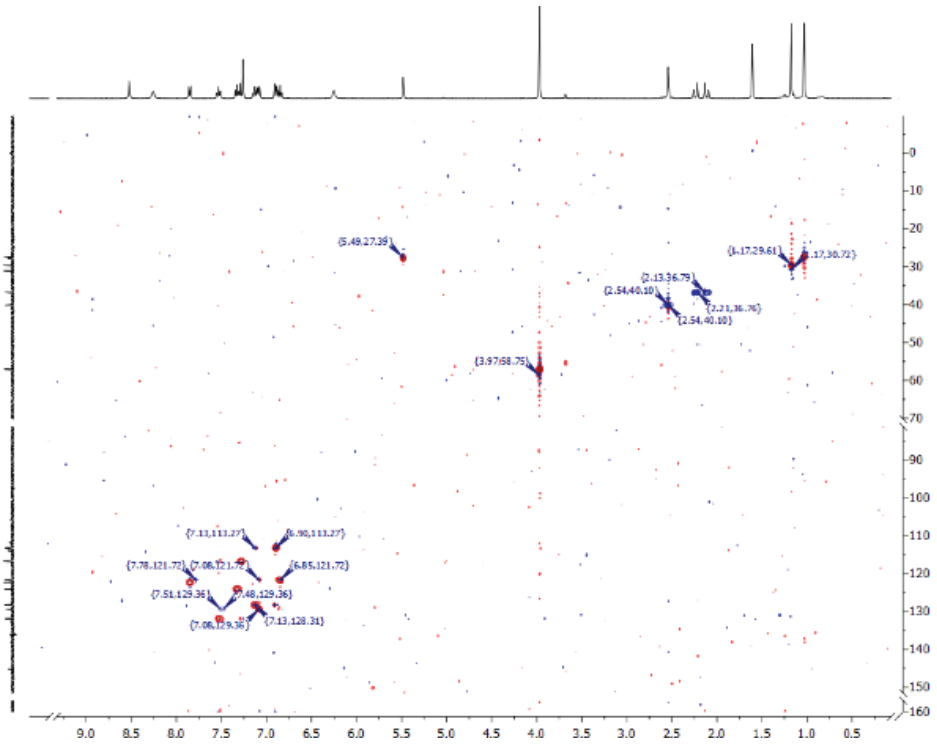

Figure S-2. HSQC spectra of 2-(7-(2-methoxyphenyl)-10,10-dimethyl-6-oxo-7,9,10,11-tetrahydro-6H,8H-chromeno[4,3-b] chromene-8-ylidene)hydrazine-1-carbothioamide **(3a)**, $CDCl_3$

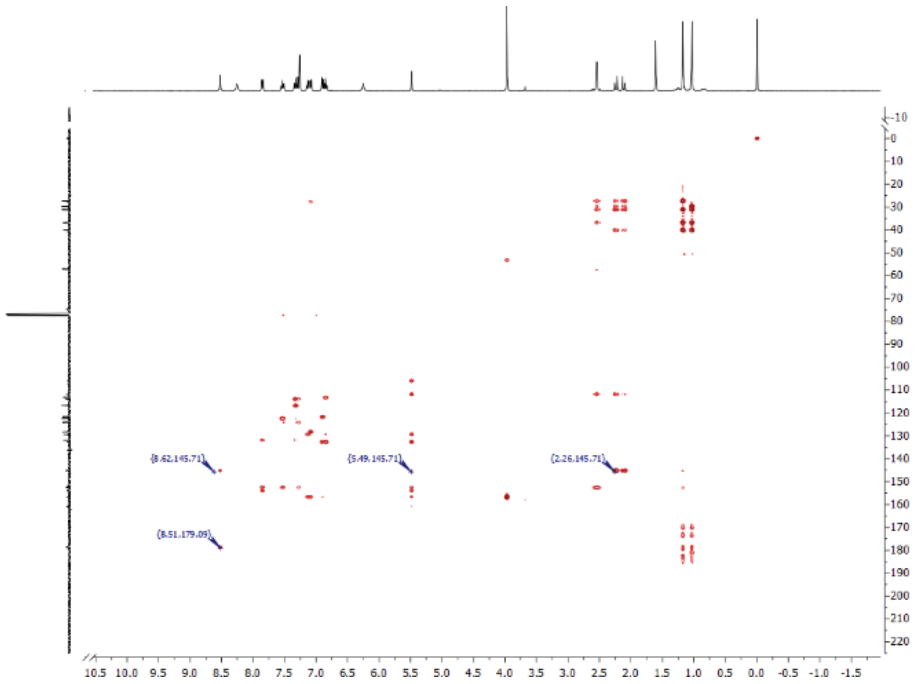

Figure S-3. HMBC spectra of 2-(7-(2-methoxyphenyl)-10,10-dimethyl-6-oxo-7,9,10,11-tetrahydro-6H,8H-chromeno[4,3-b] chromene-8-ylidene)hydrazine-1-carbothioamide **(3a)**, $CDCl_3$.

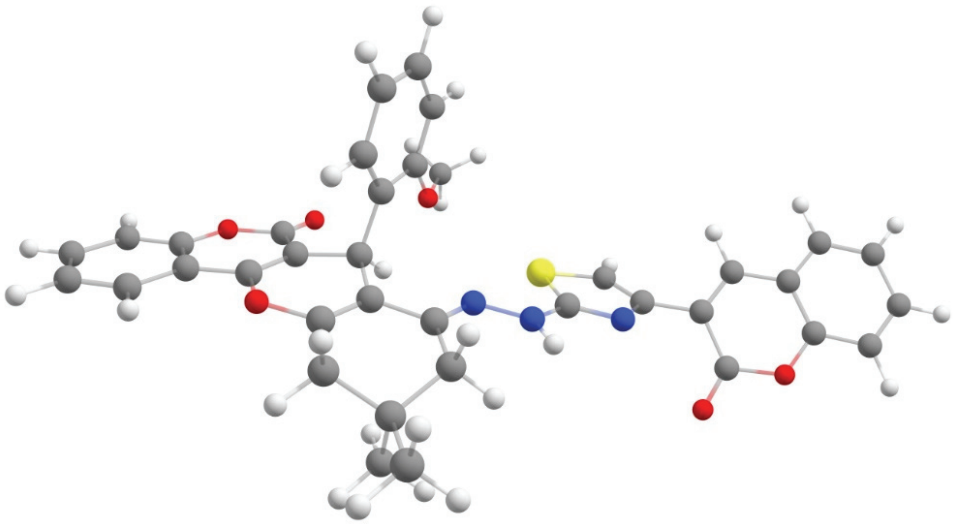

Figure S-4. Optimized geometry of 7-(2-methoxyphenyl)-10,10-dimethyl-8-(2-(4-(2-oxo-2H-chromen-3-yl)thiazol-2-yl)hydrazino)-8 ,9,10,11-tetrahydrochromeno[4,3-b]chromen-6(7H)-one **(5'a)**

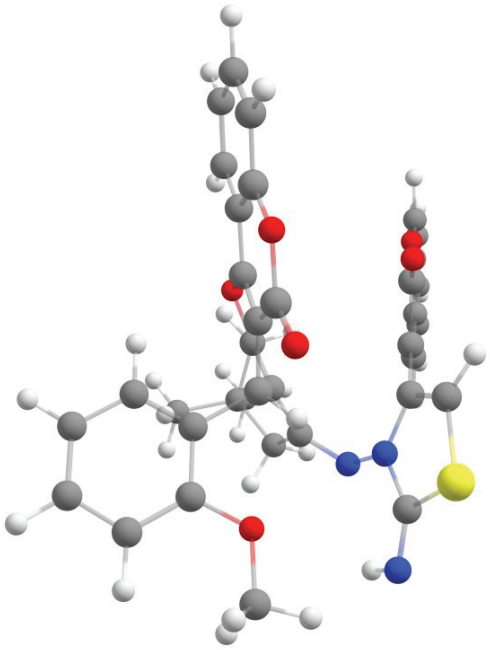

Figure S-5. Optimized geometry of 8-((2-imino-4-(2-oxo-2H-chromen-3-yl)thiazol-3(2H)-yl)imino)-7-(2-methoxyphenyl)-10, 10-dimethyl-8,9,10,11-tetrahydrochromeno[4,3-b]chromen-6(7H)-one **(6a)**

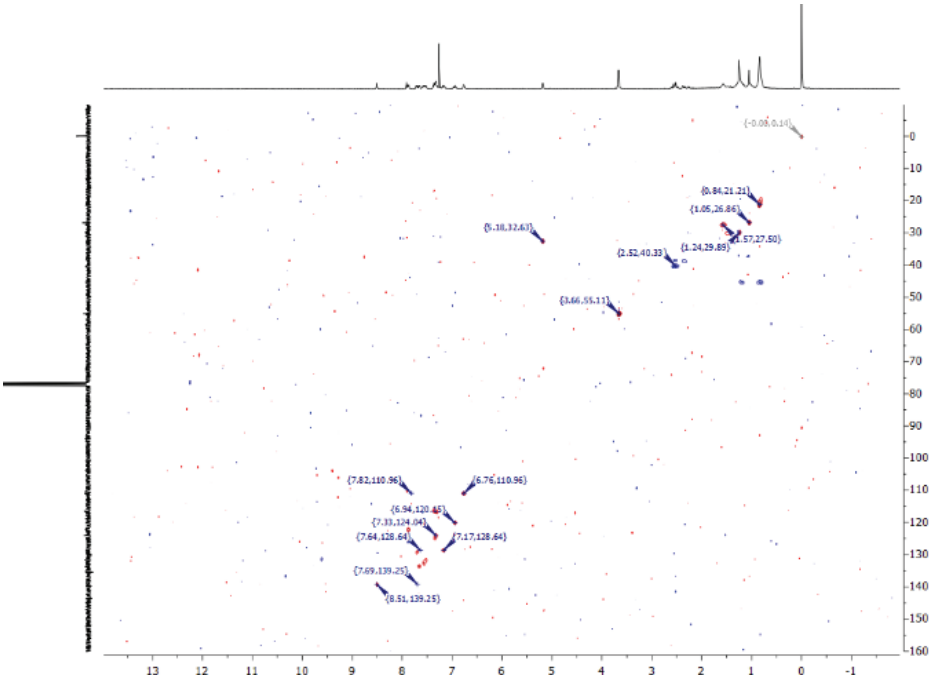

Figure S-6. HSQC spectra of 10,10-dimethyl-8-(2-(4-(2-oxo-2H-chromen-3-yl)thiazol-2-yl)hydrazilidene)-7-(2-methoxyphenyl) -8,9,10,11-tetrahydro-6H,7H-chromeno[4,3-b]chromene-6-one **(5a)**, $CDCl_3$

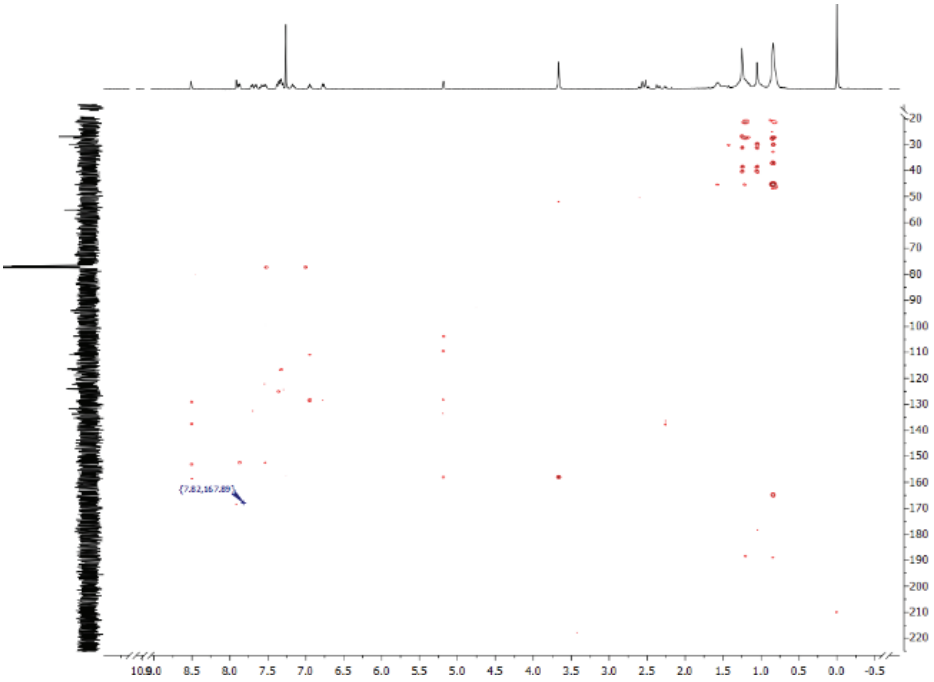

Figure S-7. HMBC spectra of 10,10-dimethyl-8-(2-(4-(2-oxo-2H-chromen-3-yl)thiazol-2-yl)hydrazilidene)-7-(2-methoxyphenyl) -8,9,10,11-tetrahydro-6H,7H-chromeno[4,3-b]chromene-6-one **(5a)**, $CDCl_3$

Table S-I. Theoretically calculated and experimentally obtained key signals of the 1H NMR spectra of the probable reaction products of the reaction 2-(7-aryl-10,10-dimethyl-6-oxo-7,9,10,11-tetrahydro-6H,8H -chromeno[4,3-b]chromen-8-ylidene)hydrazine-1-carbothioamide (3a-e) with 3-bromoacetylcoumarin

Compound	Calc (vacuum)	Calc ($CDCl_3$)	Exp ($CDCl_3$)
5a	5,7079 H_{52} (CH)	5,6405 H_{52} (CH)	
	6,787 H_{62} (CH)	6,9343 H_{62} (CH)	
	8,065 H_{63} (CH)	8,4178 H_{63} (CH)	5,17 H_{52} (CH)
	9,8601 H_{61} (NH)	9,9276 H_{61} (NH)	7,91 $H_{62(68)}$ (CH)
5'a	6,1523 H_{52} (CH)	6,0532 H_{52} (CH)	8,53 $H_{63(69)}$ (CH)
	6,8684 H_{68} (CH)	7,0554 H_{68} (CH)	10,61 $H_{61(67)}$ (NH)
	7,7973 H_{69} (CH)	8,1128 H_{69} (CH)	
	8,27 H_{67} (NH)	8.46 H_{67} (NH)	
5b	5,6635 H_{54} (CH)	5,5913 H_{54} (CH)	
	6,7941 H_{63} (CH)	6,9449 H_{63} (CH)	
	8,0588 H_{64} (CH)	8,4164 H_{64} (CH)	5.09 $H_{54(53)}$ (CH)
	9,8933 H_{62} (NH)	9,9645 H_{62} (NH)	7.87 $H_{63(69)}$ (CH)
5'b	6,0381 H_{53} (CH)	5,9312 H_{53} (CH)	8.48 $H_{64(70)}$ (CH)
	6,883 H_{69} (CH)	7,0674 H_{69} (CH)	10.62 $H_{62(68)}$ (NH)
	7,7966H_{70} (CH)	8,1104 H_{70} (CH)	
	8,2601 H_{68} (NH)	8,4557 H_{68} (NH)	
5c	5,6446 H_{52} (CH)	5,5869 H_{52} (CH)	
	6,7958 H_{62} (CH)	6,9445 H_{62} (CH)	
	8,0576 H_{63} (CH)	8,4179 H_{63} (CH)	5,23 H_{52} (CH)
	9,9938 H_{61} (NH)	10,0602 H_{61} (NH)	7,93 $H_{62(68)}$ (CH)
5'c	5,4408 H_{52} (CH)	5,3825 H_{52} (CH)	8,50 $H_{63(69)}$ (CH)
	6,8813 H_{68} (CH)	7,051 H_{68} (CH)	10,93 $H_{61(67)}$ (NH)
	7,8019 H_{69} (CH)	8,1115 H_{69} (CH)	
	8,1723 H_{67} (NH)	8,3877 H_{67} (NH)	
5d	5,6328 H_{54} (CH)	5,5729 H_{54} (CH)	
	6,7292 H_{63} (CH)	6,8766 H_{63} (CH)	
	8,0065 H_{64} (CH)	8,3662 H_{64} (CH)	5,14 $H_{54(53)}$ (CH)
	8,0065 H_{62} (NH)	9,9669 H_{62} (NH)	7,91 $H_{63(69)}$ (CH)
5'd	5,3841 H_{53} (CH)	5,3232 H_{53} (CH)	8,49 $H_{64(70)}$ (CH)
	6,9191 H_{69} (CH)	7,0928 H_{69} (CH)	10.62 $H_{62(68)}$ (NH)
	7,7911 H_{70} (CH)	8,106 H_{70} (CH)	
	8,1827 H_{68} (NH)	8,4012 H_{68} (NH)	
5e	5,6262 H_{53} (CH)	5,5702 H_{53} (CH)	
	6,7496 H_{62} (CH)	6,8976 H_{62} (CH)	
	8,0277 H_{63} (CH)	8,3876 H_{63} (CH)	5,23 $H_{54(53)}$ (CH)
	9,956 H_{61} (NH)	10,024 H_{61} (NH)	7,89 $H_{63(69)}$ (CH)
5'e	5,3814 H_{52} (CH)	5,3242 H_{52} (CH)	8,56 $H_{64(70)}$ (CH)
	6,9406 H_{68} (CH)	7,1132 H_{68} (CH)	10,74 $H_{62(68)}$ (NH)
	7,8108 H_{69} (CH)	8,125 H_{70} (CH)	
	8,179 H_{67} (NH)	8,3972 H_{67} (NH)	

21.

Journal of the Serbian Chemical Society
JSCS-info@shd.org.rs • www.shd.org.rs/JSCS
J. Serb. Chem. Soc. *91* (1) 11–22 (2026)
JSCS–5474
Original scientific paper
Published 5 February, 2026

Changes in leaf epicuticular wax with age of *Chenopodium album* L. and *Abutilon theophrasti* Medik.

FILIP VRANJEŠ[1], SAVA VRBNIČANIN[2], VELE TEŠEVIĆ[3], MIRJANA CVETKOVIĆ[4] and DRAGANA BOŽIĆ[2]*

[1]*Eurofins Agroscience Regulatory, Studentska 35/10, 11000 Belgrade, Serbia,* [2]*University of Belgrade, Faculty of Agriculture, Nemanjina 6, 11000 Zemun-Belgrade, Serbia,* [3]*University of Belgrade – Faculty of Chemistry, Studentski trg 12–16, 11000 Belgrade, Serbia and* [4]*University of Belgrade, Institute of Chemistry, Technology and Metallurgy – National Institute of the Republic of Serbia, Njegoševa 12, 11000 Belgrade, Serbia*

(Received 20 June, revised 23 July, accepted 17 November 2025)

Abstract: Epicuticular wax comprises a complex mixture of diverse organic compounds. The predominant class of compounds consists of long-chain *n*-alkanes. *Chenopodium album* and *Abutilon theophrasti* are cosmopolitan weed species, both of economic importance due to difficulties in control, and both species produce wax on the leaf surface. This study shows that in *C. album*, the proportion of epicuticular waxes has higher values in the oldest leaves and lower in the youngest leaves. Conversely, in *A. theophrasti*, the mean wax content tended to be slightly higher in the younger upper leaves compared to the lower leaves. The proportion of waxes in leaves does not reflect the stage of development in either species. In the epicuticular wax composition of *C. album* leaves, alkanes and alcohols are the most abundant compounds. Conversely, in *A. theophrasti* leaves, alkanes, alcohols, and triterpenes dominate. Quantitative variations in leaf epicuticular waxes are influenced by leaf age.

Keywords: weed; leaf characteristics; stage of development.

INTRODUCTION

Chenopodium album L. (lambsquarters) and *Abutilon theophrasti* Medik. could be considered as part of a group of the most common weed species that can be found in arable crops across the globe.[1–3] These two species have different leaf surface morphology which is significant not only for taxonomy but also to the herbicide efficacy due to the uptake and effectiveness of herbicides. *C. album*

* Corresponding author. E-mail: dbozic@agrif.bg.ac.rs
https://doi.org/10.2298/JSC250620082V

produces wax on the leaf surface, which is a barrier to the absorption of herbicides,[4] while *A. theophrasti* has a high number of trichomes on both sides of leaves,[5] and also certain amount of wax is present on its leaves.[6]

The epicuticular together with the cuticle, protect the plant's integrity and act as a barrier against biotic and abiotic stresses.[7] Beyond the epicuticular wax that resides on the leaf surface, the cuticle typically harbors an inner layer of wax. This intracuticular wax, oriented perpendicular to the cuticle surface, is embedded within the cutin matrix. Within the very-long-chain aliphatic wax components, primary alcohols tend to accumulate to higher percentages in the intracuticular wax layer, while free fatty acids and alkanes in many cases accumulate in the epicuticular layer.[8]

Epicuticular wax comprises a complex mixture of diverse organic compounds. The predominant class of compounds consists of long-chain *n*-alkanes, characterized by a carbon chain length ranging from C_{27} to C_{31}. In addition to alkanes, other chemical constituents are present in wax, including unsaturated hydrocarbons, alcohols, aldehydes, ketones, acids, esters, and other related compounds. Furthermore, cyclic compounds such as triterpenes, hydroxycinnamic acid derivateives, sterols, and flavonoids can also be found in epicuticular wax.[9] A thin-layer chromatography (TLC) was used to analyze the epicuticular wax composition of *A. theophrasti*.[6] In this findings it was revealed that this wax consists of fatty acids, primary alcohols, secondary alcohols, esters, and hydrocarbons. Notably, the chemical composition of cuticular wax undergoes changes during the ontogenetic development of leaves.

Surface waxes can be effectively analyzed using a combined approach involving gas chromatography (GC) and mass spectrometry (MS).[10] On the other hand, due to the volatile nature of wax compounds, GC/MS are well-suited for identifying and characterizing constituents within wax mixtures.[9,11] Additionally, gas chromatography (GC) and gas chromatography–mass spectrometry (GC–MS) revealed that *n*-alkanes constitute an average of approximately 10–12 % in *Pinus heldreichii* var. *Pančići Fukarek*.[12]

Epicuticular waxes form a critical barrier on the surface of leaves, with roles in limiting non-stomatal water loss, modulating interactions with pathogens, and influencing the retention and penetration of foliar-applied agrochemicals. Numerous studies on crop plants and woody perennials have shown that both the quantity and composition of surface waxes change substantially during leaf development. In *Sorghum halepense* L., for example, young expanding leaves typically exhibit lower wax loads enriched in primary alcohols and aldehydes, whereas mature leaves accumulate greater amounts of long-chain alkanes and cyclic components, resulting in more crystalline and hydrophobic surfaces.[13] In maize, alkanes and alkyl esters are dominant components of cuticular waxes of adult plant leaves. During plant development a switch from alkanes to esters as the major wax

type, which is parallel with emergence of an osmiophilic layer of the cuticle, resulting in establishment of the water barrier.[14] Similar ontogenetic shifts have been reported in *Arabidopsis* leaves, where the amount and composition of the cuticular wax mixture change as organs.[15] These developmental trajectories highlight a strong age dependence of wax deposition and structure, with potential consequences for leaf surface physiology.

In the context of weed science, investigations into epicuticular waxes have primarily addressed morphological traits, environmental stress responses, or herbicide droplet behavior, but age-related analyses are limited. For weed species, including *C. album* and *A. theophrasti* as two widespread weeds in temperate agroecosystems, information about wax changes with leaf age are missing. This represents a significant gap, given that surface waxes are known to be a major determinant of foliar herbicide uptake and biological activity.[6] By systematically characterizing wax traits across a multi-age ontogenetic series under controlled growth conditions, the present study addresses this knowledge gap and provides an improved understanding of how developmental dynamics in surface waxes may influence herbicide performance in these two problematic species.

The study aims to assess the qualitative and quantitative wax content in the leaves of *C. album* and *A. theophrasti*. In particular to determine whether there are differences in the content of wax in different maturity phases of leaves.

EXPERIMENTAL

Plant material

The seeds of *C. album* and *A. theophrasti* were collected at the end of September from the agricultural field (44°47′0.8″ N, 20°17′44.9″ E), near Belgrade, Serbia, and stored at room temperature in the dark until planting. Plants were grown in growth chambers. Temperature was set to 27 °C during daylight hours (14 h), and 22 °C during darkness (10 h), with supplemental light intensity of photosynthetic photon flux density (*PPFD*) ≈ 1300 μmol m^{-2} s^{-1} (MH Philips 600 W) at 1 m height. The plants were grown in plastic pots (diameter 10 cm) with 300 ml volume, containing a commercial potting mix (Floragard TKS1®, pH value of 5.6 with content N 140 mg L^{-1}, P 80 mg L^{-1}, K 190 mg L^{1}, Germany). Weed seeds were scattered on the surface of soil, and then covered with 1 cm of potting mix. Pots were watered after to near full water capacity and subsequently watered daily to maintain adequate soil moisture for plant growth. Emerged plants were thinned to a density of 2 uniformly sized plants per pot. When *C. album* reached 5 pairs of leaves and *A. theophrasti* reached 5 leaves, leaves samples for wax contend analyses were harvested and storage at –20 °C.

The content of wax in the leaves of C. album *and* A. theophrasti

The research focused on changes in the chemical composition of epicuticular waxes in different growth stages of *C. album* and *A. theophrasti* leaves: *C. album* at stage 10 (5 pairs) and *A. theophrasti* at stage 5 of leaf development. To ensure consistency, leaves from both species were divided into five subsamples (related to five position), with three replications (weighing approximately 1 g are taken from each phase). Each replicate consisted of pooled leaves from four plants per pot (one pot = one replicate). For each species and each of the five leaf positions, three biological replicates (n = 3) were analyzed. These samples of leaves were

to be of comparable size between stages. Leaf/leaf pairs (1–5) were defined as consecutive opposite leaves counted from the base of the stem (1 = oldest fully expanded leaves at the lowest node; 5 = youngest fully expanded leaves near the apex). This morphological criterion was applied equally to both species to ensure comparability. Prior to analysis, the samples had been carefully packed in aluminum foil and stored at –20 °C. Epicuticular waxes were extracted from the leaf surfaces using 20 ml of hexane. The extraction process involved gentle shaking for 1 minute, followed by filtration through filter paper. Since the goal of was to isolate epicuticular waxes, non-polar hexane as the solvent and a short extraction time of 1 min were chosen. The resulting extract was then dissolved in CH_2Cl_2 and subjected to analysis using gas chromatography/mass spectrometry (GC/MS).

The GC/FID (gas chromatography with flame ionization detection) and GC/MS analyses were conducted using an Agilent 7890 A instrument equipped with an automatic injection system (Agilent GC Sampler 80), an Agilent 5975C XL EI/CI quadrupole mass detector (MSD), and an HP-5 MS 5 % phenyl methyl silox capillary column (30 m×0.25 mm i.d.×0.25 μm film thickness). The temperature program involved a linear increase from 60 to 300 °C at a rate of 3 °C min^{-1}. The injector temperature was set at 250 °C, the detector temperature at 300 °C, the source temperature at 230 °C, and the quadrupole temperature at 150 °C. Helium served as the carrier gas (16.255 psi, in constant pressure mode). Samples (1 μl) were injected in splitless mode (using Agilent splitless liner PN 5190-2292) with 1.5 min splitless purge time. Splitless purge time: 1.5 min with 150 mL/min, then gas saver mode (20 mL/min) activate after 2.0 min. Liner type: splitless liner ID 4 mm, Agilent Technologies (Agilent inlet liner, Ultra Inert, splitless, single taper product number 5190-2292). Inlet pressure 16.255 psi, in constant pressure mode, He currier gas. Initially runs split 10:1 was used, and based on quality control check, it was necessary to use splitless mode to increase sensitivity and reproducibility. Moreover, *n*-alkanes C8-C40 (even series) were used to check sensitivity and to ensure that high-boiling compounds were able to reach detector during GC/MS run.

Electron ionization (EI-MS; 70 eV) was used to obtain mass spectra, and ion detection occurred within the range of *m*/*z* 30–550. Compound identification relied on comparing EI mass spectra with those from the Wiley and NIST libraries using NIST MS Search 2.0 and AMDIS software. Additionally, calculated retention indices (*RI*) were compared with library retention indices. Based on the obtained results, the relative proportions of each component in individual samples were determined. The relative percentage of the epicuticular wax constituents was calculated as percentage of normalization of FID peak area. Wax quantities were expressed relative to fresh leaf mass.

Statistical data analysis

The statistical analysis of the collected data was performed using the software Statistica® 7.0 (StatSoft, Inc., 2007), a comprehensive data analysis system. For each species and each leaf position, three biological replicates ($n = 3$) were analyzed. One-way ANOVA was applied to test differences in leaf epicuticular waxes content between positions. Prior to ANOVA, all data were tested for normality (Shapiro-Wilk test, $p > 0.05$) and homogeneity of variances (Levene's test, $p > 0.05$). Data with unequal variances were log (x+1) transformed to meet the assumption of homogeneity of variances. Specifically, we used either the *LSD* test or the *t*-test for our statistical comparisons. In addition to *p*-values, mean differences with 95 % confidence intervals were calculated to provide effect size estimates.

RESULTS AND DISCUSSION

In *C. album*, numerical differences in the proportion of epicuticular waxes were observed, with higher values in the oldest leaves and lower in the youngest leaves (Fig. 1). In *A. theophrasti*, mean wax content tended to be slightly higher in the younger upper leaves compared to the lower leaves (Fig. 1). Furthermore, a One-way ANOVA revealed that the proportion of waxes in leaves did not significantly depend on the stage of development or the position of the leaf on the plant in either species (*C. album*: $F = 0.720$, $p = 0.598$; *A. theophrasti*: $F = 0.963$, $p = 0.469$). Although numerical differences in wax proportions were observed among leaf positions, these were not statistically significant (ANOVA, $p > 0.05$). The wax content in *C. album* leaves (ranging from 0.40 to 0.31 %) exceeded that in *A. theophrasti* leaves (ranging from 0.13 to 0.18 %). Therefore, the apparent trends (higher values in older leaves of *C. album*, and slightly higher values in upper leaves of *A. theophrasti*) should be interpreted with caution as indicative tendencies rather than robust effects.

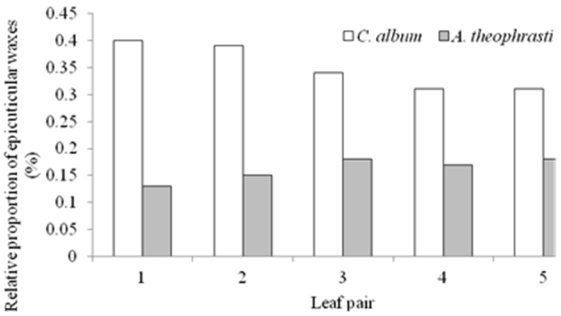

Fig. 1. Relative proportion of epicuticular waxes in *C. album* and *A. theophrasti* leaves of different maturity.

Analysis of the chemical composition revealed the presence of several compound classed in both species, including aldehydes, alkanes, alcohols, esters, ketones, and triterpenes. The dominant constituents in the wax composition of both species were alkanes and alcohols, with *A. theophrasti* also featuring a significant proportion of triterpenes. Additionally, *C. album* contained classes of esters and sterols, as well as ethers and sterols. In contrast, *A. theophrasti* contained fatty acids, lactones, and vitamin E. Quantitative variations in leaf epicuticular waxes were influenced by leaf age. The content of compound classes (Fig. 2) varied across different leaf stages. Specifically, the comprehensive compound list with retention times, retention indices and identification details is provided in the Supplementary material to this paper (Tables S-I and S-II). In *C. album*, the content of wax components (esters, esters and sterols, ethers, ketones) was significantly higher ($p < 0.05$) in the oldest leaves (1st pair), while sterols and triterpenes were

significantly more abundant ($p < 0.05$) in the youngest leaves (5th pair). Contrary, the content of aldehydes, alkanes, alkenes, and alcohols did not differ significantly among leafpositions ($p > 0.05$), indicating relative stability of these constituents across development. In the case of *A. theophrasti*, only aldehydes and esters showed lower levels in the oldest leaves ($p < 0.05$), while triterpenes were significantly more abundant in the youngest leaves. Other classes (alkanes, alcohols, ketones, fatty acids, lactones, sterols, vitamin E) remained statistically unchanged ($p > 0.05$) across leaf positions, despite minor numerical fluctuations.

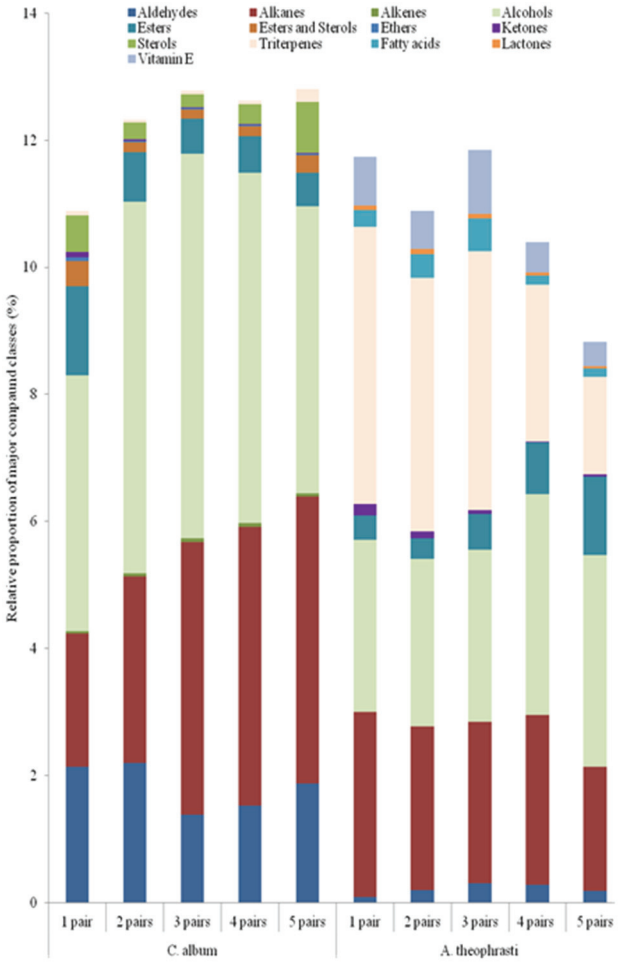

Fig. 2. Major compound classes in composition of epicuticular waxes.

As indicated, in the epicuticular wax composition of leaves of both species, alkanes and alcohols were the most abundant compounds. Regarding the content of alkanes, the chemical compounds heptacosane, nonacosane and hentriacontane

constituted the predominant share of the total wax content in leaves of *C. album* and *A. theophrasti* (as shown in Tables S-I and S-II). The content of these compounds varied across leaves of different growth stages or positions on the plant. Specifically, in *C. album*, the heptacosane, nonacosane and hentriacontane content was higher in the younger leaf pair (4th or 5th pair) compared to older leaves (1st pair). Specifically, in *C. album*, the content of these mentioned alkanes fell within the following ranges: heptacosane (1.91–5.42 %), nonacosane (13.34–28.37 %), and hentriacontane (2.42–6.10 %). In the case of *A. theophrasti*, the content of nonacosane was the most dominant component and was quantity lower in the youngest leaf (5th leaf) compared to the older leaves. Heptacosane and hentriacontane were also present in quantity higher than other components while having no such clear dependence of quantity with the age of leaves as was in *C. album* plants. For leaves of *A. theophrasti*, the measured values decreased from the oldest to the youngest leaf (heptacosane: 5.19–3.70 %, nonacosane: 21.07–10.86 % and hetriacontane: 5.47–4.71 %).

Within the class of alcohol compounds, octacosanol and triacontanol constituted the predominant share of total wax content in the leaves of both *C. album* and *A. theophrasti*. In *C. album*, the octacosanol content was lower in the oldest leaves (1st pair) and the youngest leaves (5th pair) compared to the other leaves. Similarly, the triacontanol content was lower in the oldest leaves (1st pair) compared to the remaining leaves. As we moved from the oldest to the youngest leaf in *C. album*, the content of these alcohols increased (octacosanol: 21.82–23.60 %, triacontanol: 2.08–3.34 %). For *A. theophrasti*, the content of octacosanol was lower in the oldest leaf compared to the younger (4th and 5th leaves). Additionally, a difference in triacontanol content was observed only between the oldest and youngest leaves, with higher content in the oldest leaf. The content of octacosanol compounds in leaves of *A. theophrasti* increased (5.29–7.84 %), while triacontanol content decreases (2.55–1.04 %).

In *A. theophrasti*, the presence of triterpenes in leaf waxes was noteworthy. Specifically, the compounds lup-20(29)-en-3-one, olean-12-en-3-one, and squalene dominated this class. The content of these compounds exhibited variations across different leaves. The content of lup-20(29)-en-3-one and squalene was lower in the youngest leaf (5th leaf) compared to the older leaves. Conversely, olean-12-en-3--one content was smaller in the 1st leaf compared to the other leaves. Specifically, the content of lup-20(29)-en-3-one decreased from 5.90 to 1.19 %, squalene content decreases from 9.69 to 2.15 %, olean-12-en-3-one content increased from 1.67 to 2.61 %.

Given the distinctiveness of leaf waxes across various plant species, evaluating their chemical composition and spatial distribution within and on the leaf surface hold significant importance for chemotaxonomy.[9–11] Numerous studies have consistently demonstrated that the content and thickness of epicuticular

waxes in leaves undergo changes as the leaves age. An analysis of wax content in *S. halepense*, revealed that the amount of wax per unit area was higher in younger plants at the 3-leaf stage (123 μg cm^{-2}) compared to older plants at the 6–7 leaf stage (38 μg cm^{-2}).[16] Several hypotheses might explained such phenomenon: younger cells might exhibited greater efficiency in wax production, or production levels remained constant regardless of plant age, but the overall wax amount decreased due to the expansion of leaf area. Our findings for the species examined in our study present a contradictory picture. Specifically, in *C. album*, the highest wax content was observed in older leaves, while in *A. theophrasti*, the younger upper leaves consistently exhibited higher wax content. Consequently, the results for *C. album* align with the perspective that wax content increases with leaf aging. Notably, older leaves tended to possess a greater proportion of epicuticular waxes, which can impede herbicide absorption and subsequent translocation to the site of action within the plant.[17]

Different plant species exhibited unique chemical profiles in their waxes. For instance, testing of *Brunnichia ovata* Walt. and *Campis radicans* L. leaves have shown that the predominant components include alkanes (24–49 %), alcohols (9––61 %), acids (0–11 %), and triterpenes (4–62 %).[18] Alkanes, primary alcohols and fatty acids were primary constituents of epicuticular wax, whereas intracuticular wax was composed of both, triterpenoids and long-chain aliphatic molecules.[19] In one research of the influence of external environmental factors on wax content in *A. theophrasti* leaves revealed similar findings.[6] Specifically, primary alcohols (29–31 %), alkanes (17–20 %), fatty acids (10–13 %), and esters (8–11 %) were identified as major constituents. Additionally, other species such as *Ipomoea hederacea* L., *Ipomoea lacunosa* L., *Ipomoea wrightii* Gray and *Jacquemontia tamnifolia* L. exhibited varying compositions. In these species, alkanes (2958 %), alcohols (19–46 %), acids (5–24 %) and triterpenes (0–25 %) were present, with variations depending on the specific species.[17] Similarly, wax content was explored in the leaves of three poplar clones. (*Populus euramericana* cl. Pannonia (M1), *Populus deltoides* cl. PE 19/66 and cl. B229 (Bora)).[10] Notably, the highest wax content in poplar leaves was attributed to compounds such as nonacosane (72–78 %), hexacosane (6–10 %), and untriacontane (5 %). In another findings it was noted that the wax content, except for alcohol in *B. ovata* and triterpenes in *C. radicans*, consistently remained higher in older leaves (5–7) compared to the youngest apical leaves (1–2).[18]

It should be noted that wax quantities were expressed as percentage of fresh leaf mass rather than per unit surface area. Because leaf water content varies strongly with age, obtained values cannot be consider as absolute wax coverage. Therefore, the data should be considered as indicator of trends in wax load and composition. Although this represents a limitation for direct conclusions about herbicide spray retention capacity, the clear developmental changes observed still

provide important insight into the dynamics of wax deposition in *C. album* and *A. theophrasti* under controlled conditions. In many cultivated and woody species, including *S. halepense*, various poplar clones, and several ornamentals, wax load per unit leaf area typically declines with age, largely due to surface expansion and abrasion losses.[10,16] By contrast, our results show an opposite pattern in *C. album*, where older leaves accumulated higher proportions of epicuticular waxes. This divergence may reflect species-specific differences in cuticle thickening and prolonged activity of biosynthetic pathways in older tissues. In *A. theophrasti*, the mixed pattern (higher wax in younger leaves, attenuation in older ones) suggests a stronger influence of pubescence and trichome architecture on surface deposition and persistence of waxes.

Previous research on *A. theophrasti* indicated that environmental conditions such as light intensity and water stress change wax deposition and consequently herbicide retention.[6] In this research plants were grown under controlled chamber conditions, minimizing environmental variation and allowing us to isolate ontogenetic trends. However, in field conditions, interactions between developmental stage and environmental plasticity may either mask or amplify age-related trends. Thus, the generality of our findings should be interpreted with caution when extrapolated beyond controlled conditions.

Described differences in wax content between species and leaves at different positions have important implications for approach of herbicide application. In *C. album*, the accumulation of wax on older leaves may decrease herbicide penetration, indicating the need for adjuvants involvement. Conversely, in *A. theophrasti*, dense trichomes combined with persistent wax loads in younger leaves suggest that spray retention is more affected by surface roughness than by cuticular resistance, indicating nozzle type and droplet size have critical importance on effective coverage. Such knowledge can direct herbicide application practices, including the selection of surfactants or nozzle designs, to optimize deposition and uptake by these two species.

The different wax contents observed between *C. album* (higher wax content in older leaves) and *A. theophrasti* (wax content tended to be slightly higher in the younger leaves than in older) may be partly explained by differences in leaf micromorphology and regulation of wax biosynthesis during leaf development.[20] *C. album* leaves are glabrous, enabling epicuticular waxes to accumulate on exposed surfaces with development, with relatively limited loss due to abrasion. In contrast, *A. theophrasti* leaves are densely hairy, and trichomes may alter the spatial distribution of waxes, providing a physical barrier that reduces direct deposition on the epidermal surface and potentially accelerates abrasion or redistribution of wax layers in older leaves. Also, different wax content could be consequence of different regulation of very long chain fatty acid biosynthesis genes, which drive wax production. In *A. theophrasti*, long-term activity of these pathways in developing

leaves could maintain high amounts of wax in younger tissues, while older leaves partially lose it due to environmental exposure. Such ontogenetic trends are consistent with general concepts of wax biosynthesis and development.[19]

CONCLUSION

Our controlled-environment study demonstrates species-specific patterns of epicuticular wax accumulation with leaf age. In *C. album*, older leaves tended to contain higher proportions of certain wax constituents, whereas in *A. theophrasti*, younger pubescent leaves maintained relatively high wax loads. These statistically supported trends suggest that cuticle development and surface architecture interact differently across species. Importantly, such age- and species-dependent profiles have direct implications for foliar herbicide performance. In *C. album*, increased wax in older leaves may reduce herbicide penetration, requiring optimized surfactant or adjuvant use at later growth stages. In *A. theophrasti*, persistent waxiness of young trichome-rich leaves may already hinder spray retention, highlighting the need for tailored nozzle selection and spray formulations. Integrating wax metrics into herbicide application frameworks could therefore improve the effectiveness of weed management strategies for these problematic species.

Although we observed numerical variation among leaf positions, most differences were small and not statistically significant. Reported values are expressed relative to fresh leaf mass rather than per unit surface area, which limits direct inference about spray retention capacity. Therefore, our results should be interpreted primarily as reflecting relative ontogenetic trends in wax load and composition.

SUPPLEMENTARY MATERIAL

Additional data and information are available electronically at the pages of journal website: https://www.shd-pub.org.rs/index.php/JSCS/article/view/13430, or from the corresponding author on request.

Acknowledgements. This research was funded by the Ministry of Science, Technological Development, and Innovation of the Republic of Serbia (grant numbers: 451-03-137/2025-03/200116, 451-03-136/2025-03/ 200168 and 451-03-136/2025-03/200026).

ИЗВОД

ПРОМЕНЕ ЕПИКУТИКУЛАРНОГ ВОСКА КОД ЛИСТОВА *Chenopodium album* L. И *Abutilon theophrasti* MEDIK. РАЗЛИЧИТЕ СТАРОСТИ

ФИЛИП ВРАЊЕШ[1], САВА ВРБНИЧАНИН[2], ВЕЛЕ ТЕШЕВИЋ[3], МИРЈАНА ЦВЕТКОВИЋ[4] и ДРАГАНА БОЖИЋ[2]

[1]Eurofins Agroscience Regulatory, Студентска 35/10, 11000 Београд, [2]Универзитет у Београду, Пољопривредни факултет, Немањина 6, 11000 Земун-Београд, [3]Хемијски факултет, Универзитет у Београду, Студентски трг 12-16, Београд и [4]Универзитет у Београду, Институт за хемију, технологију и металургију, одељење за хемију, Његошева 12, 11000 Београд

Епикутикуларни воскови се састоје од комплексне мешавине различитих органских једињења. Преовлађујућа класа једињења се састоји од *n*-алкана. *Chenopodium album* и *Abutilon theophrasti* су космополитске коровске врсте, обе од економског значаја због

потешкоћа у сузбијању и обе врсте синтетишу восак на површини листова.Ово истраживање је показало да је код *C. album* садржај воскова највећи код најстаријих листова, а најмањи код најмлађих листова. Насупрот томе, код *A. theophrasti* је садржај воскова константан код млађих листова као и код старијих. Удео воскова у листовима не зависи од старости листова код обе врсте. У садржају епикутикалних воскова листова *C. album* доминирају алкани и алкохоли. Док код листова *A. theophrasti* доминирају алкани, алкохоли и тритерпени. Квантитативне варијабилности епикутикуларних воскова зависе од старости листова.

(Примљено 20. јуна, ревидирано 23. јула, прихваћено 17. новембра 2025)

REFERENCES

1. S. Vrbnicanin, G. Malidza, L. Stefanovic, I. Elezović, R. Stanković Kalezić, D. Marisavljević, K. Jovanović Radovanov, D. Pavlović, M. Gavrić, *Plant Doctor* **36** (2008) 303 (https://scindeks.ceon.rs/article.aspx?artid=0354-61600805303V) (in Serbian)
2. G. Kruger, W. Johnson, S. Weller, M. Owen, D. Shaw, J. Wilcut, D. Jordan, R. Wilson, M. Bernards, B. Young, *Weed Technol.* **23** (2009) 162 (https://doi.org/10.1614/WT-08-040.1)
3. S. Follak, U. Aldrian, M. Schwarz, *Plant Prot. Sci.* **50** (2014) 157 (https://doi.org/10.17221/55/2013-PPS)
4. M. Burghardt, A. Friedmann, L. Schreiber, M. Riederer, *Pest Manag. Sci.* **62** (2006) 137 (https://doi.org/10.1002/ps.1139)
5. N. Shaheen, M. Ajab Khan, G. Yasmin, M. Qasim Hayat, M. Ahmad, M. Zafar, A. Jabeen, *J. Med. Plants Res.* **3** (2009) 1002 (https://academicjournals.org/journal/JMPR/article-full-text-pdf/D0B884E15430)
6. H. Hatterman-Valenti, A. Pitty, M. Owen, *Weed Sci.* **59** (2011) 14 (https://doi.org/10.1614/WS-D-10-00061.1)
7. S. Muhammad, K. Wuyts, G. Nuyts, K. De Wael, R. Samson, *Urban For. Urban Green.* **47** (2020) 126557 (https://doi.org/10.1016/j.ufug.2019.126557)
8. C. Buschhaus, R. Jetter, *J. Exp. Bot.* **62** (2010) 841 (https://doi.org/10.1093/jxb/erq366)
9. S. Jovanović, B. Zlatković, G. Stojanović, *Chem. Biodivers.* **13** (2016) 459 (https://doi.org/10.1002/cbdv.201500148)
10. B. Trudić, B. Anđelković, V. Tešević, S. Orlović, M. Jadranin, G. Krstić, V. Galović, *South-East Eur For*. **7** (2016) 129 (https://doi.org/10.15177/seefor.16-12)
11. S. Jovanović, B. Zlatković, G. Stojanović, *Chem. Biodivers.* **12** (2015) 767 (https://doi.org/10.1002/cbdv.201400251)
12. B. Nikolić, V. Tešević, I. Đorđević, M. Jadranin, M. Todosijević, S. Bojović, P. Marin, *J. Serb. Chem. Soc.* **75** (2010) 1337 (https://doi.org/10.2298/JSC091014109Z)
13. R. Chemelewski, B. A. McKinley, S. Finlayson, J. E. Mullet, *Front. Plant Sci.* **14** (2023) 1227859 (https://doi.org/10.3389/fpls.2023.1227859
14. R. Bourgault, S. Matschi, M. Vasquez, P. Qiao, A. Sonntag, C. Charlebois, M. Mohammadi, M. J. Scanlon, L. G. Smith, I. Molina, *Ann. Bot.* **125** (2020) 79 (https://doi.org/10.1093/aob/mcz143)
15. L. Busta, D Hegebarth, E Kroc, R Jetter, *Planta* **245** (2017) 297 (https://doi.org/10.1007/s00425-016-2603-6)
16. C. McWhorter, *Weed Sci.* **41** (1993) 475 (https://doi.org/10.1017/S0043174500052218)
17. D. Chachalis, K. Reddy, C. Dennis Elmore, M. Steele, *Weed Sci.* **49** (2001a) 628 (https://doi.org/10.1614/0043-1745(2001)049[0628:HELSAS]2.0.CO2)
18. D. Chachalis, K. Reddy, C. Dennis Elmore, *Weed Sci.* **49** (2001b) 156 (https://doi.org/10.1614/0043-1745(2001)049[0628:HELSAS]2.0.CO;2)

19. V. Zeisler-Diehl, Y. Müller, L. Schreiber, *J. Plant Physiol.* **227** (2018) 66 (https://doi.org/10.1016/j.jplph.2018.03.018)
20. F. Vranješ, D. Božić, D. Rančić, S. Vrbničanin, in *Proceedings of the VIII Congress on Plant Protection*, November 25–29, 2019, Zlatibor, Serbia, IOBC-WPRS, Plant Protection Society of Serbia, Darmstadt, 2021, pp. 37–41.

Journal of the Serbian Chemical Society
JSCS-info@shd.org.rs • www.shd.org.rs/JSCS
J. Serb. Chem. Soc. 91 (1) S15–S20 (2026) *Supplementary material*

SUPPLEMENTARY MATERIAL TO

Changes in leaf epicuticular wax with age of *Chenopodium album* L. and *Abutilon theophrasti* Medik.

FILIP VRANJEŠ[1], SAVA VRBNIČANIN[2], VELE TEŠEVIĆ[3], MIRJANA CVETKOVIĆ[4], and DRAGANA BOŽIĆ[2]*

[1]*Eurofins Agroscience Regulatory, Studentska 35/10, 11000 Belgrade, Serbia,* [2]*University of Belgrade, Faculty of Agriculture, Nemanjina 6, 11000 Zemun-Belgrade, Serbia,* [3]*University of Belgrade – Faculty of Chemistry, Studentski trg 12–16, 11000 Belgrade, Serbia and* [4]*University of Belgrade, Institute of Chemistry, Technology and Metallurgy – National Institute of the Republic of Serbia, Njegoševa 12, 11000 Belgrade, Serbia*

J. Serb. Chem. Soc. 91 (1) (2026) 11–22

* Corresponding author. E-mail: dbozic@agrif.bg.ac.rs

Table S-I. Relative abundance of identified compounds in *Abutilon theophrasti* using the gas chromatography-mass spectrometry(GC-MS) method.

	Rt (min)	Compound	Class	RI	RI_{lit}	A1 (%)	A2 (%)	A3 (%)	A4 (%)	A5 (%)
1	40,745	Hexadecanal	aldehyde	1814		0,1	0,3	0,5	0,5	0,3
2	43,466	9-Hexadecenoic acid, methyl ester, (Z)-	ester	1901	1912	0,0	0,1	0,2	0,1	0,1
3	44,553	Hexadecanoic acid, methyl ester	ester	1925	1921	0,0	0,2	0,2	0,1	0,1
4	47,665	Octadecanal	aldehyde	2018		0,1	0,2	0,3	0,3	0,2
5	47,824	Hexadecanoic acid, 1-methylethyl ester	ester	2020	2024	0,1	0,1	0,0	0,0	0,0
6	50,024	9,12-Octadecadienoic acid (Z,Z)-, methyl ester	ester	2095	2095	0,0	0,2	0,1	0,1	0,1
7	50,378	9-Octadecenoic acid (Z)-, methyl ester	ester	2098	2086	0,0	0,1	0,1	0,1	0,0
8	54,027	Eicosanal	aldehyde	2230	2224	0,1	0,2	0,5	0,4	0,2
9	56,207	Tricosane	alkane	2304	2300	0,1	0,1	0,1	0,1	0,1
10	56,499	2-Heneicosanone	ketone	2313		0,1	0,1	0,2	0,1	0,1
12	59,072	Tetracosane	alkane	2401	2400	0,1	0,1	0,1	0,1	0,1
13	59,888	Docosanal	aldehyde	2428		0,0	0,1	0,1	0,1	0,1
14	61,79	Pentacosane	alkane	2501	2500	0,4	0,9	0,8	1,2	0,6
15	64,393	Hexacosane	alkane	2598	2600	0,1	0,3	0,2	0,2	0,1
16	66,891	Heptacosane	alkane	2703	2700	5,4	3,7	6,2	7,3	3,7
17	69,254	Octacosane	alkane	2803	2800	2,1	4,7	2,7	3,1	1,0
18	70,021	Squalene	triterpene	2835		9,9	6,4	6,2	4,6	2,2
19	71,6	Nonacosane	alkane	2903	2900	21,6	19,2	16,9	19,3	10,9
20	73,755	Triacontane	alkane	3002	3000	1,6	1,2	0,7	0,8	0,4
21	73,985	NI		3010		0,1	0,2	0,4	0,4	0,4
22	74,06	Hexacosyl acetate	ester	3015	2995	0,2	0,1	0,2	0,2	0,3
23	74,68	Octacosanal	Aldehyde	3043	3014	0,2	0,3	0,2	0,2	0,2
24	75,605	NI		3084		0,4	0,3	0,3	0,4	0,1
25	75,703	15-Nonacosanone	ketone	3089	3097	0,3	0,2	0,2	0,1	0,1
26	75,933	Hentriacontane	alkane	3100	3100	5,6	2,9	3,9	4,6	4,8
27	76,099	1-Octacosanol	alcohol	3106	3110	5,3	6,4	6,9	8,3	8,2
28	76,569	Cholesterol	sterol	3124	3188	1,4	3,1	3,1	4,2	3,5
29	76,83	Vitamin E		3139	3149	0,8	0,6	1,0	0,5	0,4
30	76,874	2-(Decanoyloxy)propane-1,3-diyl dioctanoate	ester	3141	3138	0,4	0,4	0,4	0,1	0,2
31	77,028	NI		3144		0,4	0,4	0,5	0,2	0,2
32	77,37	NI				0,3	0,4	0,5	0,1	0,1
33	78,033	Dotriacontane	alkane	3196	3199	0,3	0,3	0,4	0,2	0,4
34	78,346	1-Nonacosanol	alcohol	3208	3233	0,3	0,1	0,3	0,4	1,1
35	78,616	Octacosyl acetate	ester	3227	3196	0,3	0,1	0,2	0,3	0,2
36	78,938	Campesterol	sterol	3236	3131	0,4	0,1	0,2	0,1	1,8
37	79,002	NI		3239		0,2	0,4	0,3	0,2	0,7
38	79,436	Stigmasterol	sterol	3267	3170	0,1	0,2	0,3	0,1	0,2
39	80,092	Tritriacontane	alkane	3297	3300	0,9	0,7	1,5	1,4	3,1
40	80,419	1-Triacontanol	alcohol	3305	3306	2,7	1,9	1,2	1,9	1,0
41	80,612	γ-Sitosterol	sterol	3316	3351	0,7	0,7	0,6	0,7	0,1

	Rt (min)	Compound	Class	RI	RI lit	A1 (%)	A2 (%)	A3 (%)	A4 (%)	A5 (%)
42	80,983	β-Sitosterol	sterol	3329	3408	3,1	0,4	0,2	0,2	0,5
43	81,071	Olean-12-en-3-one	triterpene	3338	3327	1,8	4,8	5,6	3,8	2,6
44	81,202	NI		3346		0,2	0,2	0,5	0,3	0,1
45	81,506	α-Amyrin	sterol	3361	3376	6,9	8,0	3,6	2,0	0,7
46	81,968	Lup-20(29)-en-3-one	triterpene	3385	3384	5,9	4,8	4,8	3,0	1,2
47	82,09	NI		3386		0,1	0,0	1,7	0,5	0,1
48	82,312	Tetratriacontane	alkane	3404	3400	0,1	0,1	0,1	0,1	0,1
49	82,448	Lupeol	sterol	3409	3382	3,3	4,2	1,2	1,2	0,5
50	82,536	9-Hexadecenoic acid, nonadecyl ester, (Z)-	ester	3413		1,5	0,4	1,9	0,2	0,3
51	82,947	Hexadecanoic acid, heptadecyl ester	ester	3437		0,2	0,2	0,3	0,2	0,5
52	84,051	Dodecanoic acid, docosyl ester	ester	3493	3553	0,4	0,3	1,1	2,4	3,9
53	84,449	NI		3509		0,4	0,3	0,4	0,4	0,1
54	84,599	NI		3513		0,3	0,3	0,3	1,4	0,1
55	84,747	NI		3523		0,3	0,1	0,3	0,7	0,1
56	85,004	9-Hexadecenoic acid, octadecyl ester	ester	3535	3528	1,4	0,9	1,2	0,4	0,9
57	85,157	NI		3540		0,3	0,3	0,3	0,3	0,1
58	85,372	Hexadecanoic acid, octadecyl ester	ester	3554	3546	0,8	0,6	0,8	0,5	0,7
59	86,015	Dodecanoic acid, tricosyl ester	ester	3586		0,1	0,1	0,2	0,3	0,7
60	86,507	NI		3608		1,3	4,6	1,7	2,3	5,7
61	87,447	NI		3643		0,2	0,2	0,3	2,1	0,3
62	88,176	Dodecanoic acid, tetracosyl ester izome 2	ester	3671		0,5	0,6	1,2	3,1	5,3
63	88,877	9-Hexadecenoic acid, 9-eicosyl ester, (Z,Z)-	ester	3695	3730	1,4	1,0	1,4	0,4	0,8
64	89,352	9-Hexadecenoic acid, eicosyl ester, izomer 2	ester	3711		1,2	0,7	0,9	0,6	1,0
65	89,792	Hexadecanoic acid, eicosyl ester	ester	3729		0,7	0,5	0,6	0,6	0,8
66	90,759	Dodecanoic acid, pentacosyl ester	ester	3762		0,1	0,0	0,2	0,4	0,6
67	91,338	NI		3786		0,6	0,3	0,5	0,3	0,3
68	92,398	NI		3825		1,4	3,9	1,5	0,2	3,3
69	92,938	Hexadecanoic acid, docosyl ester	ester	3847		0,1	0,8	1,8	0,2	8,9
70	93,496	Dodecanoic acid, hexacosyl ester	ester	3867		0,3	0,4	1,3	2,5	5,3
71	94,488	NI		3892		0,5	1,8	2,4	1,9	2,7
72	95,096	Hexadecanoic acid, dosanyl ester	ester	3913		0,6	0,3	0,5	1,9	1,5
73	95,661	9-Hexadecenoic acid, docosanyl ester, (Z)-	ester	3946		0,6	0,6	1,0	0,3	2,4
74	96,835	Dodecanoic acid, heptcosanyl ester	ester	3981		0,1	0,0	0,1	1,8	0,2
75	97,817	NI		4019		0,2	0,3	0,6	0,1	0,3
76	98,108	NI		4032		0,1	0,1	0,4	0,2	0,1
77	99,288	NI		4073		0,0	0,1	0,6	0,2	0,0
			aldehydes			0,4	1,0	1,6	1,4	1,0
			alkanes			38,2	34,0	33,4	38,3	25,2
			alcohols			8,2	8,4	8,4	10,6	10,4

	Rt (min)	Compound	Class	RI	RI_{lit}	A1 (%)	A2 (%)	A3 (%)	A4 (%)	A5 (%)
			esters			11,0	8,8	15,9	16,8	34,8
			ketones			0,4	0,3	0,4	0,2	0,2
			triterpenes			17,6	16,0	16,7	11,4	6,0
			sterols			16,0	16,6	9,1	8,5	7,2
			vitamin E			0,8	0,6	1,0	0,5	0,4
			NI			7,4	14,2	13,5	12,3	14,9
			Total			100,0	100,0	100,0	100,0	100,0

A1-fist leaf; A2- second leaf; A3- third leaf; A4- fourth leaf; A5- fifth leaf
10 largest peaks for not identified compound:
60. 57(100), 257(82), 43(76), 55(63), 71(60), 83(55), 97(53), 69(53), 171(41), 85(39)
68. 57(100), 257(94), 43(73), 55(60), 71(58), 83(56), 97(56), 69(49), 85(39), 41(32)
71. 43(100), 57(99), 69(91), 99(88), 55(80), 71(66), 41(59), 97(45), 68(44), 285(41)

Table S-II. Relative abundance of identified compounds in *Chenopodium album* L. using the gas chromatography-mass spectrometry(GC-MS) method.

	Rt (min)	Compound	Class	RI	RI_{lit}	CH1 (%)	CH2 (%)	CH3 (%)	CH4 (%)	CH5 (%)
1	65,264	Tetracosanal	aldehyde	2632	2632	0,2	0,2	0,2	0,1	0,1
2	65,822	Squalane	alkane	2656	2657	1,0	0,3	0,1	0,1	0,1
3	66,384	Hexacosanal	aldehyde	2681	2833	0,1	0,0	0,1	0,0	0,1
4	66,895	Heptacosane	alkane	2701	2700	1,9	3,0	3,8	4,2	5,7
5	71,607	Nonacosane	alkane	2904	2900	14,3	20,5	30,7	31,5	28,9
6	73,780	Triacontane	alkane	2999	3000	0,1	0,1	0,2	0,2	0,3
7	73,968	Hexacosyl acetate	ester	3009	3015	0,1	0,2	0,3	0,2	0,4
8	74,737	Octacosanal	aldehyde	3046	3043	9,9	9,7	6,1	6,8	6,8
9	75,957	Hentriacontane	alkane	3099	3100	2,4	2,5	4,0	3,6	6,3
10	76,115	1-Octacosanol	alcohol	3107	3106	22,6	31,8	33,1	30,1	24,1
11	76,537	Cholesterol	sterol	3122	3124	1,1	0,5	0,3	0,4	0,9
12	76,871	NI		3139		0,9	0,4	0,2	0,2	0,4
13	77,070	NI		3145		0,3	0,3	0,2	0,2	0,2
14	78,377	Octacosyl acetate	ester	3206	3227	0,7	0,6	0,6	0,9	2,0
15	79,029	Triacontanal	aldehyde	3242		5,7	4,9	3,1	3,6	5,9
16	80,120	9-Hexadecenoic acid, hexadecyl ester	ester	3294	3328	0,2	0,3	0,4	0,5	0,7
17	80,327	1-Triacontanol	alcohol	3307	3305	2,1	3,5	3,4	3,4	3,8
19	81,077	β-Amyrin	sterol	3340	3337	0,4	0,6	0,4	0,5	0,9
20	81,232	1-Dotriacontanol	alcohol	3349		0,2	0,1	0,1	0,1	0,2
21	81,487	Hexadecanoic acid, hexadecyl ester	estar/	3358		0,2	0,0	0,1	0,1	0,2
22	81,521	α-Amyrin	sterol	3359	3376	0,1	0,2	0,1	0,1	0,1
23	81,759	Olean-12-en-3-one	triterpene	3375	3327	0,1	0,0	0,0	0,0	0,1
24	82,568	NI		3415		0,3	0,1	0,1	0,1	0,2
25	82,990	NI		3435		0,1	0,1	0,1	0,1	0,1
26	83,112	Tetracontanal	aldehyde	3443		0,9	0,7	0,4	0,3	0,8
27	83,477	Stigmast-4-en-3-one;	triterpene	3458	3237	0,1	0,0	0,1	0,1	0,3
28	84,480	17-Pentatriacontene	alkane	3509		0,0	0,1	0,1	0,1	0,1
29	85,019	9-Hexadecenoic acid, octadecyl ester, (Z)-	ester	3538	3528	0,8	0,3	0,2	0,2	0,6
30	85,187	NI		3542		0,1	0,1	0,1	0,1	0,1
31	85,397	Hexadecanoic acid, octadecyl ester	ester	3557	3546	0,8	0,4	0,4	0,3	0,4
32	86,394	NI		3601		0,2	0,2	0,1	0,1	0,2
33	86,645	NI		3610		0,5	0,9	0,2	0,1	0,2
34	87,390	Benzoic acid, hexacosyl ester	ester	3637		2,7	1,0	0,6	1,0	0,8
35	88,088	NI		3664		0,1	0,4	0,0	0,0	0,1
36	88,812	NI		3692		0,6	0,2	0,1	0,1	0,0
37	88,905	NI		3696		0,1	0,3	0,1	0,1	0,4
38	89,388	9-Hexadecenoic acid, eicosyl ester, (Z)-	ester	3715	3700	0,7	0,3	0,1	0,2	0,4
39	89,843	Hexadecanoic acid, eicosyl ester	ester	3731	3747	3,8	3,6	3,8	2,8	1,9
40	91,370	NI		3782		0,3	0,2	0,1	0,1	0,2
41	91,629	NI		3795		0,1	0,0	0,0	0,2	0,0
42	92,655	Benzoic acid, octacosyl ester	ester	3836		15,1	6,9	3,2	4,9	3,9
43	93,004	Hexadecanoic acid, hexacosyl ester	ester	3846		1,8	0,0	0,0	0,0	0,1

	Rt (min)	Compound	Class	RI	RI_{lit}	CH1 (%)	CH2 (%)	CH3 (%)	CH4 (%)	CH5 (%)
44	94,525	NI		3911		0,3	0,2	0,0	0,1	0,2
45	95,141	NI		3924		0,2	0,1	0,1	0,1	0,2
46	95,769	Hexadecanoic acid, docosyl ester	ester	3948		5,5	3,8	2,5	1,9	0,7
47	99,735	NI		4098		0,4	0,5	0,2	0,2	0,2
aldehydes						16,8	15,5	9,8	10,9	13,6
alkanes						19,8	26,5	38,8	39,8	41,4
esters						32,3	17,4	12,3	12,9	12,0
alcohols						24,9	35,4	36,6	33,6	28,1
sterols						1,6	1,3	0,8	1,0	1,9
NI						4,5	3,9	1,6	1,8	2,6
triterpenes						0,2	0,1	0,1	0,1	0,4
Total						100,0	100,0	100,0	100,0	100,0

CH1-first leaf pair; CH2-second leaf pair; CH3-third leaf pair; CH4-fourth leaf pair; CH5-fifth leaf pair

Journal of the Serbian Chemical Society
JSCS-info@shd.org.rs • www.shd.org.rs/JSCS
J. Serb. Chem. Soc. *91* (1) 23–37 (2026)
JSCS–5475
Original scientific paper
Published 5 February, 2026

Theoretical and experimental prediction of corrosion inhibition efficiency of isatin and its derivatives by DFT calculations and weight loss method – A comparative study

JONE CELESTINA JOSEPH XAVIER RAJ[1], MUTHUMANICKAM SHENBAGAPUSHPAM[2]*, ARUL DEEPA VINCENT[1], PRIYADHARSANI SHANMUGARAJ[1], CHAKKARAVARTHI RAJ[3], SATHEESH RAJAMOHAN[2] and RAMASAMY RAJA VIRUTHACHALAM[2]

[1]*The Research Centre of Chemistry, Fatima College, Madurai – 625018, Tamilnadu, India,* [2]*Department of Chemistry, Mannar Thirumalai Naicker College, Madurai – 625004, Tamilnadu, India and* [3]*Department of Physics, Department of Science and Humanities, St. Micheal College of Engineering, Sivaganagai – 630551, Tamilnadu, India*

(Received 14 April, revised 25 May, accepted 20 November 2025)

Abstract: The corrosion inhibition performance of isatin and its N1/C5 substituted derivatives were analyzed by DFT calculation (B3LYP, 6311g, dp) in gas phase and solvation method with the help of Gaussian 09W and Gaussian 16. The calculated quantum chemical parameters such as E_{LUMO}, E_{HOMO}, ionization potential (I), electron affinity (A), electronegativity (χ), band gap energy (ΔE), softness (σ), hardness (η) and electrophilicity (ω), proved that isatin and its derivatives have the tendency to donate the electrons to the surface of metal ion on adsorption. The number of electron transfer (ΔN) from isatin and its derivatives to iron metal was calculated theoretically and was in following order IX>III>VII>IV>II>V>I>VIII>VI. The experimental studies reveal the same order of inhibition as in theoretical studies. Mulliken's charge distribution analysis of the same compounds indicates the high negative magnitude on N1 atom. The negative magnitude of N1 atom was altered by substitution in N1 and C-5 position of isatin, which was identified theoretically. Fukui local parameters were also calculated and used in the prediction of the compounds local selectivity.

Keywords: adsorption; HOMO; LUMO; Fukui local selectivity; Mulliken's charge distribution.

INTRODUCTION

Density functional theory (DFT) is an important tool in modern quantum chemistry in analyzing the electronic parameters of the compounds. It also have

* Corresponding author. E-mail: muthumanickams92@gmail.com, muthumanickams@mannarcollege.ac.in
https://doi.org/10.2298/JSC250414085R

versatile applications like drug design, solar cells, water splitting, materials discovery and design, corrosion inhibition, *etc*., with reduced computational cost.[1–6] Amongst corrosion inhibition behavior, prediction of metal surface interaction with inhibitor molecules is one of the crucial field of research over two decades.[7–9] Corrosion means destruction of metals, plastics, concrete and wood by various environmental substances surrounding it.[7–10] There are various metals used in the industry for storage of acids, bases and petrochemical products, wine, *etc*. Among them iron is the most used metal in various industries.[7–9] Added to that, acids have been utilized for pickling, descaling, acid cleaning, acidifying of oil wells, *etc*. This may also attack the surface of the metal resulting in the formation of metal oxide layers on the surface of the iron by dissolution of the metal.[7,8,11–15] For this, various types of inhibitors like organic/green/bio inhibitors have been reported in the last two decades.[16–19] Among these three inhibitors, organic inhibitors are suitable in preventing the corrosion of mild steel due to the known structure of the inhibitor. This helps to analyze the surface adsorption mechanism exactly. The above points make organic inhibitor better than bio/green inhibitor. In green inhibitors various chemical compounds are present and in addition prediction of mechanism and preserving of bio inhibitor is too difficult in varying temperature, pH and acidity.

Isatin is an organic compound and its derivatives were reported and well documented as non-toxic corrosion inhibitors for iron in various acid solutions in the last decade.[20–30] The available report of isatin, as inhibitor determined by weight loss method, is supported by electrochemical studies.[30] There is a lack of availability of computational data in the mechanism prediction of the metal surface adsorption by inhibition. Recent days, exact evaluation of nucleophilicity/electrophilicity by electron donor/acceptor has been documented with a help of Fukui indices.[31–36] This is an important parameter, to analyze the part of the compound attached for interaction with the surface of metal. In previous reports of isatin derivatives as corrosion inhibitors, Fukui indices calculation are lacking[20–30] because the reports were concentrated only on the Schiff bases of the isatin with free N–H groups. This free N–H is useful in formation of azanion in acidic solution which might be useful for surface interaction on the metal.[20–22,25–27,30] In this work the main focus is on comparison of isatin and its derivatives with electron donating/withdrawing moiety in the nitrogen N1- and C5-carbon to predict the better acceptor and donor parts of the derivatives by computational methods.

EXPERIMENTAL

DFT calculations

Isatin and its derivatives as the chosen inhibitors were subjected to DFT calculations and all the calculations were performed by Gaussian 09W and Gaussian 16 with B3LYP and 6311G basic set for optimization.[37,38] All optimized geometries were confirmed as true minima by vibrational frequency analysis using the same basic set. The calculation of energy was done

with B3LYP and 6-311G basic set. Grimme's D3(BJ) provides a gas-phase London dispersion correction to total energies and geometries were analysed using PBE0-GD3BJ/6-31G (d,p). Solvent polarization was modeled separately using the IEFPCM-water implicit solvent model using B3LYP and 6-311G (d,p). The non-covalent interactions in the gas phase, of the proposed inhibitor, were calculated by using Grimme's D3 method and the results are provided in the supporting information (Table S-9 of the Supplementary material to this paper). Corrosion on the metal surface mainly occurred in the presence of aqueous region, for this cause the energy analysis were performed using IEFPCM-water implicit solvent model for the proposed inhibitors and the results are provided in the supporting information (Table S-10 of the Supplementary material). The calculation parameters of compounds are provided in Table S-1 of the Supplementary material. The comparison of the calculations with and without dispersion correction reveals the change in the bandgap energies. The DFT calculation with dispersion correction exhibits higher local parameters, such as ionization potential (I), electron affinity (A), electronegativity (χ), band gap energy (ΔE), softness (σ), hardness (η) and electrophilicity (ω), than the calculation without dispersion correction. This is because of presence of non-covalent interactions like van der Waals force of attraction and London forces between the molecules. Energy differences occurred in the DFT calculations with or without dispersion correction but the orders of local parameters have not changed. The comparison of the local parameters between the gas phase DFT studies and IEFPCM-water studies have very slight changes due to the protonation effects of the inhibitors. The obtained result from the energy calculation (gas phase DFT) has been utilized to predict the Fukui global parameters and local parameters of the compound by using UCA Fukui software.[38] The name of the compound, optimized structure, HOMO and LUMO diagrams are given in Table I. The numbering of the atoms of the compounds have been assigned by DFT.

TABLE I. Compound number, name, structure, optimized structure, HOMO and LUMO structure of the compound

Compd. No.	Name and structure	Optimized structure	HOMO	LUMO
I	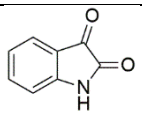 Isatin	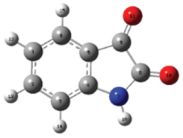	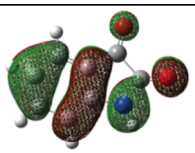	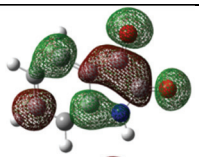
II	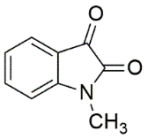 *N*-Methyl isatin	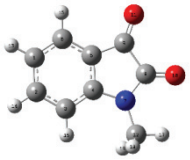	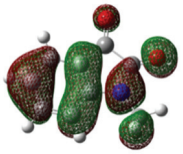	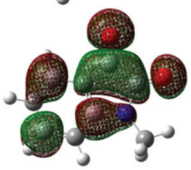
III	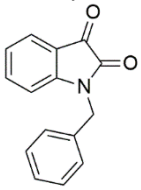 *N*-Benzyl isatin	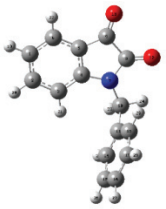	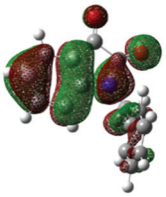	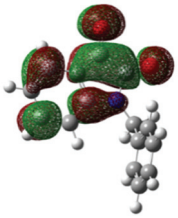

TABLE I. Continued

Compd. No.	Name and structure	Optimized structure	HOMO	LUMO
IV	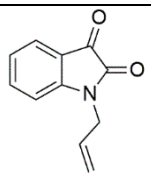 *N*-Allyl isatin	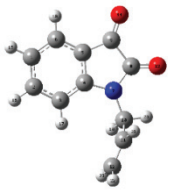	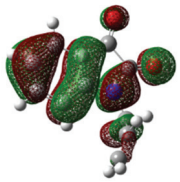	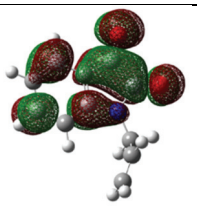
V	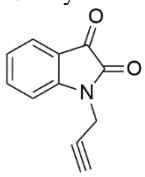 *N*-Propargyl isatin	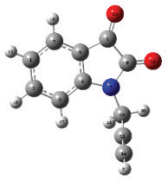	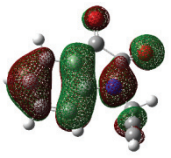	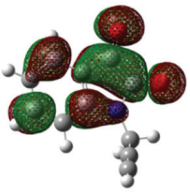
VI	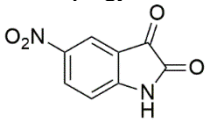 5-Nitro isatin	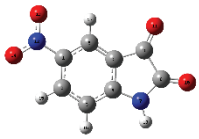	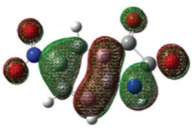	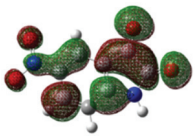
VII	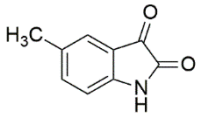 5-Methyl isatin	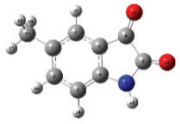	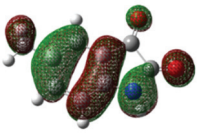	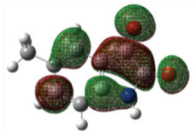
VIII	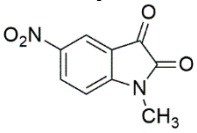 *N*-Methyl-5-nitro isatin	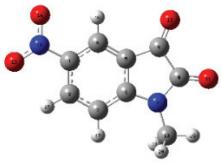	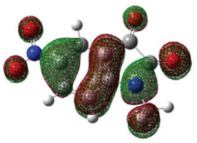	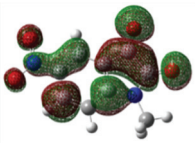
IX	 *N*-Methyl-5-methyl isatin	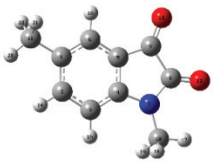	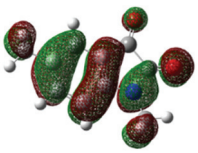	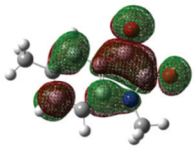

By having E_{HOMO} and E_{LUMO} energy values from DFT calculation, following quantum chemical parameters such as: I, A, χ, ΔE, σ, η and ω, were calculated.[21,38]

I is related with highest occupied molecular orbital E_{HOMO} and the expression is as follows:

$$I = -E_{HOMO} \quad (1)$$

A is related to the least unoccupied molecular orbital (E_{LUMO}) the expression is:

$$A = -E_{\mathrm{LUMO}} \tag{2}$$

The energy gap (ΔE) of isatin and its derivatives is energy difference between highest occupied molecular orbital E_{HOMO} and least unoccupied molecular orbital E_{LUMO}. The energy gap is calculated by the following equation:

$$\Delta E = E_{\mathrm{HOMO}} - E_{\mathrm{LUMO}} \tag{3}$$

$$\Delta E = I - A \tag{4}$$

η of the compound is defined as the second derivative of electronic energy (E) with respect to number of electrons (N) at constant external potential. This originates from the Lewis theory and theory of hard and soft acid and base. The expression for hardness follows:

$$\eta = \frac{1}{2}(I - A) \tag{5}$$

$$\eta = \frac{1}{2}(E_{\mathrm{HOMO}} - E_{\mathrm{LUMO}}) \tag{6}$$

σ is reciprocal of hardness and expressed as:

$$\sigma = \frac{1}{\eta} \tag{7}$$

Electronegativity is the descriptor of the direction of flow of electrons between metal and an inhibitor and it is related to I and A (E_{HOMO} and E_{LUMO}):

$$\chi = \frac{1}{2}(I + A) \tag{8}$$

$$\chi = -\frac{1}{2}(E_{\mathrm{HOMO}} - E_{\mathrm{LUMO}}) \tag{9}$$

ω is the reciprocal of electrophilicity and expressed as:

$$\omega = \frac{\mu^2}{2\eta} \tag{10}$$

The number of electrons transferred (ΔN) were calculated by the following expression using electrophilicity and hardness of Fe from the previous reported literature:

$$\Delta N = \frac{\chi_{\mathrm{Fe}} - \chi_{\mathrm{Inh}}}{2(\eta_{\mathrm{Fe}} - \eta_{\mathrm{Inh}})} \tag{11}$$

Weight loss method

Mass loss method was conducted at different temperatures in the range 308–333 K for 2 h in 1 M HCl. The specimens were immersed in 100 ml of the respective inhibitor and the test solution in a thermostatic bath. The specimens were weighed before and after immersion. The difference in weight was taken as the weight loss of mild steel. From the weight loss (ΔW), corrosion rate (λ) and the percentage of inhibition efficiency (IE in %) were calculated using the following equations:

$$\lambda(\mathrm{mpy}) = 534X\frac{\Delta W}{DAT} \tag{12}$$

$$IE = 100\frac{W_0 - W_1}{W_0} \tag{13}$$

Here, $\Delta W = W_b - W_a$, where W_b and W_a are the specimen weights before and after immersion in the tested solution, W_0 and W_1 are the weight loss of mild steel in the absence and presence of inhibitor respectively, D is the density of the iron (g/cm^3), A is the area of the specimen in in^2 and T is the period of immersion in h.

RESULTS AND DISCUSSION

From the literature reports, there seems to be a relationship between corrosion inhibition property and the electronic property of the compound.[39] The quantum chemical parameters I, A, χ, ΔE, σ, η and ω are used to predict the electronic property and how it works on the adsorption process.[39,40] The adsorption of the organic species on the surface of the metal has been deduced by the above-mentioned parameters which was calculated by using highest occupied molecular orbital (HOMO) and lowest unoccupied molecular orbital (LUMO) and calculated by DFT studies. The calculated values for various isatin derivatives are shown in Table II. In general, the interaction between the metal and the inhibitor takes place due to the transfer of electron from the inhibitor HOMO to metal d-orbital or the electron transfer from metal d-orbital to LUMO of the inhibitor. From this statement, the inhibitor molecule has highest HOMO value, it has tendency to donate electron to the metal orbital. In the same way, the inhibitor also has lowest LUMO value, as well it has tendency to accept the d-orbital electron of the metal. The both HOMO and LUMO were localized throughout the whole molecule in the isatin and its derivaties (compounds I–IX) which is witnessed in the Table I. When compared the HOMO and LUMO of isatin (compound I) with N-substituted isatin (compounds II–V), there is change in N-1 atom in compounds II–V from highest occupied to lowest unoccupied due to the substitution of electron donating and electron withdrawing group on the N-1 atom which altered the energies of the excited states. In addition, the substitution in N-1 position of isatin (compounds II to V) alters the C5 carbon from highest occupied to lowest unoccupied which also witnessed in the HOMO and LUMO images in the Table I. On the other hand, the substitution on C5 position of isatin with electron donating $-CH_3$ (compound VII) and electron withdrawing $-NO_2$ (compound VI) did not alter the HOMO and LUMO present in the N1 position of the isatin moiety. This caused the alteration of HOMO and LUMO by the substitution in N1 and C5 resulting the active donating and accepting of electron towards the metal. In this case, both HOMO and LUMO values of the 5-nitro isatin and 1-methyl-5-nitro isatin are comparatively higher than of the other derivatives such as isatin, N1-substituted and C5--substituted isatin. This confirms that the electron donating/withdrawing group (nitro/methyl) substitution polarizes the isatin molecule by electron rich position

and electron deficient position on it. This might be useful in acting as good inhibitor for corrosion.

TABLE II. Calculated global parameters by HOMO and LUMO energies (eV)

Compd. No.	ΔE	I	A	χ	η	σ	ΔN	ω	ε
I	3.7793	6.9271	3.1478	5.0324	1.8846	0.5306	0.5219	6.7189	0.1488
II	3.7258	6.7438	3.0180	4.8809	1.8629	0.5367	0.5687	6.3941	**0.1563**
III	3.6131	6.6812	3.0680	4.8746	1.8065	0.5535	0.5882	6.5766	**0.1520**
IV	3.6259	6.7054	3.0795	4.8924	1.8129	0.5515	0.5812	6.6014	**0.1514**
V	3.6749	6.8172	3.1423	4.9798	1.8374	0.5442	0.5497	6.7481	0.1481
VI	3.8798	**7.7435**	**3.8637**	**5.8036**	1.9399	0.5154	0.3083	**8.6814**	0.1151
VII	3.6188	6.6888	3.0699	4.8794	1.8094	0.5526	0.5859	6.5790	**0.1519**
VIII	3.6939	**7.4850**	**3.7886**	**5.6368**	1.8481	0.5410	0.3687	**8.6252**	0.1159
IX	**3.4942**	6.4959	3.0016	4.7487	**1.7471**	**0.5723**	**0.6442**	6.4538	**0.1549**

The energy gap (ΔE) is an important parameter of the molecule in analyzing the reactivity of the inhibitor towards the metal.[38–40] Moreover, band gap energy decreases and the reactivity of the molecule increases towards the adsorption of metal surface which leads to the increasing inhibition efficiency of the molecule with the change in redox property of the ligand. The results exhibited band gap energy adjustment of isatin by substituting electron withdrawing/donating group on its C-5, N-1 position in it. The bandgap energy of isatin decreased on introducing electron donating groups like methyl, benzyl, propargyl and allyl. The band gap energy of isatin (ΔE = 3.7793 eV) was reduced by introducing a methyl group in its N-1 position (ΔE = 3.7258 eV) and C-5 position (ΔE = 3.6188 eV) alone. The bandgap energy is reduced further to 3.4942 eV by substituting both N-1 and C-5 position of isatin simultaneously. This indicates that methyl substituted isatin have highest activity towards adsorption by donating electrons to the metal surface. On the other hand, the bandgap energy of isatin increased while introducing electron withdrawing group (NO_2) in C-5 position of isatin. From all the isatin derivatives 5-nitro isatin possess the highest bandgap energy (ΔE = 3.8798 eV) which is also reduced by substituting methyl group in N-1 position of isatin (ΔE = 3.6939 eV). This indicates that the nitro substituted isatin has higher activity towards adsorption by accepting electrons from the metal. All the nine derivatives have the bandgap energy in the same range. Among them methyl substituted and nitro substituted were highly warranted for electron accepting and donating to metals respectively in order to prevent corrosion. In addition, the HOMO and LUMO of all the compounds localized over the benzene ring help in attachment to metal atom by inhibitors π-electron which doesn't alter the skeleton of the inhibitors while adsorbing on the metal. This exhibits the good redox property of the inhibitors by sharing its π-electron with metal.

I and A are the measuring tools for the electron donating and accepting nature of the ligand, respectively. The case study of ionization potential and electron

affinity showed that the 5-methyl substituted isatin has the highest tendency to accept/donate electrons from/to the metal orbitals compared to other reported isatin derivatives. This is caused by the strongest interaction between the metal and molecule, which doesn't mean that 5-nitro substituted isatin is the only compound with corrosion inhibition efficiency compared to other reported isatin derivatives. All the reported isatin derivatives have the corrosion inhibition efficiency but 5-methyl substituted isatin has higher efficiency than other derivatives which was accounted by ionization potential and electron affinity, especially electron donating group substituted isatin derivative has the higher tendency to adsorb on the surface of the metal by donating/accepting electrons from the ligand. The parameters ionization potential and electron affinity showed that the electron donating/accepting nature of the isatin derivatives are in the order VI>VIII>I>V>II>IV>VII>III>IX.

χ is the descriptor for the flow of electron in direction between ligand and metal which is giving the E_{HOMO} and E_{LUMO} values. Isatin (compound I) has electronegativity of 5.0324 eV, it was increased to 5.8036 eV by introducing electron withdrawing nitro group (compound VI). The electronegativity is reduced by adding electron donating methyl group to compound VI and the value is found to be 5.6368 eV. Other compounds having the degeneracy values around 4.6–4.9 eV. According to Sanderson's electronegativity equivalization principle, high electronegativity quickly reaches to equalization. It results in low reactivity and low inhibition. From this statement *N*-methyl-5-methyl isatin (IX) may have higher inhibition efficiency than other compounds by having lowest electronegativity.

The measurement of stability and reactivity of the molecule are the important properties for analyzing the polarization of electron clouds of the atoms. η and σ of isatin derivatives, which were calculated by DFT calculation, are related to their molecular reactivity and stability. Generally hard molecules have lowest tendency to polarize the electron cloud of atoms or ions or molecules which have highest band gap energy and hardness value. In addition, soft molecule has highest tendency to polarize or deformation of electron clouds of atoms or ions or electrons which has lowest band gap energy and hardness value. From this statement, *N*--methyl-5-methyl isatin softness (IX) possesses lower hardness value and lowest bandgap energy compared to other isatin derivatives which have been reported in this work. Softness is in the inverse relationship with the hardness and the result was the same.

The ω and ε index is another parameter to predict whether the molecule is electrophile or nucleophile and it reflects the stabilization energy of a system by receiving or donating electron from environment. Electrophilicity and nucleophilicity both have inversion relation with each other. Electron donating substituted isatin derivatives are acting as nucleophiles but electron accepting substituted isatin derivatives act as electrophiles. The highest ω and lowest nucleophilicity value of compounds VI and VIII represent their tendency to accept electron from metal

surface. Moreover, high ε and low electrophilicity compounds II–IV, VII and IX have tendency to donate electrons to metals surface. All the compounds have tendency to donate/accept electron from/to metal surface due to the polarization of a compound. In addition, DFT calculations were performed in gas phase, compounds may be protonated in various solution phase which alter the nucleophilic/electrophilic approaches of a compound. From this study, substituted isatin derivatives have higher tendency to donate or accept electrons from metal surface than isatin.

The ΔN were also calculated for iron metal and it is tabulated in Table II. The values of ΔN show that the inhibition efficiency of all the compounds having tendency to donate electrons to metal surface have the value of $\Delta N < 3.6$, accordingly the inhibition efficiency of the compounds is in order of IX>III>VII>IV>II>>V>I>VIII>VI.

The solvation (IEFPCM-water) effect in water of the proposed inhibitors also remains and follows same order of the local parameters exhibited in gas phase DFT studies (Table S-10 of the Supplementary material). The difference in energy gap (ΔE) in this study is due to protonation effects of the inhibitors. The comparison of compound I (isatin) with its derivatives (compounds II–IX), compound II (*N*-methyl isatin) exhibits the higher ΔE and is about 0.1388 eV which is higher than 0.0679 eV of compound I. This reveals that electron donating $-CH_3$ substituted on nitrogen atom in isatin increases the availability of the lone pair on the nitrogen. The other compounds III to IX does not exhibit characteristic changes in ΔE.

Charge distribution on the atoms of a molecule is theoretically identified by Mulliken charge distribution. From this study, all the above discussed isatin and its derivatives have the tendency to donate electrons to the empty metal orbitals by having the negative magnitude on the heteroatoms present in the isatin derivatives as shown in Fig. 1. Especially negative magnitude of N-1 nitrogen is highly altered by the substituents in both N-1 and C-5 position, to be precise substituents in C-5 position highly increased the negative magnitude of N-1 nitrogen in isatin from –0.488 to –0.824 whether the substituent is EWG or EDG. That also slightly altered the negative magnitude of oxygen present in the neighboring and adjacent carbon. This suggest that, negatively charged nitrogen and oxygen in the isatin derivatives were the most predictive adsorption sites.

Fukui functions are the best tool to identify the local selectivity of molecules active binding site by analyzing whether it undergoes electrophilic or nucleophilic substitution. For this cause, aforementioned molecules were analyzed for Fukui indices to predict the local selectivity of the molecule. The global parameters of examined isatin and its derivatives has been given in Table III. As seen, the global parameters show the high electron density, high softness and low hardness of compounds VI and VIII compared to other derivatives. This confirms that compounds VI and VIII have higher electron donating property to metal d orbitals than other isatin derivatives due to the high electron density, high softness and low hardness

which allows the molecule to polarize the electron cloud in high order. Fukui indices for isatin and its derivatives have been analyzed and the data were tabulated and given in the supporting information. From the above results compounds VI and VIII have the higher tendency to make the coordination with metal surfaces than other compounds. Hence, Fukui indices for compounds VI and VIII are shown in Tables IV and V (Fukui indices of other compounds are given in the Supplementary material, Tables S-2–S8). In addition, Fukui indices are commonly negative values but in our case a non-negative atomic Fukui indices were obtained due to the large number of electron involvement ($\Delta N \approx 1$). [40]

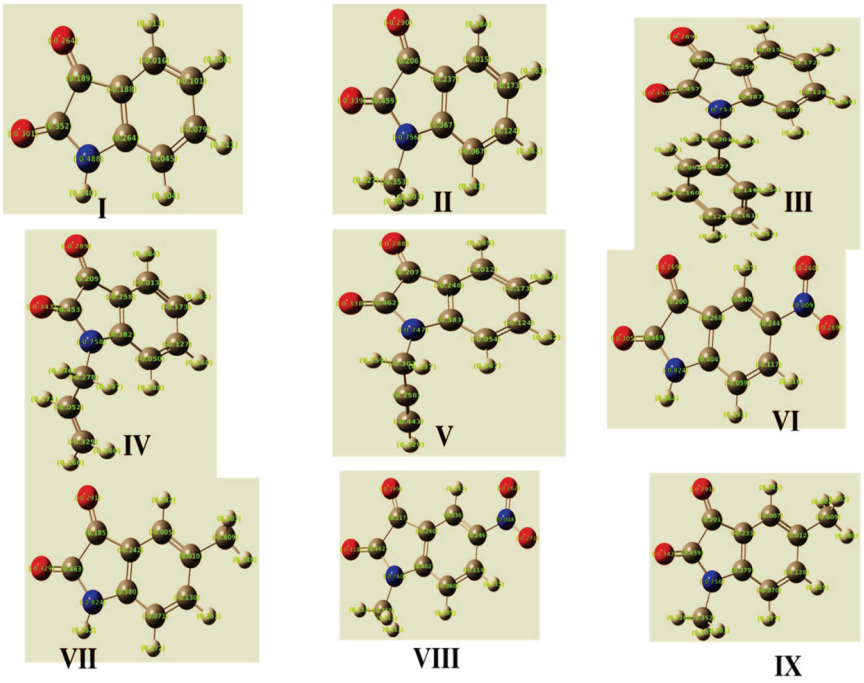

Fig. 1. Mulliken charge population analysis of isatin derivatives.

TABLE III. Global parameters (eV) calculated by Fukui function

Compd. No.	Electronic potential	Hardness	Softness	Electrophilicity
I	3.7878	7.0613	104.8615	1.0158
II	3.7279	7.0613	104.8642	0.9836
III	3.6218	6.7865	109.1255	0.9665
IV	3.7578	7.0695	104.7227	0.9983
V	3.8531	7.0967	104.3227	1.0451
VI	**6.2150**	**3.4503**	**214.6347**	**5.5959**
VII	3.7143	7.0504	105.0193	0.9789
VIII	**6.1524**	**3.4531**	**214.3816**	**5.4801**
IX	3.6572	7.0477	105.0602	0.9491

TABLE IV. Fukui local parameters of compound VI (5-nitro isatin)

N	*Z*	*f*–	*f*+	*f0*	Dual-desc.	Hardness, au	*W*– / eV	W+ / eV
1	C	0.0009	0.0338	0.0173	0.0329	–0.0053	0.0049	**0.1892**
2	C	0.0042	0.0052	0.0047	0.001	0.0004	0.0234	0.0292
3	C	0.0042	0.0037	0.004	–0.0005	0.0006	0.0235	0.021
4	C	0.0044	0.0022	0.0033	–0.0023	0.0009	0.0248	0.012
5	C	0.0248	0.0013	0.0131	–0.0235	0.007	**0.139**	0.0072
6	C	0.0024	0.0019	0.0022	–0.0005	0.0004	0.0134	0.0108
7	N	0.0572	0.0022	0.0297	–0.0549	0.0163	**0.3199**	0.0126
8	C	0.0612	0.0002	0.0307	–0.0611	0.0178	**0.3427**	0.0009
9	C	**0.1234**	0	0.0617	**–0.1234**	0.036	**0.6907**	0.0002
10	O	**0.7117**	0.0005	**0.3561**	**–0.7111**	**0.2075**	**3.9824**	0.003
11	O	0.0015	0.0001	0.0008	–0.0014	0.0004	0.0083	0.0006
12	N	0.0002	**0.4553**	**0.2277**	**0.4551**	–0.0751	0.0009	**2.5479**
13	O	0	**0.2611**	**0.1305**	**0.261**	–0.0431	0.0002	**1.4608**
14	O	0.0001	**0.2324**	**0.1162**	**0.2323**	–0.0383	0.0003	**1.3005**
15	H	0	0	0	0	0	0.0002	0
16	H	0.0005	0	0.0002	–0.0005	0.0001	0.0027	0
17	H	0.0001	0	0	–0.0001	0	0.0004	0
18	H	0.0033	0	0.0016	–0.0033	0.001	0.0184	0

TABLE V. Fukui local parameters of compound VIII (1-methyl-5-nitro isatin)

N	*Z*	*f*–	*f*+	*f0*	Dual-desc.	Hardness, au	*W*– / eV	W+ / eV
1	C	0.0005	0.0346	0.0176	0.0341	–0.0055	0.0029	**0.1896**
2	C	0.0028	0.0054	0.0041	0.0026	–0.0001	0.0153	0.0296
3	C	0.0026	0.004	0.0033	0.0015	0.0001	0.014	0.022
4	C	0.0028	0.002	0.0024	–0.0008	0.0005	0.0154	0.0111
5	C	0.0233	0.0014	0.0124	–0.0219	0.0065	**0.1278**	0.0076
6	C	0.0017	0.0018	0.0018	0.0001	0.0002	0.0096	0.0101
7	N	0.0577	0.0024	0.0301	–0.0553	0.0163	**0.3161**	0.0133
8	C	0.0523	0.0002	0.0263	–0.0521	0.0151	**0.2866**	0.0012
9	C	**0.1025**	0	0.0512	–0.1024	0.0297	**0.5616**	0.0002
10	O	0.0064	0	0.0032	–0.0064	0.0019	0.0351	0
11	O	**0.7401**	0.0007	**0.3704**	**–0.7395**	**0.2142**	**4.0565**	0.0036
12	O	0.0013	0.0001	0.0007	–0.0012	0.0003	0.0069	0.0006
13	N	0.0001	**0.4551**	**0.2276**	**0.455**	–0.074	0.0006	**2.4944**
14	O	0	**0.2603**	**0.1302**	0.2603	–0.0423	0.0001	**1.4266**
15	O	0	**0.2316**	**0.1158**	0.2315	–0.0377	0.0002	**1.2691**
16	H	0.0001	0	0	–0.0001	0	0.0003	0
17	H	0.0002	0	0.0001	–0.0002	0.0001	0.0013	0
18	H	0.0001	0	0	–0.0001	0	0.0003	0
19	H	0.0054	0	0.0027	–0.0054	0.0016	0.0298	0
20	H	0	0.0002	0.0001	0.0002	0	0.0001	0.001
21	H	0	0.0002	0.0001	0.0002	0	0.0001	0.001

To identify the interaction between iron and inhibitors (compounds I–IX) with different concentration (0, 10, 15 and 20 ppm) and different temperature (308, 313

and 323 K), were analyzed in 1 M HCl by weight loss method and the results are shown in Fig. S-1 of the Supplementary material. From Fig. S-1, the optimum concentration of the inhibitors for 1 M HCl is 15 ppm and the inhibition efficiency increases with increasing temperature. The thermodynamic parameters such as the apparent activation energy *Ea*, the enthalpy of activation change ΔH^* and the entropy of activation change ΔS^* for corrosion of mild steel in 1 M HCl solutions in the absence and presence of compounds I to IX at 308–323 K were calculated by Arrhenius and transition plots which are shown in Figs. S-2 and S-3 of the Supplementary material, respectively, and calculated values are displayed in Table S-11.[8] The positive ΔH^* values and negative ΔS^* values indicate that dissolution of steel process is endothermic and decreasing the disordering of the film formation on the mild steel in 1 M HCl by compounds I to IX. The θ values of different concentrations of inhibitor were tested by fitting to various isotherms including Langmuir, Freundlich and Temkin isotherm. The obtained results were fitted to all the three adsorption isotherms and shown in Figs. S-4–S-6 of the Supplementary material, respectively.[8] Adsorption parameters k_{ads} and free energy change (ΔG) were calculated using Langmuir, Freundlich and Temkin isotherm and shown in Tables S-12–S-14, respectively. From the calculated ΔG values from Langmuir, Freundlich, and Temkin isotherms were around –10 kJ mol^{-1} which is consistent with electrostatic interaction between charged molecules and a charged metal. This indicates the adsorption between the metal and all nine isatin and its derivatives is physisorption. The presence of electrostatic interaction between the isatin and its derivatives with mild steel in 1 M HCl is supported by the adsorption studies as prescribed in the computational studies.

CONCLUSION

The band gap energy of isatin and its derivatives were successfully identified in both gas phase and solvation effects by DFT optimization. By having DFT calculations, the quantum chemical parameters such as ionization potential (I), electron affinity (A), electronegativity (χ), band gap energy (ΔE), softness (σ), hardness (η) and electrophilicity (ω) were calculated using HOMO and LUMO values. Comparison of adsorption behavior of isatin and its derivatives were analysed theoretically by quantum chemical parameters. The quantum chemical parameters show that all the studied derivatives have the tendency to donate the electron to the metal surface on adsorption. In addition, number of electron transfer from isatin and its derivatives to iron metal were calculated theoretically and in following order IX>III>VII>IV>II>V>I>VIII>VI. In both gas phase and solvent phase, there is the same trend in all the inhibitors. The protonation of compound I (isatin) and compound II (*N*-methyl isatin) were identified by the energy gap (ΔE) difference in gas phase and solvation models. Mulliken charge analysis confirms the donation of electrons from the heteroatoms in isatin and its derivatives to the

metal ions. From the Fukui indices calculation for isatin and its derivatives, is evident that all the compounds have local selectivity for donating or accepting electrons towards the metal surface by the presence of hetero atoms. Among the derivatives, compounds VI and VIII have highest tendency to donate or accept electrons towards the metals. The adsorption studies support the presence of electrostatic interaction between the Fe and compounds I–IX suggesting the transfer of electrons from/to the metal surfaces.

SUPPLEMENTARY MATERIAL

Additional data and information are available electronically at the pages of journal website: https://www.shd-pub.org.rs/index.php/JSCS/article/view/13336, or from the corresponding author on request.

Acknowledgements. Author Dr. Muthumanickam Shenbagapushpam gratefully acknowledges the Management, Mannar Thirumali Naicker College, Madurai, for their constant support. Author Dr. Muthumanickam Shenbagapushpam gratefully acknowledges Prof. Kodirajan Selvakumar, Assistant Professor of Chemistry, Thiagarajar College, Madurai, for his guidance during earlier research carrier of mine. The authors acknowledge Vel Tech Rangarajan Dr. Sagunthala R&D Institute of Science and Technology for providing access to do DFT calculations using Gaussian.

ИЗВОД

ТЕОРИЈСКА И ЕКСПЕРИМЕНТАЛНА ПРЕДВИЂАЊА ЕФИКАСНОСТИ ИНХИБИЦИЈЕ КОРОЗИЈЕ ИЗАТИНА И ЊЕГОВИХ ДЕРИВАТА ПРИМЕНОМ DFT ПРОРАЧУНА И МЕТОДЕ ГУБИТКА МАСЕ – УПОРЕДНА СТУДИЈА

JONE CELESTINA JOSEPH XAVIER RAJ[1], MUTHUMANICKAM SHENBAGAPUSHPAM[2], ARUL DEEPA VINCENT[1], PRIYADHARSANI SHANMUGARAJ[1], CHAKKARAVARTHI RAJ[3], SATHEESH RAJAMOHAN[2] и RAMASAMY RAJA VIRUTHACHALAM[2]

[1]The Research Centre of Chemistry, Fatima College, Madurai – 625018, Tamilnadu, India, [2]Department of Chemistry, Mannar Thirumalai Naicker College, Madurai – 625004, Tamilnadu, India и [3]Department of Physics, Department of Science and Humanities, St. Micheal Coll ege of Engineering, Sivaganagai – 630551, Tamilnadu, India

Одлике инхибиције корозије меког челика изатином и његовим дериватима супституисаних на N1/C5 позицији анализиране су применом DFT прорачуна (B3LYP, 6311g, dp) у гасној фази, као у солватавионом методом помоћу Gaussian 09W и Gaussian 16 програмских пакета. Израчунати квантно-хемијски параметри, као што су E_{LUMO}, E_{HOMO}, јонизациони потенцијал (I), афинитет према електрону (A), електронегативност (χ), енергетски јаз (ΔE), мекоћа (σ), тврдоћа (η) и електрофилност (ω), показали су да изатин и његови деривати имају тенденцију да донирају електроне ка површини металног јона током адсорпције. Теоријски је израчунат број пренетих електрона (ΔN) са изатина и његових деривата на гвожђе, при чему је утврђен редослед IX>III>VII>IV>II>V>I>VIII> >VI. Експериментални резултати потврдили су исти редослед инхибиције као и теоријски. Анализа расподеле Миликенових наелектрисања за ова једињења указала је на високу негативну вредност на N1 атому. Негативна вредност на N1 атому се мења супституцијом на N1 и C-5 позицији изатина, што је теоријски потврђено. Локални Фукуи параметри такође су израчунати и коришћени за предвиђање локалне селективности ових једињења.

(Примљено 14. априла, ревидирано 25. маја, прихваћено 20. новембра 2025)

REFERENCES

1. H. Tandon, T. Chakraborthy, V. Suhag, *Res. Med. Eng. Sci*. **7** (2019) 792 (https://crimsonpublishers.com/rmes/pdf/RMES.000668.pdf)
2. M. Raftani, T. Abram, N. Bennani, M. Bouachrine, *Res. Chem.* **2** (2020) 100040 (https://dx.doi.org/10.1016/j.rechem.2020.100040)
3. H. Jouypazadeh, H. Farrokhpour, M. M. Momeni, *Surf. Inter.* **26** (2021) 101379 (https://dx.doi.org/10.1016/j.surfin.2021.101379)
4. J. Xu, Q. Wan, M. Anpo, S. Lin, *J. Phys. Chem., C* **124** (2020) 6624 (https://dx.doi.org/10.1021/acs.jpcc.9b11385)
5. Z.-Y. Liu, D. Wang, D.-T. Li, H.-Q. Wang, *Comput. Theor. Chem.* **1214** (2022) 113759 (https://dx.doi.org/10.1016/j.comptc.2022.113759)
6. S. Erdogan, Z. S. Safi, S. Kaya, D. O. Isın, L. Guo, C. Kaya, *J. Mol. Struct.* **1134** (2017) 751 (https://dx.doi.org/10.1016/j.molstruc.2017.01.037)
7. S. Perumal, S. Muthumanickam, A. Elangovan, R. Karthik, R. Sayee kannan, K. K. Mothilal, *J Bio Tribo Corros.* **3** (2017) 13 (https://dx.doi.org/10.1007/s40735-017-0072-5)
8. S. Muthumanickam, B. Jeyaprabha, R. Karthik, A. Elangovan, P. Prakash, *Int. J. Corros. Scale Inhib*. **4** (2015) 365 (https://dx.doi.org/10.17675/2305-6894-2015-4-4-6)
9. S. Perumal, S. Muthumanickam, A. Elangovan, N. Muniyappan, R. Sayee Kannan, K. Krishnamoorthi, *Lett. Appл. Nanobiosci.* **13** (2024) 12 (https://doi.org/10.33263/LIANBS131.012)
10. K. O. Sulaiman, A. T. Onawole, *Comput. Theor. Chem.* **1093** (2016) 73 (https://dx.doi.org/10.1016/j.comptc.2016.08.014)
11. M. Pitchaipillai, K. Raj, J. Balasubramanian, P. Periakaruppan, *Int. J. Miner. Metall. Mater*. **21** (2014) 1083 (https://dx.doi.org/10.1007/s12613-014-1013-7)
12. R. Karthik, P. Muthukrishnan, S.-M. Chen, B. Jeyaprabha, P. Prakash, *Int. J. Electrochem. Sci.* **10** (2015) 3707 (https://doi.org/10.1016/S1452-3981(23)06573-2)
13. I. B. Obot, A. Meroufel, I. B. Onyeachu, A. Alenazi, A. A. Sorour, *J. Mol. Liq.* **296** (2019) 111760 (https://dx.doi.org/10.1016/j.molliq.2019.111760)
14. L. M. De Andrade, C. Paternoster, P. Chevallier, S. Gambaro, P. Mengucci, D. Mantovani, *Bioact. Mater.* **11** (2022) 166 (https://doi.org/10.1016/j.bioactmat.2021.09.026)
15. L. K. M. O. Goni, M. A. J. Mazumder, M. A. Quraishi, M. M. Rahman, *Chem. Asian J.* **16** (2021) 1324 (https://dx.doi.org/10.1002/asia.202100201)
16. S. Z. Salleh, A. H. Yusoff, S. K. Zakaria, M. A. A. Taib, A. A. Seman, M. N. Masri, M. Mohamad, S. Mamat, S. A. Sobri, A. Ali, P. T. Teo, *J. Clean. Prod.* **304** (2021) 127030 (https://dx.doi.org/10.1016/j.jclepro.2021.127030)
17. N. Hossain, M. A. Chowdhury, M. Kchaou, *J. Adh. Sci. Technol.* **35** (2021) 673 (https://dx.doi.org/10.1080/01694243.2020.1816793)
18. L. Chen, D. Lu, Y. Zhang, *Materials* **15** (2022) 2023 (https://dx.doi.org/10.3390/ma15062023)
19. A. Kadhim, A. A. Al-Amiery, R. Alazawi, M. K. S. Al-Ghezi, R. H. Abass, *Int. J. Corros. Scale Inhib.* **10** (2021) 54 (https://dx.doi.org/10.17675/2305-6894-2021-10-1-3)
20. Q. Yuan, R. Cheng, S. Zou, C. Ding, H. Liu, Y. Wang, D. Yang, X. Xiao, Q. Jiang, R. Tang, J. Chen, *J. Mater. Res. Technol.* **9** (2020) 11935 (https://dx.doi.org/10.1016/j.jmrt.2020.08.012)
21. K. R. Ansari, M. A. Quraishi, *J. Taiwan Inst. Chem. Eng.* **54** (2015) 145 (https://dx.doi.org/10.1016/j.jtice.2015.03.013)

22. G. Chen, H.-J. Su, Y.-P. Song, Y. Gao, J. Zhang, X.-J. Hao, J.-R. Zhao, *Res. Chem. Intermed.* **39** (2013) 3669 (https://dx.doi.org/10.1007/s11164-012-0870-9)
23. Y. Kharbach, F. Z. Qachchachi, A. Haoudi, M. Tourabi, A. Zarrouk, C. Jama, L. O. Olasunkanmi, E. E. Ebenso, F. Bentiss, *J. Mol. Liq.* **246** (2017) 302 (https://dx.doi.org/10.1016/j.molliq.2017.09.057)
24. D. K. Verma, R. Sahu, E. Berdimurodov, C. Verma, M. A. Quraishi, V. K. Jain, K. Berdimuradov, *J. Mol. Struct.* **1294** (2023) 136313 (https://dx.doi.org/10.1016/j.molstruc.2023.136313)
25. A. A. Altalhi, *Int. J. Electrochem. Sci.* **19** (2024) 100449 (https://dx.doi.org/10.1016/j.ijoes.2023.100449)
26. H. A. El-Ghamry, A. Fawzy, T. A. Farghaly, T. M. Bawazeer, N. Alqarni, F. M. Alkhatib, M. Gaber, *Arab. J. Chem.* **15** (2022) 103522 (https://dx.doi.org/10.1016/j.arabjc.2021.103522)
27. H. M. A. El-Lateef, *Appl. Surf. Sci.* **501** (2020) 144237 (https://dx.doi.org/10.1016/j.apsusc.2019.144237)
28. D. Ma, J. Zhao, L. Zhang, J. Huang, J. Liu, T. Ren, *Mater. Chem. Phys.* **307** (2023) 128163 (https://dx.doi.org/10.1016/j.matchemphys.2023.128163)
29. A. Al-Amiery, W. N. R. W. Isahak, W. K. Al-Azzawi, *J. Mol. Struct.* **1288** (2023) 135829 (https://dx.doi.org/10.1016/j.molstruc.2023.135829)
30. T. H. A. Hasanin, A. M. A. El Malak, S. A. M. Refaey, *Egypt. J. Chem.* **64** (2021) 2377 (https://dx.doi.org/10.21608/EJCHEM.2021.43225.2873)
31. P. Udhayakala, T. V. Rajendiran, S. Gunasekaran, *J. Comp. Meth. Mol. Des.* **2** (2012) 1 (https://www.scholarsresearchlibrary.com/articles/theoretical-approach-to-the-corrosion-inhibition-efficiency-of-some-pyrimidine-derivatives-using-dft-method.pdf)
32. L. Guo, X. Ren, Y. Zhou, S. Xu, Y. Gong, S. Zhang, *Arab. J. Chem.* **10** (2017) 121 (https://dx.doi.org/10.1016/j.arabjc.2015.01.005)
33. D. M. Mamand, T. M. K. Anwer, H. M. Qadr, *Corros. Rev.* **42** (2024) 1 (https://dx.doi.org/10.1515/corrrev-2022-0112)
34. P. Kumar, I. Soni, G. K. Jayaprakash, S. Kumar, S. Rao, R. Flores-Moreno, A. S. Sowmyashree, *Inorg. Chem. Commun.* **146** (2022) 110110 (https://dx.doi.org/10.1016/j.inoche.2022.110110)
35. H. H. Rasul, D. M. Mamad, Y. H. Azeez, R. A. Omer, K. A. Omer, *Comput. Theor. Chem.* **1225** (2023) 114177 (https://dx.doi.org/10.1016/j.comptc.2023.114177)
36. D. M. Mamand, H. M. Qadr, *Corros. Rev*. **41** (2023) 427 (https://dx.doi.org/10.1515/corrrev-2022-0085)
37. N. A. Wazzan, I. B. Obot, S. Kaya, *J. Mol. Liq*. **221** (2016) 579 (https://dx.doi.org/10.1016/j.molliq.2016.06.011)
38. B. Tuzun, J. Bhawsar, *Arab. J. Chem.* **14** (2021) 102927 (https://dx.doi.org/10.1016/j.arabjc.2020.102927)
39. L. Tan, J. Li, X. Zeng, *Materials* **16** (2023) 2148 (https://dx.doi.org/10.3390/ma16062148)
40. R. K. Roy, H. Hirao, *J. Chem. Phys.* 113 (2000) 1372. (https://doi.org/10.1063/1.481927).

Journal of the Serbian Chemical Society
JSCS-info@shd.org.rs • www.shd.org.rs/JSCS
J. Serb. Chem. Soc. 91 (1) S21–S50 (2026) *Supplementary material*

SUPPLEMENTARY MATERIAL TO

Theoretical and experimental prediction of corrosion inhibition efficiency of isatin and its derivatives by DFT calculations and weight loss method – A comparative study

JONE CELESTINA JOSEPH XAVIER RAJ[1], MUTHUMANICKAM SHENBAGAPUSHPAM[2]*, ARUL DEEPA VINCENT[1], PRIYADHARSANI SHANMUGARAJ[1], CHAKKARAVARTHI RAJ[3], SATHEESH RAJAMOHAN[2] and RAMASAMY RAJA VIRUTHACHALAM[2]

[1]*The Research Centre of Chemistry, Fatima College, Madurai – 625018, Tamilnadu, India,* [2]*Department of Chemistry, Mannar Thirumalai Naicker College, Madurai – 625004, Tamilnadu, India and* [3]*Department of Physics, Department of Science and Humanities, St. Micheal College of Engineering, Sivaganagai – 630551, Tamilnadu, India*

J. Serb. Chem. Soc. 91 (1) (2026) 23–37

Table S-1. List of software, functional and basis set analysis for computational studies.

Compounds	Functions	Software	Basis set
I-IX	Optimization	Gaussian 09W	B3LYP/6-311G
	Frequency	Gaussian 09W	B3LYP/6-311G
	Dispersion Correction	Gaussian 16	PBE0-GD3BJ/6-31G (d,p)
	IEFPCM Water model	Gaussian 16	B3LYP/6-311G (d,p)

Table S-2. Fukui local parameters of compound I (isatin)

N	Z	f-	f+	f0	Dual-descriptor	Hardness (au)	W- (eV)	W+ (eV)
1	C	0.0001	0.0014	0.0007	0.0013	0	0.0001	0.0014
2	C	0.0019	0.0001	0.001	-0.0018	0.0005	0.002	0.0001
3	C	0.0031	0.004	0.0035	0.0009	0.0008	0.0032	0.0041
4	C	0.005	0.0002	0.0026	-0.0048	0.0013	0.0051	0.0002
5	C	0.0262	0.0003	0.0133	-0.0259	0.007	0.0266	0.0003
6	C	0.0008	0	0.0004	-0.0008	0.0002	0.0008	0
7	N	0.0571	0.1087	0.0829	0.0516	0.0143	0.058	0.1104
8	C	0.0608	0.5624	0.3116	0.5015	0.0111	0.0618	0.5712
9	C	0.1235	0.0136	0.0685	-0.1099	0.0331	0.1254	0.0138
10	O	0.7159	0.3057	0.5108	-0.4102	0.1897	0.7272	0.3106
11	O	0.0015	0.0035	0.0025	0.002	0.0004	0.0015	0.0036
12	H	0	0	0	0	0	0	0
13	H	0.0001	0	0	-0.0001	0	0.0001	0

* Corresponding author. E-mail: muthumanickams92@gmail.com, muthumanickams@mannarcollege.ac.in

14	H	0.0004	0	0.0002	-0.0004	0.0001	0.0005	0
15	H	0.0001	0	0	-0.0001	0	0.0001	0
16	H	0.0034	0	0.0017	-0.0034	0.0009	0.0035	0

Table S-3. Fukui local parameters of compound II (N-methyl isatin)

N	Z	f-	f+	f0	Dual-descriptor	Hardness (au)	W- (eV)	W+ (eV)
1	C	0.0001	0.0015	0.0008	0.0014	0	0.0001	0.0015
2	C	0.0012	0.0001	0.0007	-0.0012	0.0003	0.0012	0.0001
3	C	0.0017	0.0047	0.0032	0.0031	0.0004	0.0016	0.0047
4	C	0.0032	0.0004	0.0018	-0.0028	0.0009	0.0032	0.0004
5	C	0.0243	0.0004	0.0124	-0.0238	0.0065	0.0239	0.0004
6	C	0.0008	0	0.0004	-0.0008	0.0002	0.0008	0
7	N	0.0575	0.1144	0.0859	0.0569	0.0145	0.0565	**0.1125**
8	C	0.0515	**0.556**	**0.3037**	**0.5045**	0.0097	0.0506	**0.5469**
9	C	0.1026	0.0141	0.0583	-0.0885	0.0273	**0.1009**	0.0139
10	O	**0.7425**	**0.2989**	**0.5207**	**-0.4435**	**0.1959**	**0.7303**	**0.294**
11	O	0.0013	0.0034	0.0023	0.0021	0.0003	0.0013	0.0033
12	C	0.0069	0.0003	0.0036	-0.0066	0.0018	0.0068	0.0003
13	H	0	0	0	0	0	0	0
14	H	0.0001	0	0	-0.0001	0	0.0001	0
15	H	0.0002	0	0.0001	-0.0002	0.0001	0.0002	0
16	H	0	0	0	0	0	0	0
17	H	0.0061	0	0.003	-0.0061	0.0016	0.006	0
18	H	0	0.0029	0.0014	0.0028	0	0	0.0028
19	H	0	0.0029	0.0014	0.0028	0	0	0.0028

Table S-4. Fukui local parameters of compound III (N-benzyl isatin)

N	Z	f-	f+	f0	Dual-descriptor	Hardness (au)	W- (eV)	W+ (eV)
1	C	0.0001	0.0015	0.0008	0.0014	0	0.0001	0.0014
2	C	0	0.0001	0.0001	0.0001	0	0	0.0001
3	C	0.0018	0.0047	0.0032	0.0029	0.0004	0.0017	0.0045
4	C	0.0034	0.0005	0.002	-0.003	0.0009	0.0033	0.0004
5	C	0.0018	0.0004	0.0011	-0.0014	0.0005	0.0017	0.0004
6	C	0.0002	0	0.0001	-0.0002	0	0.0002	0
7	N	0.001	**0.1137**	0.0574	**0.1127**	-0.0007	0.001	**0.1099**
8	C	0.0005	**0.555**	**0.2777**	**0.5545**	-0.0045	0.0005	**0.5364**
9	C	0.0001	0.0141	0.0071	0.0141	-0.0001	0.0001	0.0137
10	C	0.0024	0.0008	0.0016	-0.0016	0.0006	0.0023	0.0007
11	C	0.0398	0.0047	0.0223	-0.035	0.0102	0.0384	0.0046
12	O	0	**0.2974**	**0.1487**	**0.2973**	-0.0025	0	**0.2874**
13	O	0	0.0034	0.0017	0.0034	0	0	0.0033
14	C	0.0679	0.0003	0.0341	-0.0676	0.0175	0.0657	0.0003
15	C	0.0623	0.0001	0.0312	-0.0622	0.0161	0.0602	0.0001
16	C	0.0353	0.0002	0.0178	-0.0351	0.0091	0.0341	0.0002
17	C	**0.3899**	0.0002	**0.1951**	-0.3897	**0.1005**	**0.3768**	0.0002
18	C	**0.3916**	0.0005	**0.1961**	-0.3911	**0.1009**	**0.3785**	0.0005
19	H	0	0	0	0	0	0	0
20	H	0	0	0	0	0	0	0

21	H	0.0009	0	0.0005	-0.0009	0.0002	0.0009	0
22	H	0	0	0	0	0	0	0
23	H	0.0001	0.0022	0.0011	0.0021	0	0.0001	0.0021
24	H	0.0001	0.0001	0.0001	0	0	0.0001	0.0001
25	H	0.0001	0	0	-0.0001	0	0.0001	0
26	H	0	0	0	0	0	0	0
27	H	0	0	0	0	0	0	0
28	H	0.0002	0	0.0001	-0.0002	0.0001	0.0002	0
29	H	0.0003	0	0.0001	-0.0002	0.0001	0.0002	0

Table S-5. Fukui local parameters of compound IV (N-allyl isatin)

N	Z	f-	f+	f0	Dual-descriptor	Hardness (au)	W- (eV)	W+ (eV)
1	C	0.0001	0.0014	0.0008	0.0013	0	0.0001	0.0014
2	C	0.0009	0.0001	0.0005	-0.0008	0.0002	0.0009	0.0001
3	C	0.002	0.0047	0.0033	0.0027	0.0005	0.002	0.0047
4	C	0.0016	0.0005	0.001	-0.0011	0.0004	0.0016	0.0005
5	C	0.0192	0.0004	0.0098	-0.0188	0.0051	0.0192	0.0004
6	C	0.0009	0	0.0005	-0.0009	0.0002	0.0009	0
7	N	0.063	**0.1126**	0.0878	0.0496	0.016	0.0629	**0.1124**
8	C	0.0471	**0.5554**	**0.3013**	**0.5083**	0.0081	0.047	**0.5545**
9	C	0.0911	0.0141	0.0526	-0.077	0.0243	0.091	0.0141
10	C	0.0074	0.0007	0.0041	-0.0068	0.002	0.0074	0.0007
11	C	0.002	0.0046	0.0033	0.0026	0.0005	0.002	0.0045
12	C	0.001	0.0011	0.001	0	0.0003	0.001	0.0011
13	O	**0.7563**	**0.2986**	**0.5274**	**-0.4577**	**0.2002**	**0.755**	**0.2981**
14	O	0.0012	0.0034	0.0023	0.0022	0.0003	0.0012	0.0034
15	H	0	0	0	0	0	0	0
16	H	0.0001	0	0	-0.0001	0	0.0001	0
17	H	0.0003	0	0.0002	-0.0003	0.0001	0.0003	0
18	H	0	0	0	0	0	0	0
19	H	0.0002	0.0021	0.0012	0.0019	0	0.0002	0.0021
20	H	0.0052	0.0001	0.0026	-0.0051	0.0014	0.0052	0.0001
21	H	0.0002	0	0.0001	-0.0002	0.0001	0.0002	0
22	H	0	0.0001	0.0001	0.0001	0	0	0.0001
23	H	0	0	0	0	0	0	0

Table S-6. Fukui local parameters of compound V (N-propargyl isatin)

N	Z	f-	f+	f0	Dual-descriptor	Hardness (au)	W- (eV)	W+ (eV)
1	C	0.0001	0.0013	0.0007	0.0012	0	0.0001	0.0014
2	C	0.0009	0.0001	0.0005	-0.0008	0.0002	0.0009	0.0001
3	C	0.0018	0.0046	0.0032	0.0028	0.0004	0.0018	0.0048
4	C	0.0022	0.0004	0.0013	-0.0018	0.0006	0.0023	0.0004
5	C	0.02	0.0004	0.0102	-0.0196	0.0054	0.0209	0.0004
6	C	0.0009	0	0.0004	-0.0009	0.0002	0.0009	0
7	N	0.0621	**0.1094**	0.0857	0.0474	0.0157	0.0649	**0.1144**
8	C	0.0486	0.551	**0.2998**	**0.5024**	0.0071	0.0508	**0.5759**
9	C	0.0939	0.0139	0.0539	-0.08	0.0254	0.0981	0.0145
10	C	0.009	0.0033	0.0061	-0.0057	0.0024	0.0094	0.0034

11	C	0.0049	0.0084	0.0066	0.0036	0.0012	0.0051	0.0088
12	O	**0.743**	**0.2968**	**0.5199**	**-0.4463**	**0.1988**	**0.7765**	**0.3101**
13	O	0.0012	0.0034	0.0023	0.0022	0.0003	0.0013	0.0036
14	C	0.005	0.0047	0.0048	-0.0003	0.0013	0.0052	0.0049
15	H	0	0	0	0	0	0	0
16	H	0.0001	0	0	-0.0001	0	0.0001	0
17	H	0.0003	0	0.0001	-0.0003	0.0001	0.0003	0
18	H	0	0	0	0	0	0	0
19	H	0	0.0022	0.0011	0.0022	0	0	0.0023
20	H	0.006	0	0.003	-0.006	0.0016	0.0063	0
21	H	0.0001	0.0002	0.0001	0.0001	0	0.0001	0.0002

Table S-7. Fukui local parameters of compound VII (5-methyl isatin)

N	Z	f-	f+	f0	Dual-descriptor	Hardness (au)	W- (eV)	W+ (eV)
1	C	0.0003	0.0013	0.0008	0.001	0.0001	0.0003	0.0013
2	C	0.0027	0.0001	0.0014	-0.0026	0.0007	0.0027	0.0001
3	C	0.0035	0.0041	0.0038	0.0006	0.0009	0.0034	0.0041
4	C	0.0051	0.0002	0.0026	-0.0049	0.0014	0.005	0.0002
5	C	0.0271	0.0003	0.0137	-0.0267	0.0072	0.0265	0.0003
6	C	0.0014	0	0.0007	-0.0014	0.0004	0.0014	0
7	N	0.0564	**0.1106**	0.0835	0.0542	0.0142	0.0552	**0.1082**
8	C	0.0608	**0.5619**	**0.3113**	**0.5011**	0.0123	0.0595	0.55
9	C	**0.1263**	0.0135	0.0699	-0.1127	0.0335	**0.1236**	0.0133
10	O	**0.7109**	**0.3042**	**0.5075**	**-0.4067**	**0.187**	**0.6959**	**0.2978**
11	O	0.0015	0.0034	0.0025	0.0019	0.0004	0.0015	0.0033
12	C	0	0	0	0	0	0	0
13	H	0.0001	0	0	-0.0001	0	0.0001	0
14	H	0.0005	0	0.0002	-0.0005	0.0001	0.0005	0
15	H	0.0001	0	0	-0.0001	0	0.0001	0
16	H	0.0035	0	0.0018	-0.0035	0.0009	0.0034	0
17	H	0	0	0	0	0	0	0
18	H	0	0.0001	0.0001	0.0001	0	0	0.0001
19	H	0	0.0001	0.0001	0.0001	0	0	0.0001

Table S-8. Fukui local parameters of compound IX (1-methyl-5-methyl isatin)

N	Z	f-	f+	f0	Dual-Descriptor	Hardness(au)	W-(eV)	W+(eV)
1	C	0	0	0	0	0	0	0
2	C	0	0	0	0	0	0	0
3	C	0.0001	0	0.0001	-0.0001	0	0.0001	0
4	C	0.0012	0.0001	0.0007	-0.0011	0.0003	0.0011	0.0001
5	C	0.0015	0.0001	0.0008	-0.0013	0.0004	0.0014	0.0001
6	C	0.0001	0	0.0001	-0.0001	0	0.0001	0
7	N	0.0023	0.0094	0.0058	0.0071	0.0006	0.0022	0.0089
8	C	0.0117	**0.6262**	**0.3189**	**0.6145**	0	0.0111	**0.5943**
9	C	0.0026	0.0055	0.0041	0.0029	0.0007	0.0025	0.0053
10	C	0.0002	0.0002	0.0002	0	0.0001	0.0002	0.0002
11	O	0	0	0	0	0	0	0
12	O	**0.98**	**0.3582**	**0.6691**	**-0.6218**	**0.2569**	**0.93**	**0.3399**

13	O	0.0001	0.0001	0.0001	-0.0001	0	0.0001	0.0001
14	H	0	0	0	0	0	0	0
15	H	0	0	0	0	0	0	0
16	H	0	0	0	0	0	0	0
17	H	0.0001	0	0.0001	-0.0001	0	0.0001	0
18	H	0	0.0001	0	0.0001	0	0	0.0001
19	H	0	0.0001	0	0.0001	0	0	0.0001
20	H	0	0	0	0	0	0	0
21	H	0	0	0	0	0	0	0
22	H	0	0	0	0	0	0	0

Table S-9. Calculated global parameters by HOMO and LUMO energies (Grimme's D3)

Compound No	ΔE (eV)	I (eV)	A (eV)	χ (eV)	η (eV)	σ (eV)	ΔN (eV)	ω (eV)	ε (eV)
I	4.3002	6.8316	2.5314	4.6815	2.1501	0.4651	0.5391	5.0966	0.1962
II	4.1527	6.6281	2.4754	4.5517	2.0763	0.4816	0.5895	4.9891	**0.2004**
III	4.1524	6.6123	2.4599	4.5361	2.0762	0.4816	0.5933	4.9552	**0.2018**
IV	4.1541	6.6265	2.4724	4.54945	2.0770	0.4814	0.5899	4.9824	**0.2007**
V	4.2033	6.7454	2.5421	4.6437	2.1016	0.4758	0.5605	5.1303	0.1949
VI	4.4096	**7.5865**	**3.1769**	**5.3817**	2.2048	0.4535	0.3669	**6.5681**	0.1522
VII	4.1453	6.6014	2.4561	4.52875	2.0726	0.4824	0.5961	4.9476	**0.2021**
VIII	4.2336	**7.3465**	**3.1129**	**5.2297**	2.1168	0.4724	0.4181	**6.4601**	0.1547
IX	**4.0494**	6.4521	2.4027	4.4274	**2.0247**	**0.4939**	**0.6353**	4.8406	**0.2065**

Table S-10. Calculated global parameters by HOMO and LUMO energies (IEFPCM-Water).

Compound No	ΔE (eV)	I (eV)	A (eV)	χ (eV)	η (eV)	σ (eV)	ΔN (eV)	ω (eV)	ε (eV)
I	3.7114	6.6276	2.9162	4.7719	1.8557	0.5389	0.6003	6.1354	0.1630
II	3.587	6.4825	2.8955	4.689	1.7935	0.5576	0.6443	6.1295	0.1631
III	3.6085	6.5421	2.9336	4.7378	1.8042	0.5542	0.6269	6.2207	0.1607
IV	3.6077	6.5288	2.9211	4.7249	1.8038	0.5544	0.6306	6.1882	0.1616
V	3.669	6.6461	2.9771	4.8116	1.8345	0.5451	0.5965	6.3100	0.1585
VI	3.8738	**7.1372**	**3.2634**	**5.2003**	1.9369	0.5163	0.4646	**6.9810**	0.1432
VII	3.5454	6.4197	2.8743	4.647	1.7727	0.5641	0.6637	6.0909	0.1642
VIII	3.7108	**6.9601**	**3.2493**	**5.1047**	1.8554	0.5389	0.5108	**7.0222**	0.1424
IX	**3.4452**	6.3002	2.8550	4.5776	**1.7226**	**0.5805**	**0.7031**	6.0822	0.1644

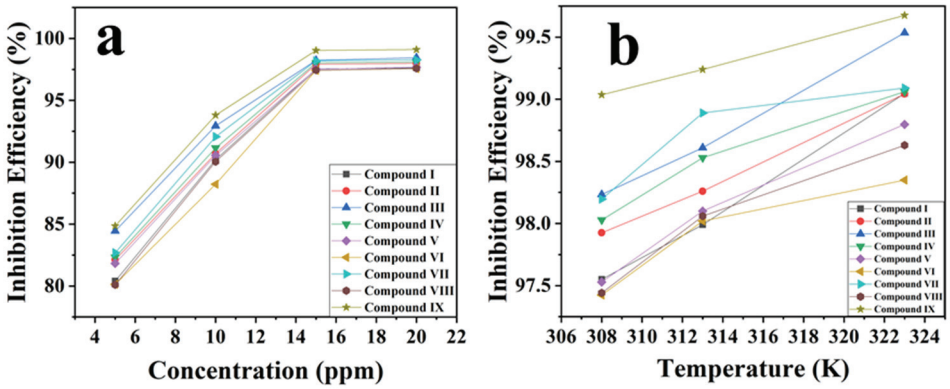

Figure S-1. Inhibition efficiency of mild steel immersed in 1 M HCl with (a) different concentrations of compounds I to IX (b) Maximum inhibition efficiency of 15 ppm of compounds I to IX with at 308, 313, 323 K.

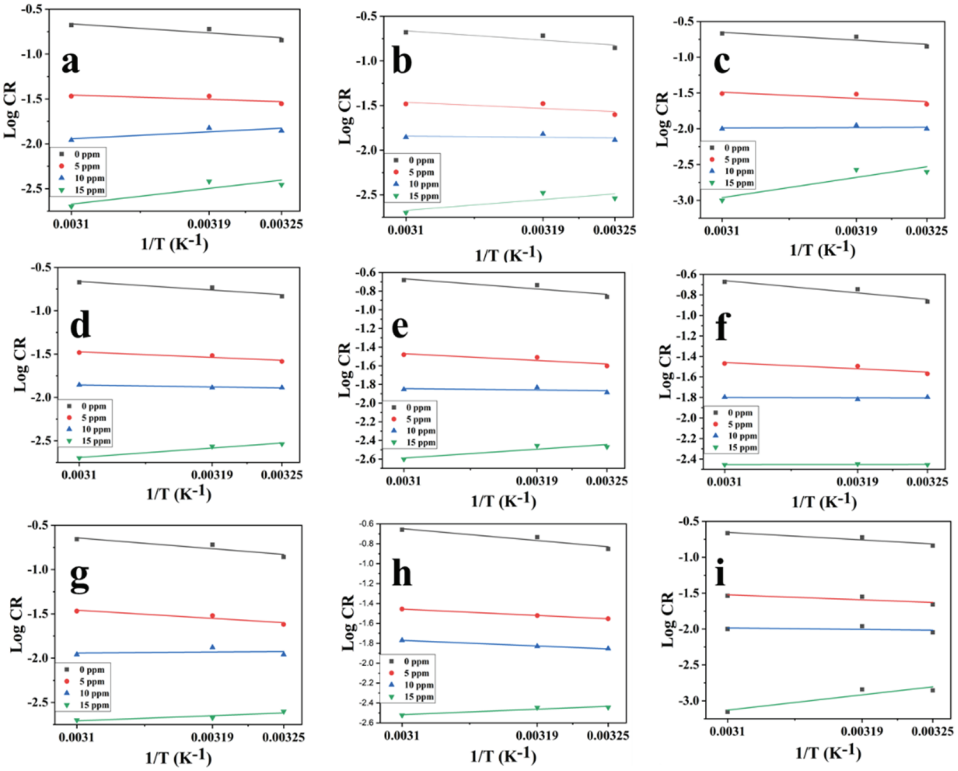

Figure S-2. Arrhenius plots of (a) compound I (b) compound II (c) compound III (d) compound IV (e) compound V (f) compound VI (g) compound VII (h) compound VIII (i) compound IX.

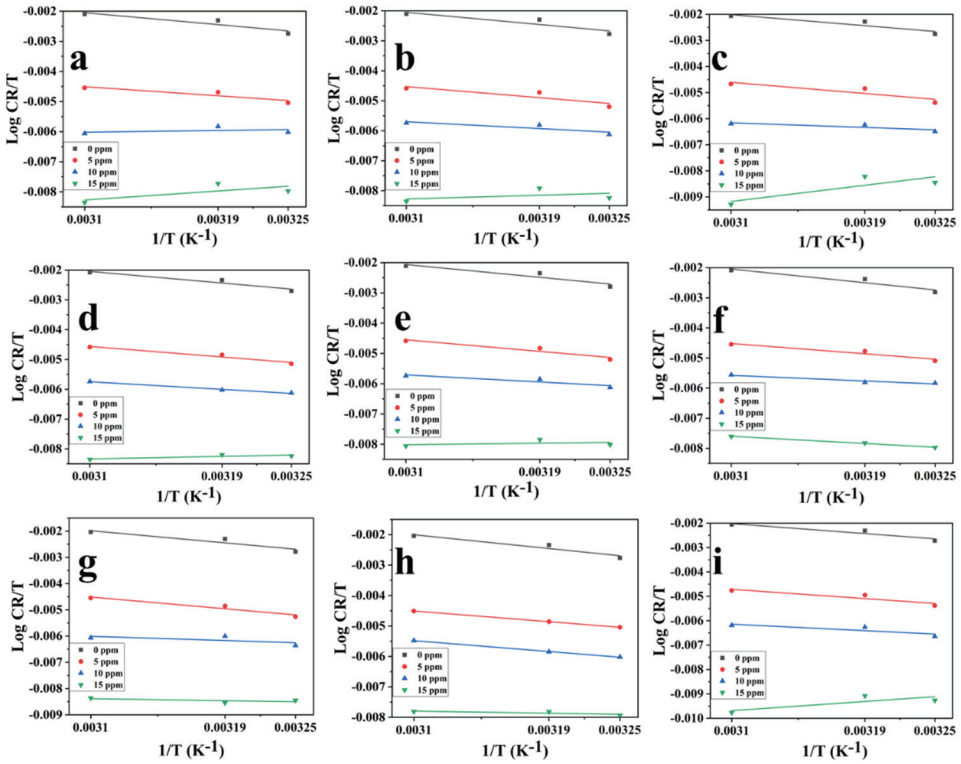

Figure S-3. Transition state plots of (a) compound I (b) compound II (c) compound III (d) compound IV (e) compound V (f) compound VI (g) compound VII (h) compound VIII (i) compound IX.

Table S-11. Corrosion kinetic parameters of mild steel in 1 M HCl in the absence and presence of isatin and its derivatives.

Compound	Concentration (ppm)	E_a (KJ mol^{-1})	ΔH (KJ mol^{-1})	-ΔS (KJ mol^{-1})
Compound I	0	19.54	76.3703	78.2303
	5	09.31	58.3556	78.333
	10	14.99	10.9885	78.2781
	15	33.97	58.2284	78.088
Compound II	0	20.23	78.6450	78.222
	5	13.21	71.2637	78.2934
	10	2.64	44.1169	78.4006
	15	23.44	24.1465	78.1939
Compound III	0	21.22	81.6032	78.2130
	5	16.63	82.8554	78.2589
	10	12.4	34.3327	78.5424
	15	54.83	119.9951	78.8884
Compound IV	0	19.28	75.3669	78.2188
	5	12.33	63.3572	78.3030
	10	4.40	49.6083	78.3834
	15	21.20	16.9893	78.2149
Compound V	0	21.14	81.6358	78.2149
	5	14.04	73.9118	78.2858
	10	2.99	45.2504	78.3968
	15	18.43	9.8435	78.2436
Compound VI	0	23.14	87.9313	78.1939
	5	11.70	66.0672	78.3088
	10	0.56	36.1804	78.4217
	15	0.19	46.4203	78.4257
Compound VII	0	23.70	89.4248	78.1881
	5	17.97	86.4053	78.2455
	10	2.03	31.0011	78.4466
	15	11.32	14.9500	78.5423
Compound VIII	0	23.07	87.4450	78.1958
	5	12.34	67.8536	78.3030
	10	10.84	69.0043	78.3183
	15	11.27	13.6864	78.5347
Compound IX	0	20.44	79.0375	78.2207
	5	13.55	73.4255	78.2896
	10	4.02	51.4100	78.3853
	15	41.18	72.8778	78.8391

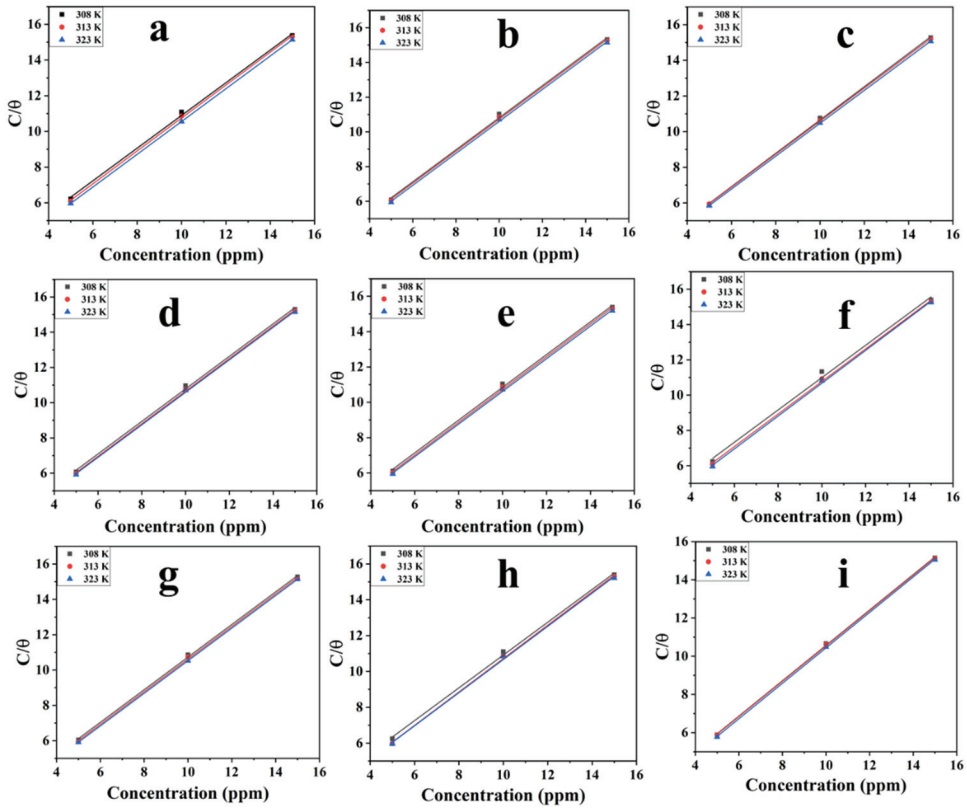

Figure S-4. Langmuir adsorption isotherm for mild steel in 1 M HCl containing different concentrations of (a) compound I (b) compound II (c) compound III (d) compound IV (e) compound V (f) compound VI (g) compound VII (h) compound VIII (i) compound IX at 308–323 K.

Table S-12. Thermodynamic parameters for Langmuir adsorption of (a) compound I (b) compound II (c) compound III (d) compound IV (e) compound V (f) compound VI (g) compound VII (h) compound VIII (i) compound IX on the mild steel in 1M HCl.

Compound	Temperature	K_{ads}	$-\Delta G$ (KJ mol^{-1})	R^2
Compound I	308	0.5762	8.873	0.998
	313	0.6526	9.341	0.999
	323	0.7267	9.928	1
Compound II	308	0.6322	9.110	0.998
	313	0.6615	9.376	0.999
	323	0.7180	9.896	0.999
Compound III	308	0.7686	9.610	0.999
	313	0.7633	9.748	1
	323	0.8070	10.209	1
Compound IV	308	0.6437	9.156	0.998
	313	0.7087	9.554	0.999

	323	0.7343	9.956	0.999
	308	0.6351	9.122	0.998
Compound V	313	0.6947	9.503	0.999
	323	0.7267	9.928	0.999
	308	0.5454	8.732	0.995
Compound VI	313	0.6449	9.310	0.999
	323	0.7263	9.926	0.999
	308	0.6667	9.246	0.999
Compound VII	313	0.7193	9.594	0.999
	323	0.7678	10.076	1
	308	0.5675	8.834	0.998
Compound VIII	313	0.7175	9.587	0.999
	323	0.7093	9.863	0.998
	308	0.7620	9.588	0.999
Compound IX	313	0.7735	9.783	0.999
	323	0.8597	10.379	0.999

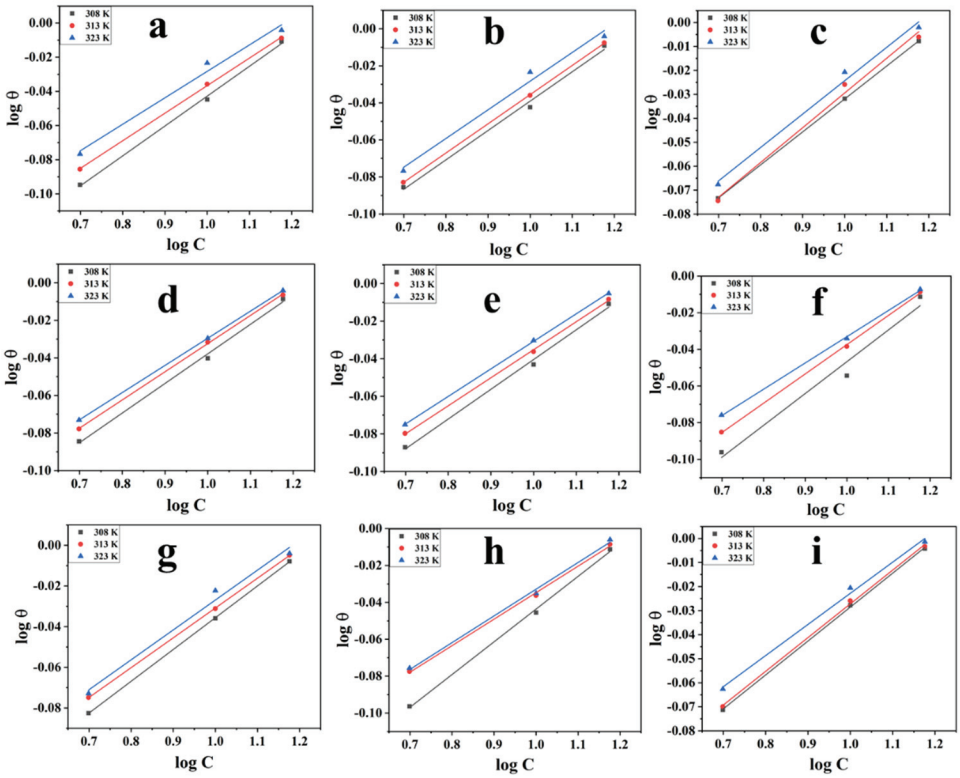

Figure S-5. Freundlich adsorption isotherm for mild steel in 1 M HCl containing different concentrations of (a) compound I (b) compound II (c) compound III (d) compound IV (e) compound V (f) compound VI (g) compound VII (h) compound VIII (i) compound IX at 308–323 K.

Table S-13. Thermodynamic parameters for Freundlich adsorption of (a) compound I (b) compound II (c) compound III (d) compound IV (e) compound V (f) compound VI (g) compound VII (h) compound VIII (i) compound IX on the mild steel in 1M HCl.

Compound	Temperature	K_{ads}	-ΔG (KJ mol^{-1})	R^2
Compound I	308	0.5530	8.767	0.995
	313	0.5887	9.072	1
	323	0.6147	9.478	0.991
Compound II	308	0.5897	8.932	0.989
	313	0.5974	9.111	0.999
	323	0.6147	9.478	0.991
Compound III	308	0.6427	9.152	0.999
	313	0.6320	9.257	0.995
	323	0.6513	9.634	0.994
Compound IV	308	0.5933	8.947	0.994
	313	0.6170	9.195	1
	323	0.6319	9.553	0.999
Compound V	308	0.5885	8.927	0.993
	313	0.6145	9.184	0.998
	323	0.6265	9.529	0.999
Compound VI	308	0.5483	8.745	0.966
	313	0.5901	9.079	0.998
	323	0.6291	9.541	0.998
Compound VII	308	0.5996	8.975	0.999
	313	0.6258	9.232	0.999
	323	0.6322	9.554	0.991
Compound VIII	308	0.5470	8.739	0.996
	313	0.6260	9.232	0.996
	323	0.6262	9.528	0.994
Compound IX	308	0.6409	9.145	1
	313	0.6446	9.309	0.999
	323	0.6738	9.725	0.9979

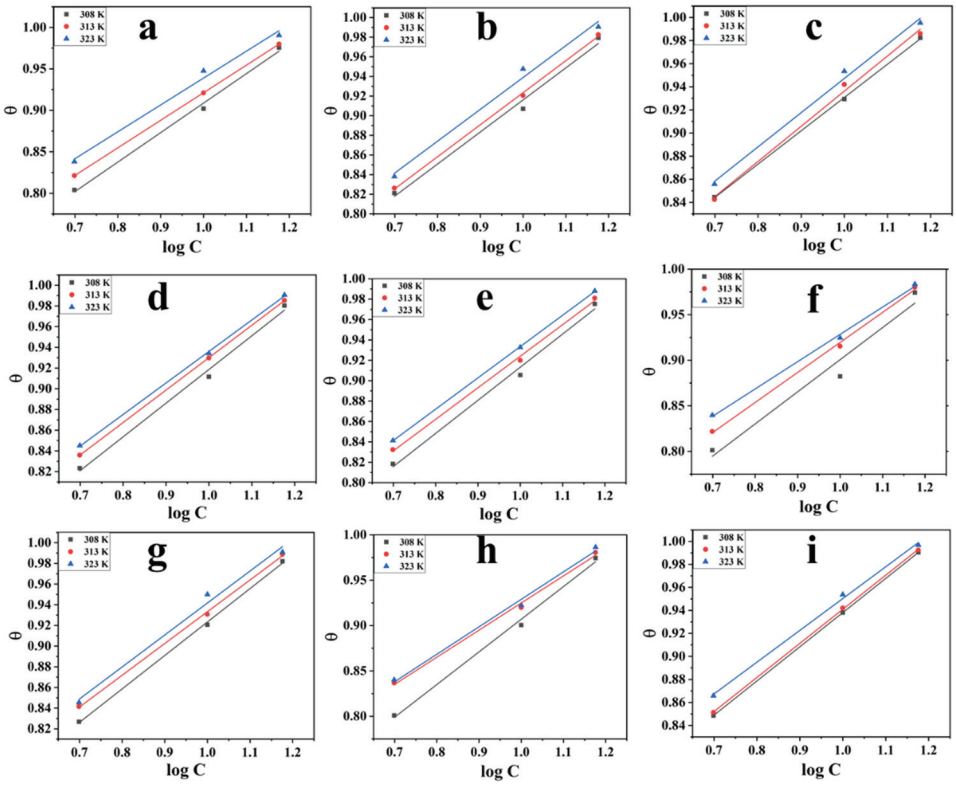

Figure S-6. Temkin adsorption isotherm for mild steel in 1 M HCl containing different concentrations of (a) compound I (b) compound II (c) compound III (d) compound IV (e) compound V (f) compound VI (g) compound VII (h) compound VIII (i) compound IX at 308–323 K.

Table S-14. Thermodynamic parameters for Temkin adsorption of (a) compound I (b) compound II (c) compound III (d) compound IV (e) compound V (f) compound VI (g) compound VII (h) compound VIII (i) compound IX on the mild steel in 1M HCl.

Compound	Temperature	K_{ads}	$-\Delta G$ (KJ mol^{-1})	R^2
Compound I	308	0.8044	9.727	0.998
	313	0.8204	9.936	0.999
	323	0.8327	10.294	0.987
Compound II	308	0.8208	9.779	0.994
	313	0.8244	9.949	0.999
	323	0.8327	10.294	0.987
Compound III	308	0.8440	9.850	1
	313	0.8398	9.997	0.992
	323	0.8489	10.345	0.991
Compound IV	308	0.8224	9.784	0.9972
	313	0.8332	9.976	0.9997
	323	0.8401	10.317	1

	308	0.8198	9.775	0.996
Compound V	313	0.8317	9.972	0.999
	323	0.8376	10.309	0.999
	308	0.8022	9.720	0.975
Compound VI	313	0.8210	9.938	0.999
	323	0.8383	10.312	0.999
	308	0.8253	9.793	1
Compound VII	313	0.8374	9.989	0.999
	323	0.8403	10.318	0.987
	308	0.8017	9.718	0.998
Compound VIII	313	0.8366	9.987	0.998
	323	0.8373	10.308	0.997
	308	0.8440	9.850	0.999
Compound IX	313	0.8458	10.015	0.999
	323	0.8587	10.376	0.996

XYZ COORDINATES OF ISATIN AND ITS DERIVATIVES WITHOUT GRIMME D3 OPTIMIZED STRUCTURE

Table S-15. Compound I (Isatin)

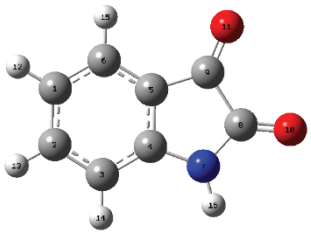

Centre Number	Atomic Number	Coordinates (Angstroms)		
		X	Y	Z
1	6	2.640644	0.809011	0.000021
2	6	2.766522	-0.58669	0.000348
3	6	1.644607	-1.43081	0.000211
4	6	0.392043	-0.83285	-0.000204
5	6	0.252448	0.572535	-0.000556
6	6	1.371801	1.399081	-0.000498
7	7	-0.88501	-1.4355	-0.000097
8	6	-1.90391	-0.49041	-0.000052
9	6	-1.17957	0.886018	0.000056
10	8	-3.11621	-0.71012	-0.000034
11	8	-1.75124	1.979303	0.000577
12	1	3.526544	1.427684	0.000117
13	1	3.753157	-1.03015	0.000742
14	1	1.760525	-2.50565	0.000539
15	1	1.248075	2.473459	-0.000671
16	1	-1.06113	-2.42563	-0.000349

Table S-16. Compound II (N-methyl isatin)

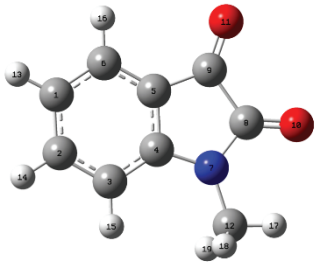

Centre Number	Atomic Number	Coordinates (Angstroms)		
		X	Y	Z
1	6	-2.91547	-0.50036	-0.00003
2	6	-2.73683	0.884986	-0.000027
3	6	-1.46363	1.468996	0.000024
4	6	-0.36684	0.618545	0.000069
5	6	-0.53678	-0.77911	0.000103
6	6	-1.80448	-1.34566	0.000013
7	7	0.995994	0.96027	-0.000034
8	6	1.794392	-0.17241	0.000016
9	6	0.800814	-1.38919	-0.000004
10	8	2.999549	-0.20804	0.000038
11	8	1.138564	-2.54519	-0.000074
12	6	1.516712	2.314489	-0.000043
13	1	-3.91613	-0.9146	-0.00007
14	1	-3.60704	1.531928	-0.000067
15	1	-1.35047	2.545812	0.000047
16	1	-1.91412	-2.42408	0.00007
17	1	2.603864	2.248257	-0.001251
18	1	1.188821	2.857761	-0.890845
19	1	1.190825	2.857119	0.891903

Table S-17. Compound III (N-Benzyl isatin)

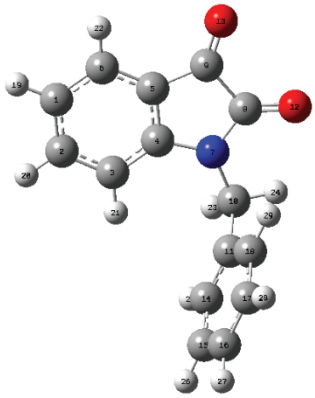

Centre Number	Atomic Number	Coordinates (Angstroms)		
		X	Y	Z
1	6	4.332837	-1.34281	-0.221448
2	6	3.312967	-2.30076	-0.162262
3	6	1.960569	-1.94252	-0.046354
4	6	1.650105	-0.58668	0.004998
5	6	2.675205	0.378957	-0.045086
6	6	4.013006	0.01669	-0.160167
7	7	0.36404	0.037754	0.119461
8	6	0.527336	1.419716	0.186885
9	6	2.045898	1.688851	0.053778
10	6	-0.80563	-0.85357	0.310983
11	6	-2.25948	-0.43797	0.099942
12	8	-0.32114	2.305276	0.322701
13	8	2.549169	2.816152	0.061761
14	6	-3.16913	-1.49523	0.306553
15	6	-4.53809	-1.32081	0.12575
16	6	-5.03533	-0.07454	-0.269678
17	6	-4.14516	0.977615	-0.469716
18	6	-2.76466	0.806596	-0.29271
19	1	5.362389	-1.65855	-0.310022
20	1	3.569455	-3.35087	-0.206563
21	1	1.20508	-2.71111	0.002487
22	1	4.774786	0.783467	-0.195422
23	1	-0.63172	-1.6755	-0.387856
24	1	-0.71601	-1.28643	1.313984
25	1	-2.79919	-2.46851	0.610551
26	1	-5.21225	-2.15117	0.290735
27	1	-6.09844	0.069679	-0.408485
28	1	-4.51563	1.951833	-0.760183
29	1	-2.11364	1.660165	-0.389966

Table S-18. Compound IV (N-allyl isatin)

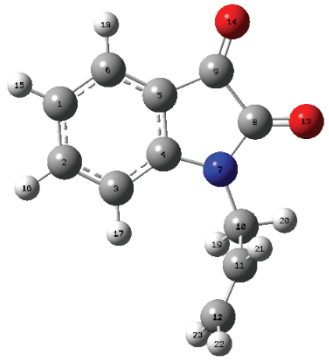

Centre Number	Atomic Number	Coordinates (Angstroms)		
		X	Y	Z
1	6	1.801626	2.579291	0.064102
2	6	0.423958	2.768749	-0.26132
3	6	-0.44739	1.676148	-0.297884
4	6	0.083818	0.407831	-0.161006
5	6	1.449647	0.225369	0.0556
6	6	2.325028	1.296081	0.106175
7	7	-0.65304	-0.80136	-0.106187
8	6	0.397473	-1.82426	-0.25862
9	6	1.721748	-1.22548	0.250797
10	6	-2.10156	-0.98869	0.060763
11	6	-2.76268	0.3448	0.221039
12	6	-4.08707	0.418519	0.388134
13	8	0.246123	-2.93664	-0.704698
14	8	2.704167	-1.77729	0.686066
15	1	2.474079	3.449488	-0.043544
16	1	0.026708	3.786635	-0.388212
17	1	-1.5294	1.822437	-0.432293
18	1	3.400743	1.140816	0.275429
19	1	-2.51462	-1.50159	-0.836487
20	1	-2.29341	-1.60879	0.964892
21	1	-2.1588	1.264083	0.201205
22	1	-4.5729	1.398387	0.505933
23	1	-4.69103	-0.50071	0.407973

Table S-19. Compound V (N-Propargyl isatin)

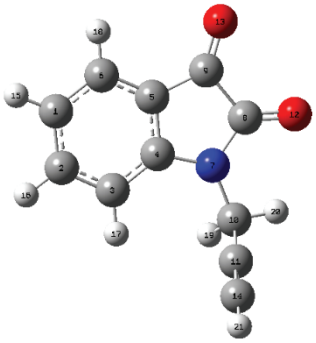

Centre Number	Atomic Number	Coordinates (Angstroms)		
		X	Y	Z
1	6	-2.79631	-1.59025	0.10676
2	6	-1.69917	-2.39279	-0.230685
3	6	-0.41451	-1.85451	-0.414055
4	6	-0.26558	-0.48403	-0.250258
5	6	-1.36444	0.334819	0.09193
6	6	-2.63119	-0.21016	0.272549
7	7	0.90283	0.307718	-0.383762
8	6	0.626822	1.650434	-0.136445
9	6	-0.88732	1.715629	0.19122
10	6	2.237973	-0.17476	-0.744217
11	6	2.842946	-1.04537	0.267931
12	8	1.436185	2.580769	-0.187884
13	8	-1.50144	2.749827	0.466374
14	6	3.353456	-1.76287	1.089788
15	1	-3.76974	-2.03978	0.24081
16	1	-1.83913	-3.45857	-0.351771
17	1	0.421613	-2.49256	-0.657931
18	1	-3.46166	0.43123	0.534327
19	1	2.185926	-0.68972	-1.707933
20	1	2.84613	0.72068	-0.887179
21	1	3.80299	-2.38696	1.820974

Table S-20. Compound VI (5-nitro isatin)

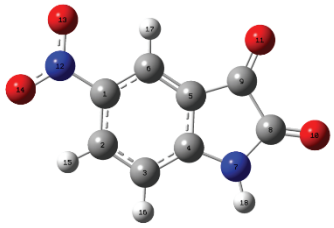

Centre Number	Atomic Number	Coordinates (Angstroms)		
		X	Y	Z
1	6	1.716441	-0.10467	-0.00023
2	6	1.478361	-1.48458	0.000296
3	6	0.172688	-1.97951	0.000585
4	6	-0.87084	-1.05712	0.000561
5	6	-0.61879	0.336584	-0.00027
6	6	0.675877	0.829045	-0.00075
7	7	-2.25216	-1.28792	0.000376
8	6	-2.98198	-0.09594	0.000012
9	6	-1.91384	1.031107	-0.00052
10	8	-4.20539	0.013833	0.000087
11	8	-2.16308	2.236531	-0.00074
12	7	3.097332	0.371653	-0.00028
13	8	3.294797	1.622927	0.002817
14	8	4.027485	-0.48978	-0.00219
15	1	2.323935	-2.1545	0.000288
16	1	-0.00955	-3.04419	0.000917
17	1	0.883257	1.888248	-0.00085
18	1	-2.69181	-2.19328	0.001077

Table S-21. compound VII (5-methyl isatin)

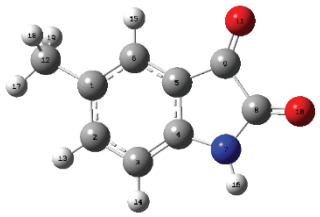

Centre Number	Atomic Number	Coordinates (Angstroms)		
		X	Y	Z
1	6	2.351864	0.210881	-0.000065
2	6	2.193143	-1.18547	0.000274
3	6	0.934023	-1.80883	0.000182
4	6	-0.18656	-0.99428	-0.000242
5	6	-0.05635	0.411034	-0.000597
6	6	1.196223	1.012165	-0.000516

7	7	-1.55658	-1.34379	-0.000009
8	6	-2.37623	-0.22312	-0.000015
9	6	-1.40335	0.990994	0.000037
10	8	-3.60875	-0.20674	0.000005
11	8	-1.75675	2.173151	0.000526
12	6	3.726366	0.841932	0.00013
13	1	3.077616	-1.8097	0.000624
14	1	0.854628	-2.88715	0.00054
15	1	1.268807	2.092528	-0.000701
16	1	-1.91794	-2.28222	-0.000314
17	1	4.510649	0.084858	-0.000974
18	1	3.875408	1.473428	-0.878971
19	1	3.876099	1.471556	0.880476

Table S-22. Compound VIII (N-methyl-5-nitro isatin)

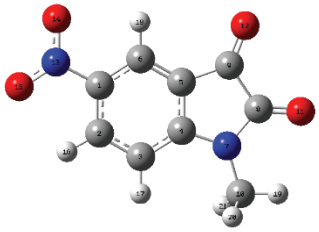

Centre Number	Atomic Number	Coordinates (Angstroms)		
		X	Y	Z
1	6	1.939666	-0.13322	-0.000256
2	6	1.532261	-1.47219	0.000259
3	6	0.174767	-1.80259	0.000501
4	6	-0.74845	-0.7582	0.000472
5	6	-0.32295	0.593767	-0.000259
6	6	1.021066	0.922575	-0.000754
7	7	-2.14887	-0.8293	0.000138
8	6	-2.71423	0.451956	-0.000358
9	6	-1.52248	1.440188	-0.000377
10	6	-2.94097	-2.05454	0.000643
11	8	-3.91773	0.71095	-0.000449
12	8	-1.62337	2.667367	-0.000207
13	7	3.367635	0.168107	-0.000307
14	8	3.719283	1.385547	0.002726
15	8	4.184888	-0.80177	-0.002165
16	1	2.288511	-2.2416	0.000217
17	1	-0.13459	-2.83675	0.000741
18	1	1.357741	1.948083	-0.000711
19	1	-3.98861	-1.76491	0.001767
20	1	-2.73659	-2.64975	-0.890135
21	1	-2.73453	-2.64988	0.890839

Table S-23. Compound IX (N-methyl-5-methyl isatin)

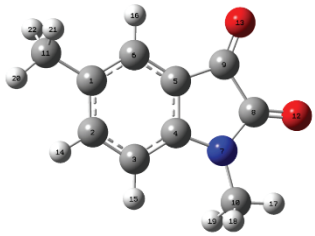

Centre Number	Atomic Number	Coordinates (Angstroms)		
		X	Y	Z
1	6	2.579981	0.037445	-0.000077
2	6	2.192296	-1.31228	0.000127
3	6	0.846258	-1.71887	0.000166
4	6	-0.12452	-0.72937	-0.000009
5	6	0.238833	0.634937	-0.000278
6	6	1.572217	1.020047	-0.000324
7	7	-1.53509	-0.85949	0.000171
8	6	-2.14741	0.388913	0.00003
9	6	-0.99453	1.426735	0.000024
10	6	-2.26858	-2.11666	-0.000147
11	6	4.039642	0.433321	0.000047
12	8	-3.36347	0.607383	-0.000038
13	8	-1.14961	2.651084	0.000262
14	1	2.961211	-2.07443	0.000254
15	1	0.591552	-2.76893	0.000345
16	1	1.823313	2.073373	-0.000477
17	1	-3.32895	-1.87646	-0.000078
18	1	-2.03622	-2.70447	-0.889961
19	1	-2.03613	-2.70489	0.889326
20	1	4.68849	-0.44264	-0.000878
21	1	4.290743	1.031729	-0.879091
22	1	4.291068	1.030086	0.880222

XYZ COORDINATES OF ISATIN AND ITS DERIVATIVES WITH GRIMME D3 OPTIMIZED STRUCTURE

Table S-24. Compound I (Isatin)

Centre Number	Atomic Number	Coordinates (Angstroms)		
		X	Y	Z
1	6	2.577738	0.837977	0.17273
2	6	2.742137	-0.55254	0.062287
3	6	1.633569	-1.39159	-0.0841
4	6	0.374899	-0.82129	-0.091509
5	6	0.217201	0.561794	-0.002629
6	6	1.303904	1.40823	0.131142

7	7	-0.84807	-1.50711	-0.296728
8	6	-1.85054	-0.49777	0.089843
9	6	-1.22904	0.895255	-0.122197
10	8	-2.96381	-0.72357	0.500788
11	8	-1.76401	1.958696	-0.327579
12	1	3.460266	1.483424	0.293126
13	1	3.752913	-0.98549	0.091302
14	1	1.760123	-2.47905	-0.190727
15	1	1.168173	2.497558	0.202626
16	1	-1.00168	-2.48804	-0.638308

Table S-25. Compound II (N-methyl isatin)

Centre Number	Atomic Number	Coordinates (Angstroms)		
		X	Y	Z
1	6	2.873646	-0.51321	-0.096731
2	6	2.719178	0.882516	-0.125675
3	6	1.446582	1.459511	-0.081711
4	6	0.347649	0.623021	-0.035063
5	6	0.506181	-0.76193	0.014676
6	6	1.758659	-1.34982	-0.016313
7	7	-1.00436	1.031247	0.081293
8	6	-1.74101	-0.21067	-0.215567
9	6	-0.83252	-1.40047	0.146056
10	8	-2.86056	-0.28253	-0.663718
11	8	-1.1239	-2.5326	0.450497
12	6	-1.5383	2.359688	0.414475
13	1	3.881835	-0.95111	-0.13772
14	1	3.608042	1.527808	-0.183486
15	1	1.322976	2.552552	-0.084177
16	1	1.872264	-2.44334	0.021268
17	1	-2.65072	2.322735	0.418469
18	1	-1.17407	2.663522	1.42133
19	1	-1.19462	3.098298	-0.343838

Table S-26 Compound III (N-Benzyl isatin)

Centre Number	Atomic Number	Coordinates (Angstroms)		
		X	Y	Z
1	6	4.478806	-0.58664	-0.016213
2	6	3.785344	-1.79913	0.131224
3	6	2.388289	-1.81972	0.177808
4	6	1.710993	-0.61767	0.101015
5	6	2.402572	0.582077	-0.066399
6	6	3.784701	0.619889	-0.126104
7	7	0.303578	-0.45655	0.064503
8	6	0.14081	0.991974	0.284574
9	6	1.421772	1.694003	-0.20332
10	6	-0.73372	-1.47757	-0.141125
11	6	-2.08433	-0.83327	-0.09945

12	8	-0.82715	1.533136	0.763481
13	8	1.584895	2.827283	-0.588482
14	6	-3.23187	-1.60739	-0.271248
15	6	-4.49032	-1.0069	-0.232351
16	6	-4.60112	0.367403	-0.021727
17	6	-3.45363	1.141421	0.150147
18	6	-2.19518	0.541032	0.111261
19	1	5.578449	-0.58754	-0.045376
20	1	4.346957	-2.74158	0.210845
21	1	1.8416	-2.76944	0.273286
22	1	4.320349	1.571801	-0.256173
23	1	-0.58503	-1.9624	-1.13199
24	1	-0.66371	-2.24452	0.662354
25	1	-3.14441	-2.69119	-0.437278
26	1	-5.39535	-1.61734	-0.367964
27	1	-5.59352	0.840828	0.00897
28	1	-3.54101	2.225286	0.316458
29	1	-1.2901	1.151476	0.246787

Table S-27. Compound IV (N-allyl isatin)

Centre Number	Atomic Number	Coordinates (Angstroms)		
		X	Y	Z
1	6	1.801626	2.579291	-0.064102
2	6	0.423958	2.768749	-0.26132
3	6	-0.44739	1.676148	-0.297884
4	6	0.083818	0.407831	-0.161006
5	6	1.449647	0.225369	0.0556
6	6	2.325028	1.296081	0.106175
7	7	-0.65304	-0.80136	-0.106187
8	6	0.397473	-1.82426	-0.25862
9	6	1.721748	-1.22548	0.250797
10	6	-2.10156	-0.98869	0.060763
11	6	-2.76268	0.3448	0.221039
12	6	-4.08707	0.418519	0.388134
13	8	0.246123	-2.93664	-0.704698
14	8	2.704167	-1.77729	0.686066
15	1	2.474079	3.449488	-0.043544
16	1	0.026708	3.786635	-0.388212
17	1	-1.5294	1.822437	-0.432293
18	1	3.400743	1.140816	0.275429
19	1	-2.51462	-1.50159	-0.836487
20	1	-2.29341	-1.60879	0.964892
21	1	-2.1588	1.264083	0.201205
22	1	-4.5729	1.398387	0.505933
23	1	-4.69103	-0.50071	0.407973

Table S-28. Compound V (N-Propargyl isatin)

Centre Number	Atomic Number	Coordinates (Angstroms)		
		X	Y	Z
1	6	0.309727	3.003985	-0.109515
2	6	-1.00062	2.528766	-0.282514
3	6	-1.26511	1.156068	-0.292483
4	6	-0.2039	0.281906	-0.153821
5	6	1.092945	0.758154	0.03872
6	6	1.371352	2.113581	0.062824
7	7	-0.29403	-1.13004	-0.073873
8	6	1.109447	-1.55069	-0.236523
9	6	2.010225	-0.39695	0.242267
10	6	-1.48748	-1.96554	0.122002
11	6	-2.66866	-1.1048	0.279402
12	8	1.48663	-2.61357	-0.66929
13	8	3.141938	-0.42199	0.664025
14	6	-3.64252	-0.39508	0.409091
15	1	0.501307	4.087152	-0.109874
16	1	-1.82665	3.243607	-0.411439
17	1	-2.29272	0.781036	-0.40791
18	1	2.398096	2.478496	0.213182
19	1	-1.62608	-2.62676	-0.762494
20	1	-1.35826	-2.58844	1.035379
21	1	-4.51845	0.243241	0.525679

Table S-29. Compound VI (5-nitro isatin)

Centre Number	Atomic Number	Coordinates (Angstroms)		
		X	Y	Z
1	6	1.740137	-0.06979	0.01346
2	6	1.501616	-1.45282	-0.041986
3	6	0.196318	-1.94839	-0.112508
4	6	-0.85014	-1.04599	-0.100418
5	6	-0.60828	0.327342	-0.066413
6	6	0.677553	0.835766	-0.008039
7	7	-2.22472	-1.36418	-0.232329
8	6	-2.88398	-0.10078	0.144957
9	6	-1.90631	1.052155	-0.149373
10	8	-3.99563	0.010554	0.604301
11	8	-2.12953	2.216357	-0.381941
12	7	2.912199	0.353414	0.082582
13	8	3.141206	1.642266	0.134607
14	8	3.913395	-0.49111	0.103109
15	1	2.350079	-2.15276	-0.029757
16	1	0.006915	-3.03008	-0.176022
17	1	0.857089	1.920624	0.020606
18	1	-2.6635	-2.27198	-0.525281

Table S-30. Compound VII (5-methyl isatin)

Centre Number	Atomic Number	Coordinates (Angstroms)		
		X	Y	Z
1	6	2.29372	0.22116	0.071031
2	6	2.179629	-1.17657	-0.007077
3	6	0.924657	-1.78449	-0.10627
4	6	-0.19774	-0.97843	-0.09965
5	6	-0.07913	0.410252	-0.043053
6	6	1.155512	1.02944	0.04384
7	7	-1.53647	-1.41489	-0.258993
8	6	-2.31093	-0.22051	0.124133
9	6	-1.43484	1.018622	-0.138097
10	8	-3.4351	-0.21476	0.566133
11	8	-1.75669	2.16178	-0.358695
12	6	3.647662	0.849857	0.184401
13	1	3.086582	-1.79891	0.009906
14	1	0.832978	-2.87767	-0.187656
15	1	1.237753	2.125413	0.090057
16	1	-1.88843	-2.35345	-0.571518
17	1	4.426913	0.055199	0.190756
18	1	3.815616	1.526552	-0.683058
19	1	3.706875	1.434836	1.129417

Table S-31. compound VIII (N-methyl-5-nitro isatin)

Centre Number	Atomic Number	Coordinates (Angstroms)		
		X	Y	Z
1	6	-1.96287	-0.12005	-0.023243
2	6	-1.54066	-1.45912	-0.060686
3	6	-0.17956	-1.77769	-0.044413
4	6	0.736535	-0.7435	-0.016499
5	6	0.312867	0.584206	0.041773
6	6	-1.03036	0.917369	0.038113
7	7	2.14419	-0.88107	0.071217
8	6	2.619185	0.48034	-0.23549
9	6	1.504305	1.470834	0.148839
10	6	2.932806	-2.08035	0.388364
11	8	3.693946	0.768356	-0.705686
12	8	1.576114	2.638045	0.451735
13	7	-3.18228	0.144811	-0.045036
14	8	-3.58232	1.391802	-0.010331
15	8	-4.06208	-0.82404	-0.102558
16	1	-2.28822	-2.26492	-0.103268
17	1	0.153993	-2.82584	-0.053643
18	1	-1.35367	1.967847	0.082169
19	1	4.016665	-1.82783	0.37026
20	1	2.655248	-2.44912	1.401164
21	1	2.723867	-2.87184	-0.36577

Table S-32. Compound IX (N-methyl-5-methyl isatin)

Centre Number	Atomic Number	Coordinates (Angstroms)		
		X	Y	Z
1	6	2.523595	-0.03268	-0.051808
2	6	2.162063	1.32401	-0.089697
3	6	0.816924	1.703841	-0.063487
4	6	-0.14472	0.712215	-0.025332
5	6	0.218956	-0.63315	0.033342
6	6	1.545679	-1.02672	0.019928
7	7	-1.54397	0.91352	0.073205
8	6	-2.08248	-0.42578	-0.225831
9	6	-1.01044	-1.46472	0.15242
10	6	-2.27501	2.147999	0.393345
11	6	3.970093	-0.41628	-0.088658
12	8	-3.17301	-0.66606	-0.686577
13	8	-1.13256	-2.62673	0.45925
14	1	2.944838	2.095168	-0.140459
15	1	0.530942	2.765984	-0.072991
16	1	1.821433	-2.09062	0.064448
17	1	-3.36929	1.944705	0.384597
18	1	-1.9728	2.506349	1.402797
19	1	-2.03653	2.927352	-0.36473
20	1	4.596658	0.501867	-0.145081
21	1	4.226574	-0.98358	0.833928
22	1	4.162531	-1.05204	-0.981655

XYZ COORDINATES OF ISATIN AND ITS DERIVATIVES (IEFPCM-WATER MODEL)

Table S-33. Compound I (Isatin)

Centre Number	Atomic Number	Coordinates (Angstroms)		
		X	Y	Z
1	6	-2.63772	0.799399	0.000188
2	6	-2.75111	-0.59402	0.000325
3	6	-1.6283	-1.42894	0.000077
4	6	-0.38019	-0.8249	-0.000291
5	6	-0.25483	0.576032	-0.000559
6	6	-1.37663	1.394291	-0.000244
7	7	0.884702	-1.42615	-0.000296
8	6	1.909469	-0.49268	0.000027
9	6	1.178667	0.903473	-0.00009
10	8	3.091773	-0.70864	0.000299
11	8	1.739842	1.968239	0.000278
12	1	-3.53057	1.412233	0.000427
13	1	-3.73675	-1.0457	0.000638
14	1	-1.73489	-2.50719	0.00014
15	1	-1.25401	2.471163	-0.000414
16	1	1.054273	-2.42021	0.000075

Table S-34. Compound II (N-methyl isatin)

Centre Number	Atomic Number	Coordinates (Angstroms)		
		X	Y	Z
1	6	2.912556	-0.50059	0.000156
2	6	2.734748	0.884936	0.000129
3	6	1.462399	1.470103	-0.000053
4	6	0.365798	0.62016	-0.000212
5	6	0.535623	-0.77684	-0.000215
6	6	1.800975	-1.34474	-0.000021
7	7	-0.99427	0.959523	-0.000289
8	6	-1.79457	-0.17371	0.000001
9	6	-0.8	-1.38973	-0.000064
10	8	-2.99884	-0.2053	0.00023
11	8	-1.13265	-2.54671	0.000036
12	6	-1.51474	2.311928	0.000085
13	1	3.912886	-0.91549	0.00032
14	1	3.605549	1.530974	0.000283
15	1	1.345526	2.546363	-0.000061
16	1	1.904632	-2.42364	-0.000032
17	1	-2.60182	2.243088	-0.000237
18	1	-1.18611	2.854172	0.891383
19	1	-1.18557	2.854832	-0.890589

Table S-35. Compound III (N-Benzyl isatin)

Centre Number	Atomic Number	Coordinates (Angstroms)		
		X	Y	Z
1	6	2.704825	2.602199	0.433825
2	6	1.477126	2.843612	-0.188295
3	6	0.642082	1.803543	-0.613252
4	6	1.078083	0.50435	-0.398262
5	6	2.309635	0.251249	0.232566
6	6	3.128436	1.290816	0.650399
7	7	0.434532	-0.6977	-0.737317
8	6	1.17676	-1.79512	-0.329843
9	6	2.475847	-1.20489	0.327392
10	6	-0.85939	-0.80151	-1.398178
11	6	-2.01272	-0.35926	-0.519312
12	8	0.872798	-2.95531	-0.452758
13	8	3.368789	-1.86618	0.791147
14	6	-2.92203	0.602139	-0.960362
15	6	-3.98612	0.996634	-0.149767
16	6	-4.1448	0.432554	1.112921
17	6	-3.23913	-0.53026	1.559893
18	6	-2.18051	-0.92445	0.748364
19	1	3.321839	3.434304	0.7497
20	1	1.154571	3.866915	-0.344659
21	1	-0.31448	2.009787	-1.073945
22	1	4.072768	1.068817	1.133801

23	1	-0.83529	-0.21639	-2.322405
24	1	-0.96621	-1.85419	-1.670253
25	1	-2.80011	1.04579	-1.943895
26	1	-4.68563	1.745562	-0.503605
27	1	-4.96891	0.739607	1.746647
28	1	-3.36076	-0.97587	2.540659
29	1	-1.48086	-1.67818	1.093522

Table S-36. Compound IV (N-allyl isatin)

Centre Number	Atomic Number	Coordinates (Angstroms)		
		X	Y	Z
1	6	-2.43887	-2.12443	0.079178
2	6	-1.17051	-2.65432	-0.171829
3	6	-0.03882	-1.84178	-0.308943
4	6	-0.21629	-0.47074	-0.189299
5	6	-1.48952	0.071678	0.064466
6	6	-2.60353	-0.74459	0.200314
7	7	0.747373	0.546705	-0.296444
8	6	0.174471	1.798657	-0.120531
9	6	-1.35207	1.532116	0.133748
10	6	2.163275	0.347929	-0.582074
11	6	2.905975	-0.28158	0.5668
12	6	3.663173	-1.36787	0.462243
13	8	0.741678	2.860915	-0.161959
14	8	-2.1727	2.390397	0.332964
15	1	-3.28965	-2.78686	0.180235
16	1	-1.05342	-3.72863	-0.260568
17	1	0.937898	-2.27104	-0.484482
18	1	-3.57291	-0.30045	0.394706
19	1	2.269916	-0.25278	-1.491289
20	1	2.559684	1.346426	-0.786743
21	1	2.798678	0.225587	1.522511
22	1	4.201831	-1.77076	1.311838
23	1	3.78086	-1.88945	-0.483574

Table S-37. Compound V (N-Propargyl isatin)

Centre Number	Atomic Number	Coordinates (Angstroms)		
		X	Y	Z
1	6	-2.75735	-1.61753	0.097592
2	6	-1.64614	-2.39568	-0.237512
3	6	-0.37472	-1.8375	-0.415846
4	6	-0.25072	-0.46618	-0.250677
5	6	-1.36192	0.325821	0.089933
6	6	-2.61694	-0.23999	0.26594
7	7	0.901323	0.327635	-0.382337
8	6	0.625161	1.665739	-0.133429
9	6	-0.91009	1.719417	0.195853
10	6	2.22734	-0.15419	-0.741957

11	6	2.817912	-1.03204	0.268975
12	8	1.407215	2.579992	-0.176874
13	8	-1.51566	2.72431	0.464573
14	6	3.294965	-1.76302	1.092401
15	1	-3.72427	-2.08738	0.228452
16	1	-1.76638	-3.46618	-0.360286
17	1	0.478562	-2.45827	-0.655359
18	1	-3.45789	0.391509	0.527908
19	1	2.176776	-0.67464	-1.705128
20	1	2.844905	0.737733	-0.877113
21	1	3.7216	-2.39981	1.828657

Table S-38. Compound VI (5-nitro isatin)

Centre Number	Atomic Number	Coordinates (Angstroms)		
		X	Y	Z
1	6	1.712432	-0.10453	0.000098
2	6	1.467465	-1.47939	0.000423
3	6	0.163491	-1.96803	0.000836
4	6	-0.87515	-1.04308	0.000653
5	6	-0.61439	0.342675	0.000235
6	6	0.679734	0.830128	-0.000023
7	7	-2.24562	-1.27851	0.001101
8	6	-2.98624	-0.098	-0.00011
9	6	-1.9082	1.04876	-0.000236
10	8	-4.18053	0.005576	-0.001064
11	8	-2.15677	2.223845	-0.000615
12	7	3.110106	0.370124	-0.000217
13	8	3.293279	1.5796	0.002514
14	8	3.996253	-0.47472	-0.003101
15	1	2.31261	-2.15401	0.000365
16	1	-0.02689	-3.03395	0.001334
17	1	0.88774	1.891536	-0.000168
18	1	-2.67754	-2.19051	-0.00084

Table S-39. Compound VII (5-methyl isatin)

Centre Number	Atomic Number	Coordinates (Angstroms)		
		X	Y	Z
1	6	2.346811	0.204842	-0.000088
2	6	2.178451	-1.1859	-0.000295
3	6	0.920432	-1.80163	-0.000104
4	6	-0.1954	-0.98311	0.00031
5	6	-0.0531	0.415452	0.000626
6	6	1.199905	1.008538	0.000354
7	7	-1.55314	-1.33431	0.000277
8	6	-2.38141	-0.22443	-0.000053
9	6	-1.39916	1.008384	0.000097
10	8	-3.5837	-0.21067	-0.000317
11	8	-1.74811	2.160448	-0.00032

12	6	3.721324	0.829981	-0.000163
13	1	3.06055	-1.81772	-0.000635
14	1	0.832462	-2.88164	-0.000245
15	1	1.274246	2.091083	0.000514
16	1	-1.90841	-2.27796	-0.000108
17	1	4.506352	0.071422	-0.002784
18	1	3.866068	1.464041	-0.879953
19	1	3.868041	1.459938	0.882261

Table S-40. compound VIII (N-methyl-5-nitro isatin)

Centre Number	Atomic Number	Coordinates (Angstroms)		
		X	Y	Z
1	6	1.933037	-0.1312	0.000066
2	6	1.520412	-1.46443	0.000288
3	6	0.165434	-1.78967	0.000437
4	6	-0.75277	-0.7436	0.000232
5	6	-0.32067	0.599793	-0.000046
6	6	1.021845	0.924427	-0.000098
7	7	-2.14169	-0.82268	-0.000012
8	6	-2.72087	0.446406	-0.000243
9	6	-1.5193	1.455463	-0.000424
10	6	-2.91032	-2.05452	0.000651
11	8	-3.89644	0.694854	-0.000256
12	8	-1.62629	2.652103	-0.000775
13	7	3.377078	0.16791	0.000009
14	8	3.707902	1.345992	0.002757
15	8	4.153779	-0.77898	-0.002779
16	1	2.276134	-2.23796	0.000268
17	1	-0.15185	-2.82398	0.000701
18	1	1.359192	1.952042	-0.000082
19	1	-3.96423	-1.78029	0.000667
20	1	-2.68986	-2.64746	-0.890849
21	1	-2.68956	-2.64671	0.892573

Table S-41. compound IX (N-methyl-5-methyl isatin)

Centre Number	Atomic Number	Coordinates (Angstroms)		
		X	Y	Z
1	6	2.571076	0.035221	-0.000115
2	6	2.176228	-1.30765	-0.000133
3	6	0.832869	-1.70839	0.000043
4	6	-0.1332	-0.71651	0.000251
5	6	0.239447	0.639651	0.00028
6	6	1.571428	1.018143	0.000075
7	7	-1.53011	-0.85293	0.000302
8	6	-2.15499	0.384169	-0.000006
9	6	-0.99266	1.441651	0.000069
10	6	-2.24179	-2.11465	-0.000101
11	6	4.029402	0.42645	-0.000099

12	8	-3.34186	0.593602	-0.000249
13	8	-1.15166	2.635082	-0.000077
14	1	2.942387	-2.07606	-0.000335
15	1	0.569912	-2.75869	-0.000009
16	1	1.823922	2.073496	0.000071
17	1	-3.30739	-1.88867	0.000229
18	1	-1.99534	-2.69926	-0.891278
19	1	-1.9949	-2.70004	0.890418
20	1	4.679398	-0.45062	-0.002693
21	1	4.276403	1.028365	-0.879792
22	1	4.277555	1.02395	0.882296

Journal of the Serbian Chemical Society
JSCS-info@shd.org.rs • www.shd.org.rs/JSCS
J. Serb. Chem. Soc. *91* (1) 39–54 (2026)
JSCS–5476
Original scientific paper
Published 5 February, 2026

Removal of nickel(II) ions during water purification with ferrous sulfate. Part 1. Mechanism and efficiency of the process

OLEG D. LINNIKOV* and IRINA V. RODINA

Institute of Solid State Chemistry, Ural Branch of the Russian Academy of Sciences, Pervomayskaya St., 91, 620990, Ekaterinburg, Russia

((Received 7 April, revised 5 May, accepted 30 October 2025)

Abstract: The purification of natural water and wastewater from nickel ions is critically important for both environmental protection and human health due to their high toxicity. This study aimed to investigate the removal of nickel ions from contaminated aqueous solutions using the coagulant $FeSO_4$. The results demonstrate that the removal of nickel ions via an iron(III) hydroxide precipitate, formed during coagulation at pH 7 and pH 8, can be accurately described by classical adsorption isotherms, including the Langmuir, Freundlich and Dubinin–Radushkevich models. The calculated free energy of adsorption, based on the Dubinin–Radushkevich equation, does not exceed 8 kJ mol^{-1}, indicating the physical nature of the adsorption process and ruling out ion-exchange interactions between nickel ions and iron(III) hydroxide. The sorption capacity of the resulting iron(III) hydroxide precipitate for nickel ions at pH 8 is 0.727 mg (mg $Fe)^{-1}$ of added Fe to the solution. At pH 7, the sorption capacity depends on the initial coagulant concentration and ranges from 0.105 to 0.730 mg (mg $Fe)^{-1}$. A comparison between the coagulants $FeSO_4$ and the previously studied $FeCl_3$ reveals that $FeSO_4$ is more effective for nickel ion removal when the initial iron ion concentration is below 70 mg L^{-1}. However, at higher initial concentrations of iron, $FeCl_3$ demonstrates greater efficacy.

Keywords: coagulation; iron(III) hydroxide; adsorption isotherms; ferrous sulphate; removal of nickel ions; water treatment.

INTRODUCTION

Due to the high toxicity of nickel ions, the purification of natural water and wastewater from nickel ions is critically important for both human health and environmental protection.[1,2] Various international standards have set stringent maximum permissible concentrations for nickel ions in purified water. For instance, the allowable concentration in drinking water ranges from 0.02 to 0.1 mg L^{-1},[3] while Russian regulations mandate that the concentration of nickel ions in

* Corresponding author. E-mail: linnikov@mail.ru
https://doi.org/10.2298/JSC250407080L

purified water discharged into natural reservoirs must not exceed 0.01 mg L^{-1}. Achieving such low residual concentrations of nickel ions during water treatment is therefore a significant challenge.

In most industrial settings, wastewater is treated with to remove nickel ions and other heavy metals. This process increases the solution's pH to 8–10, causing many heavy metals to precipitate as hydroxides. However, due to the relatively high solubility of nickel hydroxide, this method is insufficient for reducing nickel ion concentrations to levels that meet regulatory standards. One approach to address this limitation is to apply an additional purification step using sorption methods.

Currently, numerous studies[3–13] have demonstrated the potential for nickel ion sorption using various carbon, coal, and mineral sorbents. However, their industrial application is often hindered by challenges related to the disposal of spent sorbents. Over time, the sorption capacity of these materials decreases, even with regeneration, necessitating their eventual replacement. This creates concerns regarding the safe disposal or burial of used sorbents, which is not always straightforward.

In light of these challenges, there is ongoing research to identify new, efficient sorbents that can be easily disposed of or repurposed after use. Metal oxides and hydroxides, particularly those of iron, show promise as effective sorbents. These materials offer several advantages, including their compactness, small particle size, high specific surface area and the potential for recycling in metallurgical processes after use. Metal hydroxides can be precipitated directly during the water purification process using inorganic coagulants. Aluminum and iron salts are commonly used as coagulants, and alongside the removal of insoluble coarse and colloidal impurities, these coagulants have been shown to also remove dissolved heavy metal ions.[14]

Ferric chloride is one of the most widely used coagulants in water treatment. Several studies have documented its effectiveness in removing arsenic oxyanions,[15] antimony[16] and other heavy metals.[14,17,18] Recently, we conducted a comprehensive study on the use of $FeCl_3$ as a coagulant for removing nickel ions from contaminated solutions.[19] The hydrolysis of $FeCl_3$ during coagulation leads to the formation of an iron(III) hydroxide precipitate, identified as two-line ferrihydrite with the general (gross) formula $Fe_2O_3{\cdot}3H_2O$. This precipitate adsorbs nickel ions onto its surface during the coagulation process. The sorption of nickel ions by the forming iron(III) hydroxide precipitate at pH 7 and 8 is accurately described by classical adsorption isotherms, including the Freundlich, Langmuir and Dubinin–Radushkevich models. The sorption capacity of the precipitate for nickel ions is 60.5 mg g^{-1} at pH 7 and 141.9 mg g^{-1} at pH 8 – nearly an order of magnitude higher than the capacities reported for many mineral, carbon and coal sorbents.[3–13]

In this study, we investigated another commonly used iron salt coagulant, iron(II) sulfate, for the same purpose. When $FeSO_4$ is used, the formation and precipitation of iron(III) hydroxide occur due to the oxidation of Fe^{2+} by dissolved atmospheric oxygen in the solution. At low concentrations of Fe^{2+}, this process can be summarized by the following reaction:

$$4Fe^{2+} + O_2 + 2H_2O + 8OH^- \rightarrow 4Fe(OH)_3\downarrow$$

According to the literature, the iron(III) hydroxide precipitate formed in this process is reported to have varying general (gross) formulas.[20–23] Consequently, its sorption properties with respect to nickel ions are likely to differ from those of the previously studied iron(III) hydroxide precipitate derived from the hydrolysis of iron(III) chloride.[19] Furthermore, no data have been found in the literature regarding the use of $FeSO_4$ as a coagulant for the removal of nickel ions from contaminated solutions. In this context, the objective of this study is to investigate the potential of $FeSO_4$ as a coagulant for purifying contaminated solutions containing nickel ions. Additionally, the composition and structure of the iron(III) hydroxide precipitate formed from an $FeSO_4$ solution under the conditions of our experiments are of interest, as is a comparison of the effectiveness of $FeSO_4$ and $FeCl_3$ coagulants in nickel ion removal.

Given the extensive experimental data obtained, this study is presented in two parts. The first part explores the sorption of nickel ions by iron(III) hydroxide formed during the hydrolysis of $FeSO_4$ at pH 7 and 8. The second part focuses on the structure, composition and physicochemical properties of the resulting iron(III) hydroxide precipitate.

EXPERIMENTAL

Materials and devices

All studies were conducted under laboratory conditions at room temperature (25±2 °C). The temperature during the experiments was measured using a thermometer. A sodium sulfate solution with a concentration of 400 mg L^{-1} was used as a model solution. This solution simulated natural sulfate mine waters and some types of industrial pickling wastewater. The concentration of nickel ions in the model solution varied from 3.13 to 20 mg L^{-1}. Russian-made reagents were used to prepare the solutions: pure-grade $FeSO_4$ (the content of the main substance was 98 %, GOST 4148-78, supplier CJSC “KHIMREAKTIVSNAB”), chemically pure NaOH (the content of the main substance was 99.1 %, GOST 4328-77, supplier of JSC “ECOS-1”), chemically pure Na_2SO_4 (the content of the main substance was 99 %, GOST 4166-76, supplier JSC “VEKTON”), and analytical-grade $NiSO_4$ (the content of the main substance was 98 %, GOST 4465-74, supplier JSC “REAKHIM”). The solutions were mixed using a magnetic stirrer MR Hei-Tec mixer (Heidolph Instruments GmbH & Co. KG) at a speed of 650 rpm. This allowed the system to keep the iron(III) hydroxide precipitate formed in the solution in a suspended state. An ANION 4100 pH meter (Russia) was used to control the pH. During the experiments, the pH meter electrodes were constantly immersed in the model solution.

Preliminary coagulation experiments

Preliminary experiments were conducted to examine the effect of coagulation duration on the residual concentration of nickel ions in the model solution. In these experiments, a calculated amount of $FeSO_4$ solution (13.57 g L^{-1}) was added to a specified volume of the model solution containing 6.25 mg L^{-1} of nickel ions, ensuring that the concentration of Fe^{2+} reached 50 mg L^{-1}. The pH of the solution was then adjusted to either 7 or 8 using a NaOH solution (10 g L^{-1}). After the addition of alkali, the solution was continuously stirred for 30, 60 and 120 min. The precipitate of iron(III) hydroxide formed during coagulation was separated from the solution by filtration using blue ribbon filter paper (Russia), with the filtration process lasting 15 min. The residual concentration of nickel ions in the filtrate was subsequently measured. After filtration, the iron(III) hydroxide precipitate was rinsed multiple times with distilled water and dried at room temperature for further analysis. Additionally, a series of similar experiments was performed with aeration of the solution. In these experiments, air was bubbled through the model solution at a rate of 60 L h^{-1} to evaluate the effect of aeration on the removal of nickel ions by the $FeSO_4$ coagulant. The results were compared to determine the influence of air aeration on nickel ion removal efficiency.

Serial coagulation experiments

The effect of the resulting iron(III) hydroxide precipitate on the removal of nickel ions was studied in a series of experiments with different initial concentrations of iron(II) ions (12.5, 25, 50 and 100 mg L^{-1}) and nickel ions (3.13, 6.25, 10 and 20 mg L^{-1}) in the model solution. The experimental technique was the same as in the preliminary runs. Aeration of the solution was not carried out during these experiments.

The concentration of nickel ions in the solutions was determined on a KFK-2 photocolorimeter (Russia) by the photocolorimetric method with dimethylglyoxime.[24] In each experiment, three parallel measurements of the concentration of nickel ions in the solution were carried out. The results were averaged.

RESULTS AND DISCUSSION

Effect of the coagulation duration on the residual concentration of nickel ions in the solution

Fig. 1 illustrates the effect of coagulation duration on the residual concentration of nickel ions in the model solution. At pH 7, the formation of an iron(III) hydroxide precipitate reduces the nickel ion concentration by approximately threefold, from 6.25 to 1.56–2.17 mg L^{-1}. At pH 8, the reduction is even more significant, with the nickel ion concentration decreasing nearly 20-fold, from 6.25 to 0.19–0.35 mg L^{-1}. Aeration has no observable impact on the removal of nickel ions, as the experimental data for runs with and without aeration align closely on the same curve for both pH 7 and 8 (Fig. 1). After 30 min of coagulation, the residual concentration of nickel ions at both pH levels reaches a near-equilibrium value and changes minimally thereafter. This indicates that the removal process of nickel ions, as well as the nucleation and formation of the iron(III) hydroxide precipitate, were complete within the studied time intervals at the given pH values. Based on these observations, the coagulation duration was set to 30 min for all subsequent experiments.

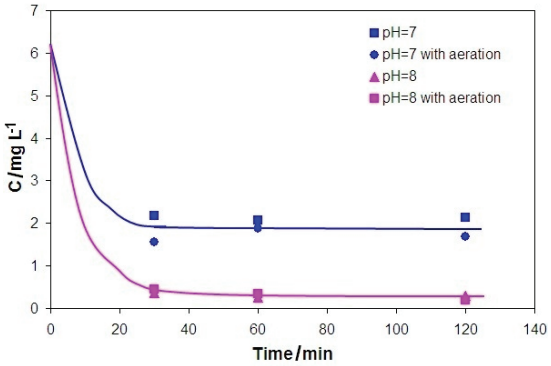

Fig. 1. Effect of the coagulation duration and pH on the residual concentration of nickel ions (C) in the model solution. The initial concentrations of iron(II) and nickel ions in the solution were 50 and 6.25 mg L^{-1}, respectively.

Coagulation removal of nickel ions at pH 7

Fig. 2a illustrates the changes in the residual concentrations of nickel ions in the model solution during the coagulation process using $FeSO_4$ at pH 7. It can be observed that as the initial concentration of iron(II) ions introduced into the solution increases, the residual concentration of nickel ions gradually decreases. For example, at the initial concentration of iron(II) in a solution of 100 mg L^{-1}, the concentration of nickel ions in it decreases from 10 to 3.12–4.03 mg L^{-1}, from 6.25 to 1.57–2.17 mg L^{-1} and from 3.13 to 0.69–0.89 mg L^{-1} (Fig. 2a).

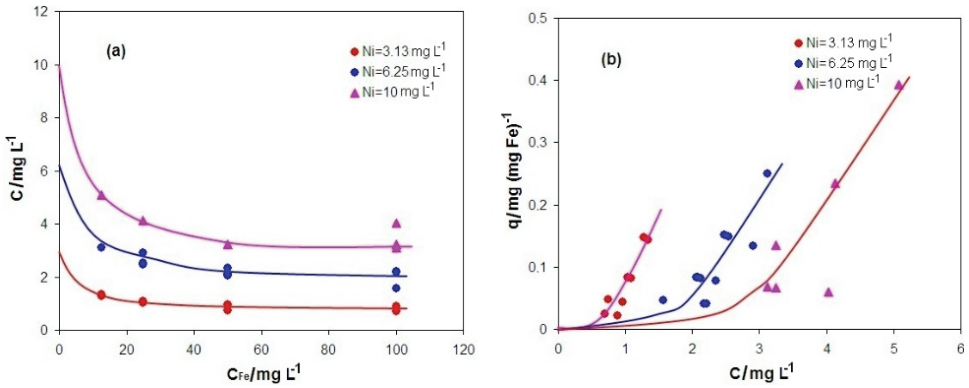

Fig. 2. Effect of the initial concentration of iron(II) ions (C_{Fe}) in the model solution on the residual concentration of nickel ions at pH 7 (a) and sorption isotherms of nickel ions on the iron(III) hydroxide precipitate formed in the solution during coagulation at pH 7 (b).

Fig. 2b presents the sorption isotherms of nickel ions on the iron(III) hydroxide precipitate formed during coagulation at pH 7. It is important to note that the sorption value, q, in this figure is expressed in units of mg (mg Fe)$^{-1}$, indicating

that the calculation is based on the initial concentration of iron(II) ions in the solution rather than on the concentration of the iron(III) hydroxide precipitate formed, which serves as the sorbent in this case:

$$q = \frac{C_{\text{in}} - C}{C_{\text{Fe}}} \tag{1}$$

where C_{in} is the initial concentration of nickel ions in the solution (mg L^{-1}). This definition of q was adopted for convenience and to facilitate the subsequent possible use of the obtained results in practice in technological calculations.

As shown in Fig. 2b, instead of a single generalized curve, three separate sorption isotherms are observed. This unusual behavior, similar to what was previously reported[25] can be explained by assuming that the iron(III) hydroxide precipitates formed at different initial concentrations of iron(II) ions in the model solution have varying specific surface areas. In other words, there is no direct proportionality between the initial concentration of iron(II) ions in the solution and the total surface area of the resulting iron(III) hydroxide precipitates. This assumption is supported by Fig. 3, which shows the sorption isotherms recalculated from Fig. 2a for identical initial concentrations of iron(II) ions introduced into the model solute-ion at the start of the experiment.

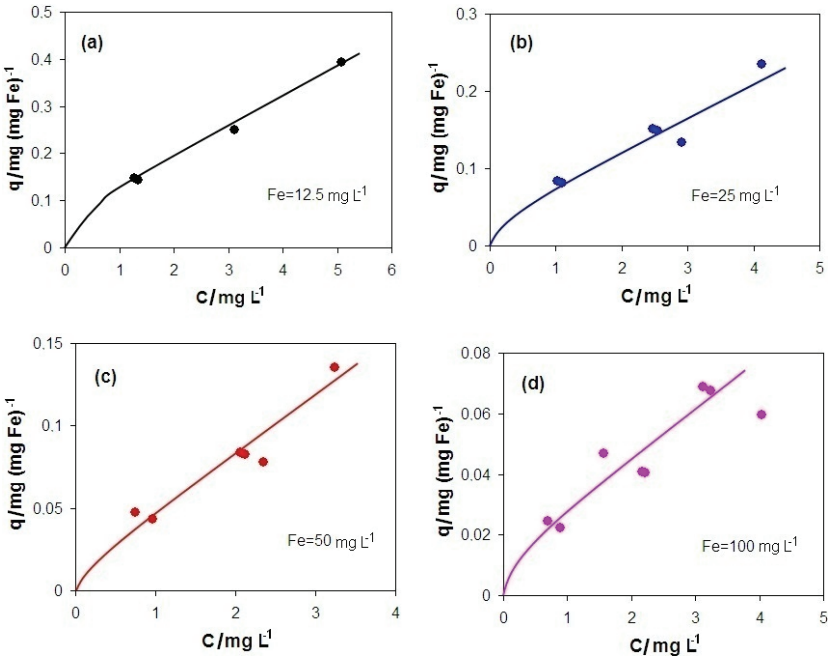

Fig. 3. Sorption isotherms of nickel ions on iron(III) hydroxide formed during coagulation process at pH 7 and different initial concentrations of iron(II) ions in solution.

As demonstrated by this calculation of sorption isotherms, they can be classified as typical L-type isotherms,[26] which are well described by the classical Langmuir equation for monomolecular adsorption:

$$q = q_\infty \frac{K_L C}{1 + K_L C} \tag{2}$$

and the empirical Freundlich equation:

$$q = K_F C^{1/n} \tag{3}$$

where q_∞ is the monolayer adsorption capacity of the sorbent, mg (mg Fe)$^{-1}$; K_L is the constant of adsorption equilibrium, L mg^{-1}; K_F is the proportionality factor; and n is the exponent ($n > 1$).

In linear form, Eqs. (2) and (3) have the following forms, respectively:

$$\frac{1}{q} = \frac{1}{q_\infty} + \frac{1}{q_\infty K_L}\frac{1}{C} \tag{4}$$

$$\log q = \log K_F + \frac{1}{n}\log C \tag{5}$$

To estimate the interaction energy of the adsorbed substance with the sorbent, the Dubinin–Radushkevich equation was used:[5,12]

$$q = q_\infty \exp(-k\varepsilon^2) \tag{6}$$

or in linear form (after taking the logarithm):

$$\ln q = \ln q_\infty - k\varepsilon^2 \tag{7}$$

where k is a constant related to the average adsorption energy; ε is the Polanyi potential, calculated as:

$$\varepsilon = RT \ln(1 + 1/C) \tag{8}$$

The free energy of adsorption (E) can be found using the equation:

$$E = \frac{1}{\sqrt{2k}} \tag{9}$$

It is known that if E lies in the range of 8–16 kJ mol^{-1}, then the adsorption process proceeds by ion exchange. At $E < 8$ kJ mol^{-1}, physical adsorption takes place.[5,12]

The results of processing the experimental data in the coordinates of Eqs. (4), (5) and (7) are presented in Fig. 4. As can be seen, all the obtained experimental points can be approximated by straight lines. This indicates that the sorption of nickel ions by the iron(III) hydroxide precipitate formed in the model solution can be described with satisfactory accuracy by the classical Langmuir, Freundlich and

Dubinin–Radushkevich isotherms. The parameters of Eqs. (2), (3) and (6) calculated from the experimental data are given in Table I.

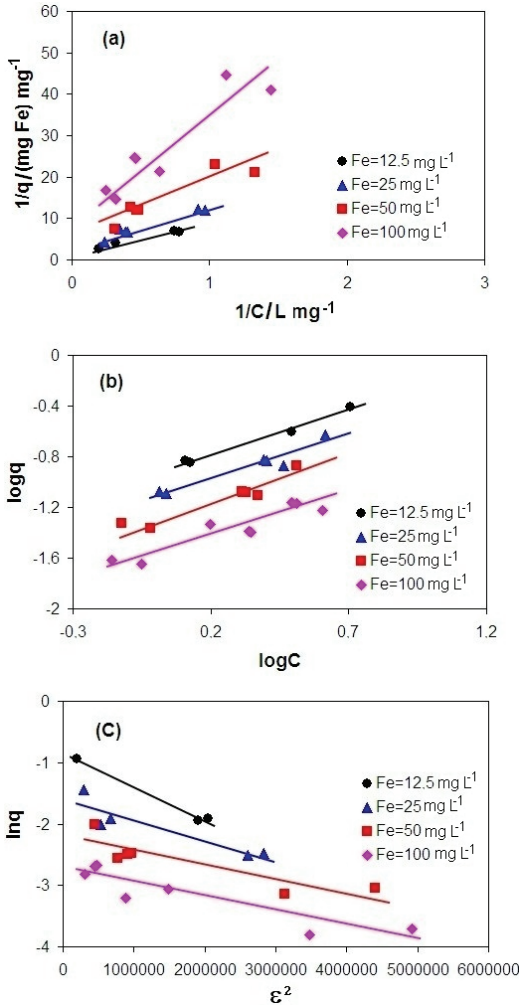

Fig. 4. Experimental data on the sorption of nickel ions by the precipitate of iron(III) hydroxide forming in the solution during the coagulation process at pH 7 in the coordinates of Eqs.: a – (4); b – (5); c – (7).

A comparison of the correlation coefficients of equations (2), (3) and (6) (see Table I) shows that they are very close to each other and have relatively high values. In general, all three classical isotherms describe with satisfactory accuracy the sorption of nickel ions by the formed precipitate of iron(III) hydroxide during its precipitation from an $FeSO_4$ solution. From a comparison of the sorption capacities of iron(III) hydroxide precipitates with respect to nickel ions calculated using

the Langmuir and Dubinin–Radushkevich equations, it can be seen that calculations using the Dubinin–Radushkevich isotherm give approximately twofold lower values. With an increase in the initial concentration of iron(II) ions in the solution, the sorption capacity of the resulting iron(III) hydroxide precipitates changes. This indirectly confirms the previously made conclusion about the dependence of the specific surface area of the precipitates on the initial concentration of iron(II) ions in the solution. In this case, there is a decrease in the specific surface area of the precipitates due, apparently, to the aggregation (coagulation) of their particles. It is clear that in this case, the surfaces of the primary iron(III) hydroxide particles overlap internally in the aggregates and part of their surface inside the aggregates becomes inaccessible to the solution. This leads to a decrease in the specific surface area of such an aggregated precipitate.

TABLE I. Parameters of the Langmuir, Freundlich and Dubinin–Radushkevich equations for the sorption of nickel ions on the forming precipitate of iron(III) hydroxide at pH 7 and different initial concentrations of iron(II) ions in the model solution. R is the correlation coefficient

Initial concentrations of iron(II) ions, mg L^{-1}	12.5	25	50	100
Langmuir constants				
q_∞ / mg (mg Fe)$^{-1}$	0.730	0.352	0.181	0.105
K_L / L mg^{-1}	0.189	0.289	0.407	0.383
R	0.990	0.971	0.928	0.920
Freundlich constants				
K_F	0.119	0.078	0.050	0.028
n	1.407	1.455	1.433	1.452
R	0.994	0.962	0.948	0.933
Dubinin–Radushkevich constants				
q_∞ / mg (mg Fe)$^{-1}$	0.438	0.199	0.109	0.065
E / kJ mol^{-1}	0.913	1.291	1.581	1.581
R	0.995	0.913	0.874	0.915

In addition to a decrease in q_∞ with an increase in C_{Fe}, there is also a change in the value of the adsorption equilibrium constant K_L, namely, its growth. This may be due to a change in the surface state of the iron(III) hydroxide precipitate during coagulation (aggregation) of its particles.

The values of the free energy of adsorption (E) calculated by the Dubinin–Radushkevich equation do not exceed 8 kJ mol^{-1} (see Table I). This indicates the physical nature of adsorption and excludes ion-exchange interaction of nickel ions with iron(III) hydroxide.

Coagulation removal of nickel ions at pH 8

The changes in the residual concentrations of nickel ions in the model solution during the coagulation process using $FeSO_4$ at pH 8 are shown in Fig. 5a. As can be seen, in this case, as at pH 7, a regular decrease in the residual concentration of

nickel ions in the solution is observed with an increase in the concentration of iron(II) ions introduced into the solution at the beginning of the experiment. In other words, the concentration of nickel ions in the solution decreases as the concentration of the formed iron(III) hydroxide precipitate increases. In this case, a deeper purification of the solution from nickel ions occurs. For example, if at pH 7 and an initial concentration of nickel ions in the solution of 10 mg L^{-1}, the residual concentration of its ions in the solution at C_{Fe} = 100 mg L^{-1} was 3.12–4.02 mg L^{-1} (Fig. 2a), then at pH 8 under the same experimental conditions C = 0.24–0.25 mg L^{-1} (Fig. 5a). Similarly, if at pH 7, C_{Fe} = 100 mg L^{-1} and an initial concentration of nickel ions in the solution of 6.25 mg L^{-1}, the residual concentration of nickel ions in the solution was 1.57–2.17 mg L^{-1} (Fig. 2a), then at pH 8 under the same experimental conditions, C = 0.15 mg L^{-1} (Fig. 5a).

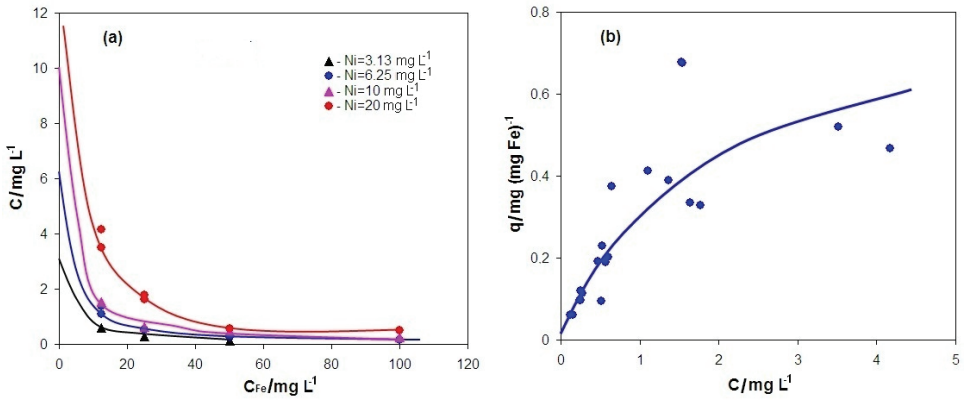

Fig. 5. Effect of the initial concentration of iron(II) ions in the model solution on the residual concentration of nickel ions in it at pH 8 (a) and the sorption isotherm of nickel ions on the formed precipitate of iron(III) hydroxide at pH 8 (b).

The sorption isotherm for nickel ions on the iron(III) hydroxide precipitate formed at pH 8, derived from the data in Fig. 5a, is shown in Fig. 5b. It is evident that there is a significant spread of experimental points; however, they all align along the same curve, which can be classified as a typical L-type isotherm.[26] Notably, there is no stratification of the sorption isotherm into multiple independent curves, as observed at pH 7 (Fig. 2b). This is likely because, at pH 8, the coagulation of iron(III) hydroxide particles is less pronounced and remains relatively consistent across all values of C_{Fe}. Consequently, the resulting precipitates exhibit nearly the same specific surface area.

The results of processing the experimental data in the coordinates of Eqs. (4), (5) and (7) are shown in Fig. 6. The corresponding parameters of Eqs. (2), (3) and (6) calculated from the experimental data are given in Table II.

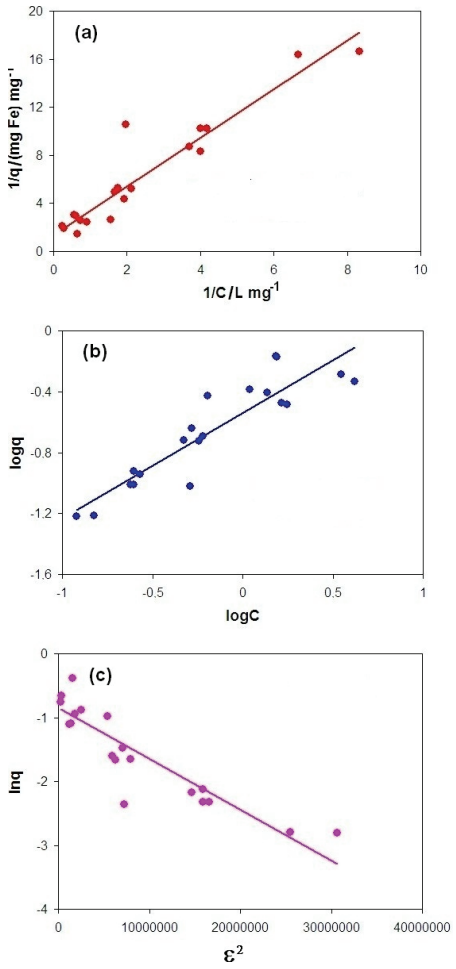

Fig. 6. Experimental data on the sorption of nickel ions by the precipitate of iron(III) hydroxide forming in the solution during the coagulation process at pH 8 in the coordinates of Eqs.: a – (4); b – (5); c – (7).

TABLE II. Parameters of the Langmuir, Freundlich and Dubinin–Radushkevich equations for the sorption of nickel ions on the forming precipitate of iron(III) hydroxide at pH 8

Langmuir constants	
q_∞ / mg (mg Fe)$^{-1}$	0.727
K_L / L mg^{-1}	0.680
R	0.948
Freundlich constants	
K_F	0.288
n	1.439
R	0.905
Dubinin–Radushkevich constants	
q_∞ / mg (mg Fe)$^{-1}$	0.438
E / kJ mol^{-1}	0.913
R	0.995

Analysis of the results presented in Table II shows that the same patterns are observed here as in the sorption at pH 7 (see Table I). At the same time, all three classical isotherms (Langmuir, Freundlich and Dubinin–Radushkevich) describe with satisfactory accuracy the sorption of nickel ions by the resulting precipitate of iron(III) hydroxide during its precipitation from an $FeSO_4$ solution. This is evidenced by the fairly high correlation coefficients. Comparison of the sorption capacities of iron(III) hydroxide precipitates with respect to nickel ions, calculated using the Langmuir and Dubinin–Radushkevich equations, shows that here, as at pH 7, calculation using the Dubinin–Radushkevich isotherm yields approximately twofold smaller q_∞ values. The value of the free energy of adsorption (E) calculated by the Dubinin–Radushkevich equation, as well as at pH 7, does not exceed 8 kJ mol^{-1} (Table II). This indicates that in this case, adsorption also has a physical nature.

It is interesting to compare these results with the findings from the study in reference,[19] which also investigated the sorption of nickel ions by the precipitate of iron(III) hydroxide formed during precipitation from $FeCl_3$ solutions at pH 7 and 8. A key difference from the previous work is that no stratification of sorption isotherms was observed at either pH 7 or 8, unlike the results found in this study at pH 7. This suggests that the specific surface area of the formed iron(III) hydroxide precipitates in reference[19] did not depend on the initial concentration of iron(III) ions in the solution.

The exponents of the Freundlich equation found in[19] are close to those determined in this work (Tables I and II). The values of K_F also have similar magnitudes. A comparison of the parameters of the Langmuir equation shows that the adsorption equilibrium constants defined in[19] exceed the similar values found in this work (Tables I and II), whereas the sorption capacities, on the contrary, have lower values. All this may indicate differences in the structure of the formed iron(III) hydroxide precipitates and their different general (gross) formulas.

Thus, the data obtained indicate that the iron(III) hydroxide precipitate formed in the solution during hydrolysis of the $FeSO_4$ coagulant is a highly effective sorbent for removing toxic nickel ions from a contaminated solution. Its sorption capacity for nickel ions at pH 8 is 0.727 mg per 1 mg of iron(II) ions introduced into the solution (0.727 mg (mg Fe)$^{-1}$), and at pH 7 it depends on the initial concentration of the coagulant in the solution and is in the range of 0.105–0.730 mg (mg Fe)$^{-1}$. This is about an order of magnitude higher than the same value for many mineral, carbon and coal sorbents.[3–13]

As noted above, a similar study was previously conducted with the coagulant $FeCl_3$.[19] A high sorption capacity of the formed iron(III) hydroxide precipitate with respect to nickel ions was also found there. In this regard, it is unclear which coagulant ($FeSO_4$ or $FeCl_3$) is preferable for the purification of contaminated solutions from nickel ions. A simple comparison of adsorption capacities does not

allow one to make such a choice, since it is also necessary to take into account the values of the adsorption equilibrium constants. For such a comparative assessment, the Langmuir equation may be useful, which, after transformations, takes the form:[25]

$$C = \frac{1}{2K_L}(-b + \sqrt{b^2 + 4K_L C_{in}}) \quad (10)$$

where $b = 1 - K_L C_{in} + q_\infty K_L C_{Fe}$.

Formula (10) allows one to calculate the residual concentration of the adsorbed substance (in this case, nickel ions) in the solution depending on the initial concentration of iron ions in it and the parameters of the Langmuir equation. The results of comparative calculations using this equation for pH 7 and 8 and an initial concentration of nickel ions in the solution of 10 mg L^{-1}, according to Tables I and II, as well as the works,[19] are graphically presented in Fig. 7.

Fig. 7 shows that at both pH 7 and pH 8, the use of iron(II) sulfate as a coagulant at its initial concentration in the solution (in terms of iron ions) of 0–70 mg L^{-1} leads to a deeper removal of nickel ions from the model solution compared with previously studied $FeCl_3$ coagulant. However, with an increase in the concentration of $FeSO_4$ in the solution above 70 mg L^{-1} (in terms of iron ions), the effectiveness of this coagulant decreases, and in this case the $FeCl_3$ coagulant already removes nickel ions from the solution more effectively.

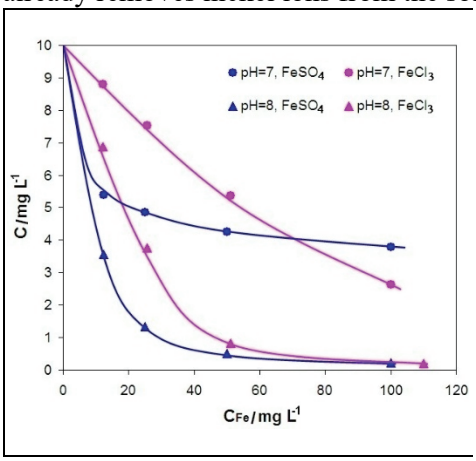

Fig. 7. Calculated change in the residual concentration of nickel ions in the model solution during its adsorption on iron(III) hydroxide precipitates formed at pH 7 and 8 using $FeSO_4$ and $FeCl_3$ coagulants.

CONCLUSION

The use of iron(II) sulfate ($FeSO_4$) as a coagulant enables the removal of not only insoluble impurities from contaminated solutions, but also toxic nickel ions. The removal of nickel ions by the iron(III) hydroxide precipitate formed during coagulation is most effective at pH 8. The sorption of nickel ions onto this precipitate is accurately described by the classical Langmuir, Freundlich and Dubinin–Radushkevich isotherms. The free energy of adsorption, calculated using the

Dubinin–Radushkevich equation, does not exceed 8 kJ mol^{-1}, indicating a physical nature of the adsorption process and ruling out ion–exchange interactions between nickel ions and iron(III) hydroxide. At pH 8, the sorption capacity of the resulting iron(III) hydroxide precipitate for nickel ions is 0.727 mg per 1 mg of Fe^{2+} introduced into the solution (0.727 mg (mg Fe)$^{-1}$). At pH 7, the sorption capacity depends on the coagulant concentration in the solution and ranges from 0.105 to 0.730 mg (mg Fe)$^{-1}$. A comparison between $FeSO_4$ and the previously studied $FeCl_3$ coagulant shows that $FeSO_4$ is more effective at removing nickel ions when the initial concentration of iron ions in the solution is below 70 mg L^{-1}. However, at higher initial concentrations of iron, $FeCl_3$ demonstrates greater removal efficiency.

Acknowledgements. This work was carried out in accordance with the assignment by the Ministry of Science and Higher Education of the Russian Federation (theme No. 124020600024-5) and also supported by Government of the Sverdlovsk region and the grant of Russian Fund for Basic Research (Project No. 20-48-660038).

И З В О Д

УКЛАЊАЊЕ НИКЛА(II) ЈОНА ТОКОМ ПРЕЧИШЋАВАЊА ВОДЕ ГВОЖЂЕ(II)-СУЛФАТОМ. 1. ДЕО. МЕХАНИЗАМ И ЕФИКАСНОСТ ПРОЦЕСА

OLEG D. LINNIKOV и IRINA V. RODINA

Institute of Solid State Chemistry, Ural Branch of the Russian Academy of Sciences, Pervomayskaya St., 91, 620990, Ekaterinburg, Russia

Пречишћавање природних и отпадних вода уклањањем јона никла је од велике важности за животну средину и здравље људи због њихове високе токсичности. Циљ овог рада био је испитивање могућности уклањања јона никла из контаминираних водених раствора помоћу коагуланта $FeSO_4$. Показано је да се уклањање јона никла из воденог раствора путем преципитата са гвожђе(III) хидроксидом, који настаје коагулацијом на pH 7 и 8, може успешно описати класичним адсорпционим изотермама, и то Ленгмир, Фројндлих и Дубинин–Радушкевич моделима. Вредности слободне енергије адсорпције израчунате на основу Дубинин–Радушкевичеве једначине не прелазе 8 kJ mol^{-1}, што указује на физичку природу адсорпције и искључује јоноизмењивачку интеракцију између јона никла и гвожђе(III)-хидроксида. Капацитет сорпције добијеног преципитата гвожђе(III)-хидроксида за јоне никла на pH 8 је 0,727 mg по 1 mg гвожђе(II) јона додатих у раствор, а на pH 7 зависи од почетне концентрације коагуланта у раствору и налази се у опсегу 0,105-0,730 mg (mg Fe)$^{-1}$. Поређење коагуланата $FeSO_4$ и раније испитиваног коагуланта $FeCl_3$ показује да при почетној концентрацији јона гвожђа у раствору мањој од 70 mg L^{-1}, $FeSO_4$ коагулант ефикасније уклања јоне никла. Међутим, при већим полазним концентрацијама гвожђа ефикаснији је $FeCl_3$.

(Примљено 7. априла, ревидирано 5. маја, прихваћено 30. октобра 2025)

REFERENCES

1. *Monographs on the Evaluation of the Carcinogenic Risks to Humans: Chromium, Nickel and Welding*, Vol. 49, IARC, Lyon, 1990
2. K. Salnikow, A. Zhitkovich, *Chem. Res. Tox.* **21** (2008) 28 (http://doi.org/10.1021/tx700198a)

3. M. K. Uddin, *Chem. Eng. J.* **308** (2017) 438 (http://dx.doi.org/10.1016/j.cej.2016.09.029)
4. M. Abbasi, E. Safari, M. Baghadi, M. Janmohammadi, *J. Water Proc. Eng.* **40** (2021) 101961 (http://doi.org/10.1016/j.jwpe.2021.101961)
5. R. Donat, A. Akdogan, E. Erdem, H. Cetisli, *J. Col. Interf. Sci.* **286** (2005) 43 (https://doi.org/10.1016/j.jcis.2005.01.045)
6. Md. A. Islam, Md. R. Awual, M. J. Angove, *J. Env. Chem. Eng.* **7** (2019) 103305 (http://doi.org/10.1016/j.jece.2019.103305)
7. S. Kolluru, S. Agarwal, S. Sireesha, I. Sreedhar, S. R. Kale, *Proc. Saf. Environ. Prot.* **150** (2021) 323 (http://doi.org/10.1016/j.psep.2021.04.025)
8. V. N. Krasil'nikov, O. D. Linnikov, O. I. Gyrdasova, I. V. Rodina, A. P. Tyutyunnik, I. V. Baklanova, E. V. Polyakov, N. A. Khlebnikov, N. V. Tarakina, *Solid State Sci.* **108** (2020) 106429 (https://doi.org/10.1016/j.solidstatesciences.2020.106429)
9. O. D. Linnikov, I. V. Rodina, I. V. Baklanova, A. Yu. Suntsov, *Prot. Met. Phys. Chem. Surf.* **57**(3) (2021) 255 (https://doi.org/10.1134/S2070205121030163)
10. S. Sivrikaya, S. Albayrak, M. Imamoglu, A. Gundogdu, C. Duran, H. Yildiz, *Desal. Water Treat.* **50** (2012) 2 (https://doi.org/10.1080/19443994.2012.708234)
11. M. Vakili, M. Rafatullah, J. Yuan, H. M. Zwain, A. Mojiri, F. Gholami, W. Wang, A. S. Giwa, Y. Yu, G. Cagnetta, G. Yu, *Rev. Chem. Eng.* **37**(6) (2021) 755 (https://doi.org/10.1515/revce-2019-0047)
12. S. Yang, J. Li, D. Shao, J. Hu, X. Wang, *J. Haz. Mat.* **166** (2009) 109 (https://doi.org/10.1016/j.jhazmat.2008.11.003)
13. S. S. Lazarević, I. M. Janković-Častvan, B. M. Jokić, D. T. Janaćković, R. D. Petrović, *J. Serb. Chem. Soc.* **81**(2) (2016) 197 (https://doi.org/10.2298/JSC150525086L)
14. P. D. Johnson, P. Girinathannair, K. N. Ohlinger, S. Ritchie, L. Teuber, J. Kirby, *Water Env. Res.* **80**(5) (2008) 472 (http://doi.org/10.2175/106143007X221490)
15. M. A. Inam, R. Khan, K-H. Lee, Y-M. Wie, *Int. J. Env. Res. Pub. Health* **18** (2021) 9812 (https://doi.org/10.3390/ijerph18189812)
16. Z. Wu, M. He, X. Guo, R. Zhou, *Sep. Pur. Techn.* **76** (2010) 184 (https://doi.org/10.1016/j.seppur.2010.10.006)
17. A. J. Hargreaves, P. Vale, J. Whelan, L. Alibardi, C. Constantino, G. Dotro, E. Cartmell, P. Campo, *Clean Techn. Env. Policy* **20** (2018) 393 (http://doi.org/10.1007/s10098-017-1481-3)
18. A. H. Jagaba, S. R. M. Kutty, G. Hayder, L. Baloo, A. A. S. Ghaleb, I. M. Lawal, S. Abubakar, B. N. S. Al-dhawi, N. M. Y. Almahbashi, I. Umaru, *Ain Shams Eng. J.* **12** (2021) 57 (http://doi.org/10.1016/j.asej.2020.06.016)
19. O. D. Linnikov, I. V. Rodina, G. S. Zakharova, K. N. Mikhalev, I. V. Baklanova, Yu.V. Kuznetsova, A. Yu. Germov, B. Yu. Goloborodskii, A. P. Tyutyunnik, Z. A. Fattakhova, *Water Env. Res.* **94**(12) (2022) e10827 (https://doi.org/10.1002/wer.10827)
20. Y. Deng, *Water Res.* **31**(6) (1997) 1347 (https://doi.org/10.1016/s0043-1354(96)00388-0)
21. M. Kiyama, T. Takada, *Bull. Chem. Soc. Japan* **45** (1972) 1923
22. R. R. Kleshcheva, D. A. Zherebtsov, V. Sh. Mirasov, D. G. Kleshchev, *Bull. South Ural State Univ.* **1** (2012) 17
23. T. Misawa, K. Yashimoto, S. Shimodaira, *Corr. Sci.* **14** (1974) 131
24. Yu. V. Novikov, K. O. Lastochkin, Z. N. Boldina, *Methods for studying the quality of water in reservoirs*, 2nd ed., Medicine, Moscow, 1990

25. O. D. Linnikov, I. V. Rodina, *Prot. Met. Phys. Chem. Surf.* **58** (2022) 1116 (https://doi.org/10.1134/S2070205122060107)
26. G. Limousin, J-P. Gauder, L. Charlet, S. Szenknect, V. Barthès, M. Krimissa, *App. Geochem.* **22** (2007) 249 (https://doi.org/10.1016/j.apgeochem.2006.09.010).

Journal of the Serbian Chemical Society
JSCS-info@shd.org.rs • www.shd.org.rs/JSCS
J. Serb. Chem. Soc. *91* (1) 55–69 (2026)
JSCS–5477
Original scientific paper
Published 5 February, 2026

Bimetallic polyaniline/silver–palladium nanocomposite for rapid and sustainable degradation of eosin yellow dye from wastewater

NOOR ZAMAN[1], FARAH NAZ TALPUR[1], ABDUL QADEER LAGHARI[2]*, JAMEEL BAIG[1], ARSHAD IQBAL[3], SHOUKAT ALI NOONARI[4], ZULFIQAR ALI BHATTI[2], AMANA BALOCH[1], IMRAN HASSAN AFARIDI[1] and MASROOR ABRO[2]

[1]*National center of Excellence in Analytical chemistry, University of Sindh, Jamshoro, Sindh, Pakistan,* [2]*Process Simulation and Modeling Research Group, Chemical Engineering Department, Mehran University of Engineering and Technology Jamshoro, Sindh, Pakistan,* [3]*Chemical Engineering Department, Dawood University of Engineering and Technology, Karachi, Pakistan and* [4]*Department of Mechanical Engineering, Isra University, Hyderabad, Sindh, Pakistan*

(Received 2 July, revised 14 August, accepted 1 October 2025)

Abstract: Eosin yellow (EY), a synthetic xanthene dye, is recognized for its high toxicity, posing serious threats to human health and aquatic environments. Chronic exposure to EY can result in skin irritation, respiratory disorders, and potential long-term organ damage due to its persistent and bioaccumulative nature. In this study, a polyaniline-based silver–palladium nanocomposite (PANI/Ag–Pd) was synthesized *via* the co-precipitation method and employed as an efficient nanocatalyst for the degradation of EY dye. The structural, morphological and elemental properties of the synthesized nanocomposite were characterized using UV–Vis spectroscopy, Fourier-transform infrared spectroscopy (FTIR), scanning electron microscopy (SEM) and energy-dispersive X-ray spectroscopy (EDX). The UV–Vis and FTIR analyses confirmed the formation of the PANI/Ag–Pd nanocomposite with a notable red shift, indicating electronic interaction among the constituents. SEM images demonstrated the successful incorporation of Ag and Pd nanoparticles into the PANI matrix, while EDX confirmed the elemental composition. The nanocomposite exhibited remarkable photocatalytic performance under microwave irradiation, achieving up to 96.63 % degradation of EY dye. This study highlights the potential of PANI/Ag–Pd nanocomposites as a promising nanocatalyst for water purification. These findings contribute to the development of polymer-stabilized nanomaterials as effective candidates for the remediation of dye-contaminated wastewater.

Keywords: wastewater treatment; nanocomposite; degradation; EY dye.

* Corresponding author. E-mail: abdul.qadeer@admin.muet.edu.pk
https://doi.org/10.2298/JSC250702073Z

INTRODUCTION

In recent decades, advanced materials such as nanomaterials, polymer-based systems and hybrids have attracted increasing scientific interest due to their exceptional chemical and physical properties.[1–4] Dyes are classified into azoic, reactive, vat, sulfur, acidic, basic, disperse and direct.[5] Over 10,000 commercially existing dyes and 1 Mt dyes are prepared annually, containing 50 % as a textile dye.[6] About 10 % of dyestuff is discarded after drying and processing.[7] 2 % of the dye component entered the aqueous matter and caused pollution.[8] Many are toxic and discharged into wastewater untreated, often in high concentrations.[9] Long-term usage of water-containing dyes causes severe health issues. Dyes are carcinogenic and mutagenic. These dyes have been associated with carcinogenic effects in the kidney, bladder and liver, and may also contribute to skin irritation and respiratory complications.[10,11] The cationic/anionic nature dyes leads to reduced amount of oxygen in the water, which is fatal for humans and aquatic life.[12] Several methods are being investigated for dyes removal from wastewater, like microbial-electro-fenton (MEF) technology,[13] catalytic degradation,[14] adsorption,[15] coagulation–flocculation,[16] electrochemical treatment,[17] reverse osmosis[18] and ion exchange.[19]

Among various treatment methods, advanced oxidation processes (AOPs) have shown promise.[20] Photocatalytic degradation using metals and metal oxides like Ag, Pd, TiO_2, ZnO and WO_3 has been explored,[21] often enhanced with additives like $NaBH_4$ to boost dye decolonization efficiency under sunlight.[22]

Polymers have recently emerged as promising alternatives to conventional nanomaterials due to their adjustable surface functionalities, superior mechanical strength, high surface area, uniform pore distribution and easy regeneration properties. Polymers such as polyaniline **(**PANI), polythiophene (PTh)**,** polyethyleneimine (PEI) and polypyrrole (PPy) have gained significant research interest for developing metal–polymer nanocomposites. These hybrid materials have broad applications in photocatalysis, sensing, adsorption, thermoelectric, electromagnetics and batteries, as well as electroluminescent and electromechanical systems. Among these, PANI is one of the most widely explored conductive polymers, owing to its electron-rich structure, environmental stability, low cost and ease of synthesis and processing.[23,24] Its multifunctionality has enabled its use in a broad range of technologies such as lithium-ion batteries,[25] flexible electronics,[26] anti-corrosion coatings,[27] wastewater treatment, dye removal[28] and printed electronics.[29] The PANI/Ag–Pd system offers several advantages over traditional catalysts. The conductive PANI matrix enhances electron transfer and provides high surface area for dye adsorption, while Ag and Pd nanoparticles create abundant active sites and exhibit strong catalytic synergy. This combination enables faster degradation rates, lower energy input and higher stability compared to single-metal or conventional catalysts. Additionally, the nanocom-

posite is reusable, environmentally benign, and effective under mild conditions, making it a sustainable alternative for wastewater treatment applications.

It is often used as a π-conjugated polymer base for integrating wide-bandgap semiconductors such as metal oxides and sulfides. These composites demonstrate enhanced photocatalytic, optical and photoelectric characteristic.[30] Additionally, PANI acts as a proficient electron donor and hole transporter under UV–Vis light exposure. When combined with high-bandgap metals like Ag, Fe, TiO_2 or ZnO, PANI facilitates electron excitation under photon irradiation. These photoexcited electrons transferred to the conduction band of the metal components, promoting the generation of reactive species such as superoxide ($O_2^{-\bullet}$) and hydroxyl radical ($^{\bullet}OH$) through reactions with water and oxygen, which then drive the degradation of eosin yellow (EY) dye. In addition to experimental strategies, theoretical modeling and statistical optimization are essential for developing sustainable treatment processes. Statistical and predictive modeling approaches, such as response surface methodology (RSM), enable systematic evaluation of multiple operating variables, reduce experimental effort and predict interactions that are often overlooked in conventional one-variable-at-a-time studies. By optimizing key parameters, RSM ensures maximum degradation efficiency under practical conditions, strengthening the reliability and scalability of nanocomposite-based wastewater remediation.

In this work, *in-situ* synthesis of a PANI/Ag–Pd nanocomposite demonstrating excellent catalytic behavior, was performed. EY degradation performance of PANI/Ag–Pd nanocomposite was investigated under different composite dose, dye dose, pH and reaction time. Subsequently, RSM was performed with the purpose of process optimization. PANI/Ag–Pd nanocomposite could be a potential candidate in dye removal process owing to its easy synthesis, low production cost and high degradation efficiency.

EXPERIMENTAL

Chemicals and reagents

All the laboratory grade chemicals, glassware and other items were bought from Sigma Aldrich. Aniline (99.95 %) was used as precursor to synthesize for polyaniline polymer. Hydrazine (98 %) was used as strong reducing agent as facilitator for synthesis of silver–palladium nanoparticles. Silver nitrate (99.8 %) and palladium(II) chloride, (99.999 %) were used for synthesis for silver–palladium nanoparticles. Ammonium persulfate (98 %) was used as strong oxidizing agent as facilitator for synthesis of PANI/Ag–Pd nanocomposite. Sulfuric acid (98 %) was added as a proton source to form the conductive emeraldine salt of polyaniline, while protonated aniline exhibits a higher oxidation potential than neutral aniline, thus delaying the onset of polymerization**.** Eosin yellow (EY) dye (99 %) was used as degradation agent. Sodium borohydride (98 %) was used to donate hydrogen atoms (or electrons), breaking down the dye molecules into less harmful by products.

Synthesis of PANI/Ag–Pd

PANI was synthesized by dissolving 1.86 mL of aniline in 200 mL of 0.1 M H_2SO_4, followed by the dropwise addition of 10 mL of 5 M APS and stirring for 8 h at room temperature. The product was filtered, washed with de-ionized water and dried. For the PANI/ /Ag–Pd nanocomposite, 1 mL of 0.02 M $AgNO_3$ was mixed with 2 mL of 0.062 M hydrazine and stirred at 60 °C for 5 min. Then, 50 mL of 0.035 M $PdCl_2$ was added and stirred for 45 min. Finally, 10 mL of the Ag–Pd solution was mixed with 0.05 g PANI and 10 mL APS, followed by filtration, washing with de-ionized water and vacuum drying at 60 °C for 12 h.

EY dye degradation

The degradation of EY dye was evaluated by monitoring the decrease in its characteristic absorbance peak using a UV–Vis spectrophotometer (Jasco V-530 UV–Vis spectrophotometer) in the range of 350–800 nm. Pure dimethylformamide (DMF) was used as the blank solvent to eliminate background interference. Absorbance was converted into concentration using a calibration curve as suggested in a previous study.[31] Degradation efficiency was calculated from the relative decrease in absorbance with time according to Eq. (1). It was assessed under varying experimental conditions, including pH 1–11, nanocomposite dose, 0.5–1.5 mg/L, initial EY dye concentration, 3–12 mg/L, and reaction time, 5–15 s. The selected pH range is closely reported in previously published data, to study its significance:[32,33]

$$\text{EY dye degradation} = 100\frac{c_0 - c_e}{c_e} \tag{1}$$

where c_0 and c_e are initial and equilibrium EY dye concentrations (mg/L).

Characterization

The FTIR analysis of the PANI/Ag–Pd nanocomposite, mixed with KBr and pressed into pellets, was carried out using a Shimadzu 8400S (Japan) spectrometer. The measurements were taken within the wavenumber range from 4000 to 400 cm^{-1}, with a resolution of 4 cm^{-1}, to identify the functional groups present in the nanocomposite. Additionally, the surface morphology, particle size and elemental composition of the synthesized PANI/Ag–Pd nanocomposite were analyzed using a scanning electron microscope (SEM) equipped with an energy dispersive X-ray (EDX) system.

Experiments design

RSM was employed to assess the individual and interactive effects of four variables, *A* (pH), *B* (composite dose), *C* (EY concentration) and *D* (reaction time) on degradation efficiency using a bimetallic polyaniline/Ag–Pd nanocomposite. A central composite design (CCD) was applied to construct a three-level matrix with factors coded as –1 (low) and +1 (high). Variable levels are detailed in Table I.

TABLE I. Level of parameters for central composite design (CCD)

Variable	Symbol	Level	
		Low (–1)	High (1)
Dose of composite, mg/L	*A*	0.5	1.5
Dose of dye, mg/L	*B*	3	12
pH	*C*	1	11
Time, s	*D*	5	15

The response analysis was performed using Design Expert 13 through a regression-based approach. The main influences of the input variables are denoted as *A*, *B*, *C* and *D*, while their combined or interaction effects are represented by terms such as *AB*, *AC*, *AD*, *BC*, *BD* and *CD*, along with the quadratic components A^2 and B^2. The relationship between the variables and the response was modeled using a second-order polynomial equation:

$$Y = a_0 + \sum_{i=1}^{n} a_i X_i + \sum_{i=1}^{n} a_{ii} X_i^2 + \sum_{j=i+1}^{n} a_{ij} X_i X_j \quad (2)$$

Where Y is predicted response, X_i are independent variables, a_0 is constant (intercept), a_i are linear coefficients, a_{ii} are quadratic coefficients (squared terms) and a_{ij} are interaction coefficients (cross-product terms).

After each run, final concentration of EY dye was determined in order to find out the degradation in %.

RESULTS AND DISCUSSION

UV–Vis spectral analysis

The UV–Vis spectra (Fig. 1) reveal key optical features of pure PANI and the PANI/Ag–Pd nanocomposite. Pure PANI shows peaks at 283 and 342 nm, indicating its doped state. In the composite, the π–π* peak shifts to 293 nm and a new band at ~425 nm appears, attributed to Ag/Pd surface plasmon resonance. These changes confirm nanoparticle incorporation and improved optical properties, supporting its photocatalytic potential.

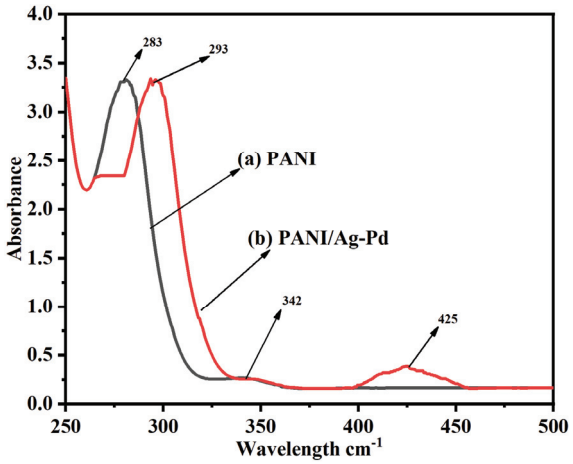

Fig. 1. UV–Vis analysis of: a) PANI and b) PANI/Ag–Pd.

FTIR analysis

The FTIR spectrum illustrates the structural differences between pure polyaniline (PANI) and the PANI/Ag–Pd nanocomposite, as shown in Fig. 2. The "a" spectrum corresponds to PANI, exhibiting characteristic peaks associated with its chemical structure. Notably, peaks in the ranges 1560–1580 and 1480–1500 cm^{-1}

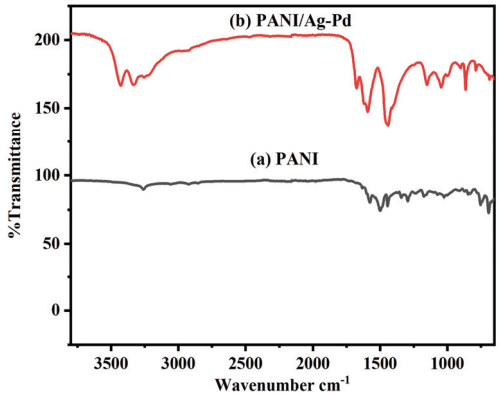

Fig. 2. FTIR analysis of: a) PANI/Ag–Pd and b) PANI.

are associated with the C=C stretching vibrations of the quinoid and benzenoid structures in the polymer chain. The absorption band close to 1300 cm^{-1} is attributed to C–N stretching, while the signal near 1140 cm^{-1} corresponds to the in-plane bending of aromatic C–H bonds, which is commonly connected to the electrical conductivity characteristics of PANI. In contrast, the "b" spectrum represents the PANI/Ag–Pd nanocomposite, which shows noticeable shifts in peak positions and variations in intensity, particularly in the 1500–1000 cm^{-1} region. These changes suggest strong interactions between the polyaniline matrix and the incorporated silver–palladium nanoparticles, likely through coordination with nitrogen atoms in the PANI backbone. The appearance of a broader peak near 3400 cm^{-1} may be attributed to N–H stretching or adsorbed water molecules. Overall, the spectral modifications confirm the successful incorporation of Ag–Pd nanoparticles into the PANI structure, potentially enhancing the composite's physicochemical properties for applications such as dye removal or catalytic activity.

Surface morphology characterization

SEM was employed for the measurement of surface morphology of PANI/Ag–Pd nanocomposite. The SEM images were taken at low and high resolution. These SEM images are shown in Fig. 3a and b at low and high resolutions. The

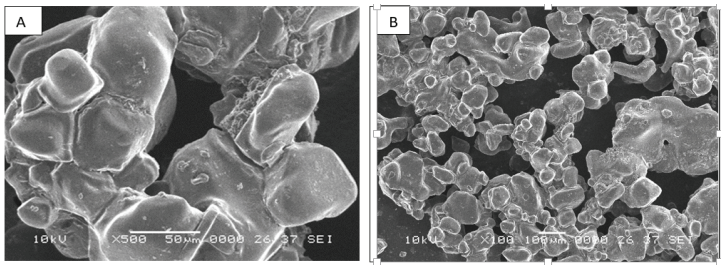

Fig. 3. The SEM images of: a) PANI and b) PANI/Ag–Pd.

SEM shows that structure of PANI/Ag–Pd nanocomposite is semi-cubical and white dots are present due to the presence of PANI/Ag–Pd nanocomposite. According to image, the silver and palladium particle were finely distributed within the PANI matrix, although some accumulation and agglomeration were observed in certain area.

EDX analysis

EDX analysis (Fig. 4) was employed to verify the elemental composition of the PANI/Ag–Pd nanocomposite. The spectrum displays distinct peaks corresponding to carbon, nitrogen and oxygen elements associated with the PANI matrix. Additionally, the presence of characteristic peaks for silver and palladium confirms the successful incorporation of metal nanoparticles into the composite structure in K-shell with 1.99, 1.86 and 33.97 %, respectively. Silver and palladium were found in L-shell with 49.93 and 12.23 %.

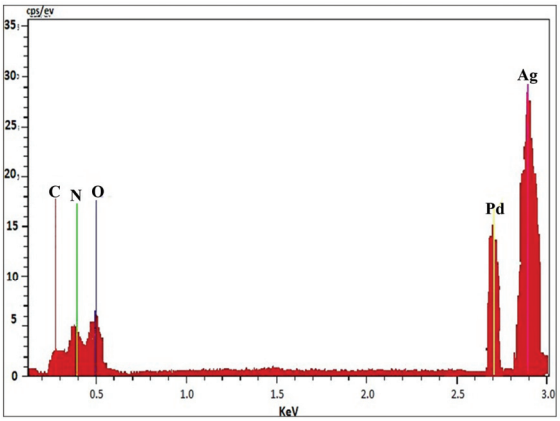

Fig. 4. EDX analysis of PANI/Ag–Pd nanocomposite.

EY dye degradation

A comparative parametric analysis was conducted to evaluate the effectiveness of various factors (pH, nanocomposite dose, initial dye concentration and reaction time) influencing the degradation of the EY dye using a PANI/Ag–Pd. The progressive degradation of the dye in the presence of PANI/Ag–Pd and $NaBH_4$ was monitored *via* UV–Vis spectroscopy, as illustrated in Fig. 5. The characteristic absorbance peak at approximately 336 nm exhibited a sharp decline with increasing reaction time, indicating a rapid reduction in dye concentration. At 5 s, the spectrum displayed the highest absorbance, corresponding to the initial dye concentration. Subsequent measurements at 10 s, showed a significant decrease in peak intensity, while the peak was almost diminished at 15 s, indicating almost total degradation. This continuous absorbance reduction witnesses

that UV–Vis spectroscopy effectively captured the real-time degradation behavior and highlights the efficiency of the PANI/Ag–Pd–$NaBH_4$ system, achieving most of dye removal within 15 s.

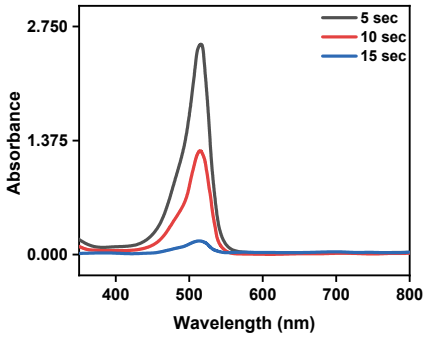

Fig. 5. UV–Vis spectra of dye degradation.

Experimental results revealed that a maximum degradation efficiency of 96.63 % was achieved under optimal conditions: pH 5.8, nanocomposite dose, 500 μg/L, initial EY dye concentration, 900 μg/L, and reaction time, 15 s; this was expected, as the integration of Ag–Pd enhances the availability of active binding sites, thereby improving the degradation efficiency.

Response surface model results

ANOVA and regression model results regression analysis was performed to predict EY dye degradation, considering factors *A*, *B*, *C* and *D*, along with their interactions (*AB*, *AC*, *AD*, *BC*, *BD*, *CD*), as summarized in Table II. The resulting equations show that positive coefficients indicate synergistic effects, while neg-

TABLE II. ANOVA for cubic model (response: EY dye degradation, %)

Source	Sum of squares	*Df*	Mean square	*F*-value	*p*-value	Significance
Model	16337.89	14	1166.99	102.39	< 0.0001	Significant
A-Dose of composite	85.97	1	85.97	7.54	0.0177	
B-Dose of EY	68.31	1	68.31	5.99	0.0307	
C-pH	2917.47	1	2917.47	255.96	< 0.0001	
D-Time	368.81	1	368.81	32.36	0.0001	
AB	0.0000	1	0.0000	0.0000	1.0000	
AC	123.19	1	123.19	10.81	0.0065	
AD	2.00	1	2.00	0.1756	0.6826	
BC	16.70	1	16.70	1.47	0.2494	
BD	7.428E-06	1	7.428E-06	6.517E-07	0.9994	
CD	361.48	1	361.48	31.71	0.0001	
A^2	127.14	1	127.14	11.15	0.0059	
B^2	13.58	1	13.58	1.19	0.2964	
C^2	10061.46	1	10061.46	882.74	< 0.0001	
D^2	204.33	1	204.33	17.93	0.0012	

ative ones suggest antagonistic impacts. These effects were analyzed to evaluate their influence on the model.

ANOVA for cubic model

The model demonstrates strong statistical significance, as indicated by a high *F*-value of 102.39 and a minimal probability (0.01 %), that this outcome is due to random variation. Variables *A*, *B*, *C* and *D*, as well as the interactions *AC*, *CD*, and the quadratic terms A^2, C^2 and D^2, significantly affect the response ($p < 0.0500$). In contrast, terms with *p*-values above 0.1000 are considered statistically insignificant. Removing these non-significant terms while maintaining model hierarchy can improve model performance. Additionally, the lack of fit test produced an *F*-value of 1.15 with a 41.59 % probability, suggesting it is not statistically significant relative to pure error.

In the Table III the predicted R^2 of 0.9482 is in reasonable agreement with the adjusted R^2 of 0.9920; *i.e.*, the difference is less than 0.2. This demonstrates a reasonable correlation between experimental and predicted results of EY dye degradation.

TABLE III. Regression model equation for response against factors and their interaction

Regression model equation	R^2	Adjusted R^2
EY dye degradation (%) = $98.90 - 2.61A - 2.50B + 26.74C - 11.10D + 0.0000AB + 3.37AC - 0.4868AD + 1.25BC + 0.0010BD + 11.13CD - 7.16A^2 + 1.09B^2 - 29.33C^2 - 11.52D^2$	0.9917	0.9820

Response contour plots

Fig. 6 presents contour plots from RSM analysis, showing the interaction effects of key variables on EY dye degradation (%). Each plot illustrates the combined impact of two factors while keeping others constant. A color gradient from blue to red indicates increasing degradation efficiency. Results show that higher composite doses and lower pH levels significantly enhance degradation due to more active sites and increased •OH generation. In contrast, higher dye concentrations reduce efficiency.

Performance evaluation of model

Performance of model was evaluated by predicted vs. actual plot which visual representation of a model's accuracy, commonly used in regression analysis and machine learning to assess predictive performance.

In Fig. 7 the data points in this plot closely align with the diagonal line, indicating that the model has high accuracy and reliability in predicting EY dye degradation. The smooth color gradient suggests a well-fitted model without significant fluctuations and provides strong predictive performance for EY dye degradation.

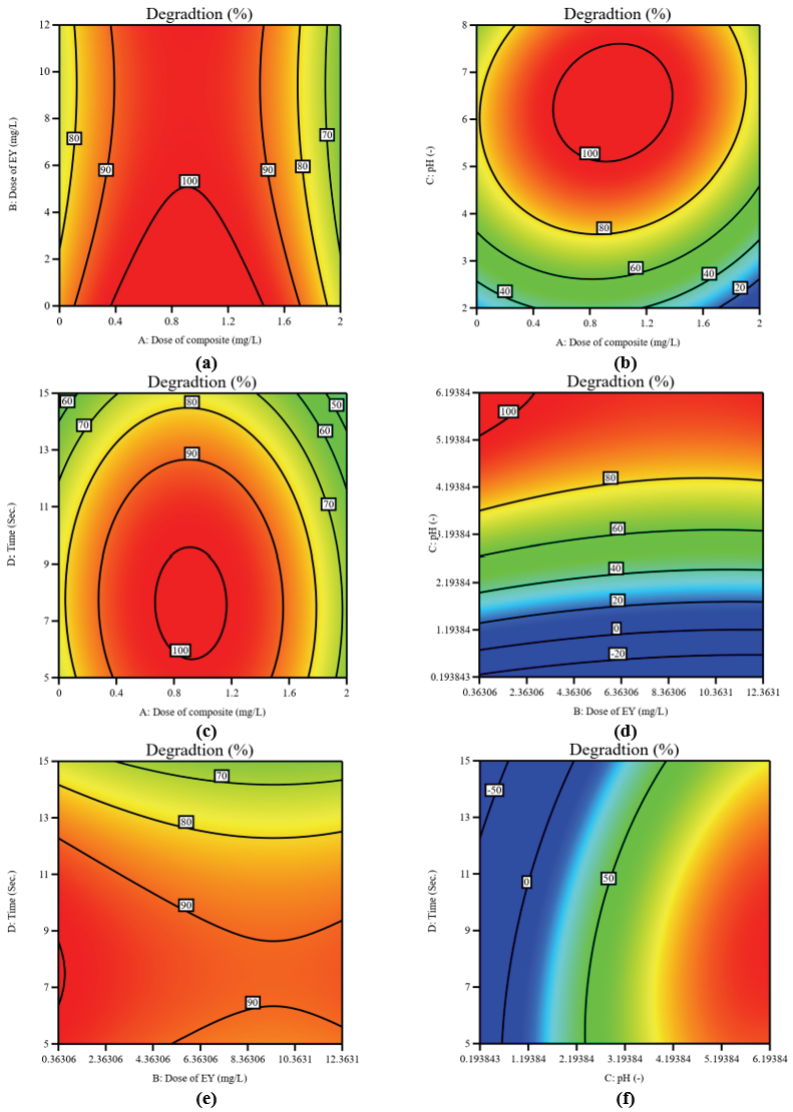

Fig. 6. Contour plots of performance evaluation: a) dose of composite and dose of EY, b) dose of composite and pH, c) dose of composite and time, d) dose of EYand time, e) Dose of EY and time and f) pH and time.

Optimization of exponential parameters

Fig. 8 presents the optimized conditions for maximizing EY dye degradation using a composite, based on desirability function analysis from an RSM model. In solution 34 (out of 100), the optimal composite dose is 1.42706 mg/L and the EY concentration is 3.22423 mg/L, indicating that higher composite loading and

lower dye concentration enhance degradation. The optimal pH is 5.80, favoring dye–composite interaction, and the reaction time is short (6.01 min), showing rapid degradation. This setup achieves 99.69 % efficiency with a desirability value of 1.000, making it highly effective for wastewater treatment.

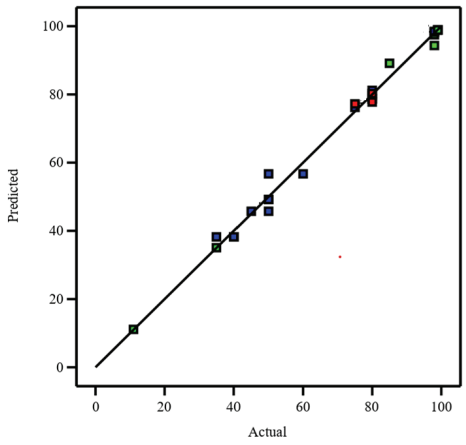

Fig. 7. Actual and predicted performance of model for EY dye degradation.

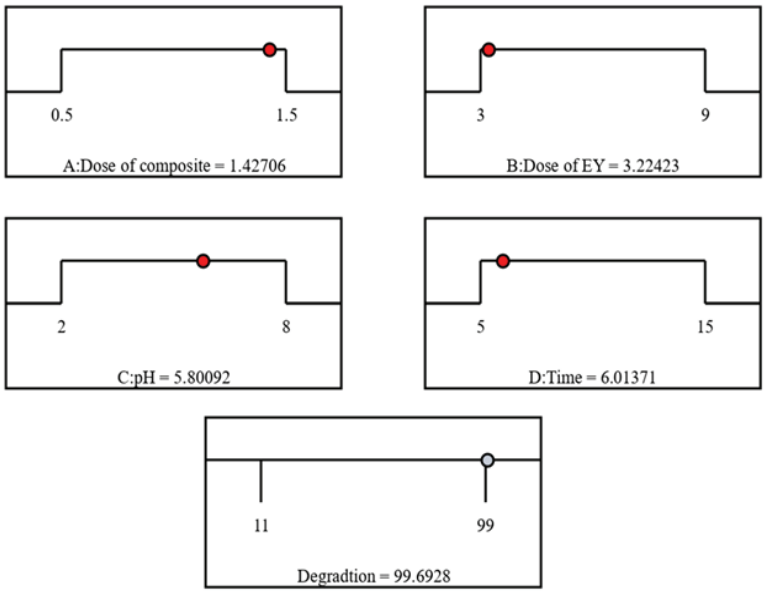

Fig. 8. Optimization of experimental parameter using PANI/Ag–Pd.

Comparison of EY dye degradation

The results of dye degradation obtained in this study are benchmarked with those reported in previous literature. This comparative analysis (summarized in

Table IV) highlights the potential of presently used PANI/Ag–Pd nanocomposite towards achieving the remarkable dye removal (96.63 %) which can be attributed to the synergistic interaction between polyaniline and bimetallic Ag–Pd nanoparticles. While previous studies demonstrated the lower degradation efficiencies ranging from 92.30 to 99 %. However, these traditional composites require high material consumption and extended processing times. In contrast, the PANI/Ag––Pd system offers a rapid, energy-efficient and environmentally sustainable solution. Its low catalyst loading and ultrafast activity highlight its potential scalability for practical wastewater treatment. Future research should examine the stability and recyclability of this nanocomposite in real effluent conditions to confirm its applicability at industrial scale.

TABLE IV. Comparison of degradation of EY dye with earlier work reported

Composite	Dose of composite, mg/L	Time s	Dye dose mg/L	Degradation %	Ref.
Poly(pyrrole-co-aniline)-coated TiO_2/nanocellulose composite (P(Py-co-An)–TiO_2/NCC)	3500	5400	23.45	92.30	[34]
New gold Salen complex doped carbon nanocomposite (Au–Salen/CC)	5000	3000	0.27	98.68	[35]
TiO_2/tetra phenyl-porphyrin sulfonic acid nanocomposite (TiO_2/TPPS)	1100	3000	10.0	99.00	[36]
PANI/Ag–Pd nanocomposite	1.42	360.6	3.0	96.63	This study

CONCLUSION

The study showed that PANI/Ag–Pd nanoparticles significantly enhance the degradation of eosin yellow (EY) dye. Characterization *via* UV–Vis, FTIR, SEM and EDX confirmed successful synthesis of the nanocomposite. Using central composite design with response surface methodology (RSM), optimal conditions 1.42706 mg/L composite dose, EY dose, 3.22423 mg/L, pH 5.80 and 6.01 min yielded 96.6 % degradation. These results highlight the nanocomposite's high catalytic efficiency and the effectiveness of RSM for process optimization in wastewater treatment. This work highlights the practical and environmental relevance of the PANI/Ag–Pd nanocomposite as a rapid, energy-efficient and sustainable material for wastewater remediation, offering a green alternative for treating dye-contaminated effluents. The ability to achieve such high degradation within seconds under mild conditions demonstrates its potential scalability for industrial applications. Future research should focus on long-term stability, recyclability, performance in real industrial wastewater and the extension of this approach to other toxic pollutants, thereby advancing the practical implement-

ation of nanocomposite-based catalytic systems in sustainable wastewater management.

ИЗВОД

БИМЕТАЛНИ ПОЛИАНИЛИН/СРЕБРО–ПАЛАДИЈУМ НАНОКОМПОЗИТ ЗА БРЗУ И ОДРЖИВУ ДЕГРАДАЦИЈУ ЕОЗИН ЖУТЕ БОЈЕ ИЗ ОТПАДНИХ ВОДА

NOOR ZAMAN[1], FARAH NAZ TALPUR[1], ABDUL QADEER LAGHARI[2], JAMEEL BAIG[1], ARSHAD IQBAL[3], SHOUKAT ALI NOONARI[4], ZULFIQAR ALI BHATTI[2], AMANA BALOCH[1], IMRAN HASSAN AFARIDI[1] и MASROOR ABRO[2]

[1]National center of Excellence in Analytical chemistry, University of Sindh, Jamshoro, Sindh, Pakistan, [2]Process Simulation and Modeling Research Group, Chemical Engineering Department, Mehran University of Engineering and Technology Jamshoro, Sindh, Pakistan, [3]Chemical Engineering Department, Dawood University of Engineering and Technology, Karachi, Pakistan и [4]Department of Mechanical Engineering, Isra University, Hyderabad, Sindh, Pakistan

Еозин жута (EY) синтетичка ксантонска боја је високо токсична, што представља озбиљну претњу људском здрављу и воденим срединама. Хронично излагање EY може довести до иритације коже, респираторних поремећаја и потенцијалног дугорочног оштећења органа због његове упорне и биоакумулативне природе. У овој студији, нанокомпозит сребра и паладијума на бази полианилина (PANI/Ag–Pd) синтетизован је методом ко-таложења и коришћен као ефикасан нанокатализатор за разградњу EY боје. Структурне, морфолошке и елементалне особине синтетизованог нанокомпозита су окарактерисане коришћењем UV–Vis спектроскопије, Фурије-трансформисане инфрацрвене спектроскопије (FTIR), скенирајуће електронске микроскопије (SEM) и енергетски дисперзивне спектроскопије X-зрака (EDX). UV–Vis и FTIR анализе су потврдиле формирање PANI/Ag–Pd нанокомпозита са значајним црвеним помаком, што указује на електронску интеракцију између састојака. SEM слике су показале успешну уградњу Ag и Pd наночестица у PANI матрицу, док је EDX потврдио је елементални састав. Нанокомпозит је показао изванредне фотокаталитичке перформансе под микроталасним зрачењем, постижући до 96,63 % деградације боје EY. Ова студија наглашава потенцијал PANI/Ag–Pd нанокомпозита као обећавајућих нанокатализатора за пречишћавање воде. Ови налази доприносе развоју наноматеријала стабилизованих полимером као ефикасних кандидата за санацију отпадних вода контаминираних бојом.

(Примљено 2. јула, ревидирано 14. августа, прихваћено 1. октобра 2025)

REFERENCES

1. M. M. Shameem, S. Sasikanth, R. Annamalai,R. G. Raman, *Mater. Today: Proc.* **45** (2021) 2536 (https://doi.org/10.1016/j.matpr.2020.11.254)
2. N. F. Alheety, A. H. Majeed,M. A. Alheety. *J. Phys.: Conf. Ser.* **1294** (2019) 052026 (https://doi.org/10.1088/1742-6596/1294/5/052026)
3. A. Kamal, M. Ashmawy, S. S, A. M. Algazzar, A. H. Elsheikh, *Proc. Inst. Mech. Eng., C* **236** (2022) 4843 (https://doi.org/10.1177/09544062211055662)
4. L. A. Adnan, N. F. Alheety, A. H. Majeed, M. A. Alheety, H. Akbaş, *Mater. Today: Proc.* **42** (2021) 2700 (https://doi.org/10.1016/j.matpr.2020.12.707)
5. S. El Harfi, A. El Harfi, *Appl. J. Environ. Eng. Sci.* **3** (2017) 311 (https://doi.org/10.48422/IMIST.PRSM/ajees-v3i3.9681)
6. P. Zarrintaj, M. K. Yazdi, H. Vahabi, P. N. Moghadam, M. R. Saeb, *Prog. Org. Coat.* **130** (2019) 144 (https://doi.org/10.1016/j.porgcoat.2019.01.053)

7. M. Berradi, R. Hsissou, M. Khudhair, M. Assouag, O. Cherkaoui, A. El Bachiri, A. El Harfi, *Heliyon* **5** (2019) e02711 (https://doi.org/10.1016/j.heliyon.2019.e02711)
8. A. Kausar, M. Iqbal, A. Javed, K. Aftab, Z.-i.-H. Nazli, H. N. Bhatti, S. Nouren, *J. Mol. Liq.* **256** (2018) 395 (https://doi.org/10.1016/j.molliq.2018.02.034)
9. E. Forgacs, T. Cserháti, G. Oros, *Environ. Int.* **30** (2004) 953 (https://doi.org/10.1016/j.envint.2004.02.001)
10. I. Ullah, A. Haider, N. Khalid, S. Ali, S. Ahmed, Y. Khan, N. Ahmed, M. Zubair, *Spectrochim. Acta, A* **204** (2018) 150 (https://doi.org/10.1016/j.saa.2018.06.046)
11. X. Muñoz, D. Clofent, M. J. Cruz, *Curr. Opin. Allergy Clin. Immunol.* **23** (2023) 70 (https://doi.org/10.1097/aci.0000000000000885)
12. S. Shahabuddin, R. Khanam, M. Khalid, N. M. Sarih, J. J. Ching, S. Mohamad, R. Saidur, *Arabian J. Chem.* **11** (2018) 1000 (https://doi.org/10.1016/j.arabjc.2018.05.004)
13. S. Rafaqat, N. Ali, C. Torres, B. Rittmann, *RSC Adv.* **12** (2022) 17104 (https://doi.org/10.1039/D2RA01831D)
14. S. Khan, T. Noor, N. Iqbal, L. Yaqoob, *ACS Omega* **9** (2024) 21751 (https://doi.org/10.1021/acsomega.4c00887)
15. S. Dutta, B. Gupta, S. K. Srivastava, A. K. Gupta, *Mater. Adv.* **2** (2021) 4497 (https://doi.org/10.1039/D1MA00354B)
16. S. Goudjil, S. Guergazi, T. Masmoudi, S. Achour, *Desalin. Water Treat.* **209** (2021) 429 (https://doi.org/10.5004/dwt.2021.26474)
17. R. Zhao, S. Zong, Q. Ma, Z. Xu, J. Yuan, *Sci. Rep.* **15** (2025) 6306 (https://doi.org/10.1038/s41598-024-75153-2)
18. T. Cui, X. Wang, Y. Chen, Y. Chen, B. Fu, Y. Tu, *Water Resour. Ind.* **30** (2023) 100217 (https://doi.org/10.1016/j.wri.2023.100217)
19. G. Zeng, X. Liu, L. Wu, Z. Meng, D. Zeng, C. Yu, *Chin. J. Struct. Chem.* **43** (2024) 100462 (https://doi.org/10.1016/j.cjsc.2024.100462)
20. F. J. Benitez, J. L. Acero, F. J. Real, *J. Hazard. Mater.* **89** (2002) 51 (https://doi.org/10.1016/S0304-3894(01)00300-4)
21. K. Rajeshwar, M. Osugi, W. Chanmanee, C. Chenthamarakshan, M. V. B. Zanoni, P. Kajitvichyanukul,R. Krishnan-Ayer, *J. Photochem. Photobiol., C* **9** (2008) 171 (https://doi.org/10.1016/j.jphotochemrev.2008.09.001)
22. V. K. Gupta, R. Saravanan, S. Agarwal, F. Gracia, M. M. Khan, J. Qin, R. V. Mangalaraja, *J. Mol. Liq.* **232** (2017) 423 (https://doi.org/10.1016/j.molliq.2017.02.095)
23. A. H. Majeed, L. A. Mohammed, O. G. Hammoodi, S. Sehgal, M. A. Alheety, K. K. Saxena, S. A. Dadoosh, I. K. Mohammed, M. M. Jasim, N. U. Salmaan, *Int. J. Polym. Sci.* **2022** (2022) 9047554 (https://doi.org/10.1155/2022/9047554)
24. J. Luo, S. Jiang, R. Liu, Y. Zhang, X. Liu, *Electrochim. Acta* **96** (2013) 103 (https://doi.org/10.1016/j.electacta.2013.02.072)
25. M. Deyab, G. Mele, E. Bloise, Q. Mohsen, *Sci. Rep.* **11** (2021) 12371 (https://doi.org/10.1038/s41598-021-91688-0)
26. J. Upadhyay, T. M. Das, R. Borah, *Int. J. Polym. Anal. Charact.* **26** (2021) 354 (https://doi.org/10.1080/1023666X.2021.1891799)
27. C. Abdul Kadar, M. Faisal, N. Maruthi, N. Raghavendra, B. Prasanna, S. Manohara, *Macromol. Res.* **30** (2022) 638 (https://doi.org/10.1007/s13233-022-0067-z)
28. A. Samadi, M. Xie, J. Li, H. Shon, C. Zheng, S. Zhao, *Chem. Eng. J.* **418** (2021) 129425 (https://doi.org/10.1016/j.cej.2021.129425)

29. R. Jamal, L. Zhang, M. Wang, Q. Zhao, T. Abdiryim, *Prog. Nat. Sci.: Mater. Int.* **26** (2016) 32 (https://doi.org/10.1016/j.pnsc.2016.01.001)
30. G. Gustafsson, Y. Cao, G. M. Treacy, F. Klavetter, N. Colaneri, A. J. Heeger, *Nature* **357** (1992) 477 (https://doi.org/10.1038/357477a0)
31. T. Anirudhan, S. Rejeena, *J. Mater.* **2015** (2015) 636409 (https://doi.org/10.1155/2015/636409)
32. V. J. Mayani, S. V. Mayani, S. W. Kim, *Sci. Rep.* **7** (2017) 7239 (https://doi.org/10.1038/s41598-017-07707-6)
33. R. Manivannan, J. Ryu, Y.-A. Son, *Colloids Surfaces, A* **608** (2021) 125601 (https://doi.org/10.1016/j.colsurfa.2020.125601).

Journal of the Serbian Chemical Society
JSCS-info@shd.org.rs • www.shd.org.rs/JSCS
J. Serb. Chem. Soc. *91* (1) 71–84 (2026)
JSCS–5478
Original scientific paper
Published 6 February,2026

Georgian bentonite clay–polymer system as a carrier for volatile oil in topical applications

LIA TSIKLAURI[1]*, ANA JANEZASHVILI[1] and MALKHAZ GETIA[2]

[1]*Department of Technology of Pharmaceutical Products, Biologically Active Additives & Cosmetics, Iovel Kutateladze Institute of Pharmacochemistry, Tbilisi State Medical University, Tbilisi, Georgia and* [2]*Department of Pharmaceutical Analysis & Standardization, Iovel Kutateladze Institute of Pharmacochemistry, Tbilisi State Medical University, Tbilisi, Georgia*

(Received 13 May, Revised 18 July, Accepted 25 November 2025)

Abstract: This study focuses on developing a polymer–clay hybrid system using a Georgian bentonite clay (Tikha-Ascane, TA) and Carbopol (CA) as a carrier for an essential oil (EO) derived from *Matricaria chamomilla* L. cultivated in East Georgia. EO was extracted *via* hydro distillation and characterized using GC–MS and FTIR techniques. The CA–TA and CA–TA–EO formulations were evaluated for key physicochemical parameters including pH, viscosity, rheology, spreadability, compatibility, moisture loss, uniformity and stability. The EO yield was 0.3 % from air-dried plant material. The main components were bisabolol oxide A (38.2 %), *α*-bisabolol oxide B (12.91 %), (*cis*)-*β*-farnesene (11.8 %), *α*-bisabolol (8.83 %), spathulenol (2.27 %), chamazulene (1.99 %), *cis*-ene-yne-dicycloether (6.51 %) and *β*-copaene (0.38 %). These results suggest that the local chamomile chemotype is rich in bisabolol oxide A. The optimized hydrogel formulation was homogeneous, stable and demonstrated favorable rheological properties, making it suitable for topical application. Chromatographic analysis confirmed the successful incorporation of the EO into the gel, which achieved an encapsulation efficiency of 58.34 %. Overall, the study confirms the compatibility of Georgian bentonite clay with the CA polymer, forming an effective matrix for volatile oil delivery in semisolid dosage forms.

Keywords: *Matricaria chamomilla*; Tikha-Ascane; essential oil-bentonite hybrid

INTRODUCTION

Essential oils (EOs), which are complex mixtures of volatile compounds, possess numerous bioactivities and have potential applications in several industries such as the pharmaceutical, cosmetics and medicine industries. The content and chemical composition of EO are different and depend on many factors such as

* Corresponding author E-mail: l.tsiklauri@tsmu.edu
https://doi.org/10.2298/JSC250513086T

geographical locations, climate, the season of sampling and the method of extraction.[1] *Matricaria chamomilla* EO (MEO) exhibits strong anti-inflammatory, antioxidant, antimicrobial and antiviral properties and is classified as generally recognized as safe (GRAS) by the FDA.[2] It is widely utilized to treat various bacterial skin infections. However, its high volatility and instability, necessitate a delivery approach that improves stability and minimizes rapid evaporation to preserve its therapeutic benefits.[3–5]

One potential solution to this issue is the encapsulation of essential oils within inorganic matrices, such as clay minerals. Clays, like bentonite are widely used as pharmaceutical ingredients or carriers due to their biocompatibility, interlayer spacing, thermal and chemical stability. The high specific surface area, excellent ion-exchange capacity, natural abundance and cost-effectiveness of bentonites make them efficient carriers for volatile oils. Loading EOs into the silicate, lowers the evaporation rate or slows the mass transfer of volatile components to the external environment. Encapsulating various types of EOs into bentonite is an efficient way to prepare novel hybrids with antifungal and antibacterial properties. Numerous studies have focused on developing EO–bentonite composites using a variety of essential oils. The use of these clays as delivery systems for essential oils represents a novel and promising approach.[4,6]

Over recent years, polymer–clay hybrid materials have been widely utilized in drug delivery systems due to their enhanced technological properties, including rheology and drug incorporation efficiency. These materials combine the advantages of both components, such as swelling, water absorption and bioadhesion.[7] In addition, polymer-based topical hydrogels are a promising drug delivery system for hydrophobic compounds.[8]

In this study, we describe for the first time the synthesis of a Carbopol based gel with EO obtained from *M. chamomilla* L. cultivated in Georgia and intercalated in Tikha-Ascane (TA). TA is a Georgian bentonite clay preparation obtained from the Askana Deposit (Ozurgeti region, Georgia) and investigated at the I. Kutateladze Institute of Pharmacochemistry (TSMU). The biomedical and pharmaceutical applications of TA have been approved by national public health authorities. Based on this preparation, various dermatological formulations have been developed at the Institute of Pharmacochemistry (TSMU).[9,10]

EXPERIMENTAL

Preparation

Tikha-Ascane (TA), obtained from Georgian bentonite clay, was available at the Pharmaceutical Technology Direction (I. Kutateladze Institute of Pharmacochemistry, TSMU). Carbopol 940 (CA) and methanol (catalogue no. 34860) were purchased from Sigma–Aldrich; *n*-hexane was obtained from Carl Roth (Karlsruhe, Germany), and calcium chloride anhydrous granules were supplied by Merck. All other solvents and chemicals obtained from commercial sources were of analytical grade.

Plant material

Matricaria chamomilla L. aerial parts, cultivated in Shiraki (41°17'38" N, 46° 20'27" E, 595 m asl Kiziki Floristic Region, Georgia) were collected in early June. An 120 g air-dried sample was crushed and hydrodistilled for 2 h (1:5 herb-to-water ratio) using a Clevenger-type apparatus. The resulting dark blue essential oil with a distinct aroma was stored at 4–5 °C until analysis.

Qualitative and quantitative analysis of essential oil

MEO constituents were analyzed using an Agilent GC–MS system (GC 7890B with 5977A mass detector) equipped with an HP-5MS UI column (30 m×0.25 mm i.d.; film thickness 0.25 μm). A 1 μL sample (1:100 by volume in hexane) was injected with a split ratio of 1:150, using helium as the carrier gas (1 mL/min flow, 3 mL/min purge). The oven was programmed from 140 to 215 °C at 3 °C/min, held for 4 min; injection temperature was 250 °C. MS detection was performed in TIC and SIM modes (70 eV, 40–550 amu). The relative content of each compound was expressed as a percentage of the total chromatographic area, based on the mean of three replicates. Identification was performed by comparing retention times and mass spectra with the NIST database.[11]

Characterization of MEO

MEO volatility was evaluated by exposing a specified quantity to the laboratory environment (room temperature, 55±5 % RH), with weight loss assessed at 3, 24, 48 and 120 h.[11]

Preparation of gel base and formulation

The CA–TA gel base was prepared using 1.5 mass % CA and 2 mass % bentonite in an optimized 80:20 ratio. A 1% concentration of essential oil was selected based on prior data, yielding hydrogels with desirable rheological properties, stability and ease of application.[13] To prepare the gel, 2 g of bentonite was dispersed in 4 mL of deionized water, followed by incorporation of MEO. With continuous stirring, the remaining water was gradually added and the MEO loaded clay dispersion was mixed with the 1.5 % CA gel to obtain the final hydrogel.

Characterization of formulations

Physical appearance and homogeneity were evaluated through visual inspection.[14]

pH Determination

The pH of all samples was determined at room temperature using a digital pH-meter (model MW150 MAX) immediately after preparation and during stability studies. The electrode was immersed into the undiluted formulations for 2 min, and the readings were recorded in triplicate.[13]

Viscosity measurement and rheological properties

A rotational viscometer (Brookfield viscometer) was used to determine the viscosity of the samples at 25±2 °C with a spindle speed of 10 rpm. The rheograms were evaluated by plotting the obtained values of shear stress *versus* shear rate.[14]

Determination of spreadability

The spreadability of the samples was evaluated using two sets of glass slides (20 cm×20 cm). 0.5 g of the formulations were weighed and placed within a circle of 1 cm diameter premarked on a glass slide. A second glass plate was positioned on it, forming a sandwich arrangement. A weight of 500 g was placed on the upper plate for about 5 min and diameters of spread circles were assessed.

The spreadability index (*Si*) was calculated using Eq. (1); results were obtained in relation to applied mass and spreading area:[15]

$$Si = d^2 \frac{\pi}{4} \quad (1)$$

where d is diameter (mm).

The spreadability factor (*Sf*) was calculated as:

$$Sf = \frac{A}{W} \quad (2)$$

where A is the total area (mm^2) and W is the total weight (g).

FTIR spectroscopy

FTIR analysis was conducted to inspect the compatibility of active components with excipients. Spectra of MEO, TA and Carbopol 940 were recorded for both unloaded and loaded gel formulations in the 400–4000 cm^{-1} range using a Jasco 600-IR spectrometer with a deuterated triglycine sulphate (DTGS) detector and KBr beam splitter. The essential oil was equilibrated at ambient temperature before analysis, and the resulting spectra were used as spectral fingerprints.

Determination of MEO content

Before GC–MS analysis, the samples were pretreated as follows: 0.1 g of CA–TA—MEO gel or 2.5 μg of MEO was mixed with methanol, filtered through a 0.45 μm filter, and 5 μL of the resulting solution was injected into the GC inlet *via* a split/splitless injector.

Moisture loss

The accurately weighed samples (2 g) were kept in closed desiccators containing anhydrous calcium chloride and reweighed after three days.[12] The percentage moisture loss was assessed using the following equation:

$$W = 100 \frac{W_0 - W_1}{W_0} \quad (3)$$

where W_0 is initial weight (g) and W_1 is final weight (g).

Optical microscopy

Light microscopy was used to study the microscopic characteristics of the optimized formulations. Samples were placed onto a microscopic slide and uniformly spread with a coverslip. The coverslipped slides were observed at room temperature under an optical microscope (Carl Zeiss Jena CF250) at 350× magnification and photomicrographs were captured on a laboratory PC.[12]

Centrifugation test

The centrifugation test was carried out to evaluate phase separation. A 2 g sample was spun at 5000 rpm for 10 min at room temperature in a 15 mL tube.

Statistical analysis

All analyses were performed in triplicate, and the means and standard deviations of the experimental data were calculated using Microsoft Office Excel.

RESULTS AND DISCUSSION

Composition of essential oil

The average yield of the oil from the dry chamomile aerial parts was calculated as 0.3 %. The components in the oil were examined using instrumental conditions

set on the GC–MS and identified using direct mass spectral comparison. The qualitative and quantitative characteristics of MEO evaluated by the GC–MS analysis are depicted in Fig. 1.

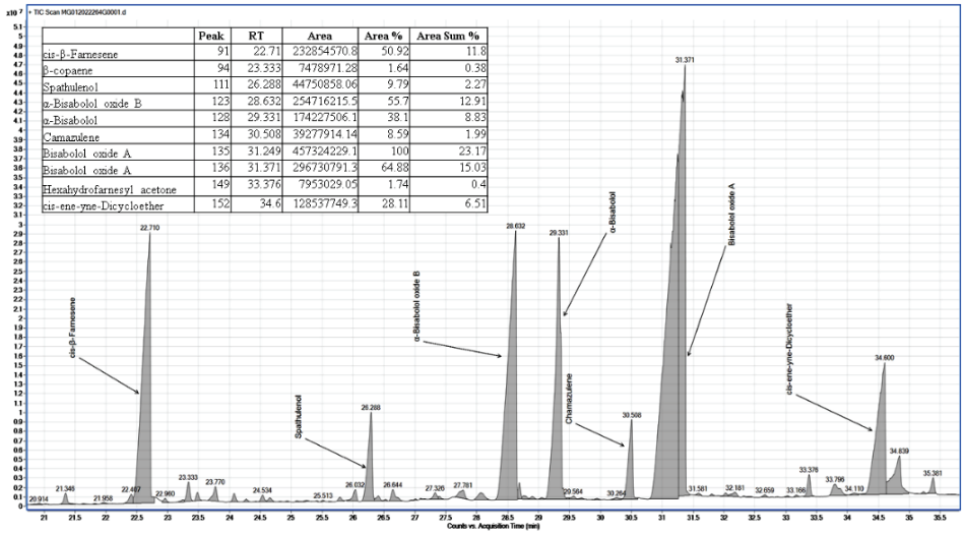

Fig. 1. GC–MS profile of essential oil extracted from dried chamomile aerial parts.

The major constituents were found to be bisabolol oxide A (38.2 %), *α*-bisabolol oxide B (12.91 %), (*cis*)-*β*-farnesene (11.8 %), *α*-bisabolol (8.83 %), spathulenol (2.27 %), chamazulene (1.99 %), *cis*-ene-yne-dicycloether (6.51 %) and *β*-copaene (0.38 %). These findings classify the East Georgian chamomile oil as a bisabolol oxide A chemotype. Bisabolol oxide A, a sesquiterpenoid, is recognized for its broad spectrum of biological activities, including anti-herpetic, antipruritic, antimicrobial, cytotoxic and antileishmanial effects.[16]

FTIR analysis

Essential oils are complex mixtures comprising volatile and aromatic compounds, often associated with a wide range of functional groups. In the present study, MEO was found to contain ethers, amines, carboxylic acid, aromatics, alkanes, aldehyde carbonyl, aldehyde and alcohols (Fig. 2). The assignments of corresponding functional groups were achieved by using frequency data available in the literature.[17–19]

The FTIR spectrum of MEO showed characteristic bands corresponding to its main components. A broad band at 3200–3600 cm^{-1} indicated O–H stretching from alcohols and phenols.[18,19] A peak at ~2926.45 cm^{-1} was assigned to C–H stretching in alkanes.[17,20] The band at ~1717 cm^{-1} was assigned to the C=O stretch

of matricin, with low intensity suggesting its conversion to chamazulene and carboxylic derivatives.[21,22] Peaks at ~1631 and 1660.41 cm^{-1} indicated C=C stretching of alkenes (*e.g.*, farnesene), while that at ~1579 cm^{-1} was assigned to aromatic C=C vibration.[19,27,22–25]

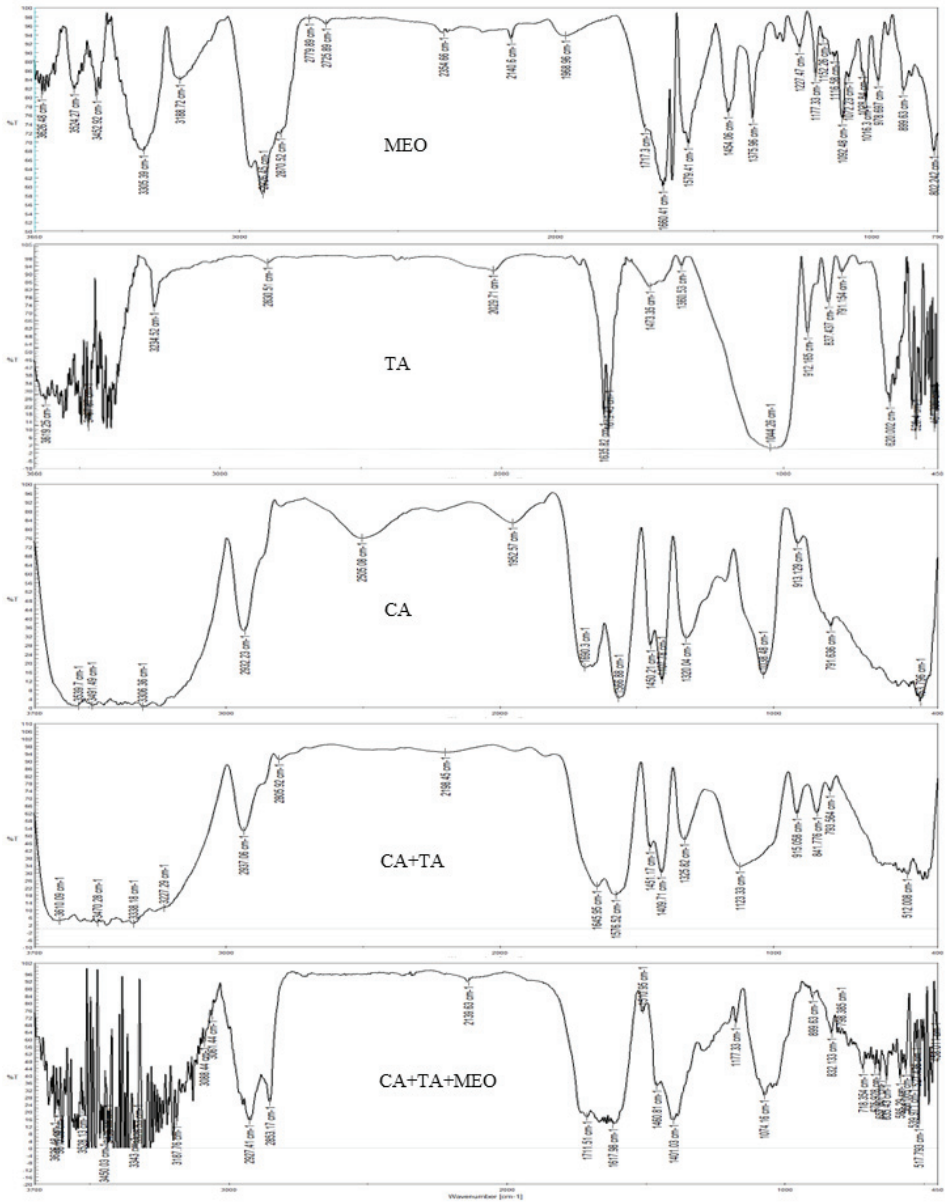

Fig. 2. FTIR spectra of the tested samples.

Bands at ~1454 and 1375 cm^{-1} reflected CH_2 and CH_3 deformation, possibly from α-bisabolol and its oxides.[19,22–25] A peak around 1227 cm^{-1} corresponded to esters and phenolic C–O stretching.[24] Bands between 1177–1016.3 cm^{-1} corresponded to alcohol or ether C–O stretches, including signals from *cis*/*trans*--en-yne-dicycloether.[23,24] Peaks in the 1092–899 cm^{-1} range matched α-bisabolol (tertiary alcohols) while the peak at ~978 cm^{-1} indicated methylene or aromatic in-plane bending.[19,21,23,25] Finally, peaks between 899–802 cm^{-1} were attributed to out-of-plane aromatic C–H bending.[21,24]

The volatilization test revealed that free MEO exhibited weight losses of 20.3, 50.8, 53.0 and 54.7 % after 3, 24, 48 and 120 h, respectively, confirming its high volatility and highlighting the limitations of conventional encapsulation strategies. Bentonite clays, due to their unique layered structure, can effectively interact with essential oil molecules.[26] In this study, the interlayer space of bentonite was activated in water, followed by mechanical intercalation of MEO. This approach enabled successful incorporation of oil into the clay framework, as confirmed by volatilization assays and light microscopy (Fig. 3). Encapsulation of MEO within the bentonite matrix reduced its volatilization by 65.26, 65.32, 68.68 and 68.94 % at 3, 24, 48 and 120 h, respectively, compared to the free, unencapsulated oil, thereby demonstrating enhanced stability and decreased volatility.

As visualized in Fig. 3C, dark, spherical droplets of MEO are distributed throughout the well-dispersed carbopol–bentonite matrix, and the network structure of the hydrogel is capable of protecting the essential oil from evaporating. After addition of Matricaria chamomilla EO, the structure of CA–TA system changed, showing a fibrous-like network, which can be expected as a result of the interactions of matrix components with MEO compounds.

Microscopic analysis of the formulations (Fig. 3) showed that the CA–TA––MEO system exhibits a nearly monodisperse microstructure with small, homogeneously dispersed oil droplets. Droplet size is known to influence the physicochemical stability and mechanical properties of emulsion gels. Generally, smaller droplets with a narrow size distribution improve physical stability.[27]

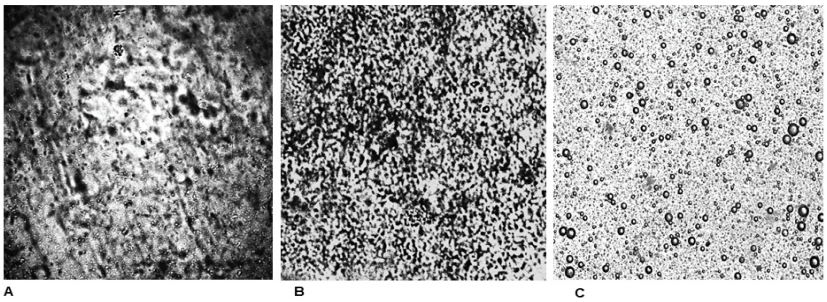

Fig. 3. Light microphotographs of tested samples. A) TA; B) CA–TA matrix; C) MEO loaded hydrogel (1 mass %).

The optical microscopy images of the hybrid microstructure of bentonite modified carbopol gel (Fig. 3B) showed a non-uniform texture. The existence of non-homogeneous areas confirms the interaction between TA and the polymer chains, providing appropriate interconnected architecture in the system. Also, Fig. 3A shows the heterogeneous texture for the aqueous TA suspension (2 mass %), typical of bentonite gels due to the clay platelets' tendency to form a structured network.

The outcome of this study showed that TA clay and the CA polymer are compatible with one another, leading to the formation of stable [TA+CA] matrix suitable for the incorporation of essential oil.

Characterization of formulations

Prepared gels were found to be blue in color, homogeneous and visually acceptable. The gel has the characteristic odor of the essential oil of *Matricaria chamomilla.*

pH Determination

The pH values of the prepared formulations are given in Table I.

The results suggest that CA–TA–MEO gel is skin-compatible and suitable for topical use.[28] The initial pH of bentonite suspensions ranged from 8.6 to 9.0, whereas the pH of CA–TA formulations remained between 6.5 and 6.71, and that of carbopol gels ranged from 6.47 to 6.63.

TABLE I. pH, spreadability and moisture loss of the formulations; *SD*: standard deviation, $n = 3$

Sample	pH (mean±*SD*)	*Sf* / mm^2 g^{-1} (mean±*SD*)	*w* / %
2 % TA	8.84±0.12	–	–
1.5 % CA 940	6.53±0.06	6.89±0.52	3.33±0.05
CA–TA	6.58±0.09	6.39±0.52	4.59±0.04
CA–TA–MEO	6.57±0.04	7.16±0.33	3.76±0.03

Viscosity measurement and determination of rheological properties

The viscosity and rheology of semisolid formulations influence their application behavior and spreadability. The highest viscosity was observed for the bentonite-modified carbopol gel (78,933 cP), while the MEO gel possessed the lowest viscosity (52,267 cP). Bentonite increased the viscosity, whereas MEO incorporation into the CA-TA matrix resulted in a decrease (Fig. 4A).

The viscosity of the CA–TA–MEO gel was assessed at different speed rates; the rheological profile of formulation demonstrated a shear-thinning behavior, where viscosity decreased with increasing shear rate – indicative of a non-Newtonian, pseudoplastic system (Fig. 4C and D).

This property is advantageous for topical applications, as it enables reduced resistance during spreading while maintaining structural integrity at rest. The MEO

gel also displayed an insignificant hysteresis loop, indicating negligible thixotropic properties, a typical feature of carbomer-based gels. Such behavior enhances application consistency and storage stability.[29,30]

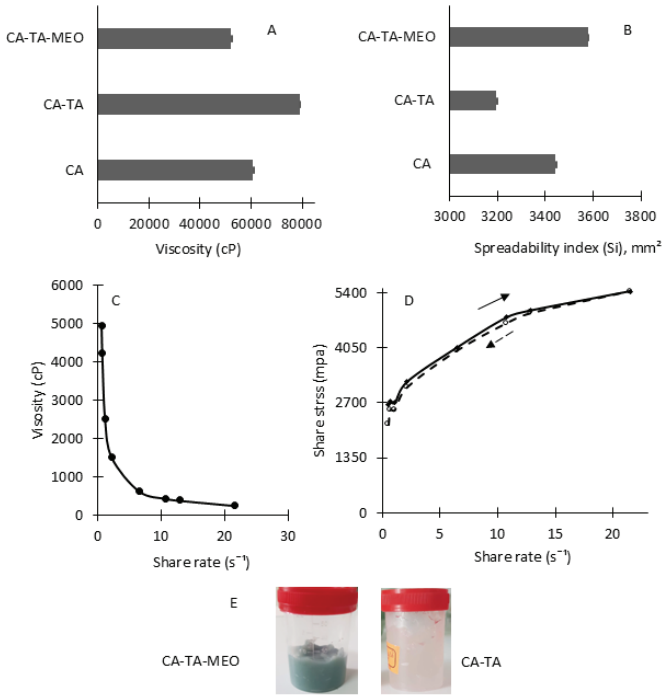

Fig. 4. Evaluation of physical properties and rheological behavior of samples: A) viscosity, B) spreadability measurements, C) viscosity at different shear rates, D) flow profile of CA–TA–EO gel and E) visual presentation of CA–TA and CA–TA–EO formulations.

Determination of spreadability

The effectiveness of topical formulations relies on uniform spreading to ensure accurate dosing and ease of application. Spreadability, a key parameter for semisolid dosage forms, is inversely related to viscosity – a decrease in viscosity leads to improved spreadability. A good spreadability for gel formulations is considered to lie within the 2500–4900 mm^2 range.[31] As shown in fig. 4B and Table I, the CA–TA–MEO gel, with the lowest viscosity, exhibited the highest spreadability index (3579.21 mm^2) and factor, indicating favorable spreading properties suitable for topical use.

FTIR analysis of samples

Infrared spectra of the optimized formulation confirmed the absence of incompatibility among the components. FTIR analysis also contributed to verify the pre-

sence of MEO within the TA-CA gel matrix. Similar to the spectra of CA and TA–CA, the TA–CA–MEO formulation exhibited the characteristic absorption bands of pure CA and TA–CA. The encapsulation of the essential oil by the TA–CA matrix could be evidenced by the appearance of additional specific bands corresponding to components present in MEO (Fig. 2). Bands at 2927.41 and 2853.17 cm^{-1} characteristic of the C–H stretching vibrations of alkanes, were displayed only in the TA–CA–MEO gel. Moreover, absorption peaks at ~1700, 1177 and 899 cm^{-1} in Fig. 2 corresponded to the C=O, stretching of aldehydes, C–O stretching of ethers, and C–H bending of aromatic compounds, respectively.[22]

In the infrared spectrum of Carbopol 940 the characteristic peaks of O–H stretch at 3306.36 cm^{-1} and C–O stretch at 1407.78 cm^{-1} were observed; the peak at 2932.23 cm^{-1} represents CH_2 stretching, whereas the 1450.21 cm^{-1} peak shows the presence of the acrylate back bone (Fig. 2). It is also noted that similar peaks were found in the spectra of the hybrid matrix and TA–CA–MEO gel, confirming the structural integrity of the polymer within the formulation.[32]

The bonds at 3467.87 and 3620.21 cm^{-1} in the spectrum of the original TA are characteristic of Si–OH and Al−OH stretching vibrations in bentonite. A sharp peak at 1044.26 cm^{-1} is associated with Si–O stretching vibration. Compared to the original bentonite, the Si−O absorption peak shifts to a lower wavenumber in the hybrid matrix spectrum, while in the TA–CA–MEO formulation, it moves to a higher wavenumber with reduced intensity–indicating gel network formation. The small peak at 912.16 cm^{-1} is attributed to the bending vibration of −OH in Al–Al–OH, a characteristic feature of bentonite.[33] As shown in Fig. 2, the peak at 791.15 cm^{-1} represents Al–Mg–OH vibrations, while the peak at 620.00 cm^{-1} corresponds to Mg–O–Si or Fe–O–Si groups. Peaks at 528.4 and 461.38 cm^{-1} are related to Al–O and Mg–O, respectively.[34]

FTIR spectral analysis of the essential oil, bentonite, and Carbopol 940 confirmed that the characteristic peaks of the essential oil were preserved in the gel formulation, indicating no significant interactions among the formulation components.

Determination of MEO content

GC–MS analysis revealed comparable chromatographic profiles across the tested formulations, verifying the presence of characteristic constituents of *M. chamomilla* EO (Fig. 5). The MEO content in the CA–TA–MEO gel assessed as a function of the initial EO loading, averaged 58.34 %.

Despite the simplicity of the formulation process, a reduction in MEO content was observed, likely due to volatility or process-related factors that require further investigation. To date, no studies have reported the encapsulation efficiency of *M. chamomilla* EO in bentonite-based gels or the CA–TA system specifically. However, *EE* values for other essential oils range from 47.69 to 57.8 %, depending on

formulation variables, polymer type and analytical methods.[35] The *EE* observed here aligns with these findings, indicating that the CA–TA system forms a stable, well-structured matrix capable of effectively encapsulating MEO.

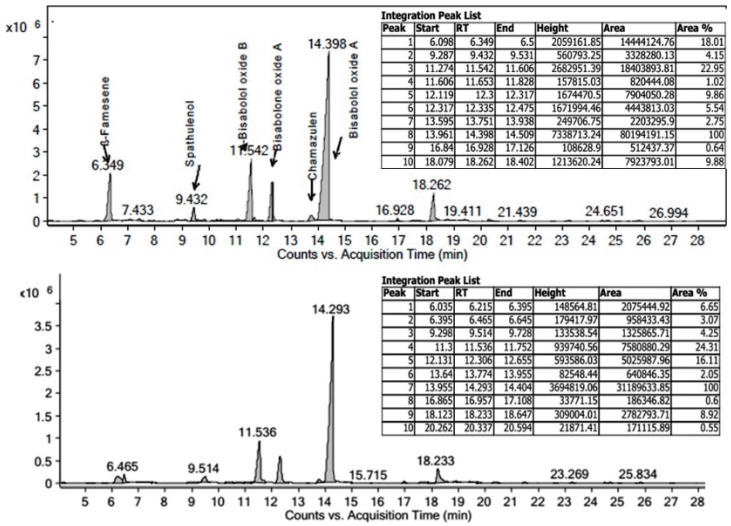

Fig. 5. GC–MS chromatograms of pure MEO (A) and CA–TA–MAO gel formulation (B).

Moisture loss

Water content is fundamental for hydrogel integrity and solubility, as evaporation significantly alters hydrogel properties.[36] Moisture loss analysis (Table I) showed that CA–TA–MEO exibited the lowest loss, which is advantageous for preserving the gel's physical properties during storage. Centrifugation tests further confirmed the physical stability, with no phase separation observed.

CONCLUSION

Matricaria chamomilla essential oil (MEO) demonstrates a wide range of pharmacological activities; however, its high volatility and chemical instability hinder its direct application in topical formulations. Furthermore, MEOs compositions can vary significantly depending on factors such as geographical origin, climate, harvesting season and extraction method.

This study developed and evaluated a Georgian bentonite clay (TA)–polymer system for topical delivery of volatile oils. The gel was formulated with Carbopol (CA) and an MEO–TA hybrid. Analysis confirmed that East Georgian chamomile cultivars belong to the bisabolol oxide A chemotype, with major constituents including bisabolol oxide A, *α*-bisabolol oxide B, (*cis*)-*β*-farnesene, *α*-bisabolol, spathulenol, chamazulene, *cis*-ene-yne-dicycloether and *β*-copaene.

To minimize evaporation and slow the mass transfer of volatile components, an MEO–TA hybrid was incorporated into an 1.5 % Carbopol gel. The resulting MEO–TA–CA formulations satisfied key requirements for semisolid dosage forms, including uniformity, physical stability and suitable rheological behavior. EO droplets were well-incorporated and evenly distributed into the matrix. FTIR analysis confirmed the preservation of MEO's characteristic peaks, indicating the absence of undesirable interactions between the formulation components.

The prepared gel showed a significant encapsulation capacity for MEO, rich in bisabolol oxide A – a bioactive compound with anti-herpes, antipruritic and antimicrobial properties – highlighting the potential of Georgian bentonite clay––polymer systems for topical delivery of volatile oils.

ИЗВОД

ХИБРИДНИ СИСТЕМ ГРУЗИЈСКИ БЕНТОНИТ–ПОЛИМЕР КАО НОСАЧ ЗА ЕТЕРИЧНО УЉЕ У ТОПИКАЛНИМ ПРИМЕНАМА

LIA TSIKLAURI[1], ANA JANEZASHVILI[1] и MALKHAZ GETIA[2]

[1]Department of Technology of Pharmaceutical Products, Biologically Active Additives & Cosmetics, Iovel Kutateladze Institute of Pharmacochemistry, Tbilisi State Medical University, Tbilisi, Georgia u [2]Department of Pharmaceutical Analysis & Standardization, Iovel Kutateladze Institute of Pharmacochemistry, Tbilisi State Medical University, Tbilisi, Georgia

Циљ овог рада је био развој хибридног система полимер–глина коришћењем грузијског бентонита (*Tikha-Ascane*, TA) и полимера *Carbopol* (CA) као носача за етерично уље (EO) добијено из камилице (*Matricaria chamomilla L.*) која је узгајана у Источној Грузији. EO је екстраховано хидродестилацијом и окарактерисано применом GC–MS и FTIR техника. Одређени су основни физичко–хемијски параметри формулација CA–TA и CA–TA––EO, као што су pH, вискозност, реологија, распростирање, компатибилност, губитак влаге и стабилност. Принос EO је био 0,3 % из биљног материјала који је сушен на ваздуху. Главне компоненте су бисаболол-оксид A (38,2 %), α-бисаболол-оксид B (12,91 %), (*cis*)-β-фарнесен (11,8 %), α-бисаболол (8,83 %), спатуленол (2,27 %), камазулен (1,99 %), *cis*-en-in-дициклоетар (6,51 %) и β-копаен (0,38 %). Ови резултати су показали да је локална камилица богата бисаболол-оксидом A. Оптимизована хидрогел формулација је била хомогена, стабилна, са добрим реолошким својствима, погодна за актуелне примене. Хроматографска анализа је потврдила успешно инкорпорирање EO у гел, са ефикасношћу имобилизације од 58,34 %. Генерално, ова испитивања су показала да је грузијски бентонит компатибилан са CA полимером и да формира ефикасну матрикцу за испоруку етеричног уља у получврстом облику.

(Примљено 13. маја, ревидирано 18. јула, прихваћено 25. новембра 2025)

REFERENCES

1. D. P. de Sousa, R. O. S. Damasceno, R. Amorati, H. A. Elshabrawy, R. D. de Castro, D. P. Bezerra, V. R. V. Nunes, R. C. Gomes, T. C. Lima, *Biomolecules* **13** (2023) 1144 (https://doi.org/10.3390/biom13071144)
2. A. El Mihyaoui, J. C. G. Esteves da Silva, S. Charfi, M. E. Candela Castillo, A. Lamarti, M. B. Arnao, *Life* **12** (2024) 479 (https://doi.org/10.3390/life12040479)

3. G. Ren, G. Ke, R. Huang, Q. Pu, J. Zhao, Q. Zheng, M. Yang, *Sci. Rep.* **12** (2022) 8153 (https://doi.org/10.1038/s41598-022-11692-w)
4. J. N. Saucedo-Zuñiga, S. Sánchez-Valdes, E. Ramírez-Vargas, L. Guillen, L. F. Ramos--deValle, A. Graciano-Verdugo, J. A. Uribe-Calderón, M. Valera-Zaragoza, T. Lozano--Ramírez, J. A. Rodríguez-González, J. J. Borjas-Ramos, J. D. Zuluaga-Parra, *Microporous Mesoporous Mater.* **316** (2021) 110882 (https://doi.org/10.1016/j.micromeso.2021.110882)
5. L. H. Oliveira, I. S. de Lima, E. R. S. da Neta, S. G. de Lima, P. Trigueiro, J. A. Osajima, E. C. da Silva-Filho, M. Jaber, M. G. Fonseca, *Appl. Clay Sci.* **245** (2023) 107158 (https://doi.org/10.1016/j.clay.2023.107158)
6. A. Giannakas, I. Tsagkalias, D. S. Achilias, A. Ladavos, *Appl. Clay Sci.* **146** (2017) 362 (https://doi.org/10.1016/j.clay.2017.06.018)
7. F. Sorouri, P. Azimzadeh Asiabi, P. Hosseini, A. Ramazani, S. Kiani, T. Akbari, M. Sharifzadeh, M. Shakoori, A. Foroumadi, L. Firoozpour, M. Amin, M. Khoobi, *Polym. Bull.* **80** (2023) 5101 (https://doi.org/10.1007/s00289-022-04306-y)
8. M. Chelu, *Gels* **10** (2024) 636 (https://doi.org/10.3390/gels10100636)
9. I. G. Kutateladze, *Tikha-Ascane for medical purpose*, Gruzmedgiz, Tbilisi, 1955, p. 40
10. L. Tsiklauri, I. Dadeshidze, G. Tsagareishvili, *Bull. Georgian Natl. Acad. Sci.* **150** (1994) 262 (ISSN 0132-1447)
11. N. Tsivelika, E. Sarrou, K. Gusheva, C. Pankou, T. Koutsos, P. Chatzopoulou, A. Mavromatis, *Biochem. Syst. Ecol.* **80** (2018) 21 (https://doi.org/10.1016/j.bse.2018.06.001)
12. R. Ensandoost, H. Izadi-Vasafi, H. Adelnia, *J. Macromol. Sci. Phys.* **61** (2021) 225 (https://doi.org/10.1080/00222348.2021.1999043)
13. N. Ullah, A. Amin, A. Farid, S. Selim, S. A. Rashid, M. I. Aziz, S. H. Kamran, M. A. Khan, N. Rahim Khan, S. Mashal, M. M. Hasan, *Gels* **9** (2023) 252 (https://doi.org/10.3390/gels9030252)
14. M. Singh, J. Kanoujia, P. Parashar, M. Arya, C. B. Tripathi, V. R. Sinha, S. K. Saraf, S. A. Saraf, *Drug Deliv. Transl. Res.* **8** (2018) 591 (https://doi.org/10.1007/s13346-018-0489-5)
15. B. Siddiqui, A. U. Rehman, I. U. Haq, N. M. Ahmad, N. Ahmed, *J. Microencapsul.* **37** (2020) 595 (https://doi.org/10.1080/02652048.2020.1829140)
16. I. Ikeda-Ogata, K. Yamasaki, K. Yokomizo, T. Ikeda, H. Seo, *Curr. Top. Phytochem.* **17** (2021) 63 (http://www.researchtrends.net/tia/article_pdf.asp?in=0&vn=17&tid=24&aid=6834)
17. Ö. Süfer, F. Bozok, *J. Therm. Anal. Calorim.* **140** (2020) 253 (https://doi.org/10.1007/s10973-019-08829-x)
18. S. Agatonovic-Kustrin, P. Ristivojevic, V. Gegechkori, T. M. Litvinova, D. W. Morton, *Appl. Sci.* **10** (2020) 7294 (https://doi.org/10.3390/app10207294)
19. L. Ciko, A. Andoni, F. Ylli, E. Plaku, K. Taraj, *J. Int. Environ. Appl. Sci.* **11** (2016) 154 (https://dergipark.org.tr/tr/download/article-file/571496)
20. M. I. Morar, F. Fetea, A. M. Rotar, M. Nagy, C. A. Semeniuc, *Bull. UASVM Food Sci. Technol.* **74** (2017) 37 (https://doi.org/10.15835/buasvmcn-fst:12634)
21. H. Schulz, M. Baranska, H. H. Belz, P. Rösch, M. A. Strehle, J. Popp, *Vib. Spectrosc.* **35** (2004) 81 (https://doi.org/10.1016/j.vibspec.2003.12.014)

22. K. Taraj, I. Malollari, A. Andoni, L. Ciko, P. Lazo, F. Ylli, A. Smeni, A. Como, *J. Environ. Prot. Ecol.* **18** (2017) 117 (https://scibulcom.net/en/article/Sut8GqESZGR7LPJJlKEw)
23. M. D. Berechet, E. Manaila, M. D. Stelescu, G. T. Craciun, *Rev. Chim.* **68** (2017) 2787 (https://doi.org/10.37358/RC.17.12.5979)
24. Y. Q. Li, D. X. Kong, H. Wu, *Ind. Crops Prod.* **41** (2013) 269 (https://doi.org/10.1016/j.indcrop.2012.04.056)
25. A. Andoni, F. Ylli, P. Lazo, K. Taraj, A. Çomo, *BSHN (UT)* **24** (2017) 152 (https://api.fshn.edu.al/uploads/1_Andoni_et_al_rreg_3bb9aef7ff.pdf)
26. L. H. de Oliveira, P. Trigueiro, J. S. N. Souza, M. S. de Carvalho, J. A. Osajima, E. C. da Silva-Filho, M. G. Fonseca, *Colloids Surfaces, B* **209** (2022) 112186 (https://doi.org/10.1016/j.colsurfb.2021.112186)
27. J. Santos, L. A. Trujillo-Cayado, F. Carrillo, M. L. López-Castejón, M. C. Alfaro-Rodríguez, *Polymers* **14** (2022) 2195 (https://doi.org/10.3390/polym14112195)
28. X. Nqoro, S. A. Adeyemi, P. Ubanako, D. T. Ndintehal, P. Kumar, Y. E. Choonara, B. A. Aderibigbe, *Polym. Bull.* **81** (2024) 3459 (https://doi.org/10.1007/s00289-023-04879-2)
29. M. F. A. Khan, A. Ur Rehman, H. Howari, A. Alhodaib, F. Ullah, Z. ul Mustafa, A. Elaissari, N. Ahmed, *Gels* **8** (2022) 277 (https://doi.org/10.3390/gels8050277)
30. Y. Maslii, O. Ruban, G. Kasparaviciene, Z. Kalveniene, A. Materiienko, L. Ivanauskas, A. Mazurkeviciute, D. M. Kopustinskiene, J. Bernatoniene, *Molecules* **25** (2020) 5018 (https://doi.org/10.3390/molecules25215018)
31. M. X. Chen, K. S. Alexander, G. Baki, *J. Pharm. (Cairo)* **2016** (2016) 5754349 (https://doi.org/10.1155/2016/5754349)
32. J. El Karkouri, M. Bouhrim, O. M. Al Kamaly, H. Mechchate, A. Kchibale, I. Adadi, S. Amine, S. Alaoui Ismaili, T. Zair, *Plants* **10** (2021) 2068 (https://doi.org/10.3390/plants10102068)
33. M. G. Martins, D. O. A. Martins, B. L. C. de Carvalho, L. A. Mercante, S. Soriano, M. Andruh, M. D. Vieira, M. G. F. Vaz, *J. Solid State Chem.* **228** (2015) 99 (https://doi.org/10.1016/j.jssc.2015.04.024)
34. M. Edraki, D. Zaarei, *J. Nanoanalysis* **5** (2018) 26 (https://sanad.iau.ir/fa/Journal/jnanoanalysis/DownloadFile/988806)
35. K. G. Torres, R. R. Almeida, S. Y. de Carvalho, J. F. Haddad, A. A. Leitao, L. G. Guimaraes, *Mater. Today Commun.* **24** (2020) 101252 (https://doi.org/10.1016/j.mtcomm.2020.101252)
36. A. Vesković, D. Nakarada, A. Popović Bijelić, *Polym. Test.* **98** (2021) 107187 (https://doi.org/10.1016/j.polymertesting.2021.107187).

Journal of the Serbian Chemical Society
JSCS@tmf.bg.ac.rs • www.shd.org.rs/JSCS
J. Serb. Chem. Soc. *91* (1) 85–97 (2026)
JSCS–5479
Original scientific paper
Published 6 February,2026

Temporal and spatial distribution of physicochemical parameters and water quality indices in an oligotrophic dam lake: A case of Maksutlu Dam Lake, Sivas, Türkiye

MENEKŞE TAŞ DİVRİK[1]* and RUTKAY ATUN[2]

[1]*Sivas Cumhuriyet University, Şarkışla Aşık Veysel Vocational School, Şarkışla, 58400, Sivas, Türkiye and* [2]*Sivas Cumhuriyet University, Faculty of Engineering, Department of Geomatics Engineering, 58140, Sivas, Türkiye*

(Received 7 January, revised 3 February, accepted 11 April 2025)

Abstract: This study was conducted at three selected stations in Maksutlu Dam Lake (Şarkışla, Sivas), covering both the dry season (August 2023) and the rainy season (May 2024). Water samples were collected from the lake and a total of 18 physicochemical parameters were analyzed. The eutrophication index (*EI*), organic pollution index (*OPI*) and nutrient pollution index (*NPI*) values were calculated for both seasons based on the physicochemical parameters of the lake water. Additionally, a Geographic Information System (GIS) was used to show the seasonal variation in index values. Bray–Curtis and Pearson correlation analyses were applied to the physicochemical parameters of the water. As a result, it was found that both the physicochemical parameters and water quality indices of the lake exhibited seasonal variation. Phosphate pollution was detected in the lake and it was found that the lake may be oligotrophic in terms of NO_3 and Mg values. Several suggestions were also made for the sustainable management of the dam lake.

Keywords: geographic information system; reservoir; organic pollution index.

INTRODUCTION

Dam lakes are aquatic ecosystems formed by the accumulation of water in large areas behind embankments, created by building a dike across a river valley, typically at its narrowest point. While dam lakes were once the primary sources of drinking water and agricultural irrigation, they now play a significant role in activities such as energy production, transportation, industry and tourism. Dam lakes are also crucial structures for flood protection. Acidification, eutrophication, and various changes in hydrology and geomorphology are the primary pressures affecting the integrity of these lakes.[2]

* Corresponding author. E-mail: menekse.tas@cumhuriyet.edu.tr
https://doi.org/10.2298/JSC250107027T

The excessive input of plant nutrients, particularly nitrogen and phosphorus, into lakes promotes the growth of organic matter, algae, periphyton and macrophytes, leading to eutrophication. This growth results in changes to aquatic organisms and water quality.[3] As a consequence of eutrophication, decreases in dissolved oxygen levels can lead to hypoxia and toxic algal blooms.[3]

Human activities, including domestic and industrial wastewater discharge and agricultural runoff, contribute to the physical, chemical, and biological pollution of freshwater resources, leading to the deterioration of water quality. This situation also limits the use of freshwater resources for various purposes.[4] Additionally, intensive and excessive use of these resources can harm both the environment and the organisms that depend on them.

Sivas Province is located in the central part of the Anatolian Peninsula, in the Upper Kızılırmak section of the Central Anatolia Region. The province, with an average altitude of over 1,000 m, exhibits continental climate characteristics. Summers are very hot, dry and short, while winters are cold, long and snowy. There are 15 dam lakes in Sivas Province, used for irrigation, energy production and drinking water. In the Şarkışla district, there are three dam lakes: Maksutlu, Yapıaltın and Kanak. Kanak Dam was built to meet the drinking and utility water needs in Şarkışla and to irrigate agricultural lands. Maksutlu and Yapıaltın dams are primarily used for irrigation. Recreation and picnic areas are located around Maksutlu Dam Lake, which is situated close to the Şarkışla district center.[5]

There are few studies on the dam lakes in Şarkışla.[6,7] One study evaluated both the physicochemical data and benthic macroinvertebrates of Kanak Dam Lake by sampling water and benthos monthly for one year.[6] Another study compared the filling rates of Maksutlu Dam Lake between 2010 and 2019.[7] It emphasized that there were decreases in the filling rates of the dam due to drought and that the dam lake should be used rationally. The study also reported that necessary measures should be taken to address the water crisis that may occur during dry periods and that a water management plan should be prepared for Maksutlu Dam Lake.

This study examined certain physicochemical parameters during both the dry and rainy periods of Maksutlu Dam Lake, which has not been studied in detail before. First, water quality values were determined according to various criteria.[8,9] Second, three different water quality indices were applied to the physicochemical parameters. Third, the spatial distribution of the index values across the dam lake was mapped using the IDW interpolation method. Fourth, the relationships between the physicochemical data were investigated using various statistical methods. Finally, several recommendations were made for the sustainable use of the dam lake.

EXPERIMENTAL

Details related to the sampling locations are given in the Supplementary material to this paper.

The research was conducted through both field and laboratory work. During the fieldwork, water temperature was measured using a simple thermometer (°C), electrical conductivity (*EC*) was measured with a conductivity meter (μS cm^{-1}), pH was determined using a pH meter and total dissolved solids (TDS) were measured with a portable device (ppm). For the measurement of other physicochemical parameters *(DO*, BOD_5, *COD*, Cl, salinity, Ca, Mg, total hardness (*TH*), NO_3, NO_2, NH_4-N, SO_4, PO_4), water samples were collected using a Ruttner water sampler and transferred to the laboratory in 2-L dark glass bottles.

The water samples brought to the laboratory were prepared for analysis without delay. Classical titrimetric and spectrophotometric methods were used for this purpose.[10] The quality of the water samples was determined according to specific criteria.[8,9]

All statistical data were analyzed using Microsoft Office Excel 20 (LogBase10) and SPSS 9.0 software to reveal the similarity between stations and physicochemical parameters.[11] The relationship between physicochemical parameters was examined using Pearson correlation analysis conducted in IBM SPSS Statistics, version 27.[12]

Water quality indices

The *EI* is used to evaluate the trophic conditions of the surface water body. *COD*, dissolved inorganic nitrogen (*DIN* / mg L^{-1}), and dissolved inorganic phosphorus (*DIP* / mg L^{-1}) are used to calculate the *EI* values, which are computed using the formula below. An *EI* value less than 1 indicates the absence of eutrophication, while a value of 1 or greater indicates the presence of eutrophication:[3,13]

$$EI = 10^6 \frac{COD \times DIN \times DIP}{4500} \tag{1}$$

OPI is used to assess the organic pollution status of surface water resources. *COD*, *DIN*, *DIP*, *DO* and their standard concentration values are used to calculate the *OPI*. The standard concentration values of COD_S, DIN_S, DIP_S and DO_S were taken from the references in the previous study.[8,13] The value obtained from the formula was evaluated as follows. <0: Excellent water quality, 0–1: good water quality, 1–2: water starting to be polluted, 2–3: lightly polluted water, 3–4: moderately polluted water, >4: heavily polluted water.[13,14] *OPI* values were calculated using the following formula:

$$OPI = \frac{COD}{COD_S} + \frac{DIN}{DIN_S} + \frac{DIP}{DIP_S} + \frac{DO}{DO_S} \tag{2}$$

The *NPI* values of the dam lake were calculated using the NO_3 and PO_4 parameters in surface water sources. These values were calculated using the following formula. The obtained value categorizes the pollution levels as follows. <1: no pollution, 1–3: moderately polluted, 3–6: significantly polluted, >6: very high pollution.[13,15] The NO_3-N maximum limit (mg L^{-1}) is referred to as MAC_N, and the PO_4-P maximum limit (mg L^{-1}) is referred to as MAC_P, with values taken from the criteria:[13]

$$NPI = \frac{C_N}{MAC_N} + \frac{C_P}{MAC_P} \tag{3}$$

The IDW interpolation technique was used to show the spatial distribution of index values on the dam. In IDW interpolation, the distances between the data points are first calculated for estimation. Then, weight values are determined based on the distance of each data point. Finally, the predicted value at a specific location is calculated by taking the weighted average of the points with known locations.[16] In the formula, $Z(x)$ represents the predicted value; $Z(x_i)$ represents

the values of known points in the environment; w_i is the weight of each point; and N represents the number of points in the environment:

$$Z(x) = \frac{\sum_{i=1}^{N} w_i Z(x_i)}{\sum_{i=1}^{N} Z w_i} \quad (4)$$

RESULTS AND DISCUSSION

The water quality classes, based on physicochemical data and the average values obtained from sampling in Maksutlu Dam Lake during the dry and rainy seasons, are given in Table I.[8,9]

TABLE I. Water parameters and mean values of Maksutlu Dam Lake in dry and rainy seasons. Min: Minimum; Max; Maximum; Ave: Average; *WT*: water temperature; *EC*: electrical conductivity; *DO*: dissolved oxygen; BOD_5: biological oxygen demand; *COD*: chemical oxygen demand; *TDS*: total dissolved solids; *TSS*: total suspend solid; Cl: chloride; Ca: Calcium; Mg: magnesium; *TH*: total hardness; NO_3: nitrate nitrogen; NO_2: nitrite nitrogen; NH_4-N: ammonium nitrogen; PO_4: phosphate; SO_4: sulfate

Parameter	Unit	Dry season			Rainy season			Min–Max	Ave	Class
		Station			Station					
		1	2	3	1	2	3			
WT	°C	32.5	32.2	34	19.3	18.3	18	18–34	25.7	I
EC		384	268	344	573	495	513	268–573	429.5	I and II
pH		8.23	8.56	7.86	8.01	8.31	7.91	7.86–8.56	8.15	II
DO	mg L^{-1}	4.37	4.76	3.04	7.23	7.80	6.66	3.04–7.80	5.64	III
BOD_5	mg L^{-1}	32.3	25.4	42.3	10.2	15.01	9.78	9.78–42.3	22.5	III
COD	mg L^{-1}	54.8	35.5	55.2	14.5	18	14.2	14.2–55.2	32.03	I and II
TSS	mg L^{-1}	120	360	210	105	318	165	105–360	213	
TDS	ppm	176	268	167	286	247	256	167–286	233.3	I
Cl	mg L^{-1}	38.98	41.98	39.98	29.99	26.99	31.99	26.99–41.98	34.99	I and II
Salinity	‰	0.02	0.01	0.03	0.02	0.03	0.03	0.01–0.03	0.02	
Ca	mg L^{-1}	26.45	24.08	20.04	101	48	70	20.04–101	48.26	
Mg	mg L^{-1}	3.41	2.69	2.38	2.96	1.33	1.99	1.33–3.41	2.46	
TS	FS °	12.4	13	10.6	0.8	1	1.2	1–12.4	6.50	
NO_3	mg L^{-1}	16.50	21.27	16.50	44	47.90	53.51	16.50–53.5	33.28	I and II
NO_2	mg L^{-1}	0	0	0.023	0.02	0.02	0	0–0.023	0.01	I
NH_4-N	mg L^{-1}	0.013	0.019	0.017	0.044	0.012	0.008	0.008–0.04	0.02	I
PO_4	mg L^{-1}	0.19	0.32	1.56	1.245	0.023	1.305	0.023–1.56	0.77	
SO_4	mg L^{-1}	5.57	11.56	5.95	9.89	10.33	10.39	5.57–11.56	8.95	I

Water temperature is a highly effective factor on biotic components in aquatic ecosystems. It plays an important role in reproduction, nutrition, and metabolic activities. Increase in temperature increases the rate of biological activity and decreases oxygen saturation.[17] It was observed that the water temperature values of the dam lake vary seasonally. During the dry season sampling, an increase in both

air and water temperatures was noted. The average water temperature placed the lake in class I water quality.

The *EC* value is an indicator of the total amount of dissolved substances in water. *EC* values vary depending on the geological structure and the amount of precipitation. It was found that the *EI* values of the lake water were higher in the rainy season (Table I). The primary reason for this is the significant outflow into the lake during the rainy season. During this period, a large amount of material from outside the lake is transported into it by rain or snowmelt. The average *EI* values were found to range between Class I and Class II water quality.[8] The pH value is an indicator of water acidity.[18] When the average pH value of the dam lake was analyzed, it was determined that the water quality was Class II.[8] It can be concluded that the lake water exhibits basic properties.

The solubility of oxygen in water is inversely proportional to temperature. Additionally, a wavy lake surface and high moisture content increase the solubility of oxygen. As the salt concentration in the water increases, the amount of dissolved oxygen decreases.[19] It was observed that the *DO* values of the lake varied significantly between the dry and rainy periods. During the dry season, the water temperature increased due to heat, and the lake water evaporated. As a result, the *DO* values were found to be quite low in the dry season. However, during the rainy season, the water level of the lake increased due to rainfall, which in turn increased the *DO*. In terms of *DO*, it was determined that the lake water fell under Class III water quality. BOD_5 is defined as the amount of oxygen required by bacteria to break down organic matter under aerobic conditions.[20] Based on the average BOD_5, the dam lake was classified as Class III water quality. *COD* is the amount of oxygen required for the breakdown of chemical compounds. The *COD* value is inversely proportional to the *DO*. *COD* values are generally higher than BOD_5 values because *COD* measures the total organic matter present in a water sample, while BOD_5 only indicates the amount of biodegradable organic matter.[21] In this study, *COD* values were higher than BOD_5 values, supporting the findings in the literature. It was determined that the lake waters were classified as between Class I and Class II water quality based on the average *COD*.

Knowing the total amount of soluble substances or minerals in natural waters is an important parameter for defining the chemical composition of water. It also provides general information about the bottom structure, which contributes to the productivity of the water.[20] The TDS originate from agricultural runoff, industrial wastewater, natural sources, and domestic activities. The main ions that contribute to the *TDS* include bicarbonates, carbonates, sulfates, chlorides, nitrates, magnesium, sodium, potassium, calcium and others. In addition, silt, clay, small organic particles, inorganic substances, soluble organic compounds, plankton and other microscopic organisms also contribute to the *TDS*.

The Cl is an important component of all natural waters and is generally found in low concentrations. High concentrations indicate that salinity and *EC* values are also high.[22] Based on the average Cl values, the lake water was found to fall between Class I and Class II water quality.

The Ca is one of the most abundant elements in natural waters.[23,24] The source of Ca ions in water comes from calcium carbonate and calcium sulfate minerals. Therefore, Ca can be found in waters at varying concentrations. The Ca is the most important ion contributing to water hardness.[25] According to some researchers, water is classified as soft if Ca is less than 10 mg L^{-1}, moderately hard if it ranges from 20–25 mg L^{-1}, and hard if it exceeds 25 mg L^{-1}.[20] In this study, the average value was found to be 48.26 mg L^{-1}. Since the lithological structure of the study area consists of volcanic formations, the concentration of Ca ions may be high. This elevated value indicates that the lake has very hard water.

The Mg is one of the ions that contribute to the hardness of water. Since Mg is present in the composition of chlorophyll, it is vital for chlorophyllous plants. It also regulates phosphorus metabolism in algae, fungi and bacteria. Low Mg levels in lakes significantly affect phytoplankton productivity, resulting in the lake acquiring oligotrophic characteristics.[26] Mg concentrations in natural waters typically range between 10–50 mg L^{-1}.[17] The average Mg value in this study was found to be 2.46 mg L^{-1}.

The nitrates are the most common mineral form of nitrogen in oxygen-rich waters and is an important factor that can either limit or promote algal growth. It is found in trace amounts in surface waters. The amount of nitrogen is low in oligotrophic waters and quite high in eutrophic waters. NO_3-N, an essential element for the intensive development of phytoplankton, is typically found in waters at concentrations between 1–10 mg L^{-1}. It was determined that the lake water falls between Class I and Class II water quality in terms of the average NO_3-N value. The NO_2 is an intermediate product in the biological oxidation of ammonium to nitrate. The concentration of NO_2 is generally low in natural waters but can reach high levels in areas with organic pollution and low oxygen levels.[26] In this study, it was found that the average NO_2-N values of the lake were classified as Class I water quality. In clean and oxygenated waters, NH_4 compounds are found at very low levels. NH_4 is a waste product of aquatic organisms and is reabsorbed by other organisms.[19] Many algae and higher plants can directly take up NH_4. Generally, NH_4 levels should be 1 mg L^{-1} or less. Based on this parameter, the water quality was considered Class I.[12]

It has been reported that productivity is high in waters with PO_4 content between 0.15 and 0.30 mg L^{-1}, but when the PO_4 content exceeds 0.30 mg L^{-1}, the water is considered polluted. When the phosphate level exceeds 0.50 mg L^{-1}, the water shows excessive pollution and causes eutrophication.[23] Waters with a total phosphorus concentration of 20 μg L^{-1} or higher are considered eutrophic.[27]

The SO_4 is an ion that must be present in natural waters to enhance biological efficiency. If its concentration is insufficient, phytoplankton development is inhibited and plant growth slows down. SO_4 values in natural lakes typically range from 3 to 30 mg L^{-1}.[28] An increase in SO_4 concentrations in aquatic environments, caused by various industrial wastes, agricultural runoff, and domestic effluents, is an indicator of pollution. SO_4 levels greater than 250 mg L^{-1} signify serious contamination.[23] It was found that the lake had Class I water quality based on the average SO_4 concentration.

Pearson correlation analysis was applied to the physicochemical parameters of lake water that show a normal distribution. According to the Pearson correlation analysis with *WT*, very strong positive correlations were observed between BOD_5, *COD* and chloride Cl. A positive correlation was found between *TDS* and NO_3 and sulfate SO_4. Since NO_3 and SO_4 are ions that form part of salts, the of *TDS* in water increases as they dissolve. A negative correlation was found between BOD_5 and *TDS* and SO_4 in relation to *WT* and NO_3. Additionally, a general relationship was observed between SO_4, *WT*, BOD_5 and *COD*. The correlation coefficients from the Pearson correlation analysis are presented in Table II.

TABLE II. Pearson correlation analysis and correlation coefficients. *WT*: water temperature; BOD_5: biological oxygen demand; *COD*: chemical oxygen demand; *TDS*: total dissolved solids; Cl: chloride; SO_4: sulphate; NO_3: nitrate; *: correlation is significant at 0.01 level ($p < 0.01$); **: correlation is significant at 0.01 level (2-tailed). –: indicating that no statistically significant correlation was detected

	WT	BOD_5	*COD*	*TDS*	Cl	SO_4	NO_3
WT	1						
BOD_5	**0.923****	1					
COD	**0.941****	**0.962****	1				
TDS	–0.676	**–0.835***	**–0.878***	1			
Cl	**0.943****	0.777	**0.813***	–0.498	1		
SO_4	–0.582	–0.768	–0.808	**0.927****	–0.390	1	
NO_3	**–0.988****	**–0.930****	**–0.948****	0.682	–0.895*	0.627	1

The *EI*, *OPI* and *NPI* index values of the dam lake were calculated (Table III) using the formulas provided above. When evaluating the *EI* values in terms of stations, they were ranked as 1 < 2 < 3 during the dry season and 2 < 1 < 3 during the rainy season. The *OPI* values were also ranked as 1 < 2 < 3 in the dry season and 2 < 1 < 3 in the rainy season. For the *NPI* values, the ranking was 2 < 1 < 3 in both the dry and rainy seasons. The lowest *EI* value was observed at station 2 during the rainy season (326), while the highest *EI* value was recorded at station 3 during the dry season (23122). The lowest *OPI* value was found at station 2 during the rainy season (3.29), while the highest value was observed at station 3 during the dry season (13.16). The lowest *NPI* value was recorded at station 1 during the

dry season, while the highest value was found at station 3 during the rainy season. Water quality index values are presented in Table III.

TABLE IV. Water quality index values (*EI*, *OPI* and *NPI*) of stations in the dry and rainy seasons

Station	Dry season			Rainy season		
	EI	*OPI*	*NPI*	*EI*	*OPI*	*NPI*
1	2835	4.05	2.48	1311	3.62	11.42
2	3981	4.41	1.70	326	3.29	3.75
3	23122	13.16	12.63	16307	12.03	12.53

The Bray–Curtis similarity dendrogram for the stations is presented in Fig. 2. This dendrogram summarizes the similarity of physicochemical data between the stations based on Bray–Curtis similarity analysis. The first and third stations showed the highest similarity (91.60 %), while the second station had a lower similarity to the other two stations (82.35 %).

Fig. 2. Bray–Curtis Similarity dendogram of stations.

Remote sensing methods, which have significantly increased in use in recent years, can be employed to determine both water quality and pollution levels.[28,29] In this study, maps showing the distribution of index values across stations were created using a Geographic Information System (GIS). The index values for the stations were generated using GIS, and the corresponding maps are presented in Fig. 3. The spatial distribution of *EI*, *OPI* and *NPI* index values in dry and wet seasons using the IDW method is also presented in Fig. 3.

In the dry season, *EI* values ranged from 2835 (low) to 23122 (high). Lower values were observed in the western and southwestern parts of the map, particularly near the 1st station, while higher values were concentrated around the center and 3rd station. This was due to a significant decrease in the lake's water level caused by evaporation from warming air, which resulted in high eutrophication index values due to increased NO_3 and PO_4 concentrations. These elevated values in the central regions may indicate the accumulation of nutrient loads, which could contribute to eutrophication (Fig. 3a). During the rainy season, *EI* values decreased significantly, ranging from 326 (low) to 16307 (high). Although there was a general decrease in *EI* values, high values were still observed around the 3rd station. This could be due to the dilution of nutrient enrichment caused by increased precipitation (Fig. 3b).

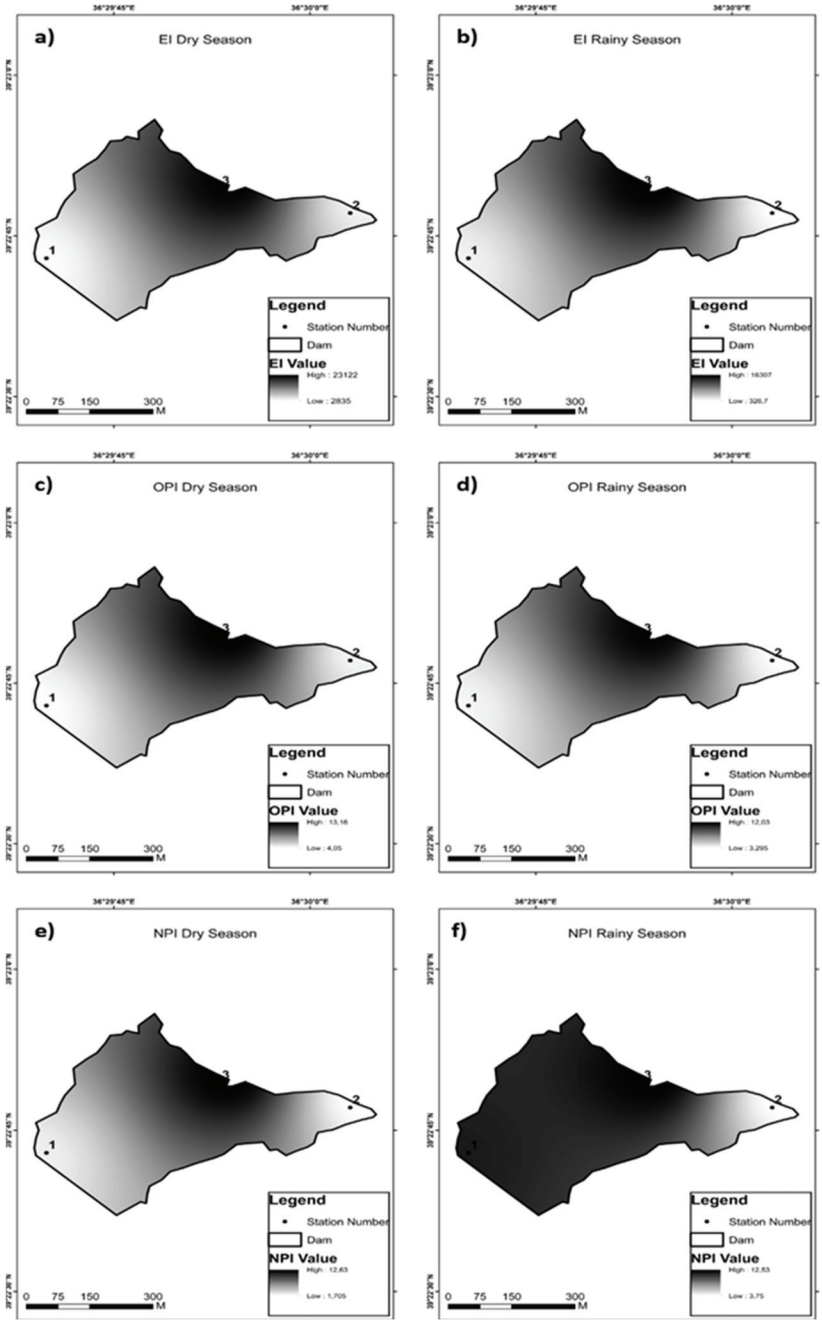

Fig. 3. a) Spatial distribution of *EI* in dry season. b) Spatial distribution of *EI* in rainy season. c) Spatial distribution of *OPI* in dry season. d) Spatial distribution of *OPI* in rainy season. e) Spatial distribution of *NPI* in dry season. f) Spatial distribution of *NPI* in rainy season.

In the dry season, *OPI* values ranged from 4.05 (low) to 13.16 (high). During the rainy season, *OPI* values ranged from 3.29 (low) to 12.03 (high). While *OPI* values generally decreased slightly compared to the dry season, the organic load remained high in the central regions and around the 3rd station (Fig. 3d). This suggests that organic pollution persists even during wetter conditions, particularly near the 3rd station.

In the dry season, *NPI* values ranged from 1.705 (low) to 12.63 (high). High *NPI* values were observed around the 3rd station and some central areas, while the region around the 1st station exhibited low values (Fig. 3e). This indicates moderate to high levels of pollution in the central areas, particularly near the 3rd station. In the rainy season, *NPI* values varied between 3.75 (low) and 12.53 (high). The *NPI* index generally increased across all areas during the rainy season (Fig. 3f), possibly due to the dilution of pollutants and the introduction of additional runoff from surrounding regions.

During the rainy season, *OPI* the values range from 3.29 (low) to 12.03 (high). Although the *OPI* values generally decreased slightly during the rainy season, the organic load remains high in the center and 3rd station (Fig. 3d). In the dry season, the *NPI* index ranges from 1.705 (low) to 12.63 (high). The area around 3rd station and some parts of the center show high *NPI* values in the dry season. The area around 1st station shows low values (Fig. 3e). In the rainy season, the index varies between 3.75 (low) and 12.53 (high). Accordingly, the *NPI* seems to have generally increased in all areas during the rainy season (Fig. 3f). In addition, 3rd station has high values for all three indices, which is an indication that this area is a serious impact zone. In summary, the effect of seasonal variations is evident at all stations.

In this study, seasonal changes in the physicochemical parameters of Maksutlu Dam Lake were analyzed, and the application of pollution indices such as *EI*, *OPI*, and *NPI* revealed varying levels of eutrophication, organic pollution, and nutrient pollution across different seasons. As a result, while our study shows similarities with some studies, it also reveals differences. Anthropogenic activities occurring in water bodies lead to an increase in nutrient levels, reduce water quality and limit its intended uses. Excessive nutrient input causes the overgrowth of aquatic plants, which leads to algal blooms and a decrease in the oxygen content of the water.

CONCLUSION

In the present study, some physicochemical parameters of Maksutlu Dam Lake were evaluated during both dry and rainy periods. According to the results, the average values of *WT*, *TDS*, NO_2-N, NH_4-N, and SO_4 were classified as Class I water quality; the average values of *EC*, *COD*, Cl and NO_3-N were found to fall between Class I and Class II water quality; the average pH value was classified as Class II water quality; and the average values of *DO* and BOD_5 were classified as Class III water quality. The *EI*, *OPI*, and *NPI* index values were also evaluated for

both seasons in the study. These index values were analyzed using GIS. In conclusion, the NO_3-N and Mg parameters, along with the water quality index values, indicate that the lake may be oligotrophic. The findings obtained from the study show that the dam lake is suitable for irrigation. It was also found that the lake is under the influence of eutrophication, organic pollution and nutrient pollution. To ensure the sustainability of the dam lake, two suggestions can be made below.

1) These and similar studies should be conducted periodically, and the physicochemical, pesticide and toxicological content of the lake, as well as benthic macroinvertebrates, should be examined and monitored comprehensively.

2) Satellite data and GIS should be utilized for large-scale monitoring of nutrient levels and eutrophication trends in water bodies. Monitoring water quality with satellite data and GIS has been proven to secure the long-term biodiversity and sustainability of water resources, as well as maintain ecosystem health.

SUPPLEMENTARY MATERIAL

Additional data and information are available electronically at the pages of journal website: https://www.shd-pub.org.rs/index.php/JSCS/article/view/13203, or from the corresponding author on request.

ИЗВОД

ВРЕМЕНСКА И ПРОСТОРНА ДИСТРИБУЦИЈА ФИЗИЧКО–ХЕМИЈСКИХ ПАРАМЕТАРА И ИНДЕКСА КВАЛИТЕТА ВОДЕ У ОЛИГОТРОФНОМ ВЕШТАЧКОМ ЈЕЗЕРУ: СЛУЧАЈ ЈЕЗЕРА МАКСУТЛУ, СИВАС, ТУРСКА

MENEKŞE TAŞ DİVRİK[1] и RUTKAY ATUN[2]

[1]*Sivas Cumhuriyet University, Şarkışla Aşık Veysel Vocational School, Şarkışla, 58400, Sivas, Türkiye и* [2]*Sivas Cumhuriyet University, Faculty of Engineering, Department of Geomatics Engineering, 58140, Sivas, Türkiye*

Ова студија је спроведена на три одабране станице у језеру Максутлу Дам (Шаркисла, Сивас), покривајући сушну сезону (август 2023. год.), као и кишну сезону (мај 2024. год.). Из језера су прикупљени узорци воде, а анализирано је укупно 18 физичко–хемијских параметара. Вредности индекса еутрофикације (*EI*), индекса органског загађења (*OPI*) и индекса загађења нутријентима (*NPI*), израчунате су за обе сезоне на основу физичко––хемијских параметара језерске воде. Поред тога, коришћен је Географски информациони систем (GIS) за приказ сезонских варијација у вредностима индекса. На физичко–хемијске параметре воде примењене су Bray–Curtis и Pearson корелационе анализе. Као резултат тога, утврђено је да и физичко–хемијски параметри и индекси квалитета језерске воде показују сезонске варијације. У језеру је детектовано фосфатно загађење и установљено је да језеро може бити олиготрофно у погледу садржаја NO_3 и Mg. Дато је и неколико предлога за одрживо управљање вештачким језером које је настало изградњом бране.

(Примљено 7. јануара, ревидирано 6. фебруара, прихваћено 11. априла 2025)

REFERENCES

1. M. E. Sönmez, *Gaziantep Üniversitesi Sosyal Bilimler Dergisi* **11** (2012) 213 (https://dergipark.org.tr/en/download/article-file/223356) (in Turkish)

2. J. Young, A. Watt, P. Nowicki, D. Alard, J. Clitherow, K. Henel, R. Johnson, E. Laczko, D. McCracken, S. Matouch, J. Niemela, C. Richards, *Conserv. Biol.* **14** (2005) 1641 (https://doi.org/10.1007/s10531-004-0536-z)
3. C. W. Chen, Y. R. Ju, C. F. Chen, C. D. Dong, *Int. Biodeterior, Biodegrad*. **113** (2016) 318 (https://doi.org/10.1016/j.ibiod.2016.03.024)
4. V. Kumar, A. Sharma, R. Kumar, R. Bhardwaj, K. A. Thukral, J. Rodrigo-Comino, *Hum. Ecol. Risk Assess*. **26** (2020) 1 (https://doi.org/10.1080/10807039.2018.1497946)
5. *Sivas Province Environmental Status Report*, Republic of Turkey Sivas Governorship Provincial Directorate of Environment, Urbanization and Climate Change, Sivas, 2023
6. M. Taş Divrik, M. Öz Laçin, K. Kalkan, S. Yurtoğlu, *Aqua Sci. Eng*. **36** (2021) 1 (https://doi.org/10.26650/ASE2020699151)
7. S. Dirican, *Anim. Fish. Res*. **5** (2021) 1 (https://dx.doi.org/10.22161/ijfaf.5.6.1)
8. *TSWQR Turkish Water Quality Regulation*, Official Gazette No 28483, 2021, Turkey
9. *Turkey Surface Water Quality Regulation*, Water Pollution Quality Control Regulation, Official Gazette Number: 25687, 2004, Türkiye (in Turkish)
10. O. Egemen, U. Sunlu, *Water quality*, Ege University Printing and Publishing house, İzmir, 1999
11. N. McAleece, J. D. G. Gage, P. J. D. Lambshead, G. L. J. Paterson, *BioDiversity professional statistic analysis software*, Jointly developed by the Scottish Association for Marine Science and the Natural History Museum, London, 1997
12. C. J. Krebs, *Ecological Methodology*, Benjamin, Cummings, CA, 1999
13. M. Varol, C. Tokatlı, *Chemosphere* **311** (2023) 137096 (https://doi.org/10.1016/j.chemosfer.2022.137096)
14. P. Barnwal, S. Mishra, S. K. Singhal, *J. Int. Sci. Technol*. **3** (2015) 22 (http://www.pubs.iscience.in/journal/index.php/jist/article/view/266/149)
15. B. O. Isiuku, C. E. Enyoh, *Environ. Adv*. **2** (2020) 100018 (https://doi.org/10.1016/j.envadv.2020.100018)
16. E. Köse, A. Çiçek, S. Aksu, C. Tokatlı, Ö. Emiroğlu, *Bull. Environ. Contam. Toxicol*. **111** (2023) 38 (https://doi.org/10.1007/s00128-023-03781-x)
17. M. Mugwanya, M. A. O. Dawood, F. Kimera, H. Sewilam, *Aquacult. Fish*. **7** (2022) 223 (https://doi.org/10.1016/j.aaf.2021.12.005)
18. S. K. Dewangan, D. N. Toppo, A. Kujur, *Int. J. Res. App. Sci. Eng. Tech*. **9** (2023) 765 (https://doi.org/10.22214/ijraset.2023.55733)
19. S. Cirik, Ş. Cirik, Limnoloji Ege Üniversitesi Su Ürünleri Fakültesi Yayınları, Ege Üniversitesi Basımevi, İzmir, 1999
20. J. Noskovič, M. Babošová, J. Ivanič Porhajašová, *Pol. J. Environ. Stud*. **26** (2017) 1607 (https://doi.org/10.15244/pjoes/67749)
21. A.B. Abdullahi, A.R. Siregar, W. Pakiding, M. Riwu, in Proceedings of The 3rd International Conference of Animal Science and Technology, 2021, Antalya, Türkiye, IOP Conf. Ser.: Earth Environ. Sci, IOP Publishing, Indonesia, Abstract No. 012155, (https://doi.org/10.1088/1755-1315/788/1/012155)
22. D. L. Corwin, K. Yemeto, *Soil Sci. Soc. Am. J*. **83** (2019) 1 (https://doi.org/10.2136/sssaj2018.06.0221)
23. S. O. Akinnowa, *Environ. Chall.* **12** (2023) 100733 (https://doi.org/10.1016/j.envc.2023.100733)
24. Ç. Güler, Z. S. Çobanoğlu, *Sağlık Bakanlığı Yayınları*, Ankara, 1997
25. Y. Yan, T. Yu, H. Zhang, J. Song, C. Qu, J. Li, B. Yang, *Crystals* **11** (2021) 1494 (https://doi.org/10.3390/cryst11121494)

26. R. V. Thomann, J. A. Mueller, *Principle of surface water quality modelling and control*, Harper and Row Publishers, New York, 1987
27. T. Atıcı, O. Obalı, *Gazi Üniversitesi Gazi Eğitim Fakültesi Dergisi* **19** (1999) (https://doi.org/10.17693/yunusae.vi.272240)
28. Ö. Gürsoy, R. Atun, *Cumhuriyet Sci. J.* **39** (2018) 543 (https://doi.org/10.17776/csj.422897)
29. Ö. Gürsoy, R. Atun, *Polish J. Environ. Stud*. **28** (2019) 2139 (https://doi.org/10.15244/pjoes/90598).

Journal of the Serbian Chemical Society
JSCS@tmf.bg.ac.rs • www.shd.org.rs/JSCS
J. Serb. Chem. Soc. 91 (1) S51–S52 (2026) *Supplementary material*

SUPPLEMENTARY MATERIAL TO

Temporal and spatial distribution of physicochemical parameters and water quality indices in an oligotrophic dam lake: A case of Maksutlu Dam Lake, Sivas, Türkiye

MENEKŞE TAŞ DİVRİK[1]* and RUTKAY ATUN[2]

[1]Sivas Cumhuriyet University, Şarkışla Aşık Veysel Vocational School, Şarkışla, 58400, Sivas, Türkiye and [2]Sivas Cumhuriyet University, Faculty of Engineering, Department of Geomatics Engineering, 58140, Sivas, Türkiye

J. Serb. Chem. Soc. 91 (1) (2026) 85–97

Maksutlu Dam Lake was constructed for irrigation purposes on the Maksutlu Stream, upstream of Maksutlu village in the Şarkışla district of Sivas Province. The dam, which is of the clay-core homogeneous fill type, serves irrigation needs. The dam lake has a volume of 2,950,000 m³ and irrigates an area of 400 hectares. The dam's height from the riverbed is 19 m. At the normal water level, the lake's volume is 2.95 hm³ and its surface area is 0.42 km².[1] Three stations that best represent the characteristics of the dam lake were selected for this study. Information about these stations and their characteristics is presented in Table S-I.

TABLE S-I. Coordinates and Characteristics of the Stations

Stations	Coordinates	Characteristics of Stations
1	39º 22′ 42″ N 36º 29′ 39″ E	It is just behind the dam embankment.
2	39º 22′ 48″ N 36º 30′ 04″ E	This station is located opposite the dam embankment, very close to agricultural areas.
3	39º 22′ 50″ N 36º 29′ 54″ E	It was selected from a part of the dam lake close to the picnic areas.

The map of the study area and sampling locations is given in Fig. S-1.

* Corresponding author. E-mail: menekse.tas@cumhuriyet.edu.tr

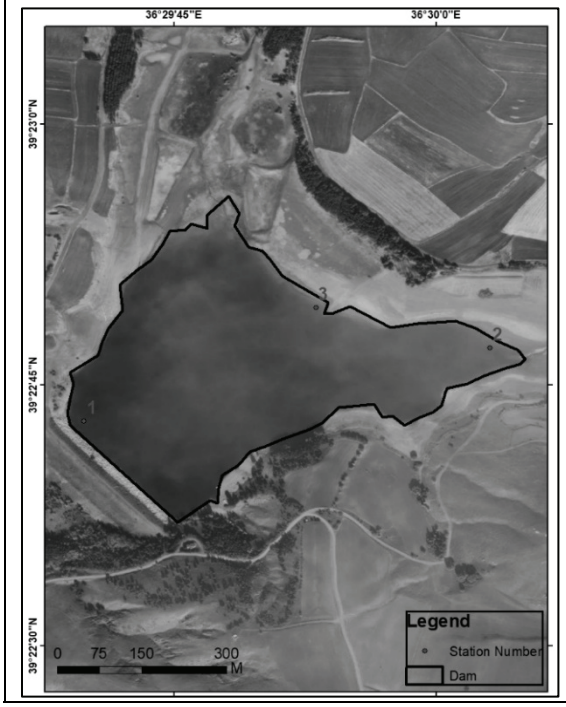

Fig. S-1. Maksutlu Dam Lake and sampling locations.

REFERENCES

1. *Sivas Province Environmental Status Report*, Republic of Turkey Sivas Governorship Provincial Directorate of Environment, Urbanization and Climate Change, Sivas, 2023.